The neural networks used in FDM printing study

Adriana Munteanu*, and *Dragos-Florin* Chitariu

Technical University Gheorghe Asachi of Iasi, Department of Machining Tool, Romania

Abstract. Neural networks have aroused a lively interest since 1943 when Warren McCulloch and Walter Pitts proposed a neural network model (a single layer model), that has remained fundamentally structural even today for most neural networks. Problem solving and implicit the study of a system's operating model such as 3D printing involves the association between input data, hypotheses and output data, and neural networks provide the ability to form their own model of solving. The main difference between neural networks and other information processing systems is the ability to learn from interacting with the environment and so improving performance. A correct representation of information, allowing interpretation, prediction, and response to an external stimulus, can allow the network to build a model of the considered process, in the paper case fused deposition modelling (FDM) process.

1 Introduction

3D printing techniques are used today because products are getting much faster by reducing time and it is possible to obtain nowadays almost any kind of geometry that is intended to be realised. If only 10 years ago it was possible to print just one item, now the capability of the equipment permits the use of over 2000 parts so it is possible to infer where the production of the components will be over 10 years. 3D printing technologies allow the delivery of solutions that are somewhere at the border between processing, digital technologies and the internet, and the beneficiaries discover how easy it is to create and produce almost anything. The biggest benefit is that the user can use a simple interface to get a personalized product, and that's what every customer wants.

The concept of personalized printing is interesting for almost everybody. This is a revolutionary method for creating 3D models and is great for making fast prototypes. By using the utility of inkjet technology saves time and now, it is create a complete model in a single process using 3D printing [1-2].

The rapid prototyping have different advantages as the capability of the method or of the system to produce functional assemblies with the computer aided design help so that to reduce production time. The development of new materials increases the applicability of this technology.

Paper on FDM [1, 3, 4] shown that process parameters such as layer thickness, part build orientation and other parameters have significantly influence on the part dimensional accuracy, roughness and strength of the realized part. The determination of these

* Corresponding author: adycypmunteanu@yahoo.com

parameters for part quality improvement, particularly roughness, by using traditional methodologies will be costly and time consuming for the required level of precision. To solve this problem, present study proposes the artificial neural network (ANN) method for modelling the relationship between temperature, speed and layer thickness.

Many studies are made on the influence of various process parameters on mechanical proprieties of the print [5-7]. From these parameters the layer thickness, the raster angle and the air gap influence mostly the elastic performance of the ABS printing.

2 Experimental researches

In general, any experiment aims to determine the relationships established between the factors who characterize the phenomenon investigated. Due to the complexity of the phenomena, some aspects have to be considered in this study:

- The impossibility of considering the phenomenon in its entirety, with all its interactions and all the factors that determine it;
- The existence of a natural variability of processes and phenomena as a universal feature of the material world.
- The complexity of technological processes that involves a deeply study of them by taking into account some simplifying assumptions.

One of the main issues of technological process research is the establishment of technological parameters that meet certain requirements regarding the productivity and quality of the obtained parts. These researches must be carried out with as little work as possible and with minimal costs.

The quality and precision of the processed surfaces is a criterion of utmost importance in terms of general efforts to raise the quality of production, especially in the case of final operations.

In order to improve process knowledge regarding the 3D printing and particular the FDM technology and to provide a viable guide to the feature optimization of the process, one can use a new tool such as artificial neural network. This technique allowed developing multiple-variables, non-linear models that can be integrated into real-time process control plan [2]. So that by means of a free available program DTREG, one may create various models like: classical, single-tree models and also TreeBoost and Decision Tree Forest models, consisting of assemblies of many trees. DTREG also can generate Neural Networks, Support Vector Machine (SVM), Gene Expression Programming/Symbolic Regression, K-Means clustering, GMDH polynomial networks, Discriminant Analysis, Linear Regression and Logistic Regression models [3, 8].

Table 1. Input values versus output values.

No.	Inputs			Output	
				Experimental	Theoretic
	T [°C]	**V**[mm/s]	$\mathbf{d_s}$ [mm]	Ra	Ra^t
1.	240	30	0.1	5.891	5,812
2.	270	30	0.1	6.195	6,25
3.	240	70	0.1	6.825	6,435
4.	270	70	0.1	7.156	6,123
5.	240	30	0.2	7.972	8,052
6.	270	30	0.2	8.542	8,49
7.	240	70	0.2	8.287	8,675
8.	270	70	0.2	7.329	8,363
Mean values	M M^t			**7,275**	**7,275**

The quality of the printed parts is appreciated in the present work by the roughness of the surfaces, which represents the assembly of relatively small micron regularity relative to the depth and which forms the relief of the actual surface of a part.

The measurement was realized by using a Mitutoyo type inductive roughness. The roughening measurement conditions and the output parameter are presented in Table 1. For experimental data acquisition it has taken into account, in choosing process input parameters, the capability of the 3D printer and the preliminary tests made. These preliminary tests have allowed the establishment of the levels of each factor and the consideration of the technological possibilities of 3D printing (the research was made for a non commercial printer). The technological parameters was considered and varied depending on printer capability, for an ABS material with a filament diameter of 1.75 mm that has good mechanical properties, with excellent impact strength. In terms of print speed, the printer can operate at speeds between 30-70 mm / s. The thickness of the deposited layer may vary between 0.05 mm and 0.3 mm. The printer has a single extruder with a diameter of 0.4 mm that can withstand temperatures up to 300 °C. The quality of the fused deposition modeling parts depends on a great number of parameters both of the workpiece material and of the process. The parameters chosen was made with Taguchi method so that to reduce the input parameters without losing the precision of the experiment results.

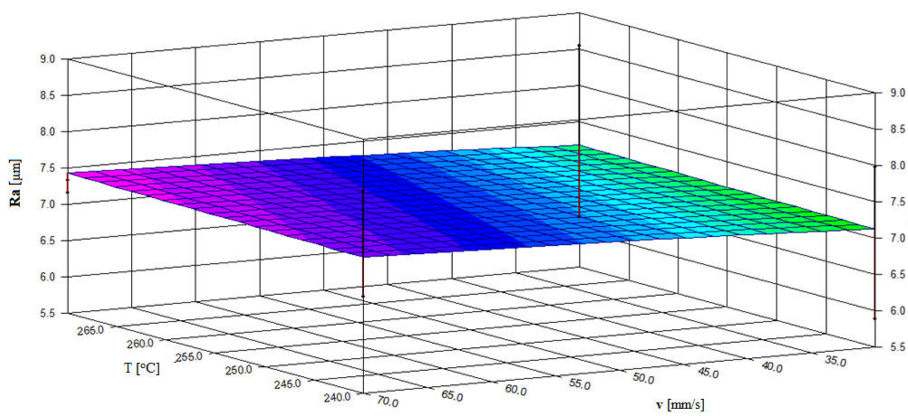

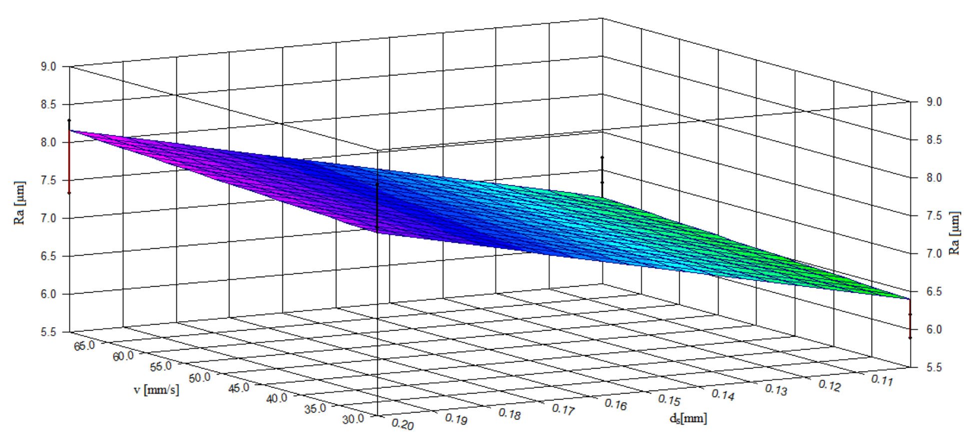

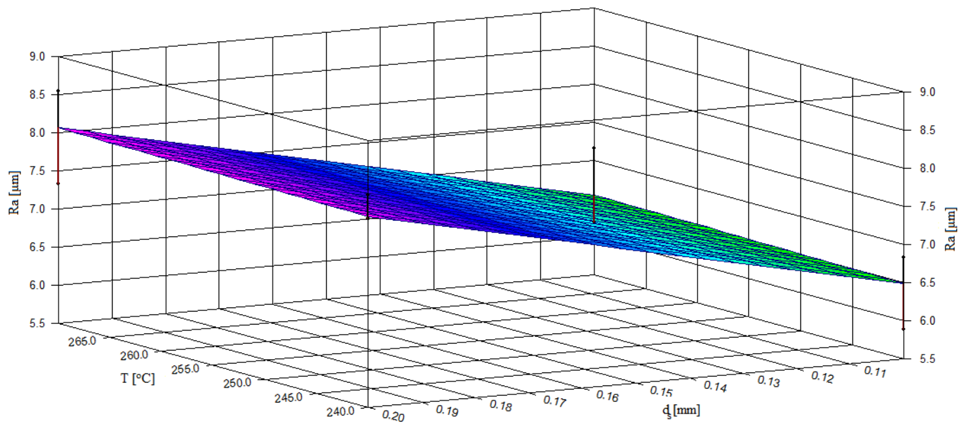

Fig. 1. The variation of the input parameter for Ra parameter.

The variation of the output parameter according to the input parameters can be seen in the graphs of the Figure 1.The graphs show that for this particular case that: the input parameters d_s and v act to increase the roughness (positive response of the system for the increase of these factors); the input factor T acts to decrease the roughness of the printed surface when is increasing this factor and the factor d has the greatest influence (the slope being the largest) and acts in the sense of increasing the roughness of the printed surface by the FDM process, is the main factor [8].

The ANN has the ability to learn from examples make them attractive because did not follow a set of rules and learn by underlying rules of given collection of representative examples. For parameter prediction in case of roughness of the printed part the program can predict the value of an output parameter giving enough input parameter information. In order to model this parameter, an architecture that has 3 levels of layers (1 hidden) was used. The neural networks for roughness is a multilayer perceptron neural network type with one hidden layer, with a variable number of units in the input layer and the hidden layer.

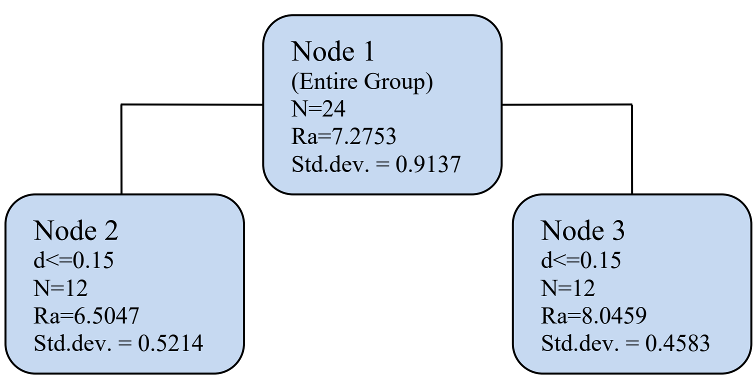

Fig. 2. The main values in nodes.

The number of predictor variables was 3. The neurons found in hidden layer were supposed from 2 to 20, and it was established at 14. The main values for the roughness are presented in figure 2 through the single tree models with the main values in nodes.

A graphic representation of the experimental data obtained versus predicted values for the *Ra* (roughness parameter) is presented in the Figure 3.

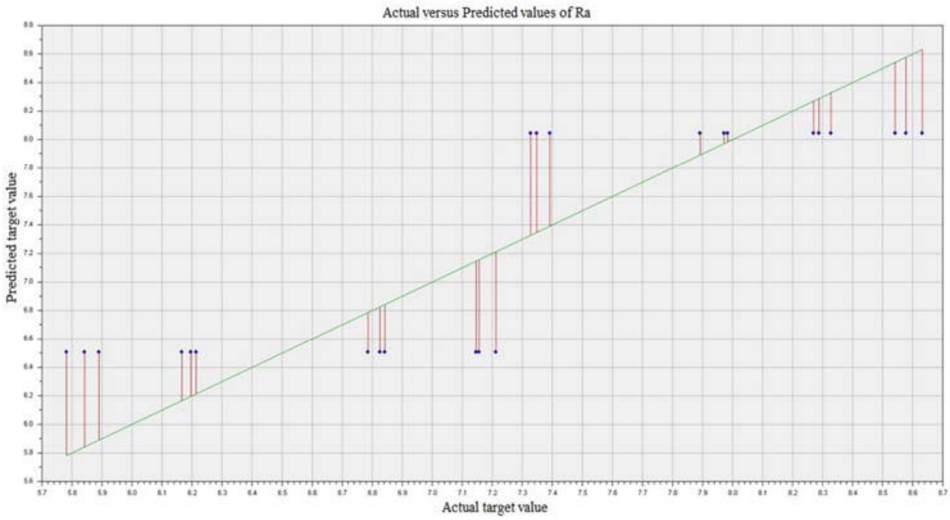

Fig. 3. Actual versus predicted values for Ra.

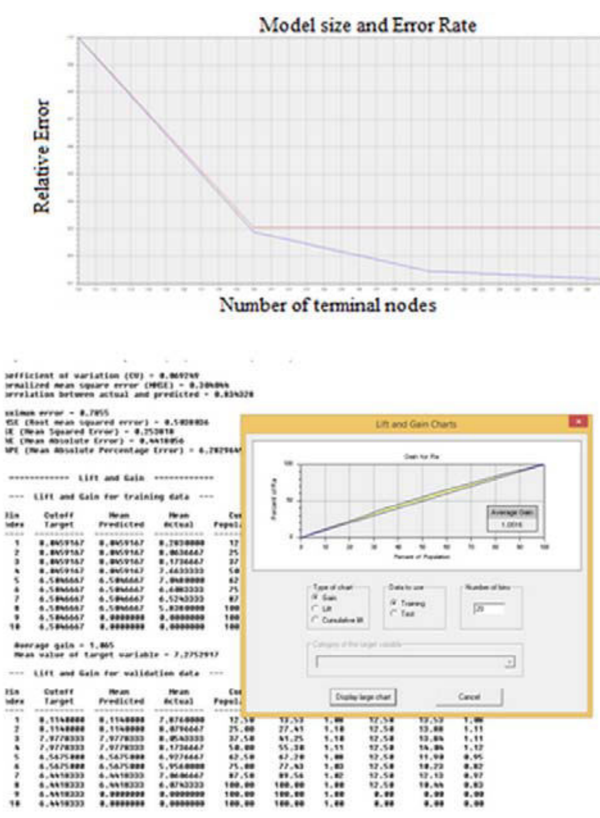

Fig. 4. Model size.

The Actual versus Predicted chart is available only for building the model in Figure 3. When the predicted value differs from the actual value, the points are offset from the diagonal line, and the vertical distance from the line to the point corresponds to the error (residual).

3 Conclusions

The prototype parts solve the necessity of the industrial beneficiaries regarding the products, that must be functional, with a reasonably price and easy to use. This innovative and modern technology (fused deposition modelling) FDM has proven its value assuring functional prototypes of plastic with time, money and manpower saving. The application of artificial neural networks modelling technique allowed the improvement of the process knowledge, and therefore to use this aspect to facilitate process control. The Taguchi method was used for parameters chosen so that to reduce the input parameters number (only three input parameter was considered) without losing the precision of the experiment results.

The model size (graphical representation) emphasize that the output parameter Ra is closer to the expected output (the superior curve, Figure 4). The main difference between neural networks and other information processing systems is the ability to learn from interacting with the environment and so improving performance. From the results, the prediction of the surface roughness of FDM parts emphasize that the main factor was the layer thickness (d_s). The importance of the layer thickness is 100 % relative to the other two input parameters, the temperature and deposition speed.

The reason of neural networks use is its ability meaning from imprecise data so that to extract patterns and detect trends. In upcoming works the research will also focus on analyzing other parameters and then summing these analyzes to make an optimization of chosen the parameters for the particular printer case.

References

1. B.H. Lee, J. Abdullah, Z.A. Khan*,* J Mat. Process. Tech., **169**, 54–61 (2005)
2. K. J.Anil, K.M.Mohiuddin, J.Mao, IEEE, (1996)
3. Anoop Kumar Sood, R. K. Ohdar, S. S. Mahapatra*,* Swarm, Evol. and Mem. Comp., **6466**, 396-403 (2010)
4. A.K. Sood, R.K. Ohdar, S.S. Mahapatra, Mater. and Des. **30(10),** 4243–4252 (2009)
5. D. Ahn, J.H. Kweon, S. Kwon, J. Song, S. Lee, J. of Mater Process Technol. **209**(15-16), 5593–5600 (2009)
6. A. Bernarand, A. Fischer, CIRP annals-Man. Tech., **51**, 635–52 (2002)
7. L. Novakova - Marcincinova, Manuf. and Ind. Eng., **11**, 35-37 (2012)
8. * * * P.H. Sherrod, *DTREG Predictive modelling software.* Available from www.dtreg.com (2018)

polymers

Article

Thermal Expansion of Plastics Used for 3D Printing

Bruno Rădulescu [1], Andrei Marius Mihalache [2], Adelina Hrițuc [2,*], Mara Rădulescu [1], Laurențiu Slătineanu [2], Adriana Munteanu [1], Oana Dodun [2] and Gheorghe Nagîț [2]

[1] Department of Digital Production Systems, "Gheorghe Asachi" Technical University of Iași, 700050 Iaşi, Romania; bruno.radulescu@academic.tuiasi.ro (B.R.); mara.radulescu@academic.tuiasi.ro (M.R.); adriana.munteanu@academic.tuiasi.ro (A.M.)

[2] Department of Machine Manufacturing Technology, "Gheorghe Asachi" Technical University of Iași, 700050 Iaşi, Romania; andrei.mihalache@tuiasi.ro (A.M.M.); slati@tcm.tuiasi.ro (L.S.); oanad@tcm.tuiasi.ro (O.D.); nagit@tcm.tuiasi.ro (G.N.)

* Correspondence: adelina.hrituc@student.tuiasi.ro; Tel.: +40-751640117

Abstract: The thermal properties of parts obtained by 3D printing from polymeric materials may be interesting in certain practical situations. One of these thermal properties is the ability of a material to expand as the temperature rises or shrink when the temperature drops. A test experiment device was designed based on the thermal expansion or negative thermal expansion of spiral test samples, made by 3D printing of polymeric materials to investigate the behavior of some polymeric materials in terms of thermal expansion or contraction. A spiral test sample was placed on an aluminum alloy plate in a spiral groove. A finite element modeling highlighted the possibility that areas of the plate and the spiral test sample have different temperatures, which means thermal expansions or contractions have different values in the spiral areas. A global experimental evaluation of four spiral test samples was made by 3D printing four distinct polymeric materials: styrene-butadiene acrylonitrile, polyethylene terephthalate, thermoplastic polyurethane, and polylactic acid, has been proposed. The mathematical processing of the experimental results using specialized software led to establishing empirical mathematical models valid for heating the test samples from −9 °C to 13 °C and cooling the test samples in temperature ranges between 70 °C and 30 °C, respectively. It was found that the negative thermal expansion has the highest values in the case of polyethylene terephthalate and the lowest in the case of thermoplastic polyurethane.

Keywords: thermal expansion; experimental device; acrylonitrile butadiene styrene; polyethylene terephthalate; thermoplastic polyurethane; polylactic acid; experimental measurements; empirical mathematical models

check for updates

Citation: Rădulescu, B.; Mihalache, A.M.; Hrițuc, A.; Rădulescu, M.; Slătineanu, L.; Munteanu, A.; Dodun, O.; Nagîț, G. Thermal Expansion of Plastics Used for 3D Printing. *Polymers* **2022**, *14*, 3061. https://doi.org/10.3390/polym14153061

Academic Editor: Diego Antonioli

Received: 7 June 2022
Accepted: 25 July 2022
Published: 28 July 2022

Publisher's Note: MDPI stays neutral with regard to jurisdictional claims in published maps and institutional affiliations.

1. Introduction

Thermal expansion of solid materials is a property that considers the increase in size that characterizes the solid body as its temperature rises. The inverse property of thermal expansion is thermal contraction or negative thermal expansion.

Thermal expansion of a part is important in situations where this expansion could affect the integrity or behavior of the assembly of which the part is a component. Because the forces that occur during thermal expansion can be relatively large, they can cause deformation or even breakage of other parts or even the part affected by the expansion.

Thermal expansion is evaluated by considering the ratio between the increase in size under the action of increasing the temperature and the initial value of the dimension affected by heating. This ratio is the coefficient of thermal expansion and is usually used in the case of linear dimensions or volumes of parts affected by thermal expansion.

Significant differences exist between the expansion of metallic materials, plastics, or ceramics. It is appreciated that, in general, the thermal expansion of ceramic materials is less than the thermal expansion of metallic materials, as polymeric plastics have an expansion of about 10 times greater than those of metallic materials. Devices called dilatometers are used to evaluate linear thermal expansion.

With the increasing use of parts made of polymers by 3D printing, it has become important to know the thermal properties of polymers. These properties include thermal expansion.

Seven additive manufacturing technologies are currently considered: vat photopolymerization, material extrusion, material jetting, binder jetting, powder bed fusion, direct energy deposition, and sheet lamination [1]. The process used in this paper was material extrusion. This process involves a wire advanced and extruded through a heated nozzle and deposited in successive layers as a result of precisely controlled movements between the nozzle and the table of the 3D printer until the final part is obtained. Many input factors influence how successive layering occurs in the 3D printing process. These factors include the nozzle hole diameter, the relative movement speed between the nozzle and the printer table, the proposed level for the density of the workpiece material, the nozzle and printer table temperatures, and the cooling level during the 3D printing process, etc.). Due to the values of the input factors, the material of the part manufactured by 3D printing may have different degrees of densification and filling of the space inside the part, which will affect some thermal properties of the part material. Among these properties, there is thermal capacity expansion.

The need to consider thermal expansion as a property of the materials from which 3D printing processes made parts was highlighted by researchers [2–5]. Effective experimental attempts to study thermal expansion specific to polymeric materials used in manufacturing parts by 3D printing were performed by Wang [3] and Miller [6]. The importance of thermal expansion in the use of thermoactivated morphing materials has been highlighted by Nam [7]. The analysis of some thermal properties of the filaments used for 3D printing of parts of polymeric materials was developed by Trhlikova et al. [8] and Savu [9]. Zhang referred to the thermal expansion of power electronic components when he studied applications of additive manufacturing in this field [10].

The generation of 3D printed parts' deviations due to thermal and negative thermal expansion was analyzed by researchers interested in a better knowledge of additive manufacturing processes, namely those of 3D printing [3,5,8,9].

Wang et al. [11] studied some characteristics of isotactic polypropylene. They found that the high crystallization rate of isotactic polypropylene can cause significant difficulties in the case of additive manufacturing processes. When studying the behavior of a composite material based on isotactic polypropylene, it was observed that the value of the coefficient of thermal expansion of isotactic polypropylene is about 10% higher than that of a composite material containing spray-dried cellulose nanofibrils.

Blanco considered thermal expansion when reviewing the applications of thermal analysis methods that can be used to manufacture parts by 3D printing processes [12]. He highlighted the availability of thermogravimetric analysis, differential scanning calorimetry, and dynamic mechanical analysis to assess the thermal expansion capacity of materials used to manufacture filaments when applying 3D printing processes.

In an overview of the additive manufacturing of polymer and polymer composite parts, Nat and Nilufar appreciated that the negative thermal expansion of parts after applying an additive manufacturing process induces residual stresses that can affect the behavior of parts during mechanical stresses [13]. They found a library created by Huang et al. [14] in connection with the possibilities of designing the parts so that the dimensions of the 3D printed part are affected as little as possible after the thermal shrinkage.

Zohdi et al. investigated the anisotropy of some thermal properties, as it is, among others, thermal expansion [15].

Hwang et al. have shown that a reduction in the value of the coefficient of thermal expansion is possible when copper particles are introduced into the ABS specimens [16]. For example, for a content of 50 wt.% of copper, the coefficient of thermal expansion decreases by about 29.5% compared to the value of the same coefficient valid for pure ABS, which means a decrease in the coefficient of thermal expansion from 108.2 ppm/°C to

76.2 ppm/°C. This way, the test samples' significant deformation during thermal shrinkage is avoided.

The anisotropic character of the thermal expansion was highlighted by Baker et al. [17]. They compared the values of the coefficient of thermal expansion for test pieces printed along with longitudinal and transverse directions.

A relatively simple device has been proposed to allow direct observation of the spiral polymeric test samples during thermal or negative thermal expansion. This paper presents the research results to highlight the thermal expansion of spiral test parts made by the 3D printing of four different polymeric materials (styrene-butadiene acrylonitrile, polyethylene terephthalate, thermoplastic polyurethane, and polylactic acid). The experimental results were mathematically processed, and empirical mathematical models corresponding to the thermal contraction of the test samples were determined.

2. Materials and Methods

2.1. Initial Considerations

In principle, it is considered that thermal expansion can be explained by the asymmetry of the potential energy, which determines an increase in the mean distance between atoms when the atoms vibrate along the line of interaction between them. However, non-vibrational contributions to the development of the thermal expansion process have also been highlighted [18].

When increasing the body temperature from a value θ_1 to a value θ_2, the magnitude ΔL of the thermal expansion of the body of length L_0 is determined by using the relation:

$$\Delta L = \alpha L_0(\theta_1 - \theta_2), \tag{1}$$

or:

$$\Delta L = \alpha L_0 \Delta\theta, \tag{2}$$

where α is the coefficient of linear thermal expansion, and $\Delta\theta$ is the temperature variation.

Consistent with the above equation, the values of the coefficient of linear thermal expansion α correspond to the following relation:

$$\alpha = \frac{\Delta L}{L_0 \Delta\theta}. \tag{3}$$

It is still possible to investigate the thermal expansion of the volume of a body. In this case, the volume thermal expansion coefficient β is valid:

$$\beta = \frac{\Delta V}{V_0 \Delta\theta}. \tag{4}$$

where V_0 is the initial volume of the body, and ΔV—the increase in body volume.

In most cases, the value of the linear expansion coefficient is important.

Devices called dilatometers, or dilatation analyzers, are used to determine the thermal expansion coefficients' values experimentally. Pushrod dilatometers using optical interferometry or X-ray diffraction, optical dilatometers, capacitance dilatometers, etc., are known. A mention shall be made about horizontal and vertical dilatometers, respectively, concerning the position of a rod made of a material whose coefficient of thermal expansion is determined. In principle, when the temperature of a rod in the investigated material increases, the displacement of the edge of one end of the rod is determined using suitable optical means.

The expansion of the use of polymeric materials has led to the need to know some characteristics of the behavior of parts made of such materials to temperature variation. Manufacturers of polymeric materials generally provide brief information on the expansion properties of these materials. In industrial practice, there is sometimes the problem of more detailed knowledge of the thermal expansion of a body of polymeric materials at different temperatures.

On the other hand, the last decades have highlighted the possibilities of obtaining polymer parts of various shapes and sizes.

Under the conditions mentioned above and to design and materialize an easily accessible dilatometer, the idea of increasing the length of the bar in the material whose thermal expansion is of interest was formulated using a polymer test sample in the shape of an Archimedean spiral. It was accepted that, among the different categories of spirals, the Archimedean spiral ensures a maximum length of the test sample within a flat surface of predetermined dimensions.

Using a spiral-shaped test sample located in a spiral-shaped groove and allowing the spiral to elongate only in the direction of the outer end of the spiral test sample, the length of the test sample whose thermal expansion is to be measured could be increased (Figure 1). In this way, it would be possible to increase the accuracy of assessing the value of the linear thermal expansion coefficient due to considering the longer length of the test sample.

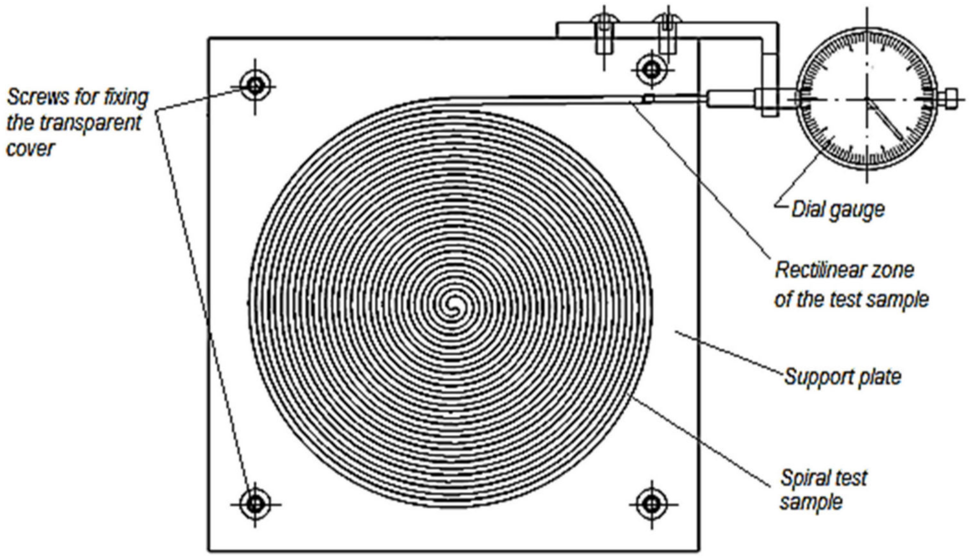

Figure 1. Schematic representation of the device for measuring the thermal expansion of a polymer spiral test sample in the variant involving a dial gauge.

2.2. Experimental Conditions

Under the theoretical conditions mentioned above, a device has been designed to measure the thermal expansion of a spiral-shaped polymer test sample (Figure 1).

A groove in the shape of an Archimedean spiral was machined by milling on a numerically controlled machine tool [19]. An essential part of the device was an aluminum alloy plate. The outer end of the spiral groove is provided with a rectilinear segment. Inside the groove with a cross-section of 1.8×2.3 mm^2, a polymeric test sample can be placed, having a shape corresponding to that of the groove in the aluminum alloy plate, providing a lateral gap of about 0.03 mm. A transparent material cover can be placed over the aluminum alloy plate and fixed to the plate with screws to avoid the external deformation of the test sample during thermal expansion.

The aluminum alloy from which the plate was made was of the EN-AW-2017 type AlCu4MgSi(A) alloy and contained 0.2–0.8% Si, 0.70% Fe, 3.5–4.5% Cu, 0.4–1.0% Mn, 0.4–1.0% Mg, 0.10% Cr, 0.25% Zn, 0.25% Ti, 0.05% other chemical elements and the rest—aluminum. As values of the main thermal properties of the aluminum alloy, it can mention solidification temperature 510 °C, melting temperature 645 °C, heat transfer capacity 873 J·kg^{-1}·K^{-1}, thermal expansion coefficient 22.9 µm·m^{-1}·K^{-1}, thermal conductivity 134 W·m^{-1}·K^{-1}.

The free end movement from outside the spiral test sample in the rectilinear segment could be highlighted using a dial gauge (Figure 1). However, it was appreciated that a higher accuracy would be obtained using an optical microscope. The microscope objective was fixed near the outer end of the linear segment of the test sample (Figure 2).

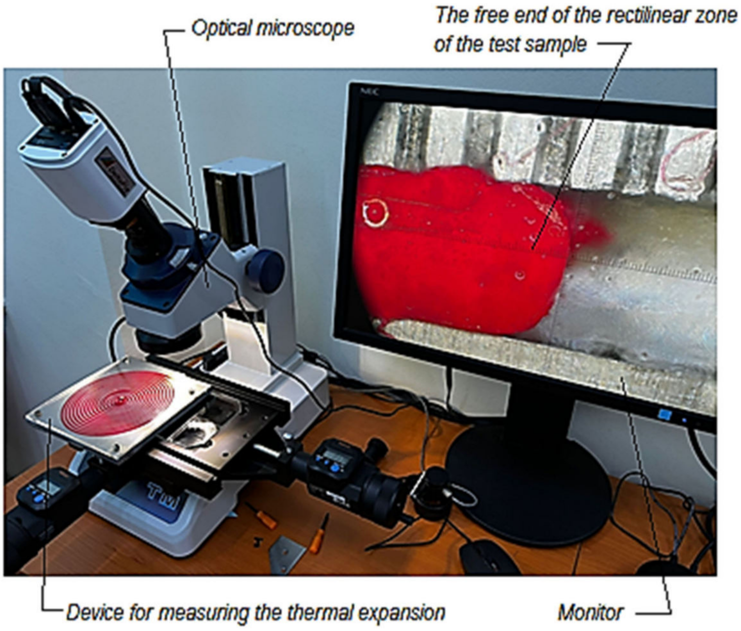

Figure 2. Image of the device for measuring the thermal or negative thermal expansion of the spiral test sample made of polymeric material Flexifill 98A, in the variant involving an optical microscope.

Regarding the proper way of measuring the variation of the length of the test sample, the cooling of the test sample in a freezer was first considered. The aluminum alloy plate, together with the test sample, could be removed from the freezer and placed in the working area of the optical microscope so that minute-by-minute measurements of the thermal expansion of the test sample could be performed. Therefore, the temperature of the aluminum alloy plate and the polymeric test sample could be measured using a gun-type infrared thermometer, which measures the infrared radiation emitted by a given surface. A non-contact infrared thermometer (manufactured by HOPPLINE—Hungary) was used for this purpose, with a measuring range between −50 °C and +400 °C (measuring distance of 5–15 cm, measuring accuracy of ±1.5 °C).

The approximate distance from which the temperature was measured using the infrared thermometer was about 15 cm. Since the process of heat exchange between the aluminum alloy plate together with the spiral test piece and the external environment does not develop with the same intensity in all directions, the aluminum alloy plate temperature has different values at different points of the aluminum plate and, therefore, the average values of three measurements were considered.

The temperature evaluation of the aluminum plate was performed at 1-min intervals, determined by using a digital clock with a stopwatch (approximate time measurement accuracy of ±5 s). In the calculations, the average values of the measured temperatures were taken into account. As observed by using the finite element method and by measuring the temperature in different areas of the aluminum alloy plate, there are temperature differences, even when heated on the table of the 3D printer.

The following materials were considered as materials for the spiral test samples:

(1) Black ABS (styrene-butadiene acrylonitrile). This material is used, for example, for the manufacture of general-purpose goods, such as toys, carcass parts, furniture, refrigerator interiors, helmets, etc.;

(2) Red PET G (polyethylene terephthalate type G). Such material is used mainly in the textile industry, but also as a bottling or packaging material due to the lack of reaction with water or food;
(3) Red color thermoplastic polyurethane (trade name: Flexfill 98A). This material has a hardness equal to that of rubber (98A). It is used especially in the manufacture of solid wheels for scooters and skateboards or in the manufacture of protective cases of smartphones;
(4) Polylactic acid (type T PLA) silver color. This material is well adapted to the requirements of 3D printing processes. Its use in 3D printing does not require a heated substrate or a high melting temperature and increases the printing speed. It also ensures low manufacturing costs. A disadvantage is the increased sensitivity to the action of ultraviolet radiation. Parts with fine details can be easily made from polylactic acid. This material can be used to manufacture toys, jewelry, statues, etc.

The coefficient values of thermal expansion of these materials indicated in some specialized works can be observed in the second column of Table 1.

Table 1. Values of thermal expansion coefficients for materials used in experimental research.

Polymeric Material	Values of the Coefficient of Thermal Expansion Indicated in Specialized Documents, in m/(m·K) [20,21]
ABS (black)	$72 \cdot 10^{-6}$
PET G (violet)	$7 \cdot 10^{-5}$
Flexfill 98A (red)	$145 \cdot 10^{-6}$ (approximate value, determined by comparison with those of similar materials)
PLA (silver)	$41 \cdot 10^{-6}$

The thermal expansion of the polymer test sample from a temperature of about −9 °C (when it was removed from the freezer) to a temperature close to that of the environment in the laboratory, 13 °C) was thus measured using an optical microscope TM-1005B (manufactured by the Japanese company Mitutoyo.

2.3. Evaluation of the Length of an Archimedean Spiral Test Sample

There are different ways to determine the length of an Archimedes spiral segment [22]. The length of the test sample in the form of an Archimedean spiral was calculated using the "Measure" function in the SolidWorks software. The lengths of the two side surfaces of the profile (with a rectangular cross-section, measuring 1.8×2.3 mm^2) were measured. The arithmetic mean of the lengths of the two side surfaces was calculated, resulting in an average fiber length of 3337.63 mm.

A problem with the device is that during the thermal expansion or contraction of the polymer spiral test sample, not only the spiral test sample expands or contracts but also the aluminum alloy plate in which the spiral groove the test sample is placed.

It is generally considered that the value of the coefficient of thermal expansion in the case of a metallic material is about ten times lower than that of a polymeric material. Specifically, in the case of aluminum alloy, the value indicated of the coefficient of thermal expansion is α_{Al} = 22.9 m/(m·K), while, for example, in the case of the PLA polymer is indicated $\alpha_{\text{PLA}} = 41 \cdot 10^{-6}$ m/m·K, and in the case of the ABS polymer, $\alpha_{\text{ABS}} = 72 \cdot 10^{-6}$ m/(m·K).

Suppose it takes into account that the size of the side of the square-shaped area of the aluminum alloy plate in which the spiral groove is located is about 128 mm, and assuming a temperature difference of 40 °C, this means a linear variation of the size of the aluminum alloy plate side:

$$\Delta L_{Al} = \alpha_{Al} L_{0\ Al} \Delta\theta = 22.9 \cdot 128 \cdot 40 = 117.2\ \mu\text{m}. \tag{5}$$

Taking into account a length L ≈ 3337.63 mm of the spiral test sample in PLA and, respectively, in ABS and considering the values indicated for the coefficients of thermal expansion [20,21], it would be possible to increase the length of the spiral test sample

ΔL_{PLA} = 5.47 mm and ΔL_{ABS} = 9.61 mm. It is found that the share w of the influence of the linear expansion of the aluminum alloy plate on the thermal expansion of the spiral test sample is very low (w = 0.1172 · 100/5.47 = 2.14% in the case of the spiral test sample made of PLA and w = 0.1172 · 100/9.61 = 1.21% in the case of the ABS spiral test sample, respectively. This situation allows us to neglect the influence exerted by the linear thermal expansion of the aluminum alloy plate on the thermal expansion of the spiral test sample of polymeric material.

2.4. Simulation by the Finite Element Method of the Thermal Expansion of the Test Piece

The investigated process was modeled using the finite element method (FEM) and the ANSYS 3D software to evaluate the thermal expansion capacity of the spiral test samples of polymeric materials used in manufacturing parts by 3D printing. For the purpose mentioned above, the situation of a spiral test sample located in the spiral-shaped groove in the aluminum alloy plate was considered.

One of the results of finite element modeling is shown in Figure 3. The experimental tests will manage an uneven cooling or heating of the aluminum alloy plate. Due to heating or cooling at uneven speeds of different areas of the aluminum alloy plate where the polymer spiral test sample is located, there will be a distributed variation in temperature along with the spiral test sample. The value of the thermal expansion coefficient is variable with the temperature of the polymer spiral test sample. This means that the results will lead to an overall value of the evolution of the magnitude of the thermal expansion coefficient or negative thermal expansion coefficient.

It was developed a steady-state thermal FEM analysis considering the convection phenomena. Approximate convection coefficient values for aluminum alloys were confronted with those presented by Geng et al. [23]. It has conducted the analyses on ABS simulating the heat transfer for the cool environment, which starts from around −10 ° C and records about 13 °C on the top side of the cover plate (Table 2). The results are consistent with those measured by experimental means (Figure 3a). The FEM.-based purpose was to analyze further heat transfer on the spiral test sample by transferring steady-state thermal results into the static structural analysis. Results were plotted in the form of thermal strain, equivalent stress von Mises, equivalent elastic strain, and directional deformation in the direction of the heat flow. Thus, it may further visually assess the influence of heat transfer on various polymers. For example, it was clear that uneven cooling leads to a random distribution in the case of equivalent elastic strain (Figure 3b). The spiral undergoes multiple stages of deformation before it shrinks or expands in the designated groove. Static structural results highlight changes that occur to the original body. Directional deformation on the Y-axis gives approximate values to those obtained by experimental means.

Table 2. Experimental results regarding the thermal expansion of some polymeric materials.

Time, min	ABS Black		PET G Violet		FLEXIFILL 98A Red		PLA Silver	
	Temperature, °C	Thermal Expansion, mm	Temperature, °C	Thermal Expansion, mm	Temperature, °C	Thermal Expansion, mm	Temperature, °C	Thermal Expansion, mm
0	−8.8	0	−11.5	0	−8.3	0	−9.2	0
1	−2.6	−0.009	−2.5	−0.015	−5.7	−0.008	−6.3	−0.006235
2	−2.3	−0.015	−2.3	−0.022	−3.9	−0.01	−3.7	−0.009896
3	−0.6	−0.022	−1.3	−0.027	−3.4	−0.015	−2.5	−0.012831
4	−0.6	−0.029	−0.5	−0.03	−1.2	−0.019	−1.1	−0.0147
5	1.3	−0.036	0	−0.035	−0	−0.021	−0.1	−0.017148
6	2.2	−0.044	1.7	−0.041	−0.1	−0.026	−0.9	−0.021195
7	2.4	−0.048	2.7	−0.051	1.8	−0.028	1.7	−0.027816
8	4	−0.055	3.4	−0.066	3	−0.031	3.2	−0.037932
9	5	−0.061	4.7	−0.071	3.9	−0.034	4.3	−0.042731

Table 2. *Cont.*

Time, min	ABS Black		PET G Violet		FLEXIFILL 98A Red		PLA Silver	
	Temperature, °C	Thermal Expansion, mm	Temperature, °C	Thermal Expansion, mm	Temperature, °C	Thermal Expansion, mm	Temperature, °C	Thermal Expansion, mm
10	6	−0.062	5.2	−0.079	4.1	−0.037	4.8	−0.046699
11	6.5	−0.065	5.5	−0.085	4.6	−0.04	5.5	−0.053651
12	6.8	−0.066	6.5	−0.09	5.7	−0.043	6.3	−0.056203
13	7.4	−0.067	7.2	−0.094	6.5	−0.048	7.4	−0.060043
14	8.2	−0.067	7.5	−0.098	6.8	−0.051	7.9	−0.06196
15	8.3	−0.068	7.9	−0.103	7.2	−0.053	8.2	−0.067081
16	9.1	−0.069	8.3	−0.106	7.9	−0.056	8.7	−0.069362
17	9.3	−0.071	8.8	−0.111	8.5	−0.058	9.2	−0.073242
18	9.8	−0.073	9.5	−0.114	9.2	−0.059	9.7	−0.075759
19	10.1	−0.076	10	−0.117	9.9	−0.061	10.2	−0.078333
20	10.6	−0.077	10.2	−0.119	10.4	−0.063	10.6	−0.079781
21	10.9	−0.078	10.5	−0.121	10.8	−0.066	10.9	−0.08126
22	11	−0.079	10.8	−0.124	11.1	−0.068	11.2	−0.085492
23	11.5	−0.081	11	−0.126	11.4	−0.071	11.5	−0.086936
24	11.9	−0.083	11.3	−0.13	11.6	−0.073	11.8	−0.090123
25	12	−0.085	11.9	−0.131	12.1	−0.075	12.1	−0.090997
26	12.1	−0.086	12	−0.132	12.3	−0.076	12.3	−0.091983
27	12.3	−0.088	12.2	−0.133	12.5	−0.077	12.4	−0.093028
28	12.4	−0.089	12.4	−0.135	12.6	−0.078	12.6	−0.094724
29	12.5	−0.091	12.5	−0.137	12.7	−0.08	12.7	−0.096244
30	12.7	−0.091	12.6	−0.138	12.9	−0.081	12.9	−0.094936
31	12.8	−0.092	12.9	−0.141	13.1	−0.081	13.2	−0.09782
32	12.9	−0.092	13.1	−0.143	13.2	−0.081	13.3	−0.09745
33	13.1	−0.092	13.2	−0.143	13.2	−0.081	13.4	−0.098847

The initial conditions for steady-state thermal analysis include an initial ambient temperature of 22 °C and a temperature of −13.1 °C applied in increments on the lower surface of the plate, respectively. A process of free air convection of up to 2.5 W/mm^2 °C applied to the upper surface of the plate was considered. The boundary conditions took into account both the contacts and the joints. The contacts are of three types, two of which include the frictionless thermal expansion of the 3D printed spiral and one that takes into account the friction between the spiral test sample and the groove walls. The joints refer to the spiral's contact with the groove's flat surface. Such conditions make it easier for the software to consider the material must flow only along the spiral groove.

The thermal imaging camera HT-18 (produced by Hti Instrument) was used to check the uneven heating of the aluminum plate on the table of the 3D printer. As it can be seen from Figure 3c, the image obtained by using the thermal imaging camera shows a real unevenness in the heating of the aluminum plate under the action of the table of the 3D printer. This uneven heating of the aluminum plate results in an uneven distribution of the spiral test sample temperature.

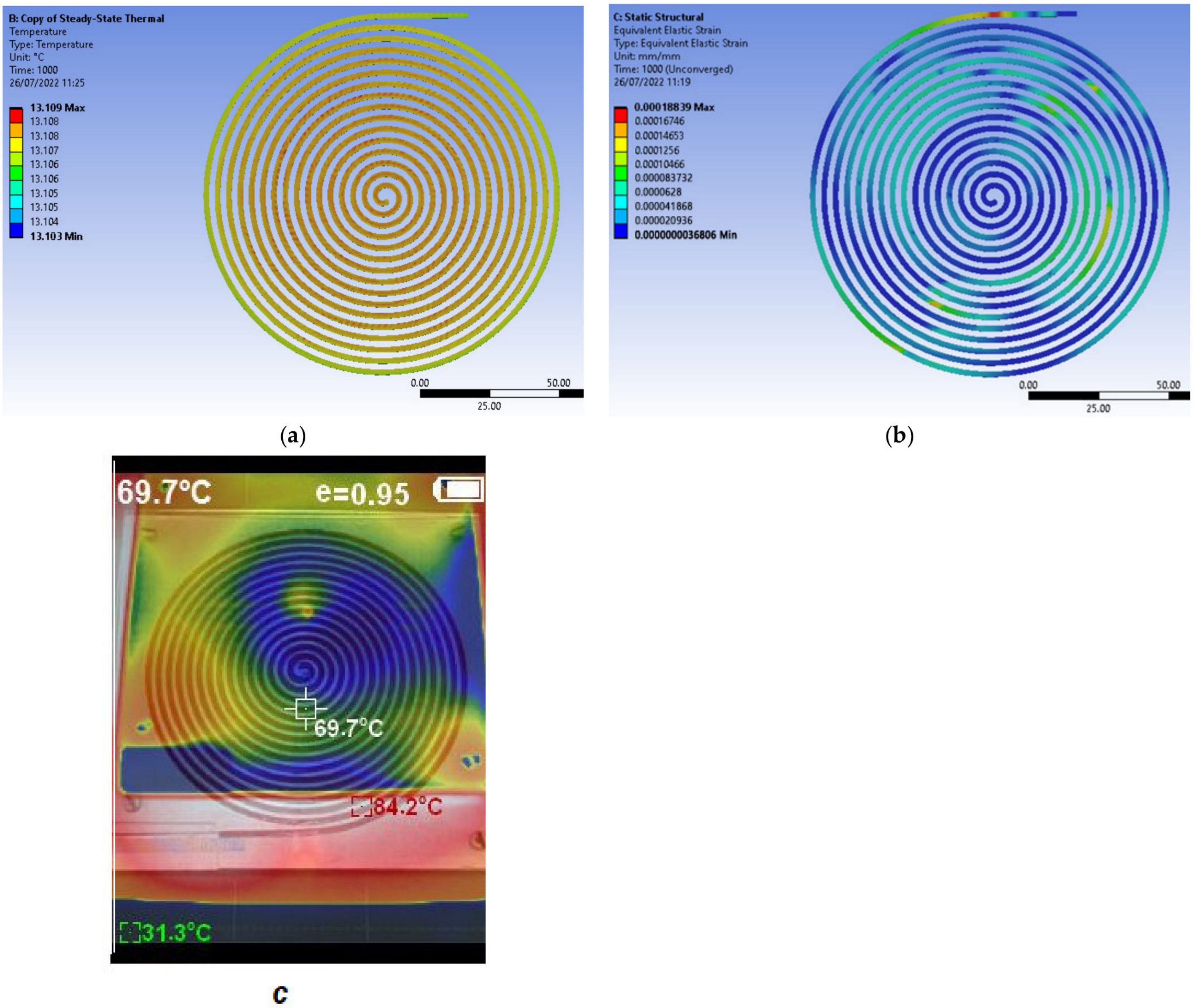

Figure 3. Uneven cooling/heating of the spiral test sample due to different heat transfer rates in distinct areas of the aluminum alloy plate: (**a**) temperature distribution in the steady-state thermal scenario; (**b**) equivalent elastic strain distribution in the static-structural scenario; (**c**) image obtained using the thermal imaging camera.

3. Results

The results obtained in the experimental tests regarding the thermal expansion of the test samples made of the four materials are presented in Table 2. A graphical representation of the ΔL increase in the lengths of the test samples made of polymeric materials when the temperature increases from approximately -9 °C to +13 °C and corresponding to the experimental results in Table 2 can be observed in Figure 4.

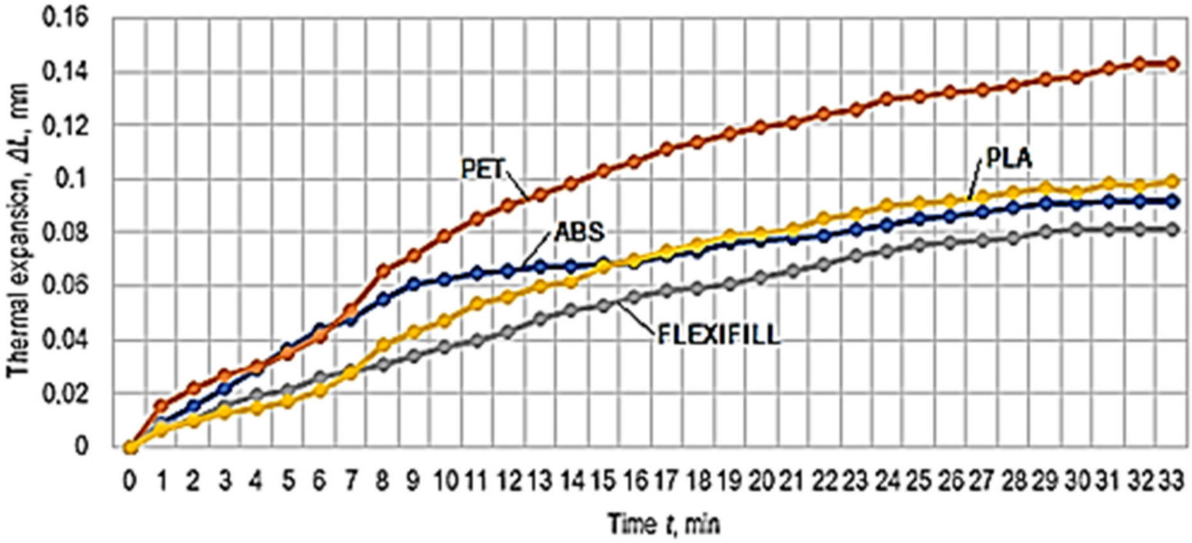

Figure 4. The evolution of thermal expansion over time, with small differences between the initial temperatures.

Later, the idea of measuring the linear negative thermal expansion of the test samples appeared. The heating of the aluminum alloy plate on the table of a 3D printer was considered (Figure 5). In such a case, the temperature of the upper area of the table can be programmed, this being an input factor in the 3D printing process. Thus, measurements of the negative thermal expansion were performed when the test sample cooled, from a temperature of 70 °C to the ambient temperature in the laboratory (30 °C), during the measurements. The measurement results of the test samples shrinkage are included in Table 3. By considering the results in Table 3, a graphical representation of the evolution of negative thermal expansion over time was made (Figure 6).

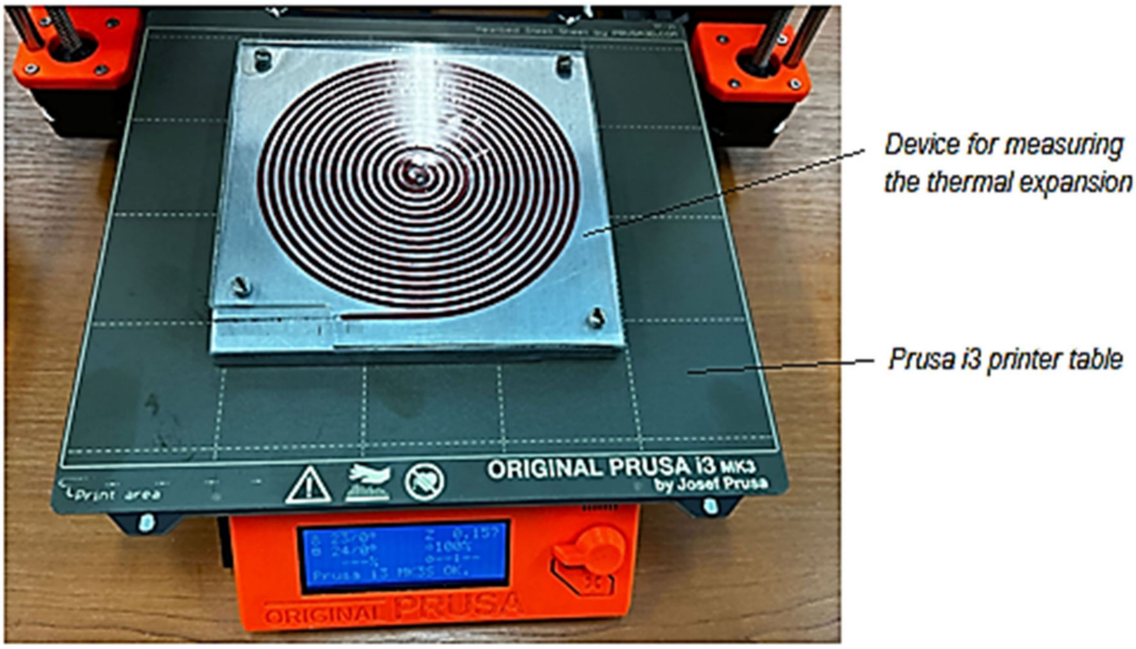

Figure 5. Image of a device for measuring the expansion or thermal shrinkage of a polymer spiral test sample together with the aluminum alloy plate placed on the printer's table to reach the temperature at which the spiral test sample begins to cool and contract.

Table 3. Experimental results regarding the negative thermal expansion of some polymeric materials.

Time, min	ABS Black		PET G Violet		FLEXIFILL 98A Red		PLA Silver	
	Temperature, °C	Negative Thermal Expansion, mm	Temperature, °C	Negative Thermal Expansion, mm	Temperature, °C	Negative Thermal Expansion, mm	Temperature, °C	Negative Thermal Expansion, mm
0	69.7	0	70	0	71.8	0	71	0
1	64.9	−0.08	62	−0.32	66.7	−0.01	61	−0.132
2	61.5	−0.118	60	−0.514	63.8	−0.022	57.7	−0.24
3	58.8	−0.147	57.2	−0.685	59	−0.028	56.2	−0.332
4	56.8	−0.174	55.6	−0.86	55.8	−0.032	53	−0.432
5	54.7	−0.197	54.2	−1.015	54.9	−0.035	51.6	−0.527
6	52.6	−0.216	52	−1.164	52	−0.039	49.5	−0.617
7	51.3	−0.235	50.2	−1.273	51.4	−0.044	48	−0.71
8	50.2	−0.254	48.8	−1.382	50.3	−0.05	46.5	−0.797
9	47.9	−0.27	47.1	−1.481	48.5	−0.054	45.2	−0.88
10	47	−0.285	45.4	−1.556	45.7	−0.057	43.9	−0.964
11	45.3	−0.297	44.5	−1.652	44.5	−0.064	42.7	−1.03
12	44.4	−0.308	43.4	−1.729	42.5	−0.073	41.6	−1.091
13	43.8	−0.321	42.2	−1.798	41.8	−0.081	40.4	−1.149
14	42.2	−0.335	41	−1.844	40.7	−0.088	39.7	−1.197
15	41.6	−0.343	40.4	−1.92	39.1	−0.097	38.6	−1.238
16	40.7	−0.354	39.3	−1.956	38.6	−0.11	37.6	−1.296
17	39.7	−0.364	38.6	−2.013	38.2	−0.13	37.1	−1.336
18	38.6	−0.372	37.8	−2.053	37.7	−0.14	36.3	−1.376
19	38	−0.381	37	−2.088	36.9	−0.16	35.7	−1.412
20	37	−0.391	36.3	−2.128	36.2	−0.19	35.1	−1.44
21	36.7	−0.396	35.6	−2.166	35.4	−0.2	34.9	−1.462
22	35.8	−0.408	34.9	−2.209	35.1	−0.21	34.5	−1.501
23	35.1	−0.412	34.3	−2.242	34.5	−0.22	33.5	−1.553
24	34.8	−0.42	33.7	−2.267	33.9	−0.23	32.8	−1.582
25	33.8	−0.426	33.1	−2.293	33.3	−0.23	32	−1.592
26	33.6	−0.434	32.8	−2.323	32.8	−0.24	31.3	−1.614
27	33.2	−0.441	32.5	−2.357	32.4	−0.24	30.1	−1.642
28	32.7	−0.448	32	−2.378	31.9	−0.25	29.2	−1.663
29	32.2	−0.454	31.6	−2.398	31.5	−0.26	28.7	−1.679
30	32	−0.461	30.8	−2.424	30.9	−0.27	28.5	−1.698
31	31.5	−0.463	30.2	−2.432	30.4	−0.28	28.4	−1.702
32	31.1	−0.464	29.5	−2.438	29.8	−0.28	28.2	−1.711
33	30.4	−0.465	28.8	−2.441	29.3	−0.29	27.9	−1.712

The results of measurements on the thermal expansion of the previously polymer spiral test sample in the freezer can be seen in Table 2. In contrast, the results of the thermal shrinkage of the polymer spiral test sample previously heated on the table of a 3D printer were included in Table 3.

The values indicated in Table 4 were determined by comparing the maximum values of thermal expansion and negative thermal expansion, respectively, at the temperature variation intervals in the case of experimental research.

For the experimental results in Table 4, which show more pronounced differences in terms of negative thermal expansion for the four materials used in the experimental research, mathematical processing was used by means of specialized software [24], to determine empirical mathematical models able to highlight the influence of temperature on linear negative thermal expansion.

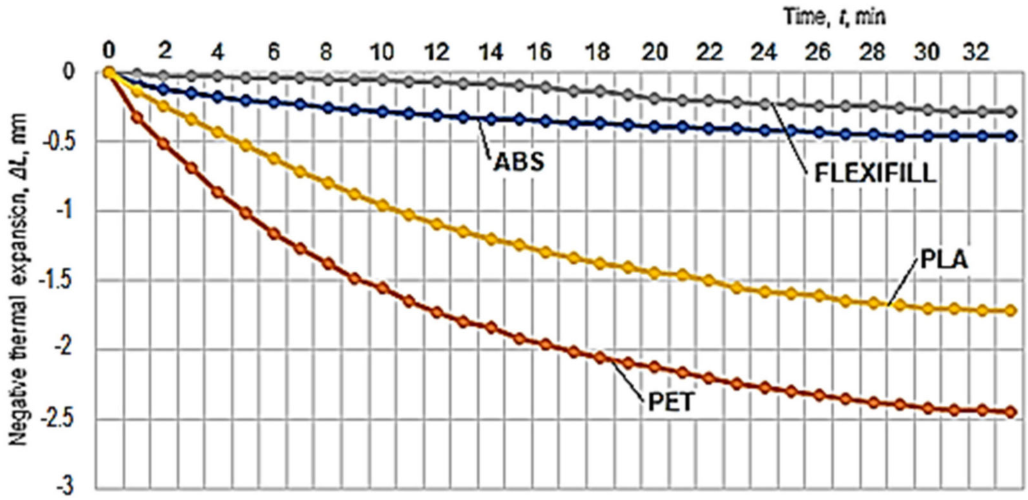

Figure 6. The evolution in time of negative thermal expansion of some spiral specimens made of polymeric materials, there being small differences between the initial temperatures.

Table 4. Calculated values of the thermal and negative thermal expansion coefficients, considering the experimental results presented in Tables 2 and 3.

Material	On Heating			On Cooling		
	The Maximum Value of the Thermal Expansion, ΔL, mm	**Temperature Variation, $\Delta\theta$, K**	**Value of the Coefficient of Thermal Expansion α**	**The Maximum Value of Negative Thermal Expansion, ΔL, mm**	**Temperature Variation, $\Delta\theta$, K**	**Value of the Coefficient of Thermal Negative Expansion α**
Column no. 1	**2**	**3**	**4**	**5**	**6**	**7**
ABS (black)	0.092	8.8 + 13.1 = 21.9	$1.25 \cdot 10^{-6}$	0.465	69.7 − 30.4 = 39.3	$3.54 \cdot 10^{-6}$
PET G violet	0.143	11.5 + 13.2 = 24.7	$1.73 \cdot 10^{-6}$	2.441	70 − 28.8 = 41.2	17.7510^{-6}
Flexifill 98A violet	0.081	8.3 + 19.2 = 21.5	$1.12 \cdot 10^{-6}$	0.290	71.8 − 29.3 = 42.5	$2.04 \cdot 10^{-6}$
PLA silver	0.098	9.2 + 13.4 =22.6	$1.31 \cdot 10^{-6}$	1.712	71 − 27.9 = 43.1	$11.90 \cdot 10^{-6}$

The specialized software was generated by taking into account the least squares method. It provides conditions for selecting the most appropriate empirical mathematical model from five such models: the first-degree polynomial, the second-degree polynomial, the power function, the exponential function, and the hyperbolic function. For the selection, the value of the so-called Gauss criterion was used. This value (the Gauss's criterion value) is defined using the sum of the squares of the differences between the ordinate's values determined by the empirical mathematical model considered and the values determined experimentally. The lower the value of the Gauss criterion, the more appropriate the mathematical model is to the experimental results used.

The most appropriate empirical mathematical models determined using specialized software, and the models determined were included in the second column of Table 5.

Table 5. Empirical mathematical models designed to highlight the negative thermal expansion to the temperature decrease, considering the experimental results.

Polymer	The Most Appropriate Empirical Mathematical Model for the Experimental Results and the S_G Value of Gauss's Criterion	Empirical Mathematical Model of the Power Function Type and the S_G Value of Gauss's Criterion
Black ABS	Second-degree polynomial $\Delta L = -0.739 + 0.00757\theta + 0.0000457\theta^2$ $S_G = 1.078667 \cdot 10^{-4}$	$\Delta L = 3074565\theta^{-3.76}$ $S_G = 1.840823 \cdot 10^{-2}$
Violet PET G	Second degree polynomial $\Delta L = 3.805 - 0.0356\theta - 0.000298\theta^2$ $S_G = 2.356737 \cdot 10^{-3}$	$\Delta L = 16728331\theta^{-3.789}$ $S_G = 0.7223308$
Red FLEXIFILL 98A	Exponential function $\Delta L = 6.281 \cdot 0.904^{\theta}$ $S_G = 2.715475 \cdot 10^{-4}$	$\Delta L = 114572241\theta^{-4.468}$ $S_G = 1.078153 \cdot 10^{-3}$
Silver PLA	Second-degree polynomial $\Delta L = 3.658 - 0.0753\theta + 0.0003305\theta^2$ $S_G = 3.64125 \cdot 10^{-3}$	$\Delta L = 24638730\theta^{-4.062}$ $S_G = 0.4127897$

4. Discussion

In many situations in manufacturing engineering, empirical mathematical models of the power function type have been determined and used. Such empirical mathematical models are sometimes used to determine the influence of various factors on the cutting speed, the size of the components of the cutting forces, the size of a roughness parameter of the machined surface, etc. [25–27]. An advantage of using empirical mathematical models of power function type derives from the possibility of evaluating the intensity of the influence exerted by a certain factor by analyzing the value of the exponent attached to that factor in the function of power type to the values of exponents attached to other factors. However, empirical mathematical models of the power function type are particularly appropriate when dealing with monotonous evolutions of the output parameter as the value of the input factor increases or decreases in the investigated process. Such a situation, i.e., the lack of minimums or maximums, was confirmed, for example, by the graphical representation in Figure 5, where there is a continuous increase in thermal expansion when the temperature increases by heating the spiral test samples. For this reason, power function empirical mathematical models for the four polymeric materials were also determined, and those models can be seen in the second column of Table 5.

By considering the values of temperatures and thermal expansions or negative thermal expansions in Tables 2 and 3, it was possible to determine the values of the coefficients of thermal expansion corresponding to each of the four materials used to make the spiral test samples. Some aspects of calculating the coefficients of thermal expansion coefficients starting from the experimental values and Equation (3) are presented in Table 5.

The graphical representations in Figures 4 and 6 have been elaborated considering the experimental results in Tables 2 and 3. In the case of the graphical representation in Figure 3, there is a certain reversal of the thermal expansion values in the cases of ABS and PLA polymeric materials for the period from the beginning of heating. Subsequently, with the development of the expansion process, it is found that the thermal expansion of PLA exceeds that of ABS.

A clearer highlight of the differences between the negative thermal expansion of the spiral test samples in the two materials is provided by the content of the graphical representation in Figure 7, which confirms the order defined by the results recorded for longer time intervals than those in the case of the diagram in Figure 4.

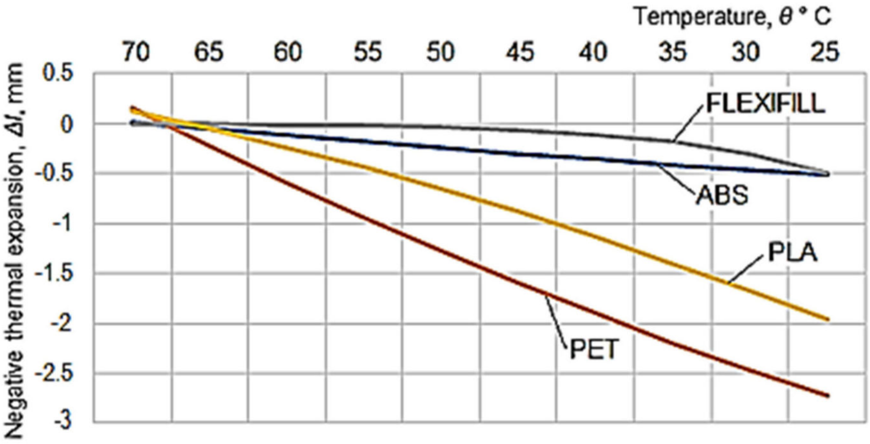

Figure 7. Evolution of negative thermal expansion to the initial temperature, according to the most appropriate empirical mathematical models to the experimental results, for the four polymeric materials.

The most appropriate empirical mathematical models for the experimental results were used to draw the graphical representation in Figure 7. The descending order of the intensity of the influence exerted by the cooling process on the negative thermal expansion can be noticed in this diagram, where polymeric materials are arranged, from this point of view, in the order: polyethylene terephthalate (PET)—polylactic acid (PLA)—styrene-butadiene acrylonitrile (ABS)—thermoplastic polyurethane (Flexfill).

As seen from Table 3, at the beginning of the experiment, heating the aluminum alloy plate and the test samples on the table of the 3D printer, was made on a temperature of 70 °C.

To reduce the friction between the spiral test samples and the spiral groove walls, a thin layer of mineral oil-based lubricant was applied to the support plate before the insertion of the test samples, both when applying the thermal expansion or negative thermal expansion.

In a cross-section, the profile of the spiral test samples made of the four materials has the shape of a rectangle with sides of 1.8 mm and 2.3 mm. The test sample width was 1.8 mm (value measured at a temperature of 22 °C). After the insertion of the spiral test sample in the groove with the shape of an Archimedean spiral, the lateral clearance between the test sample and the groove was about 0.03 mm, at a temperature of 22 °C.

Comparing the maximum values of thermal and negative thermal expansion, respectively, at the temperature variation intervals in the case of experimental research, we reach the values indicated in Table 4.

Comparing the results obtained experimentally with the values indicated in other works shows that the determined coefficients of thermal expansion were lower (Figure 8).

Possible explanations for this could be the following:

- There are, of course, differences between the properties of a part made by 3D printing and the properties of the bulk material. Due to the characteristics of the 3D printing manufacturing process, the material density of the 3D printing test sample may be much lower than in the case of bulk material. This could be the main cause of the relatively large differences between the values of the coefficients of linear thermal expansion indicated by the materials manufacturers or identified in specialized documents and the values determined experimentally using the proposed equipment. It should be noted that the values of the coefficients of thermal expansion determined experimentally were lower than those of the coefficients of linear expansion indicated by the manufacturers of the materials or identified in specialized documents in the case of all four materials;
- The thermal expansion way of the spiral sample is different from that of a strictly linear test sample;

- The relatively small gap between the spiral test sample and the spiral groove in the aluminum alloy plate could lead to frictional forces along the relatively long length of the spiral test sample, and these forces diminish the free expansion of the test sample;
- The existence of roughness resulting from the spiral groove as a result of the spiral groove generation by milling could also contribute to a braking of the free thermal expansion;
- A possible gap at the end of the test sample inside the spiral groove could also reduce the thermal expansion or the negative thermal expansion measured at the end of the segment in the form of a straight line of the spiral test sample.

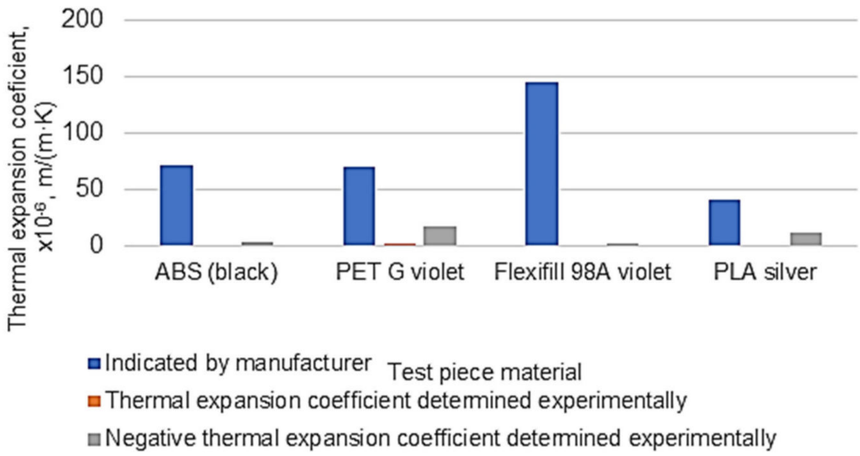

Figure 8. Highlighting the differences between the values of the coefficients of linear thermal expansion indicated by the material manufacturers or identified in specialized documents [20,21] and the values obtained in case of thermal expansion of the spiral test sample.

A certain adjustment of the density of the material of the test sample made by 3D printing is possible by acting on a size that provides some information about the printing process and is called "infill". It must still be taken into account that the density of the test sample material is not uniform, being higher near the outer walls and lower inside the test sample, where there may even be gaps of different sizes. There are, moreover, other print parameters of the printer whose values can change the density of the printed material and therefore can affect the values of the coefficient of thermal expansion. As such, it is expected that there will be a difference between the values of thermal expansion determined using a dilatometer and the proposed equipment, respectively, as long as the dilatometer indicates the value of the linear thermal expansion and the proposed equipment—the thermal expansion along a flat spiral.

Such issues may be further examined in the future to determine their influence on the final results on the values of the coefficients of expansion.

References to the coefficient of linear thermal expansion exist in ASTM E831, ASTM D696, and ISO 11359. These documents describe the test procedure valid for thermomechanical analysis when aiming at linear expansion of the test sample. As this paper aims to expand along a spiral and uses the equipment for such testing, only a few of the provisions included in the above standards could be met, including considering the equipment available for conducting experimental research.

Some aspects that may lead to differences between the results of determining the coefficient of thermal expansion using the proposed equipment and a dilatometer, respectively, have been briefly presented above. In the case of thermomechanical analysis and the use of a dilatometer, the test sample must be 12.7 mm (0.5″) wide and 75 mm (3″) long. The end surfaces of the test sample must be flat. Together with the support on which it is placed, the test sample is introduced into heating equipment and a gradual increase in temperature takes place, with a predetermined heating rate (for example, 10 °C/min) and in a temperature range default (for example, from −30–+30 °C). This ensures conditions for a controlled and as uniform heating as possible of the test sample. In the case of the proposed equipment, simple and accessible heating sources were used, but which do not allow slow and uniform heating of the spiral test sample. Additionally, the existence of a gap between the spiral test sample and the groove in the aluminum plate could affect to some extent the final result, as the thermal expansion of the aluminum plate exerts a certain influence on the value of the determined coefficient of expansion.

5. Conclusions

For different practical situations, it may be necessary to know the ability of materials used for 3D printing of parts to expand as the temperature rises, and how they shrink when the temperature decreases. A physical quantity used to evaluate this property is the coefficient of thermal expansion. The possibility of determining the size of the coefficient of thermal expansion in the case of four materials used for the manufacture of parts by 3D printing was considered. The materials called acrylonitrile butadiene styrene, polyethylene terephthalate, thermoplastic polyurethane, and polylactic acid were taken into consideration. An experimental device was designed based on an aluminum alloy plate, in which a spiral groove was made by milling. Test samples of the four polymeric materials manufactured by 3D printing were placed in this spiral groove. It was considered that using a spiral test sample would allow an increase in the length of the test sample whose thermal expansion is measured and could provide additional information on the process of thermal expanding or negative thermal expanding of the test sample. Finite element modeling of the heating of the spiral test sample in the spiral groove in the aluminum alloy plate has led to the observation that there is a variation in temperature along the spiral due to cooling at different speeds of the aluminum alloy plate spiral groove is located. In the case of experimental research, the expansion measurement of the outer end of a rectilinear segment of the test sample was performed using an optical microscope. The experimental results were mathematically processed using specialized software based on the least squares method. The specialized software allowed the selection of the most appropriate empirical mathematical models from five mathematical models frequently used in experimental research of different processes in manufacturing technology. The graphical representations elaborated by considering the experimental results and the empirical mathematical models determined by the experimental results showed that, among the materials analyzed, the most intense negative thermal expansion is obtained in the case of polyethylene terephthalate. At the same time, the lowest heat shrinkage was noticed in the case of thermoplastic polyurethane material. In the future, it is intended to expand the experimental research on test samples made of other polymeric materials and deepen the research related to the non-uniform material heating of the test sample in the aluminum alloy plate. Experimental research will also be carried out on changing the thermal expansion or negative thermal expansion coefficients with temperature variation.

Author Contributions: Conceptualization. L.S. and B.R.; methodology. L.S.; software. A.M.M. and B.R.; validation. B.R. and L.S.; formal analysis. O.D. and M.R.; investigation. B.R. and A.M.; resources. G.N.; data curation. A.M.; writing—original draft preparation. L.S.; writing—review and editing. O.D.; visualization. A.H. and M.R.; supervision B.R.; project administration. A.H. and G.N.; funding acquisition. B.R and G.N. All authors have read and agreed to the published version of the manuscript.

Funding: The A.P.C. is funded by the university funding.

Data Availability Statement: Data are available on request from the authors.

Conflicts of Interest: The authors declare no conflict of interest.

References

1. Manufactur3D. The 7 Types of Additive Manufacturing Technologies. 2018. Available online: https://manufactur3dmag.com/7-types-additive-manufacturing-technologies/ (accessed on 5 July 2022).
2. Qu, J.; Kadic, M.; Naber, A.; Wegener, M. Micro-Structured Two-Component 3D Metamaterials with Negative Thermal-Expansion Coefficient from Positive Constituents. *Sci. Rep.* **2017**, *7*, 40643. [CrossRef] [PubMed]
3. Wang, X.; Jiang, M.; Zhou, Z.; Gou, J.; Hui, D. 3D printing of polymer matrix composites: A review and prospective. *Compos. B Eng.* **2017**, *110*, 442–458. [CrossRef]
4. Van de Werken, N.; Tekinalp, H.; Khanbolouki, P.; Ozcan, S.; Williams, A.; Tehrani, M. Additively manufactured carbon fiber-reinforced composites: State of the art and perspective. *Addit. Manuf.* **2020**, *31*, 100962. [CrossRef]
5. Xu, W.; Jambhulkar, S.; Zhu, Y.; Ravichandran, D.; Kakarla, M.; Vernonc, B.; Lott, D.G.; Cornella, J.L.; Shefi, O.; Miquelard-Garnier, G.; et al. 3D printing for polymer/particle-based processing: A review. *Compos. B Eng.* **2021**, *223*, 109102. [CrossRef]
6. Miller, D.J. Material Coefficient of Thermal Expansion Investigation for Use in Additive Manufacturing Fused Deposition Modeling for Composite Tooling. Master's Thesis, University of Southern Mississippi, Hattiesburg, MS, USA, 2015; pp. 31–33. Available online: https://aquila.usm.edu/cgi/viewcontent.cgi?referer=&httpsredir=1&article=1083&context=masters_theses (accessed on 24 July 2022).
7. Nam, R. Additive Manufacturing of Thermoactivated Morphing Materials. Master's Thesis, University of Toronto, Toronto, ON, Canada, 2021; pp. 59–65. Available online: https://tspace.library.utoronto.ca/bitstream/1807/104863/1/Nam_Ryan_202103_MAS_thesis.pdf (accessed on 24 July 2022).
8. Trhlíková, L.; Zmeskal, O.; Psencik, P.; Florian, P. Study of the thermal properties of filaments for 3D printing. *AIP Conf. Proc.* **2016**, *1752*, 040027. [CrossRef]
9. Savu, I.D.; Savu, S.V.; Simion, D.; Sîrbu, N.-A.; Ciornei, M.; Ratiu, S.A. PP in 3D printing—Technical and economic aspects. *Mat. Plast.* **2019**, *56*, 931–936. Available online: https://revmaterialeplastice.ro/pdf/35%2-0SAVU%2-04%2-019.pdf (accessed on 24 July 2022). [CrossRef]
10. Zhang, Z.; Yuan, X. Applications and future of automated and additive manufacturing for power electronics components and converters. *IEEE J. Emerg. Sel. Top. Power Electron.* **2021**. [CrossRef]
11. Wang, L.; Gramlich, W.M.; Gardner, D.J.; Han, Y.; Tajvidi, M. Spray-dried cellulose nanofibril-reinforced polypropylene composites for extrusion-based additive manufacturing: Nonisothermal crystallization kinetics and thermal expansion. *J. Compos. Sci.* **2018**, *2*, 7. [CrossRef]
12. Blanco, I. A brief review of the applications of selected thermal analysis methods to 3D printing. *Thermo* **2022**, *2*, 74–83. [CrossRef]
13. Nath, S.D.; Nilufar, S. An overview of additive manufacturing of polymers and associated composites. *Polymers* **2020**, *12*, 2719. [CrossRef] [PubMed]
14. Huang, Q. 3D Printing Shrinkage Compensation Using Radial and Angular Layer Perimeter Point Information. U.S. Patent 9,886,526, 6 February 2018.
15. Zohdi, N.; Yang, R. Material Anisotropy in Additively Manufactured Polymers and Polymer Composites: A Review. *Polymers* **2021**, *13*, 3368. [CrossRef] [PubMed]
16. Hwang, S.; Reyes, E.I.; Moon, K.-S.; Rumpf, R.C.; Kim, N.S. Thermo-mechanical characterization of metal/polymer composite filaments and printing parameter study for fused deposition modeling in the 3D printing process. *J. Electron. Mater.* **2015**, *44*, 771–777. [CrossRef]
17. Baker, A.M.; Mccoy, J.; Majumdar, B.S.; Rumley-Ouellette, B.; Wahry, J.; Marchi, A.N.; Bernardin, J.D.; Spernjak, D. Measurement and modelling of thermal and mechanical anisotropy of parts additively manufactured using fused deposition modelling (FDM). In Proceedings of the 11th International Workshop on Structural Health Monitoring. Stanford, CA, USA, 12–14 September 2017. [CrossRef]
18. Baron, T.H.K. Generalized theory of thermal expansion of solids. In *Thermal Expansion of Solids*; Ho, C.H., Taylor, R.E., Eds.; ASM International: Metals Park, OH, USA, 1998; pp. 1–2.
19. Rădulescu, B.; Mihalache, A.-M.; Rădulescu, M.; Slătineanu, L.; Hrițuc, A.; Dodun, O.; Nagîț, G.; Coteață, M. Selection of a method for machining an archimedean spiral groove. *Acta Tech. Napoc. Ser. Appl. Math. Mech. Eng.* **2022**, *65*, 231–238. Available online: https://atna-mam.utcluj.ro/index.php/Acta/article/view/1755/1416 (accessed on 24 July 2022).
20. SD3D. ABS Technical Data Sheet. Available online: https://www.sd3d.com/wp-content/uploads/2-015/1-0/MaterialTDS-ABSWeb.pdf (accessed on 10 January 2022).
21. SD3D. PLA Technical Data Sheet. Available online: https://www.sd3d.com/wp-content/uploads/2-017/-06/MaterialTDS-PLA_-01.pdf (accessed on 10 January 2022).
22. Hrituc, A.; Nagîț, G.; Dodun, O.; Slătineanu, L. Measuring the length of a spiral when evaluating the plastic processability by injection molding. *IOP Conf. Ser. Mater. Sci. Eng.* **2019**, *564*, 012025. [CrossRef]
23. Geng, H.; Wang, Y.; Wang, Z.; Zhang, Y. Investigation on contact heating of aluminum alloy sheets in hot stamping process. *Metals* **2019**, *9*, 1341. [CrossRef]
24. Cretu, G. *Fundamentals of Experimental Research. Laboratory Handbook*; "Gheorghe Asachi" Technical University of Iași: Iași, Romania, 1992. (In Romanian)
25. Groover, M.P. *Fundamentals of Modern Manufacturing*; John Wiley & Sons, Inc.: Hoboken, NJ, USA, 2007; p. 548.
26. Kalpakjian, S.; Schmid, S.R. *Manufacturing Engineering and Technology*, 4th ed.; Prentice Hall: Hoboken, NJ, USA, 2001; pp. 549–578.
27. Danilevsky, N. *Manufacturing Engineering*; Mir Publishers: Moskow, Russia, 1973; pp. 127–128.

applied sciences

MDPI

Article

A Study on the Errors of 2D Circular Trajectories Generated on a 3D Printer

Adriana Munteanu [1], Dragos-Florin Chitariu [1,*], Mihaita Horodinca [1], Catalin-Gabriel Dumitras [1], Florin Negoescu [1], Anatolie Savin [2] and Florin Chifan [1]

[1] Digital Manufacturing Systems Department, Gheorghe Asachi Technical University of Iasi, 700050 Iasi, Romania; adriana.munteanu@academic.tuiasi.ro (A.M.); mihaita.horodinca@academic.tuiasi.ro (M.H.); catalin-gabriel.dumitras@academic.tuiasi.ro (C.-G.D.); florin.negoescu@academic.tuiasi.ro (F.N.); florin.chifan@academic.tuiasi.ro (F.C.)

[2] Veoneer, 700259 Iasi, Romania; anatolie.savin@yahoo.ro

* Correspondence: dragos.chitariu@tuiasi.ro

Abstract: This paper presents a study on the movement precision and accuracy of an extruder system related to the print bed on a 3D printer evaluated using the features of 2D circular trajectories generated by simultaneous displacement on x and y-axes. A computer-assisted experimental setup allows the sampling of displacement evolutions, measured with two non-contact optical sensors. Some processing procedures of the displacement signals are proposed in order to evaluate and to describe the circular trajectories errors (e.g., open and closed curves fitting, the detection of recurrent periodical patterns in x and y-motions, low pass numerical filtering, etc.). The description of these errors is suitable to certify that the 3D printer works correctly (keeping the characteristics declared by the manufacturer) for maintenance purpose sand, especially, for computer-aided correction of accuracy (e.g., by error compensation).

Keywords: 3D printer; circular trajectories; signals processing; errors evaluation

Citation: Munteanu, A.; Chitariu, D.-F.; Horodinca, M.; Dumitras, C.-G.; Negoescu, F.; Savin, A.; Chifan, F. A Study on the Errors of 2D Circular Trajectories Generated on a 3D Printer. *Appl. Sci.* **2021**, *11*, 11695. https://doi.org/10.3390/app112411695

Academic Editor: Gabi Chaushu

Received: 15 November 2021
Accepted: 6 December 2021
Published: 9 December 2021

1. Introduction

The additive fabrication is a common topic in various domains of activity (industry, biology, medicine). The compliance with precision conditions of 3D-printed parts (shape and dimensions tolerances, surface quality, etc.) becomes more and more a critical issue. Their use in some technical applications where precision and accuracy (P&A) are required is severely restricted since, for the present, other manufacturing technologies offer better results. Many studies in engineering and scientific research are focused on ensuring the P&A of 3D printers by error avoidance [1]. Other studies are involved in experimental research (measurements and data processing) in order to verify and to correct the errors generated by the lack of P&A on 3D printers by error compensation [1].

There are many issues involved in the appearance of errors in additive fabrication. Not surprisingly, some of them are not related with the 3D printer features (e.g., structure, P&A of kinematics, dynamics, position control, deposition process, temperature, etc.). For example, in [2] is established that the accuracy of STL (.stl) files (from Standard Tessellation Language or Standard Triangle Language, commonly used by Fused Deposition Modelling on 3D printers) essentially depends on the design of 3D CAD models (six different CAD systems generate STL files with different accuracies). In [3], is established that the conversion in STL format is done with errors by some CAD software products. The software interface used to drive the printer (slicer software, establishing the way the model is built) is often a source of inaccuracy [4] when inappropriate values of setting parameters are suggested by the software and accepted by user [5].

Sometimes the CAD models are generated with errors (and these errors are transferred to the printed object), especially when these models are generated as a virtual copy of a real object, e.g., by imaging, segmentation, and post processing of medical models [6,7] or by reverse engineering using a 3D-scanning and design process [8,9].

Some sources of errors are related to material deposition during additive manufacturing (e.g., flow properties) as susceptible to random variations [5]. The effect of print layer height on the accuracy of orthodontic models is considered in [10]. The effect of orientation (effect of gravity) and the effect of the support are investigated by [1]. A study on the influence of the accuracy related to size/position of printed benchmarks and the position of working planes on 3D printers is revealed in [11].The influence on P&A and mechanical properties (measured by tensile test) of a specimen object related to the print position of a specimen object is presented in [12,13].

The influence of different common printing technologies on the accuracy of mandibular models was considered in the research results shown in [14]. The influence of different types of thermoplastic filament materials used in additive fabrication on surface roughness was evaluated in [15].

The evolution in time of internal material tension, dimension and shape (by aging) as source of errors in 3D printing is a topic studied in [16]. A simple method to appreciate the P&A of 3D printers (and to calibrate it as well) is the measurement of a printed object (the most common being "#3D Benchy" from Creative Tools) or the quality of a printed structure (e.g.,"#All in one test 3D printer"). In [17], an insitu measurement method (by the scanning of layers) during the additive manufacturing process is proposed. The use of a coordinate measurement machine is proposed to describe the accuracy of medical models in [18,19]) and the optical scanning is mentioned in [6]). A metrology feedback procedure is used in [20,21] to improve the geometrical accuracy by errors compensation using a 3D scanning on sacrificial printed objects.

The displacement errors and the errors of the relative position of movable parts are often related by kinematics of a 3D printer. Frequently, the contouring errors due to axis misalignment (also a relevant topic, investigated in our study) are involved in a bad P&A. The measurement of these errors and their compensation in the computer numerical control system of the printer is a major challenge in improving the additive fabrication performances. Thus, in [22] is proposed a simple compensation model for kinematic errors based on measurement results done on the printer using a Renishaw QC10 ball bar device (from Renishaw, UK). For the 3D printers based on parallel robotic systems, in [23,24] some theoretical kinematic error models useful in automatic compensation are proposed. A volumetric experimental compensation technique for kinematic errors is exposed in [25]. In order to minimize the tracking errors of desired trajectories, a feed forward control procedure is proposed in [26].

This brief study of the literature reveals that few reports are focused on non-contact measurement methods of the errors produced by the kinematics of a 3D printer during complex motions of the extruder related to the print bed (especially 2D closed trajectories).

Our approach on this paper was based on this obvious remark: the open-loop computer-aided control of each of three motions of a printer (usually 3D printers don't use feedback control related to real position) is vulnerable to some uncontrollable (constant or variable) phenomena generated by mechanical parts (elastic deformations in toothed belts, mechanical backlashes, hysteresis behaviour, errors in lead screw threads, variation of friction forces in axes carriages, mechanical wear, structural vibrations induced by stepper motors, etc.). Because the 3D printing is achieved by deposition of material layer by layer (in a horizontal plane), an important characterization of P&A for any printer should be done by the P&A displacement, position and, especially, of 2D complex closed trajectories with the printer running in absence of the printing process. On this line of thinking we consider that a circular trajectory (of the extruder system related to the print bed) is one of the best theoretical approaches mainly because two simultaneous, strictly correlated linear motions are involved (on the x and y-axis). With a constant speed on the circular trajectory, these motions should be described by two almost identical harmonic evolutions (except the $\pi/2$ phase shift between), with periodic changes of the position, direction, speed and acceleration. An important argument for our approach based on circular trajectories is this one: the 2D circular trajectories are systematically involved in ISO standards methods for P&A evaluation of CNC manufacturing systems (ISO 230-4, [27]).

The benefits of this approach with 2D circular trajectories in P&A evaluation is confirmed by the work from [22].

In addition, from an experimental point of view, it is appropriate to work with circular trajectories generated by two simultaneous, simple harmonic linear motions (cosine motion of the extruder system on the x-axis, sine motion of the print bed on the y-axis) measured with a computer-assisted experimental setup based on two optical (non-contact) position sensors. We consider that this is a better approach, in contrast with the measurement system proposed in [22], which uses a ball bar measurement device placed between the extruder and the print bed. Because of this device, the relative motion of the extruder related to the print bed is not totally free.

The Section 2 of this paper presents the computer-aided experimental measurement setup, the Section 3 presents the theoretical and experimental considerations and comments related with the results (signal processing and P&A estimation, based mainly on real trajectory circular fitting), and the Section 4 is dedicated to conclusions and future work.

2. Experimental Setup

The experimental research was done on an Anet A8 3D printer [28], previously used in additive manufacturing for 230 operating hours. The 3D printer has the print bed movable on the y-axis, while the extruder system moves along the x and z-axes independently. On the x-axis, motion is numerically controlled (in open loop) via a stepper motor and a toothed belt (similarly on the y-axis); on the z-axis, the motion is controlled (in open loop) with two synchronized stepper motors with screw-nut systems. The absolute displacement measurement on the y-axis is done with a non-contact ILD 2000-20 [29] laser triangulation sensor (from MICRO-EPSILON MESSTECHNIK GmbH & Co, Ortenburg, Germany) with 20 mm measurement range (1 µm resolution and 10,000 s^{-1} sampling rate) with the laser beam placed perpendicularly on the target (the print bed) as Figure 1 indicates. Here the point of incidence is placed in the center of the red rectangle. An identical sensor is firmly placed on the print bed, with the laser beam placed perpendicularly to the extruder system (which moves as a sensor target in x-direction), as Figure 2 indicates.

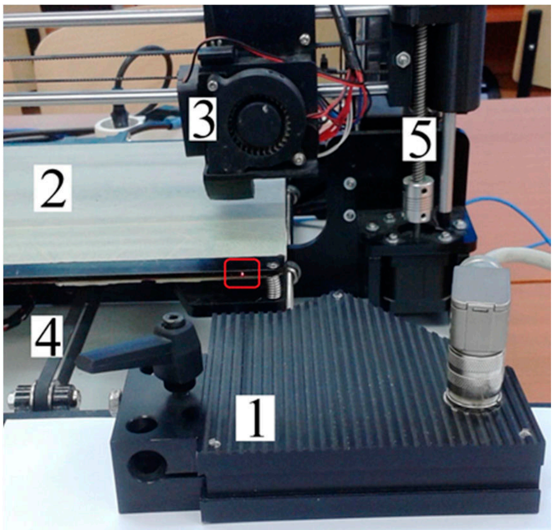

Figure 1. A partial view of the setup with optical sensor on y-axis. 1-optical sensor; 2-print bed; 3-the extruder system; 4-toothed belt for y-axis displacement; 5-first screw for z-axis displacement.

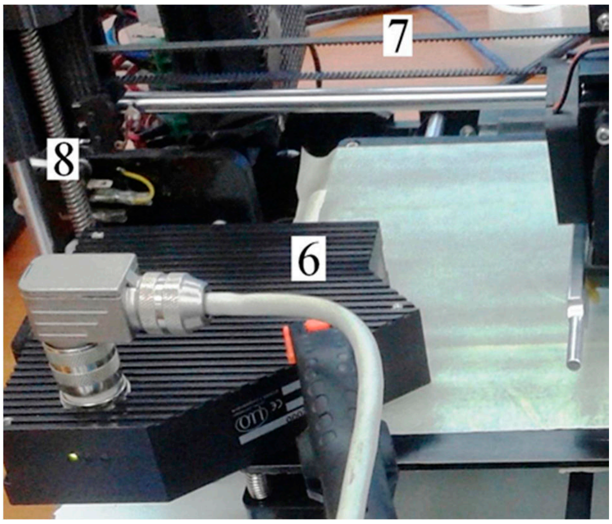

Figure 2. A partial view of the setup with optical sensor on x-axis; 6-optical sensor; 7-toothed belt for x-axis displacement; 8-s screw for z-axis displacement.

The signals generated by these sensors are two voltages proportional with the displacements (with 1.975 mm/V as proportionality factor for the x-axis sensor and 2.0185 mm/V for the y-axis sensor) related to the middle of the measurement range.

These signals are simultaneously numerically described (by sampling and data acquisition)with a PicoScope 4824 numerical oscilloscope (from PicoTechnology UK, 8 channels, 12 bits, 80 MS/s maximum sampling rate, 256 MS memory) and delivered in numerical format to a computer for processing and analysis. Figure 3 presents a scheme of the computer-assisted experimental setup with only the movable parts of the 3D printer involved in 2D circular trajectories (the extruder and the print bed), the optical sensors for x and y-motion non-contact measurement, the power supply for sensors, the numerical oscilloscope and the computer.

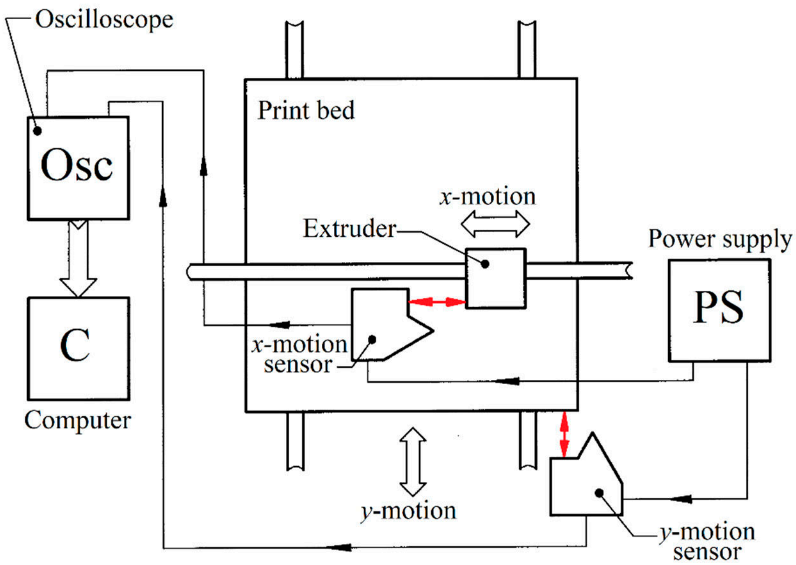

Figure 3. A scheme of the computer-assisted experimental setup.

Using an appropriate programming of the drive system written in G-code, the 3D printer was programmed to generate some identical repetitive circular trajectories of the extruder system related to the print bed (with 8.987 mm radius, each one covered in 8.987 s) for 50 s (for almost 5.5 complete trajectories). There are not special reasons to have this coincidence of values for radius and time, except the fact that these values should be accurately found by curve fitting (with the sine model) of the motions involved in the achieving of circular trajectory. However, these values assure a relatively small speed on the 2D circular trajectory. These trajectories are generated using two theoretical pure harmonic motions (x-motion accomplished by the extruder system, y-motion accomplished by the print bed) on the x and y-axes (both having a period T of 8.987 s), experimentally revealed by the computer measurement setup, as a detail in Figure 4 indicates. Here the blue-colored curve describes the motion on the x-axis; the one colored in red describes the motion on y-axis, both with 20,000 s^{-1} sampling rate. The choosing of this sampling rate is based on this argument: it should be at least two times bigger than the sampling rate of the sensors (10,000 s^{-1}). The sampling rate of the sensors acts as the Nyquist frequency for the sampling rate of the oscilloscope. It is not difficult to remark the resources of these two simultaneous evolutions for P&A evaluation. In Figure 5, a zoomed in detail in area A of Figure 4 proves that each of two real x and y-motions are not strictly pure, simple harmonic shapes (especially the y-motion). As a result, in a summary valuation, the trajectory of the extruder system related to the print bed does not have a strictly circular shape as expected.

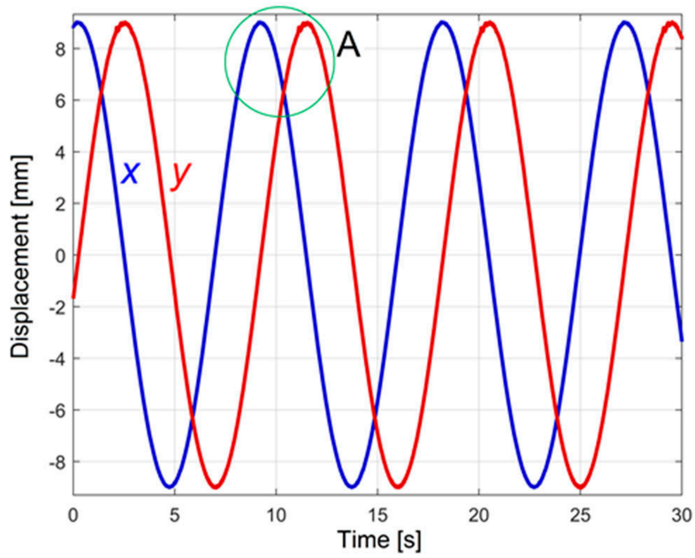

Figure 4. The evolution of x and y-motions during a repetitive circular trajectory.

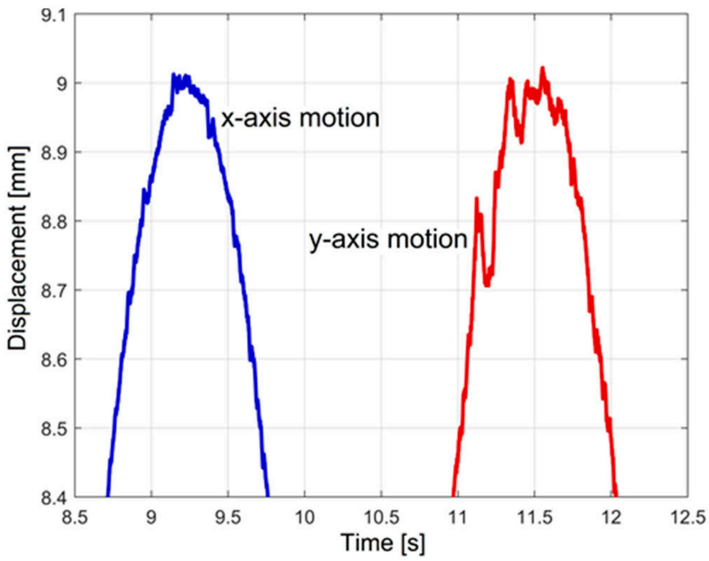

Figure 5. A zoomed in portion of Figure 4 (in area A).

These two evolutions are useful for P&A evaluation of the circular trajectories on a 3D printer in experimental terms. For this purpose, some different techniques of computer-aided signal processing will be applied (e.g., the recurrent periodical pattern detection on x and y-motion, curve fitting, circular fitting, low pass numerical filtering).

3. Experimental Results and Discussion

There are many important exploitable resources of x and y-motions description already partially revealed in Figures 4 and 5. As a first interesting approach, we propose the signals fitting, each one with a single harmonic function (fitting with a sine model). The Curve Fitting Tool from Matlab provides the best analytical approximation x_a and y_a of x and y-motion, as follows:

$$x_a(t) = 8.987 \cdot \sin(0.6991 \cdot t + 1.398) y_a(t) = 8.987 \cdot \sin(0.6991 \cdot t - 0.1883) \quad (1)$$

The fitting quality is confirmed for both motions by the same amplitude (8.987 mm, this being the radius of the circular trajectory) and angular frequency ω = 0.6991 rad/s (for a period $T = 2\pi/\omega$ = 8.987 s). These values found by curve fitting were already used in circular trajectory programming. However, there is a shift of phase by 1.5863 radians between motions (1.5863 > π/2 = 1.5707). This means that the x and y-axes are not rigorously perpendicular (there is an axes misalignment), as a first indicator for the lack of P&A. The printer works in a non-orthogonal $x0y$ system (with an angle of 90.893 degrees between axes). As a result, a programmed circular trajectory will be executed as an elliptical one. Nevertheless, this non-perpendicularity of x and y-axes revealed here can be compensated by programming. In a short definition, this compensation should solve this question: what kind of elliptical trajectory should be programmed in order to achieve a desired circular trajectory?

The evolution of residuals $x_r(t) = x(t) - x_a(t)$ and $y_r(t) = y(t) - y_a(t)$ from curve fitting of x and y-motions using a sine model are described in Figures 6 and 7 (with the same scale). The shape and the magnitude of residuals proves that x and y-motions are not perfectly harmonic (as expected), as a new indicator for the lack of P&A of circular trajectories.

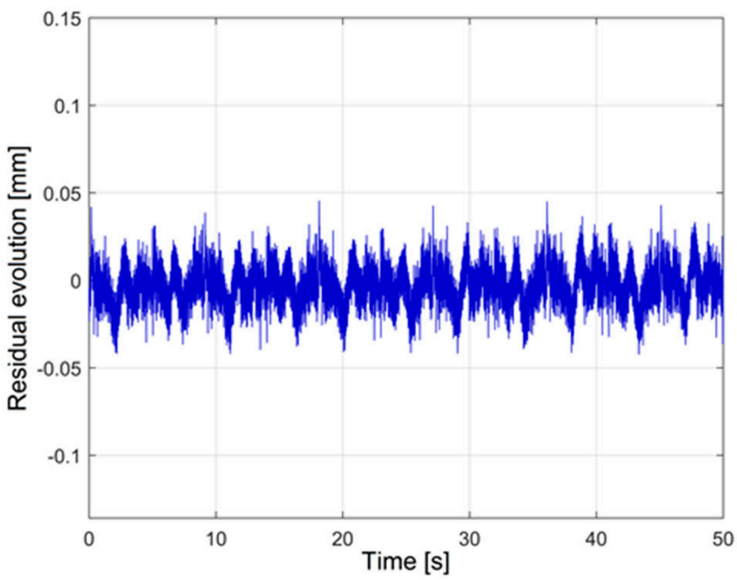

Figure 6. The evolution of residual x_r from the harmonic fitting model for x-motion.

The evolution of residuals from Figures 6 and 7 indicates that the negative effect on P&A of x-motion errors is smaller than of y-motion errors.

It is interesting to find out if there is a recurrent (or repeating)periodical pattern of the residual evolutions (x_r, y_r) on a complete period T of each motion (x, y). A simple way to check if there is a recurrent periodical pattern on x_r, and y_r evolutions is to build an average evolution of the residual (x_{Ar}, y_{Ar}) on a single period T with these definitions:

$$x_{Ar}(t) = \frac{1}{k}\sum_{i=0}^{k-1} x_r(t+i\cdot T) y_{Ar}(t) = \frac{1}{k}\sum_{i=0}^{k-1} y_r(t+i\cdot T) \quad (2)$$

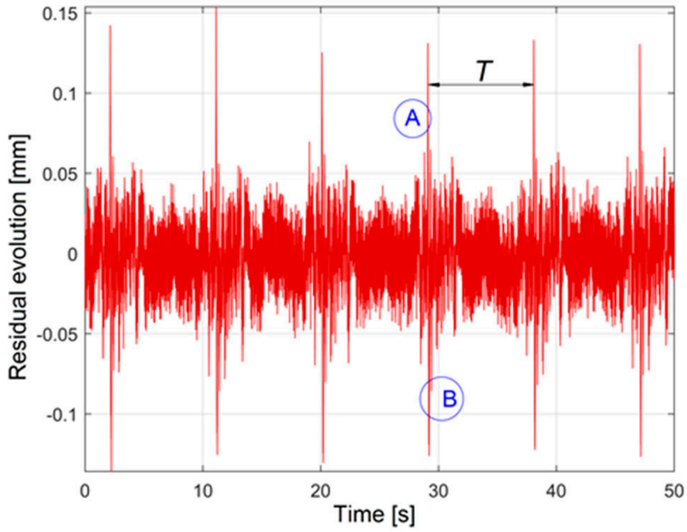

Figure 7. The evolution of residual y_r from the harmonic fitting model for y-motion.

Figure 8 presents the evolution of x_{Ar}(t = 0 ÷ T, with 179,740 samples) with k = 5 (for five completely circular trajectories), each sample of x_{Ar} being an average of k correlated samples of x_r. It is obvious that the x-motion has a well-defined repetitive periodical pattern, with systematic errors. In other words, x_r (and x-motion as well) is well correlated with itself.

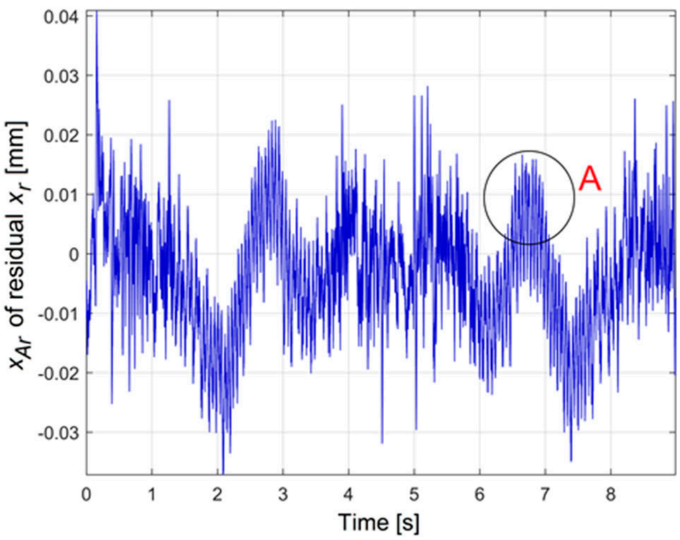

Figure 8. The average evolution x_{Ar} of the residual x_r for x-motion.

The curve fitting of x_{Ar} evolution using a sum of sine model delivers the analytical evolution x_{aAr} of x_{Ar} as Figure 9 indicates. In Equation (3) is depicted the analytical model for x_{aAr} as it follows:

$$x_{aAr}(t) = \sum_{j=1}^{n} a_{xj}\cdot \sin\left(b_{xj}\cdot t + c_{xj}\right) \quad (3)$$

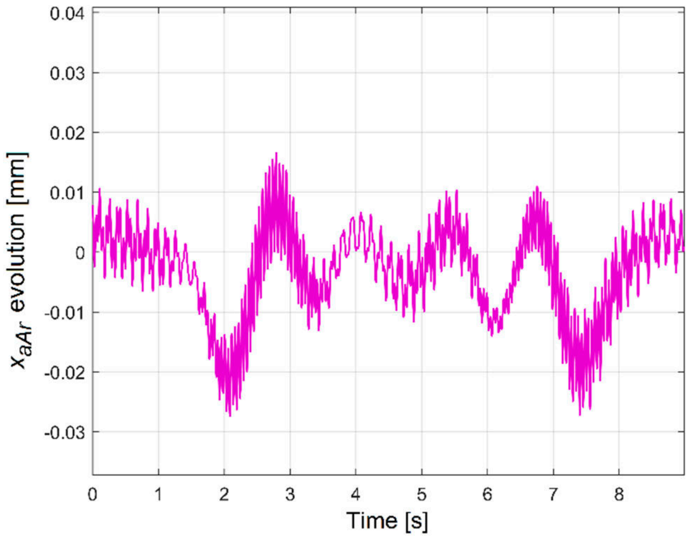

Figure 9. The evolution of an analytical model x_{aAr} (with n = 16) of the average residual x_{Ar}.

With n = 16, the values of a_{xj}, b_{xj} and c_{xj} involved in x_{aAr} model from Equation (3) are depicted in Table 1 (as results of x_{Ar} curve fitting).

Table 1. The values of a_{xj}, b_{xj} and c_{xj} involved in x_{aAr} model from Equation (3) with n = 16.

j	a_{xj}[mm]	b_{xj}[rad/s]	c_{xj}[rad]	j	a_{xj}[mm]	b_{xj}[rad/s]	c_{xj}[rad]
1	0.203	0.3379	1.969	**9**	0.001888	6.191	−2.542
2	0.004801	4.885	0.3713	**10**	0.002353	119.3	1.698
3	0.004398	1.383	1.758	**11**	0.1188	121.8	2.263
4	0.003755	2.083	1.377	**12**	0.001696	44.14	−3.301
5	0.004055	4.163	−2.608	**13**	0.00148	120.4	−0.3449
6	0.004279	3.47	−2.578	**14**	−0.1166	121.8	2.283
7	0.1981	0.3481	−1.225	**15**	0.001224	123.3	−2.064
8	0.001892	42.6	−2.541	**16**	0.0004954	118.6	−2.431

A better model x_{aAr} for x_{Ar} is available by increasing the value of n. There is not a total fit between x_{aAr} and x_{Ar}, mainly because the model is not able to describe the phenomena characterized by temporary variations of amplitudes.

On this subject, Figure 10 presents a detail with x_{aAr} and x_{Ar} evolutions located in the area A of Figure 8 with n = 105 (105 components in sum of sine model from Equation (3)). The strong variation of displacement depicted here is likely the result of structural vibrations of the 3D printer induced by the stepper motor.

The x_{Ar} and x_{aAr} evolutions are certain arguments that the experimental setup is able to describe the P&A of x-motion. Moreover, the analytical model from Equation (3) and Table 1 helps (at least in theoretical terms) to compensate for the errors of x-motion.

Figure 11 presents the evolution of y_{Ar} with k = 5 (for five completely circular trajectories, each sample of y_{Ar} being an average of k correlated samples of y_r). As with x-motion, it is obvious that the y-motion also has a well-defined periodic recurrent pattern (the same period T as x_{Ar}), having systematic errors. In other words, y_r (and y-motion as well) is well correlated with itself. Unfortunately, it was not possible to find an acceptable analytical model y_{aAr} with harmonic components (similar to the x_{aAr} model for x_{Ar} based on Equation (3)). A very high number of harmonic components (n) is necessary in this sum of sine model. A future approach intends to identify a more appropriate analytical model. There are strong repetitive irregularities on y-motion (and y_r and y_{Ar} as well) revealed in A, B areas of Figures 8 and 11. Likely they are irregularities generated by a suddenly releasing of a mechanical stress inside the toothed belt used to produce the y-motion.

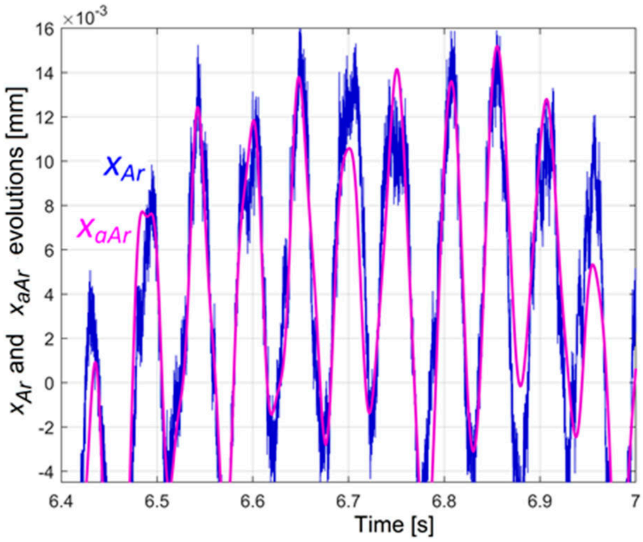

Figure 10. The evolution of x_{Ar} and an analytical model x_{aAr} (with n = 105) in area A of Figure 8.

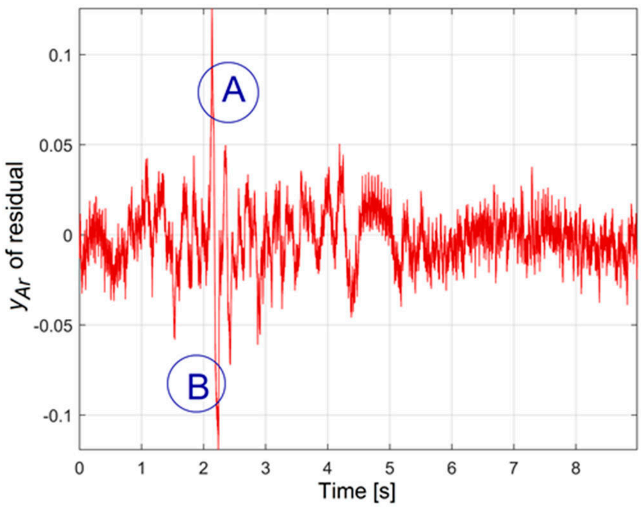

Figure 11. The average evolution y_{Ar} of the residual y_r for y-motion.

It is interesting now to examine the average trajectory generated by the 3D printer with $x_a(t) + x_{Ar}(t) = x_e(t)$ as x-motion and $y_a(t) + y_{Ar}(t) = y_e(t)$ as y-motion. It is obvious that this trajectory is not a perfect circle (at least because the wrong phase shift between x_a and y_a). A computer program was developed in order to find out the description of the least square circle (the coordinates x_c, y_c of center and the radius R_c as well) by circular fitting. This program is available for the fitting of any closed curve with known analytical description. The circular fitting supposes to find out the values x_c, y_c and R_c for which a fitting criterion ε described in Equation (4) reaches a minimum value.

$$\varepsilon = \sum_{i=1}^{N} \left[(x_{ei} - x_c)^2 + (y_{ei} - y_c)^2 - R_c^2 \right] \quad (4)$$

In Equation (4), N is the number of samples x_{ei} or y_{ei} (N = 179,740) used for x_e-motion or y_e-motion description of the average trajectory. If the average trajectory is a perfect circle, then a perfect fitting produces a value $\varepsilon = 0$ for the fitting criterion. The circular fitting of average trajectory produces x_c = 0.00303 mm, y_c = 0.00252 mm and R_c = 8.9873 mm (this radius being very close to the amplitudes of x_a and y_a already revealed in Equation (1)). A first conventional graphical description of the circularity error of the average trajectory (as a first trajectory fitting residual, TFR_1) is available in polar coordinates (d_{i1}, α_{i1}), related to the least square circle, with d_{i1}, α_{i1} defined as:

$$d_{i1} = \left|\sqrt{(x_{ei}-x_c)^2+(y_{ei}-y_c)^2}-R_c\right| \alpha_{i1} = \arctan^4\left(\frac{y_{ei}-y_c}{x_{ei}-x_c}\right) \quad (5)$$

Here d_{i1} is the distance from average trajectory to the least square circle, α_{i1} is the polar angle, with *arctan*^{4} the inverse of tangent function in four quadrants. This TFR_1 is also available in Cartesian coordinates as a curve described by a movable point having $d_{i1}\cdot cos(\alpha_{i1}) + x_c$ as abscissa and $d_{i1}\cdot sin(\alpha_{i1}) + y_c$ as ordinate. If the average trajectory is a perfect circle, then TFR_1 is a point placed in the center of the least square circle.

Figure 12 presents the TFR_1 of the average trajectory with a circular grid (with a 20 μm increment on radius). Here the maximum value of distance d_{i1} is 145.8 μm.

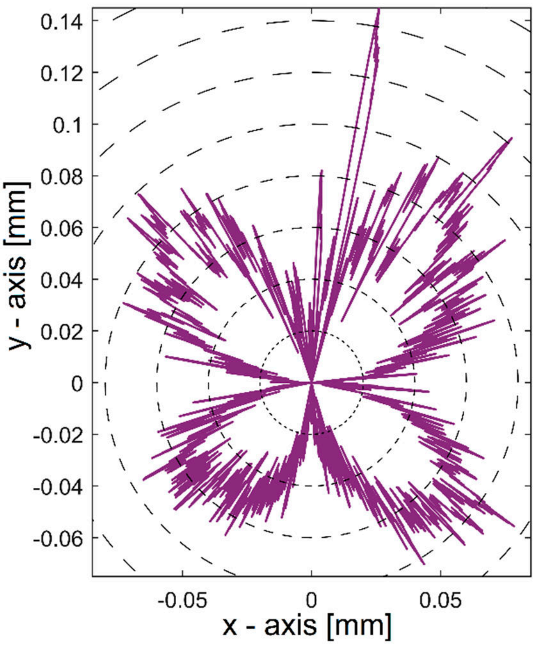

Figure 12. The evolution of TFR_1.

It is interesting to explain why TFR_1 from Figure 12 has four almost similar lobes. The dominant component (as amplitude) in x_e-motion is x_a, while the dominant component in y_e-motion is y_a (with x_a and y_a experimentally revealed by fitting and depicted in Equation (1) as pure harmonic motions).

As previously shown, these two components (having the same amplitude and angular frequency) are not rigorously shifted with $\pi/2$ (as expected).This means that the dominant part of the average trajectory (generated by x_a and y_a motions composition) is not a circle (as expected) but an ellipse. The circular fitting of an ellipse produces a least square circle which intersects the ellipse in four points and a TFR_1 with four lobes, according to the simulation results from Figure 13 (with an elliptical trajectory generated by two harmonic signals shifted with 2.1863 radians). A better explanation for these four lobes in Figure 12 is produced if over this figure is added the TFR_1 of the trajectory generated only by x_a and y_a-motions, with green color, as Figure 14 indicates (here both curves being traversed counter clockwise). A better approach to the shape of TFR_1 involved in Figure 14 is produced if the distances d_{i1} from Equation (5) are calculated related by a circle with smaller radius than the radius of the least square circle (R_c), as TFR_{1a}. As example, in TFR_{1a} from Figure 15, this radius is $R_c - 0.025$ μm.

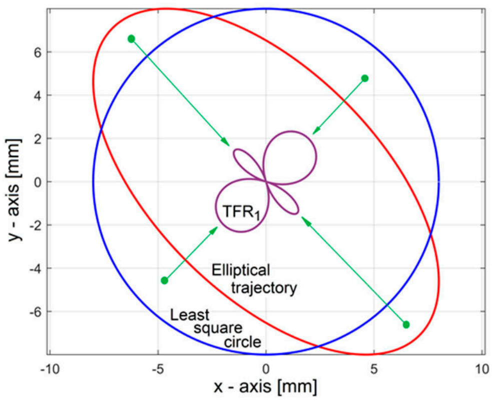

Figure 13. The evolution of TFR_1 generated by circular fitting on an elliptical trajectory (simulation).

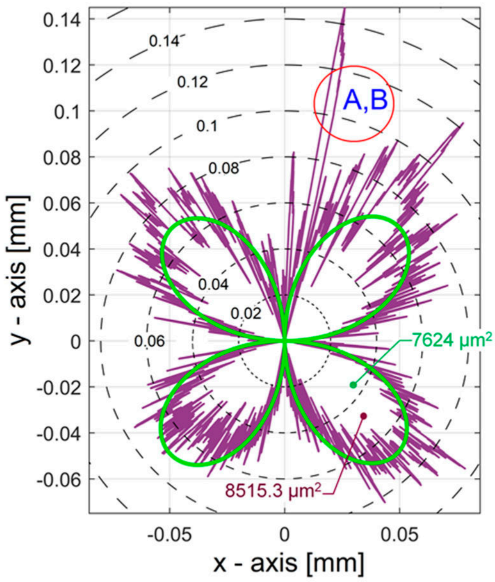

Figure 14. The evolution of TFR_1 generated by x_e and y_e and TFR_1 generated only by x_a and y_a (with green color).

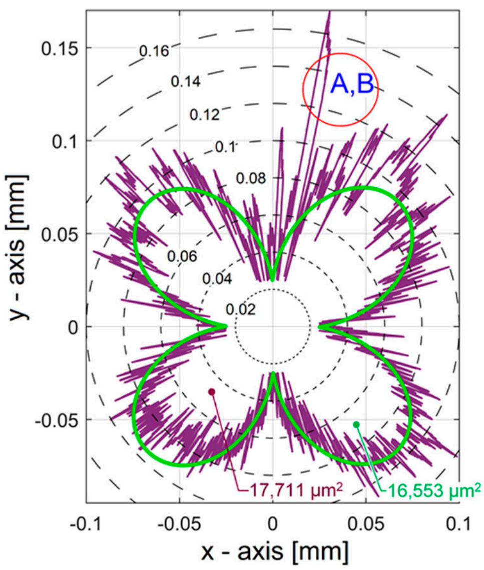

Figure 15. The evolutions of TFR_{1a}.

For P&A evaluation of the average circular trajectory (the result of x_e and y_e simultaneous motions), an important item is the size of the surface delimited by the trajectories fitting residuals (TFR_1 and TFR_{1a}). Each area is a sum of the areas of *N-1*neighboring triangles. All triangles share a common vertex placed in the origin of coordinate systems. The other two vertices are two successive points on TFR. With the area formula of a triangle from [30] (based on the vertices coordinates), the total area delimited by TFR_1 generated by x_e and y_e (Figure 12 or Figure 14) is calculated as 8515.3 μm^2, while the total area delimited by TFR_1 generated by x_a and y_a (Figure 14) is 7624 μm^2.

A second conventional graphical description of the circularity error of the average trajectory (as a second trajectory fitting residual, TFR_2) is available in polar coordinates (d_{i2}, α_{i2}) related to the minimum circumscribed circle (having the same center as the center of the least square circle), with d_{i2}, α_{i2} defined as:

$$d_{i2} = \sqrt{(x_{ei} - x_c)^2 + (y_{ei} - y_c)^2} - R_{cc}\alpha_{i2} = \arctan^4\left(\frac{y_{ei} - y_c}{x_{ei} - x_c}\right) \quad (6)$$

In the first Equation from (6), $R_{cc} = \min\left(\sqrt{(x_{ei} - x_c)^2 + (y_{ei} - y_c)^2}\right)$ is the radius of the minimum circumscribed circle.

Figure 16 presents the TFR_2 of the average trajectory generated by x_e and y_e (R_{cc} = 8.8434 mm) and TFR_2 generated by x_a and y_a (with green color, R_{cc} = 8.9171 mm), with circular grid (with a 50 μm increment on radius). Here the maximum value of distance d_{i2} is 246 μm.

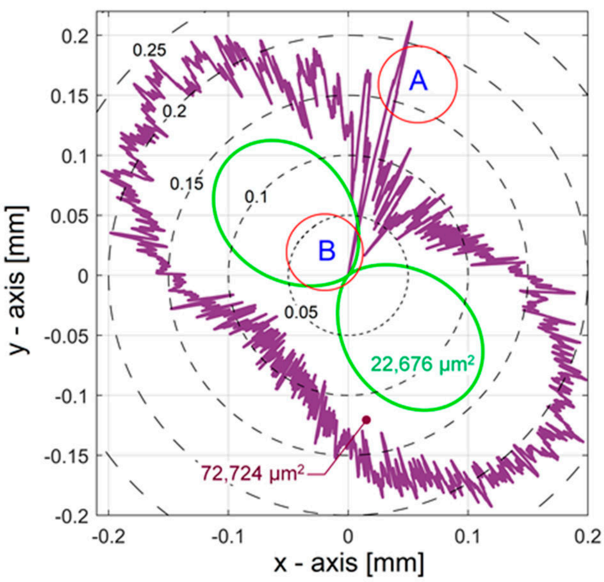

Figure 16. The evolution of TFR_2 generated by x_e and y_e and TFR_2 generated only by x_a and y_a (with green color).

A TFR_2 for a perfect circular average trajectory is a point placed in the origin of the least square circle.

The existence of these two lobes on TFR_2 in Figure 16 is explicable if, in addition to the comments and simulation done in Figure 13, we take into account that the minimum circumscribed circle touches the elliptical trajectory in two symmetrical points. The TFR_2 evolution of a pure elliptical trajectory related to the minimum circumscribed circle is depicted in Figure 17 (by simulation).

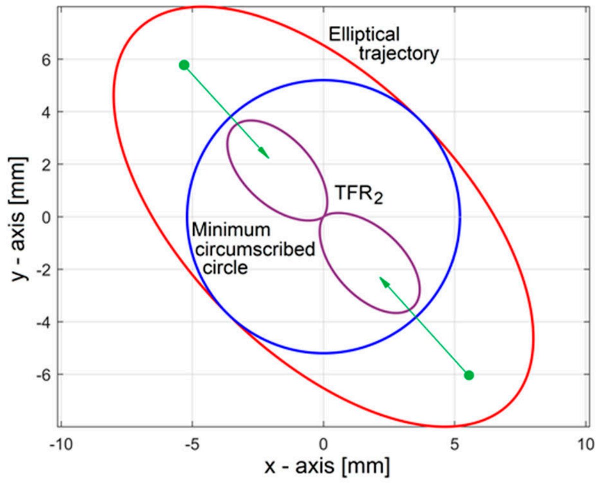

Figure 17. The evolution of TFR_2 generated by circular fitting on an elliptical trajectory (simulation).

Some supplementary resources on the P&A of circular trajectories are revealed by circular fitting of the 2D curve generated only by x_{Ar}-motion (already described in Figure 8) and y_{Ar}-motion (already described in Figure 11), as Figure 18 indicates.

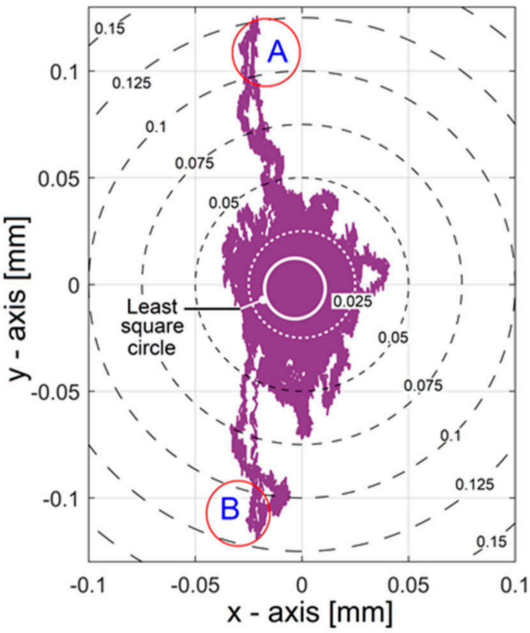

Figure 18. The evolution of the average trajectory generated by x_{Ar} and y_{Ar}.

The least square circle (14.2 µm radius, with center at $x_c = -3.3$ µm and $y_c = -1.9$ µm) should also be considered as an indicator for P&A of the average trajectory.

We should mention that the effect of strong repetitive irregularities on y-motion (y_r and y_{Ar}) already revealed in A, B areas on Figures 8 and 11 are also well described in Figures 14–16 and Figure 18. Moreover, the mirroring of these events A, B in Figure 14 or Figure 15 confirms the previously formulated hypothesis (the comments in Figure 11) that they are related by a sudden release of a mechanical stress inside the toothed belt used for y-motion. In Figure 11, a maximum positive peak from A is immediately followed by a minimum negative peak from B. Therefore, in Figure 14, these two peaks A, B are described as a single peak because of modulus in definition of d_{i1} (Equation (5)).

As it is clearly indicated in Figures 8 and 11, there are strong vibrations on both motions (on x and y), with a negative effect on the P&A of circular trajectories. There are two different strategies available to reduce or to eliminate these vibrations.

The first strategy (probably as the better approach) is to use each stepper motor also as an actuator inside an open-loop active vibration suppression system. The second strategy is to use passive dynamic vibration absorbers or tune mass dampers as well [31] placed on the print bed and on the extruder system. The effect of vibration suppression on TFR_1 or TFR_{1a} shapes should be similar to the effect of a low pass numerical filtering of x_e and y_e. Figure 19 presents the new shape of TFR_{1a} (as TFR_{1af}) if x_e and y_e motions are filtered with a moving average numerical filter (with 1000 samples in the average). As expected, the size of the surface delimited by the TFR_{1af} is not significantly changed (17,399 μm^2 here by comparison with 17,711 μm^2 on TFR_{1a} from Figure 15). The evolution of TFR_{1af} from Figure 19 is also useful when only the influence of the low frequency variable components from x_e and y_e-motions on P&A is investigated and used for errors compensation. The compensation is a feasible option with an appropriate control of stepper motors since they are operated using the microstepping drive technique [32].

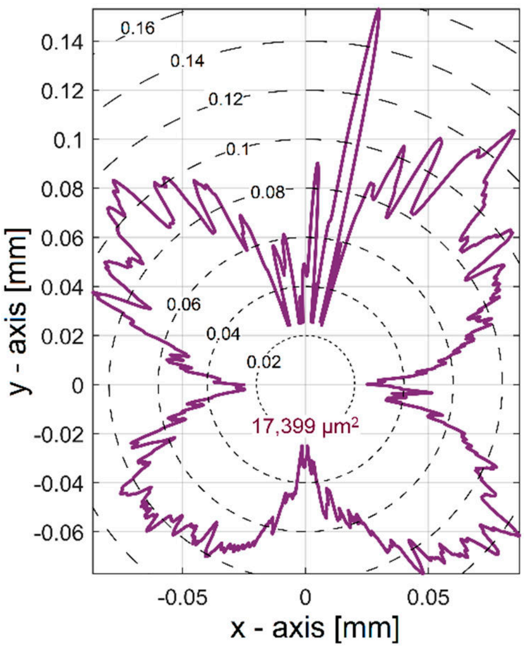

Figure 19. The evolution of TFR_{1a} from Figure 15 with a low pass filtering of x_e and y_e (as TFR_{1af}).

If the accuracy describes how close the real trajectory is to a desired circle (or how close the shapes of TFR_1, TFR_{1a} and TFR_{1af} by a point are), the precision describes the repeatability of real trajectories, each trajectory being generated using a complete cycle (period) of x and y-motions, partially described in Figure 4. The best way to compare these real trajectories is to use the comparison between trajectories fitting residuals related to a circle with a smaller radius than the radius of least square circle (defined similarly to TFR_{1a}) but using low pass filtered x and y-motions (as TFR_{3af}). A perfect coincidence of real trajectories should produce a perfect coincidence of TFR_{3af} trajectories. Figure 20 presents the evolution of TFR_{3af} for five successive real trajectories ($TFR_{3af1} \div TFR_{3af5}$) and the evolution of TFR_{1a}.

Figure 21 presents a zoomed in detail of Figure 20 in area B. As expected, there is not a perfect coincidence of TFR_{3af} trajectories, despite some certain shape similarities (except in area A on Figure 20 where the trajectory TFR_{3af2} is extremely different). It is obvious that the difference between trajectories is less than 10 μm (except in area A). Without any improvement of the 3D printer structure and kinematics, this should also be the theoretical precision after an eventual compensation of the errors (using an appropriate control of the stepper motors). With ideal errors compensations, the trajectories TFR_{1f} should be bordered outside by a circle with 10 μm radius (or 35 μm radius for the trajectories TFR_{3af}).

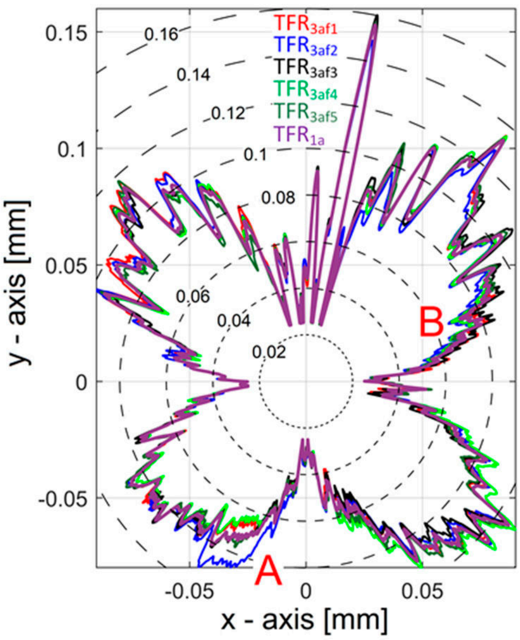

Figure 20. The evolution of TFR_{3af} trajectory for five successive real trajectories ($TFR_{3af1} \div TFR_{3af5}$) and the evolution of TFR_{1a}.

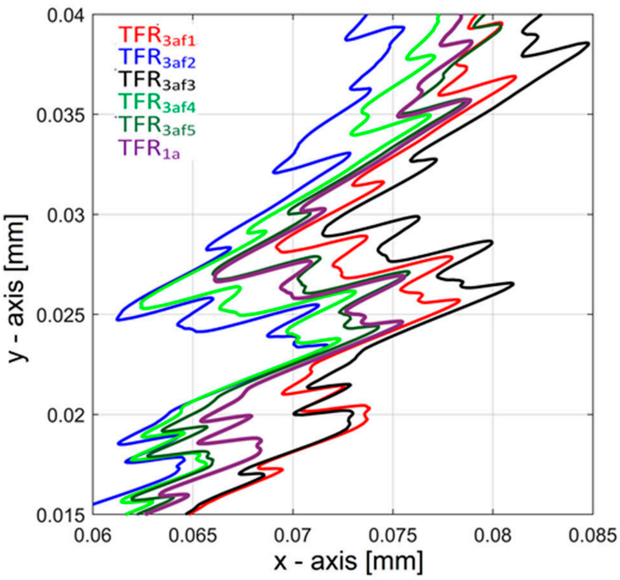

Figure 21. A zoomed in detail of Figure 20 (in B area).

A complete estimation of 3D printer P&A should consider specific trajectories (e.g., circles as in this study) placed in different positions in different 2D locations of the printing volume travelled with different speeds, clockwise and counter clockwise.

4. Conclusions and Future Work

Some theoretical and experimental approaches related to the precision and accuracy (P&A) of a 3D printer, particularly for 2D circular trajectories, were achieved in this paper. The choosing of 2D circular trajectories was inspired from ISO standards methods for P&A evaluation of CNC manufacturing systems (ISO 230-4 [27]) due to some similarities in terms of motion control. The evolution of the simultaneous displacement on two theoretically orthogonal axes (x and y) during a repetitive 2D circular trajectory of the extruder system related to the print bed was simultaneously and continuously measured using a computer-assisted setup based with two contactless optical sensors and a numerical oscilloscope (for sampling and data acquisition). The signals of description for x and y-motions were numerically processed in order to find out some motions characteristics involved in the evaluation of P&A for circular trajectories.

First, a non-perpendicularity of x and y-axes (or an axis misalignment) were experimentally detected (with 0.893 degrees error) by means of the curve fitting (using a pure sine model) of the dominant harmonic components of each signal (x and y-motions signal). Because of this error, a circular programmed trajectory is executed as an elliptical one (typically for a non-orthogonal $x0y$ coordinate system), a topic also confirmed by some supplementary signal processing results.

Second, it was established that the x and y-motions are not simple pure harmonic motions. The residuals of previous curve fitting on each axis movement describe the deviation from pure harmonic shape. A procedure for finding a repetitive periodical pattern in the evolution of these residuals was established and applied with good results. The model of each repetitive pattern is useful in the amelioration of P&A by correction and compensation. The analytical description of the x-motion residual pattern was already established (by curve fitting with a sum of sine model); a future approach intends to do the same for y-motion residual.

Third, a procedure of the description for an average 2D trajectory (an average of several successive theoretically identical circular trajectories) was established. A computer-aided procedure of fitting for closed curves (particularly a circular trajectory) was developed. The circular fitting of the 2D average trajectory was done related to the least square circle. Two conventional graphical descriptions of the circularity errors of the average trajectory were proposed (as trajectory fitting residuals TFR_1 and TFR_2): first description being related to the least square circle, second related to the minimum circumscribed circle.

The shape of these trajectories fitting residuals and the size of the surface delimited by them are useful in P&A evaluation of circular trajectories in order to verify that the 3D printer works properly and, especially, for systematic errors compensation purposes. For example, the non-perpendicularity of x and y-axes previously detected is mirrored in the shape of the average trajectory and, finally, in the shape of these two trajectory fitting residuals (with four similar lobes on TFR_1 and two similar lobes on TFR_2). The deviation from the harmonic shape for x and y-motions is described on these trajectories.

A future approach will be focused on finding a complete procedure of experimental research of P&A using high range/resolution non-contact displacement sensors placed on each of three axes. Some complex 3D curves will be used as test trajectories. A numerical interface between the experimental setup and the 3D printer will be developed in order to perform automated testing and errors compensation.

These signal processing procedures are available to verify the P&A of 2Dcircular trajectories on any other similar equipment (e.g., a 3D CNC manufacturing system).

Author Contributions: Conceptualization, M.H. and C.-G.D.; methodology, M.H. and C.-G.D.; software, A.M.; validation, A.M., M.H. and D.-F.C.; formal analysis, D.-F.C.; investigation, F.N. and C.-G.D.; resources, D.-F.C.; data curation, A.S. and F.C.; writing—original draft preparation, M.H.; writing—review and editing, M.H. and D.-F.C.; visualization, A.S. and A.M. supervision, M.H.; project administration, D.-F.C.; funding acquisition, D.-F.C. All authors have read and agreed to the published version of the manuscript.

Funding: This work was supported by the Technical University Gheorghe Asachi din Iasi, Romania, through the grant GI/P29/2021.

Institutional Review Board Statement: Not applicable.

Informed Consent Statement: Not applicable.

Data Availability Statement: Not applicable.

Conflicts of Interest: The authors declare no conflict of interest.

References

1. Tiwari, K.; Kumar, S. Analysis of the factors affecting the dimensional accuracy of 3D printed products. *Mater. Today Proc.* **2018**, *5*, 18674–18680. [CrossRef]
2. Hällgren, S.S.; Pejryd, L.; Ekengren, J. 3D Data Export for Additive Manufacturing—Improving Geometric Accuracy, 26th CIRP Design Conference. *Procedia CIRP* **2016**, *50*, 518–523. [CrossRef]
3. Lianghua, Z.; Xinfeng, Z. Error Analysis and Experimental Research on 3D Printing. *IOP Conf. Ser. Mater. Sci. Eng.* **2019**, *592*, 012150.
4. Baumann, F.; Bugdayci, H.; Grunert, J.; Keller, F.; Roller, D. Influence of slicing tools on quality of 3D printed parts. *Comput. Aided Des. Appl.* **2016**, *13*, 14–31. [CrossRef]
5. Hernandez, D.D. Factors Affecting Dimensional Precision of Consumer 3D Printing. *J. Aviat. Aeronaut. Aerosp.* **2015**, *2*, art.2. [CrossRef]
6. George, E.; Liacouras, P.; Rybicki, F.J.; Mitsouras, D. Measuring and Establishing the Accuracy and Reproducibility of 3D Printed Medical Models. *Radiographics* **2017**, *37*, 1424–1450. [CrossRef] [PubMed]
7. Chae, M.P.; Chung, R.D.; Smith, J.A.; Hunter-Smith, D.J.; Rozen, W.M. The accuracy of clinical 3D printing in reconstructive surgery: Literature review and in vivo validation study. *Gland Surg.* **2021**, *10*, 2293–2303. [CrossRef]
8. Abdelmomen, M.; Dengiz, F.O.; Tamre, M. Survey on 3D Technologies: Case Study on 3D Scanning, Processing and Printing with a Model. In Proceedings of the 2020 21st International Conference on Research and Education in Mechatronics (REM), Cracow, Poland, 9–11 December 2020; pp. 1–6.
9. Xu, J.; Ding, L.; Love, P.D. Digital reproduction of historical building ornamental components: From 3D scanning to 3D printing. *Autom. Constr.* **2017**, *78*, 85–96. [CrossRef]
10. Favero, C.S.; English, J.D.; Cozad, B.E.; Wirthlin, J.O.; Short, M.M.; Kasperc, F.K. Effect of print layer height and printer type on the accuracy of 3-dimensional printed orthodontic models. *Am. J. Orthod. Dentofac. Orthop.* **2017**, *152*, 557–565. [CrossRef]
11. Vitolo, F.; Martorelli, M.; Gerbino, S.; Patalano, S.; Lanzotti, A. Controlling form errors in 3D printed models associated to size and position on the working plane. *Int. J. Interact. Des. Manuf.* **2018**, *12*, 969–977. [CrossRef]
12. Tanoto, Y.Y.; Anggono, J.; Siahaan, I.H.; Budiman, W. The Effect of Orientation Difference in Fused Deposition Modelling of ABS Polymer on the Processing Time, Dimension Accuracy, and Strength, International Conference on Engineering, Science and Nanotechnology 2016 (ICESNANO 2016). *AIP Conf. Proc.* **2016**, *1788*, 030051-1-030051-7.
13. Divyathej, M.V.; Varun, M.; Rajeev, P. Analysis of mechanical behavior of 3D printed ABS parts by experiments. *Int. J. Sci. Eng. Res.* **2016**, *7*, 116–124.
14. Msallem, B.; Sharma, N.; Cao, S.; Halbeisen, F.S.; Zeilhofer, H.F.; Thieringer, F. Evaluation of the Dimensional Accuracy of 3D-Printed Anatomical Mandibular Models Using FFF, SLA, SLS, MJ, and BJ Printing Technology. *J. Clin. Med.* **2020**, *9*, 817. [CrossRef] [PubMed]
15. Alsoufi, M.S.; Elsayed, A.E. Surface Roughness Quality and Dimensional Accuracy—A Comprehensive Analysis of 100% Infill Printed Parts Fabricated by a Personal/Desktop Cost-Effective FDM 3D Printer. *Mater. Sci. Appl.* **2018**, *9*, 11–40. [CrossRef]
16. Mantada, P.; Mendricky, R.; Safka, J. Parameters Influencing the Precision of Various 3D Printing Technologies. *MM Sci. J.* **2017**, *5*, 2004–2012. [CrossRef]
17. Li, L.; McGuan, R.; Isaac, R.; Kavehpour, P.; Candler, R. Improving precision of material extrusion 3D printing by in-situ monitoring & predicting 3D geometric deviation using conditional adversarial networks. *Addit. Manuf.* **2021**, *38*, 101695.
18. Salmi, M.; Paloheimo, K.S.; Tuomi, J.; Wolff, J.; Mäkitie, A. Accuracy of medical models made by additive manufacturing (rapid manufacturing). *J. Cranio-Maxillo-Facial Surg.* **2013**, *41*, 603–609. [CrossRef]
19. Kacmarcik, J.; Spahic, D.; Varda, K.; Porca, E.; Zaimovic-Uzunovic, N. An investigation of geometrical accuracy of desktop 3D printers using CMM. *IOP Conf. Ser. Mater. Sci. Eng.* **2018**, *393*, 012085. [CrossRef]
20. Jadayel, M.; Khameneifar, F. Improving Geometric Accuracy of 3D Printed Parts Using 3D Metrology Feedback and Mesh Morphing. *J. Manuf. Mater. Process.* **2020**, *4*, 112. [CrossRef]
21. Majarena, A.C.; Aguilar, J.J.; Santolaria, J. Development of an error compensation case study for 3D printers. *Procedia Manuf.* **2017**, *13*, 864–871. [CrossRef]
22. Keaveney, S.; Connolly, P.; O'Cearbhaill, E.D. Kinematic error modeling and error compensation of desktop 3D printer. *Nanotechnol. Precis. Eng.* **2018**, *1*, 180–186. [CrossRef]
23. Qian, S.; Bao, K.; Zi, B.; Wang, N. Kinematic Calibration of a Cable-Driven Parallel Robot for 3D Printing. *Sensors* **2018**, *18*, 2898. [CrossRef]
24. Kochetkov, A.V.; Ivanova, T.N.; Seliverstova, L.V.; Zakharov, O.V. *Kinematic Error Modelling of Delta 3D Printer*; Materials Science Forum, Trans Tech Publications, Ltd.: Zurich, Switzerland, 2021; Volume 1037, pp. 77–83.
25. Cajal, C.; Santolaria, J.; Velazquez, J.; Aguado, S.; Albajez, J. Volumetric error compensation technique for 3D printers. *Procedia Eng.* **2013**, *63*, 642–649. [CrossRef]
26. Duan, M.; Yoon, D.; Okwudire, C.E. A limited-preview filtered B-spline approach to tracking control—With application to vibration-induced error compensation of a 3D printer. *Mechatronics* **2018**, *56*, 287–296. [CrossRef]
27. *Test Code for Machine Tools—Part 4: Circular Tests for Numerically Controlled Machine Tools*; ISO230-4; ISO: Geneva, Switzerland, 2005.
28. Anet. Available online: https://anet3d.com/pages/a8 (accessed on 7 November 2021).
29. MICRO-EPSILON. Available online: http://www.img.ufl.edu/wiki/images/ILD_2000_Datasheet.pdf (accessed on 7 November 2021).

30. Math Open Reference. Available online: https://www.mathopenref.com/coordtrianglearea.html (accessed on 7 November 2021).
31. Yang, F.; Sedaghati, R.; Esmailzadeh, E. Vibration suppression of structures using tuned mass damper technology: A state-of-the-art review. *J. Vib. Control* **2021**, in press. [CrossRef]
32. Barabas, Z.A.; Morar, A. High performance microstepping driver system based on five-phase stepper motor (sine wave drive). *Procedia Technol.* **2014**, *12*, 90–97. [CrossRef]

BULETINUL INSTITUTULUI POLITEHNIC DIN IAŞI
Publicat de
Universitatea Tehnică „Gheorghe Asachi" din Iaşi
Volumul 63 (67), Numărul 1, 2017
Secţia
CONSTRUCŢII DE MAŞINI

PORTABLE DEVICE FOR CONTROL OF INNER CYLINDRICAL SURFACES - THE COAXIALITY PARTICULAR CASE

BY

ADRIANA MUNTEANU*, FLORENTIN CIOATĂ and CRISTIAN COBZARU

"Gheorghe Asachi" Technical University of Iaşi,
Faculty of Machine Manufacturing and Industrial Management

Received: December 15, 2016
Accepted for publication: September 15, 2017

Abstract. One of the most complex and difficult tasks regarding the geometrical tolerances is the measurement of coaxial deviation of inner cylindrical features. The paper addresses the difficulties met in the evaluation of coaxiality tolerances and starting from the idea that the exact methods are difficult to implement but also complex and expensive. Instead verification methods for checking coaxiality with mandrel control or plugs are easy to apply but does not offer accuracy regarding the results and are in the impossibility of obtained validation, the portable methods for measuring either do not provide the accuracy required or are time consuming and adjusting processing machine payoffs is very high. This paper presents a portable device capable of providing precision but to be easy to handle and adjust.

Keywords: coaxial deviation; portable device; selfcentering device.

1. Introduction

Concentricity and coaxiality deviations are a part of surfaces relative position deviations, which together with guidance deviations, determine the

*Corresponding author; *e-mail*: adycypmunteanu@yahoo.com

orientation and accuracy of relative position of geometric elements of machine features.

Deviation from coaxiality represents the maximum distance between the real adjacent rotation axis of considered surface and the datum axis measured within the reference length. The datum axis can be the rotation axis of other adjacent surfaces or the common axis of multiple rotation adjacent surfaces (Xuebao, 2009). In case of the machine parts joints with outer and inner rotating surfaces, coaxial deviations of the mounting surface constitute a decisive factor in the correct combination of joint parts and of the assembly functioning at the specified parameters (Kaisarlis *et al*., 2011; Gherghel and Seghedin, 2006).

In the shaft piece type case, the coaxiality deviation of inner surfaces determines the incorrect position of fitted parts and during the operation these items will rotate eccentrically.

Measurement of coaxiality deviation of the inner cylindrical surfaces, sleeve type pieces, is generally performed using stationary devices, equipped with indicating instruments; when a portable equipment is required, there are necessary mechanisms and centering elements on the inner cylindrical surface, specified as given.

The coaxiality deviation control of inner cylindrical surfaces of the holes, in carcasses (frame) case, is achieved by testing and measuring using distinct control methods (Seghedin, 2006) briefly presented in Fig. 1.

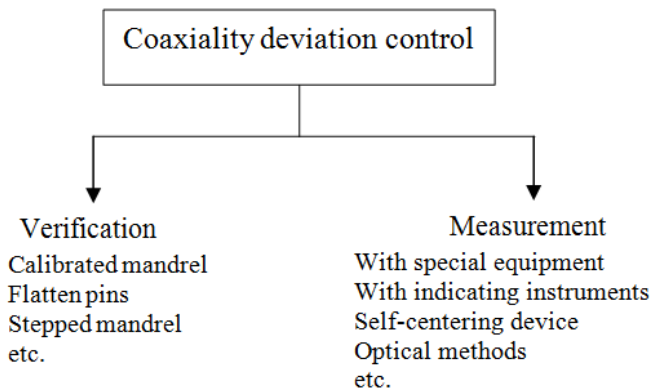

Fig. 1 − Methods for coaxiality deviation control.

Taking in consideration the analysis of the methods for measuring coaxial deviation of the inner cylindrical surfaces, socket type parts, namely, carcasses, the following conclusions could be emphasized (Demian, 1980; Mircea, 2004; Seghedin, 2006):

• the precise measurement methods are difficult to implement in case of the stationary control means and require a complex and costly range of measuring instruments and accessories;

• the verification methods with pins or testing mandrel are easy to apply, but do not provide appropriate verification accuracy, leading to irrelevant results of the verification, especially in the case of carcasses with large distances between walls (Drăghici *et al.*, 1981; Sturzu, 1977);

• the measurement methods that use portable devices either do not provide adequate accuracy or are time-consuming regarding adjustment, measurement and processing of measurement results.

2. Schematic Diagram of the Portable Device

To establish a method of measuring the deviation from coaxiality, it was considered its definition, as the maximum distance between the axis of the inner considered cylindrical surface and the axis of cylindrical inner pair, specified as datum axis, measured within the reference length. Thus, a method characterized by the following elements was considered (ISO System Standard; Dimensional Engineering, Based on the ASME Y14.5M-1994):

• Materialization of inner cylindrical surface axis specified as datum axis;

• Materialization of tolerated axis of cylindrical inner surface (pair surface);

• Measuring the distance between the two axes materialized (Coaxiality Tolerance, available at: https://books.google.ro/books, 2016).

To measure the deviation from coaxiality, the materialization of the axes of the two inner cylindrical surfaces is required (Fig. 2). For this purpose, a contact could be achieved among the inner cylindrical surfaces *a* and *b,* the levers 2 and 3, which move in radial direction with the same distance (movement III), in bearing 4, which can be locked with locking screws 5. Each support can move on the cylindrical rods 6 and 7 (movement II) and locks in the desired position by locking screws.

In this way, it materializes the axes of the two inner cylindrical surfaces *a* and *b*, which coincide with the axes of cylindrical rods 6 and 7. On the cylindrical rod 6, there is mounted the support 8 of the indicating instrument 9, whose measuring tip is placed in contact with the surface *c*, of a calibrated roller 10. It is mounted to fit with minimum clearance equal to zero on the cylindrical rod 7; thus, calibrated roller axis 10 coincides with the axis of the cylindrical rod 7.

The support 8 of the indicator instrument 9 can rotate without clearance, on the cylindrical rod 6 (rotational movement I). After contacting the feeler with *c* surface, the indicating instrument (a dial gauge or a digital comparator) is set to zero. It is rotated, then the indicating instrument maintains a permanent contact between the feeler and measured surface *c* of a calibrated roller 10, during a complete revolution and one will note the extreme indications of the instrument δ_{max} and δ_{min}.

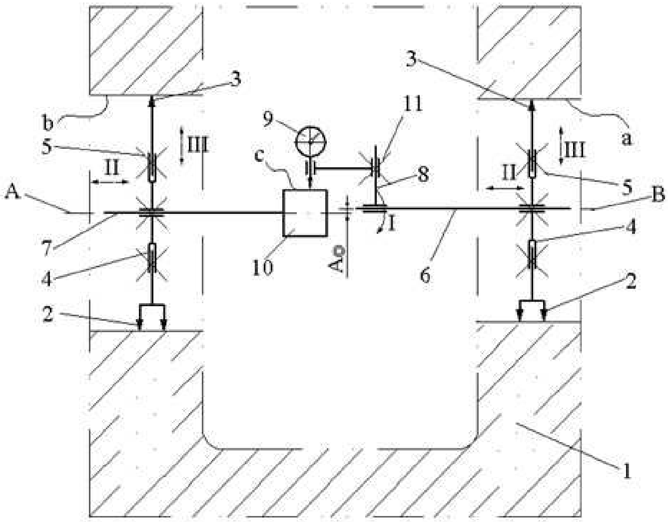

Fig. 2 − The materialization of inner cylindrical surface axis specified as datum axis.

The coaxiality deviation of the cylindrical surface axis with the axis of the inner surface *b*, specified as datum axis, is expressed by the relationship:

$$A_{\odot} = \frac{\delta_{max} - \delta_{min}}{2} \tag{1}$$

The measurement schemes may guide to the development of a diagram both for a stationary or portable technological device, applicable to measure the deviation from coaxiality of the axes of inner cylindrical surfaces in case of sleeve and carcasses pieces.

The analysis of the presented method have highlighted the following conclusions:

• There was considered a measurement method based on the definition of deviation from coaxiality of the cylindrical surfaces as the maximum distance between the axis of the considered surface and the axis specified as datum;

• The measuring method is the difference method; the coaxiality deviation is measured between the two axes considered coincident with the position of their own;

• It is necessary zeroing the indicating instrument for the position of the inner cylindrical surfaces axis specified as datum axis;

• The deviation from coaxiality measurement can be achieved using controlled workpieces with axes oriented horizontally or vertically.

These conclusions highlighted that the analysis of the presented measurement method are at the same time requirements that must meet the control device presented in this paper.

The essential advantage of the examined devices is the accuracy of centering; the most important disadvantage is that solutions that provide greater accuracy of centering are not covered by a sufficient range values of inner cylindrical surfaces diameter and they are characterized by a high complexity (for example, selfcentering devices with plungers).

In this paper it is proposed as solution a selfcentering mechanism which eliminates the two drawbacks mentioned above, having a medium complexity and providing for a sufficient diameters values range, so that it is characterized by a high degree of universality (Fig. 3).

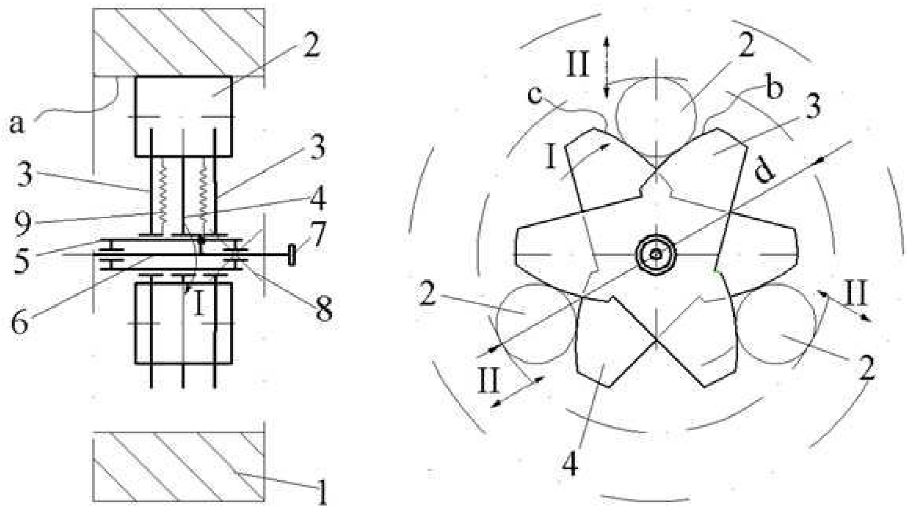

Fig. 3 − Selfcentering mechanism with calibrating rollers.

This mechanism is named selfcentering mechanism with calibrating rollers, because the contact elements with the surface *a* of the workpiece 1, is achieved by three cylindrical rollers 2. The rollers surfaces are made so that they materialize the geometric cylinder (the deviation from cylindricity is minimum). The contact of the calibrated rollers (arranged uniformly on the circumference) with the cylindrical inner surface *a* is performed along their generators. The calibrated rollers are supported by active edges of the profile *b* of the discs 3 and *c* shaped edge of the disc 4. The two discs 3 are mounted on the cylindrical body 5 secured to it, and the disc 4 is also mounted on the cylindrical body; it is placed between the discs 3. The disc 4 can be moved on the cylindrical body 5 (rotational movement I), in relation to the disk 3, and it is trained in rotation by the shaft 6, driven by handwheel 7 and may be locked in the desired position using the locking screw 8.

By rotation of the disc 4, there is changed the relative position of the active edge profile *b* and *c*, on which the two calibrated rollers are leaned and which determines the displacement, in a radial direction, of two calibrated rollers (movement II).

At the mobile disc 4 rotation, the three calibrated rollers 2 move radially with the same distance, so that the generators most distant from the common axis of the discs 3 and 4 of the rollers will materialize an adjacent cylinder whose diameter is variable.

Permanent contact of the calibrated rollers with the active shaped edges of discs 3 and 4 is provided by stretching coil springs 9.

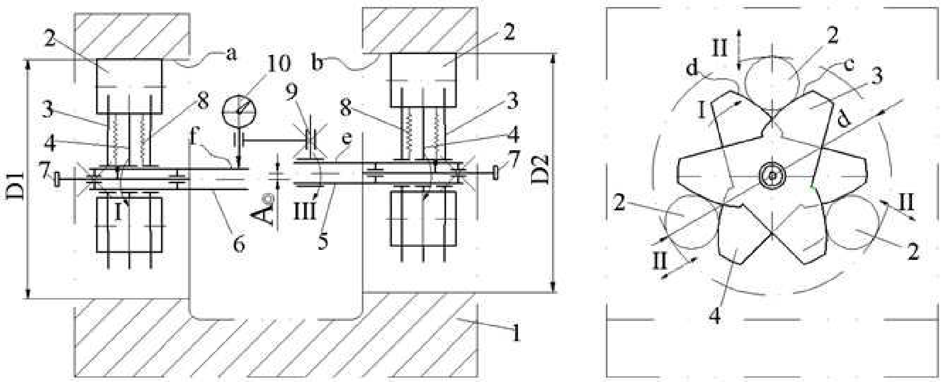

Fig. 4 – Schematic diagram for portable device.

In the present paper, the above mentioned device for coaxial deviation measurement case is particularized. Schematic diagram of the technological device for measuring coaxial deviation from the inner cylindrical surfaces is simple, using two selfcentering mechanisms and a mechanism for the guidance and fixing of the indicator instrument (Fig. 4).

In this case, it is noted that the control device diagram complies with the measurement scheme adopted in Fig. 2. To materialize the axes of inner cylindrical surfaces *a* and *b,* there are used two selfcentering mechanisms with calibrated rollers formed by calibrated rollers 2, fix disks 3 and mobile disks 4, cylindrical bodies 5 and 6 with the active surfaces *e*, respectively *f,* and the mechanisms of the mobile disc 4 rotation driven by hand wheels 7.

When the two calibrated rollers come into contact with the internal cylindrical surfaces *a* and *b*, the active surfaces *e* and *f*, of the cylindrical bodies

5 and 6, are coaxial with the corresponding inner cylindrical surface. Thus, one can measure the deviation from coaxiality of the inner surfaces *b* to *a*, by measuring the maximum distance between the axes of the active surfaces *e* and *f* of the cylindrical bodies. With this aim in view, the active surface *f* is brought into contact with the feeler of the indicating instrument 10 and the instrument is set to zero. The indicating instrument is fixed to the holder 9, which is mounted on the cylindrical body 5 that can be rotated on the active surface *e*.

After zeroing, the indicating instruments is rotated, with a full rotation, in permanent contact with the surface *f* of the cylindrical body 6 and the extreme indications δ_{max} and δ_{min} of the instrument are noted, so that to the coaxiality deviation could be determined.

Deviation from the coaxiality of the axis of cylindrical surface with the axis of the inner surface *b*, specified as datum, is obtained using the Eq. (1).

3. Portable Device for Measuring the Coaxiality Deviation

Starting from the schematic diagram of the control device above mentioned (Fig. 4) and knowing the requirements that must be fulfilled, it has developed a constructive version of a portable technological device designed to control the coaxial deviation of cylindrical inner surfaces (for bush type workpieces) with diameters in the range from 90 mm to 130 mm (Figs. 5 and 6).

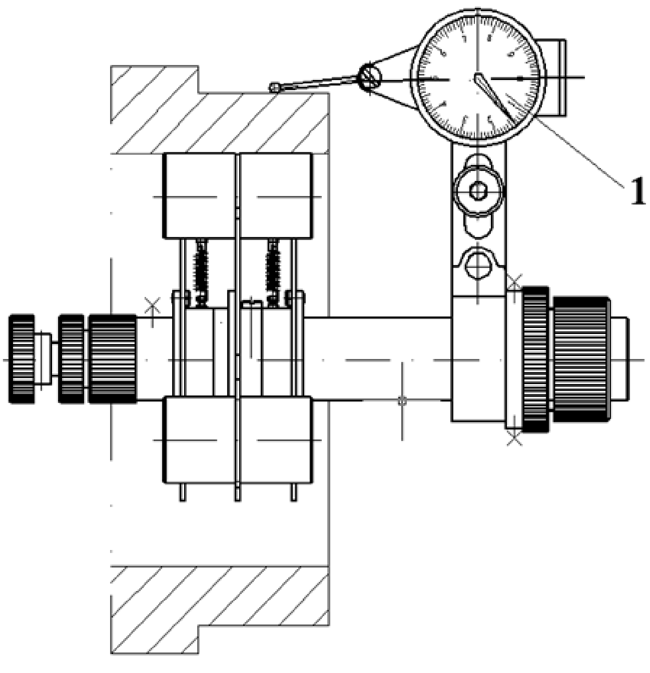

Fig. 5 − Coaxiality control portable device – front view.

Characteristic of this control device is that, being a portable device, all the important components for determining the positioning and orientation of the controlled workpiece, respectively the indicating instrument, are all unitarily integrated into the device body.

The technological device for the control of coaxiality of inner cylindrical surfaces consists of the following distinct subsets:

• The subassembly device of orientation and positioning;

• The measurement subassembly;

• Auxiliary elements and mechanisms.

The first two types of subassembly with the auxiliary elements and mechanisms are mounted on the tubular body of the control device.

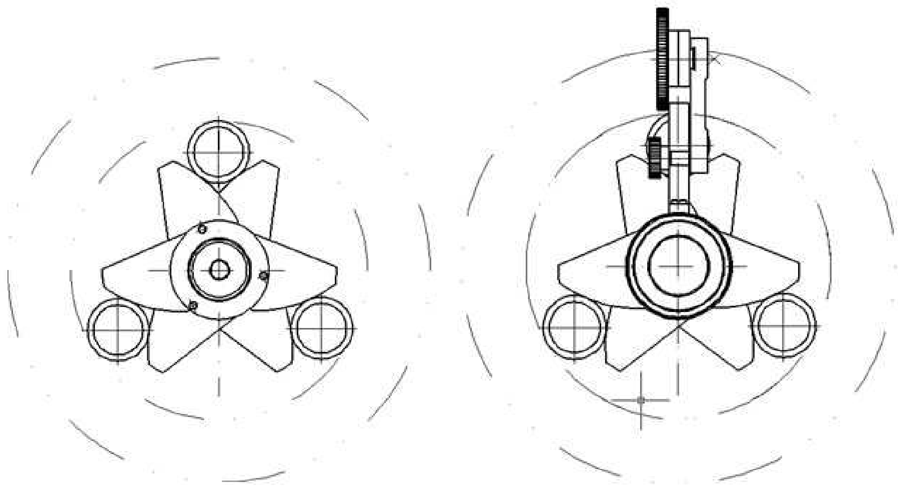

Fig. 6 − Coaxiality control portable device – top view.

The assembly of orientation and positioning of the control device is designed to guide it in relation to the control piece and to position it on the inner cylindrical surface of the workpiece, type sleeve, in order to measure the deviation from coaxiality; simultaneously, this subset materializes the axis of rotation of the adjacent inner cylindrical surface, which will support the measuring device (Fig. 7).

The subset consists of a centering mechanism with calibrated rollers. Centering mechanism comes into contact with the inner cylindrical surface of the workpiece, along three straight lines that are the generators which are most distant from the center of the calibrated rollers 3; in this way, the three straight-line generators, evenly distributed over the circumference of the cylindrical surface, materialize the adjacent cylinder of the measured inner surface which forms the datum axis.

The calibrated rollers rest on the edges of the active profile of the two disks, coming into contact with them, in three points: two points on edges assets of the two fix disks and a contact point on the active edge of a mobile disc.

To prevent axial movement of calibrated rollers to active edges of the fixed disks, on the calibrated cylindrical surface of the rollers is realize a channel, in which is includes the removable disk edge. The permanent contact between the calibrated rollers and the edges of active disks is provided by stretching coil springs (two springs for each roll calibrated).

The assembly for measuring ensures the determination of deviation from coaxiality of the tolerated inner cylindrical surface compared to the datum axis materialized by the orientation and positioning subassembly; this measurement assembly captures the measurement information and sends it to indicator instrument (Fig. 7).

The measurement information is transmitted directly to one indicating instrument (Fig. 7), because the item capture is just the feeler of this instrument; spherical probe of the indicating instrument 1 is brought into contact with the control inner cylindrical surface. It has chosen like indicating instrument, for example a pupitast that can be placed in locations with limited volume, because of its small overall dimensions. This indicating instrument is mounted on an adjustable support so that one can control the fixing height. This support is mounted on the active surface of the cylindrical device body with minimum clearance equal to zero and can perform two movements:

• a movement of rotation round of the axis of the cylindrical body; this movement is achieved during measurement to ensure the crossing of one complete rotation;

• a movement of axial displacement of the active surface of the cylindrical body; this movement is performed to adjust the device so that the probe is brought into the control inner cylindrical surface.

The axial movement, that is achieved when the adjusting device runs, must be blocked during the measurement and with this aim in view, an elasticized sleeve mounted on the cylindrical body was used; this solution with elasticized sleeve was imposed by the necessity of blocking only the axial movement, but to permit freely rotation around the axis of the cylindrical body. Thus, the two assemblies, which forms the device (the mechanism of selfcentering with calibrated rollers and the mechanism of fixing the indicating instrument), are mounted on the same element, namely, its cylindrical body. This fact gives an increased accuracy of the control device measurement, because:

• Arrangement of the three discs, fixed and mobile, in centering mechanism structure on the same cylindrical surface of the device body determines the coincidence of the axis of the adjacent cylinder materialized by calibrated rollers with the axis of the active surface of the cylindrical body;

• Fixing mechanism (displacement) layout of the indicator instrument on the active surface of the cylindrical body determines the instrument rotation around the axis of the adjacent cylinder specified as datum axis.

The measurement technique of the coaxiality deviation is presented in Fig. 7, where 1 is the workpiece, 2 and 2' are calibrated rollers, 4 and 4' are cylindrical bodies, 5, 5', 6 and 6' are adjustment elements, 7 is the indicating instrument feeler, 8 is the indicating instrument, 9 is the fixing support and 10 is bushing cantilever.

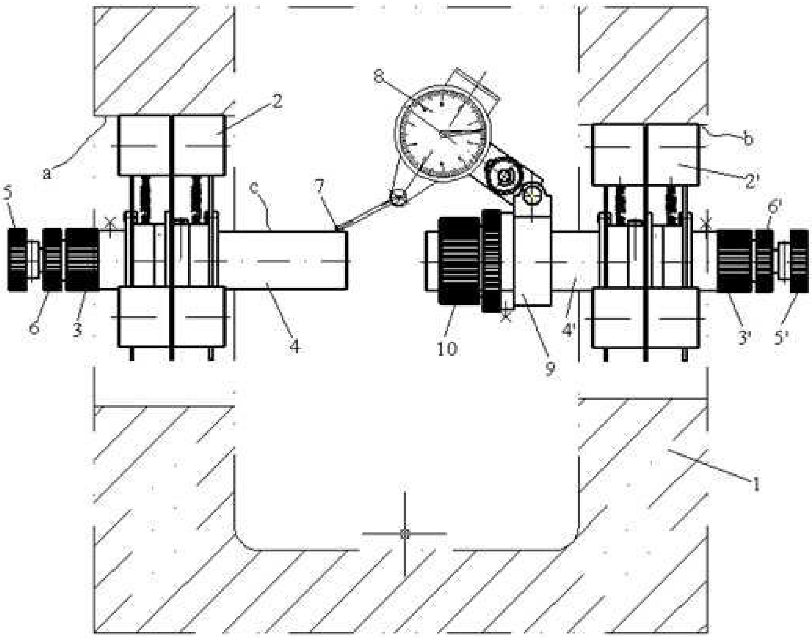

Fig. 7 – Measurement technique.

4. Conclusions

Considering the above mentioned aspects, the aim of this paper was to establish a system of rule checking for device that overcomes the highlighted drawbacks and to combine advantages of stationary devices, characterized by high precision measurement, but that cover a range values for diameters of controlled inner cylindrical surfaces between 90 mm and 130 mm. Thus, the device is based on a new solution of selfcentering mechanism with contact on the inner cylindrical surface. This selfcentering mechanism with calibrated roller mechanism has a great accuracy of materializing the rotation adjacent surfaces.

The portable device presented in present paper has some specific characteristic:

– The possibility of materializing the adjacent cylinder to both the inner cylindrical surface of control, as well as specified datum;

– The possibility of using the parts controlled axis oriented horizontally or vertically;

– The device has a small number of mobile joints, which increases the measurement accuracy;

– The high degree of versatility allows the use in multiple categories of items: fixed or rotating bushing type, skeletal etc.;

– Covers a wide range of diameters of materialized surfaces and ensures a quick adjustment on adjacent cylinder to be materialized;

– It has reduced constructive complexity, with reduced overall dimensions and mass.

The device can maintain the values to which there was safe to be adjusted and easy to be handled, and to ensure fast measurements.

The aim of future research is to study the possibility of using this new device in other types of measurements.

REFERENCES

Demian T., *Constructive Elements of Fine Mechanics* (in Romanian), Edit. Didactică şi Pedagogică, Bucharest, 1980.

Drăghici I. *et al*., *Guidelines in Machine Design* (in Romanian), vol. **1** and **2**, Bucharest, Edit. Tehnică, 1981.

Kaisarlis G., Provatidis C., Sfantsikopoulos M., *A New Approach for the Effectiveness of Coaxiality Tolerance Verification*, International Journal of Applied Science and Technology, **4**, *3*, 39-49 (2011).

Gherghel N., Seghedin N., *Conception and Design of Technological Devices Supports* (in Romanian), Iaşi, Tehnopress Publishing House, 2006.

Mircea D., *Dimensional Control in Machine Manufacturing* (in Romanian), Iași, Tehnopress Publishing House, 2004.

Seghedin N., *Technological Devices for Fine Mechanics* (in Romanian), Iași, Tehnopress Publishing House, 2006.

Sturzu A., *Basics of Research and Design of Control Devices for the Accuracy of form and Position of Surfaces* (in Romanian), Bucharest, Edit. Tehnică, 1977.

Xuebao G., *Improvement Coaxiality Measurement Method for Transmission Shaft*, Acta Photonica Sinica, **38**, *11*, 2932-2936 (2009).

*** ISO System of Tolerances and Fits (Collection of Standards).

*** *Coaxiality Tolerance*, available at: https://books.google.ro/books?id=Pw4x1wzBHmoC&pg=PA308&lpg=PA308&dq=coaxiality+tolerance+definition&source=bl&ots=GmucQjE992&sig=VWCkToYlXoaS09PJ9gR7RwTSN2c&hl=ro&sa=X&ved=0ahUKEwi7iLWD893RAhWCkiwKHSQWAJY4ChDoAQhAMAU#v=onepage&q=coaxiality%20tolerance%20definition&f=false, accessed: December 2016.

*** Dimensional Engineering, Based on the ASME Y14.5M-1994 Dimensioning and Tolerance Standard.

DISPOZITIV PORTABIL PENTRU CONTROLUL SUPRAFEȚELOR CILINDRICE INTERIOARE - CAZUL PARTICULAR AL COAXIALITĂȚII

(Rezumat)

Una dintre sarcinile cele mai complexe și dificile în ceea ce privește toleranțele geometrice este măsurarea abaterilor la coaxialitate ale suprafețelor cilindrice interioare. Lucrarea abordează dificultățile întâmpinate în evaluarea abaterilor la coaxialitate, plecând de la ideea că metodele precise sunt greu de implementat, dar și complexe şi scumpe. În schimb, metodele de verificare a coaxialității cu dornuri de control sau cu cepuri sunt uşor de aplicat, dar nu oferă acuratețe, ducând la imposibilitatea validării rezultatelor obținute, iar metodele portabile de măsurare fie nu asigură precizia cerută, fie timpul de reglare și prelucrare a rezultatelor este foarte mare. Se prezintă un dispozitiv portabil capabil să asigure o bună precizie, dar să fie și ușor de manevrat și de reglat.

MATEC Web of Conferences **112**, 01001 (2017) DOI: 10.1051/matecconf/201711201001
IManE&E 2017

Portable selfcentred device with calibrated rollers

Adriana Munteanu*, *Florentin* Cioata, and *Emilian* Paduraru

Technical University Gheorghe Asachi of Iaşi, Department of Machining Tool, Bdul Mangeron, 59A, 700050, Iaşi, România

Abstract. The critical analysis of the self-centering devices for inner cylindrical surfaces highlights a number of advantages and disadvantages of these solutions. The key benefit is the precision but the most important disadvantage it is that doesn't covers a sufficiently range of values for the inner diameters and are very complex. In the present paper a solution of centering mechanism with calibrated rollers that eliminates the disadvantages mentioned above, with a medium complexity but ensuring a sufficient range of values for measured surfaces is proposed. The method used to obtain the specified range of values is graphic method.

1 Introduction

The inspection of geometrical deviations (especially the coaxial deviation and concentricity deviation) is an issue developed in specified standards [1, 2]. There are several methods for inspecting but these methods are more or less precise [3].

In industrial practice the measurement of geometrical deviations is an economic aspect that imposes specified inspection methods if the production is mass one. So because of this are used inspection methods more precise that are normally more time consuming and more costly. When the manufacturing production is small the less precise inspection methods that are normally less time consuming and less costly are used [4].

In the coaxiality and concentricity deviation measurement the literature propose in various cases the deviations measuring with the coordinate measuring machines [5] that are time consuming so the development was focused on optical technology, high-speed electronics and computers. But those are expensive. In exclusive production type is necessary a device control that satisfies the following conditions:
• High manoeuvrability, so as to ensure quick measurement of the considered deviation;
• Zeroing quick and easy, without requiring costly additional accessories;
• High degree of universality that would ensure a measuring range as large as possible;
• The indicator instrument: the control device to be fitted with indicator instrument;
• The degree of mobility: control device to be portable;
• Fixing and positioning elements: the control device must have in its structure, fixing and positioning elements for instrument indicator, respectively its orientation relative to the controlled workpiece [6, 7].

*Corresponding author: adycypmunteanu@yahoo.com

2 The schematic diagram of the portable device

In any design process when it is establish a schematic diagram for a control device based on adopted measurement scheme following aspects must be resolved [7, 8, 9]:
• The method of difference application, as a method of measuring of coaxial deviation of inner cylindrical surfaces;
• The compliance of adopted measuring scheme;
• The orientation and the positioning of control device on the inner cylindrical surface specified as datum, in order to materialized its axis;
• To establishing a simple solution for displacement in the radial direction, of the contact elements to the inspected surface;
• The existence, in the device structure, of an element for the realization of inner cylindrical surface tolerated axis;
•The device must be fitted with some indicator whose feeler can perform a circular motion, or if this feeler has a linear movement to establish a variant of displacement transmission of the feeler at the measuring tip;
• To ensure for a sufficiently range values of inner diameters of the two cylindrical surfaces (adjusting solution);
• The possibility to zeroing the control device with calibrated elements accurate mounting on the device;

The proposed solution of selfcentering mechanism (presented in a previous paper [3]) provide greater accuracy of centering and covers a sufficiently typo dimensional values for the cylindrical inner surfaces diameter and is characterized by a high degree of universality (Figure 1).

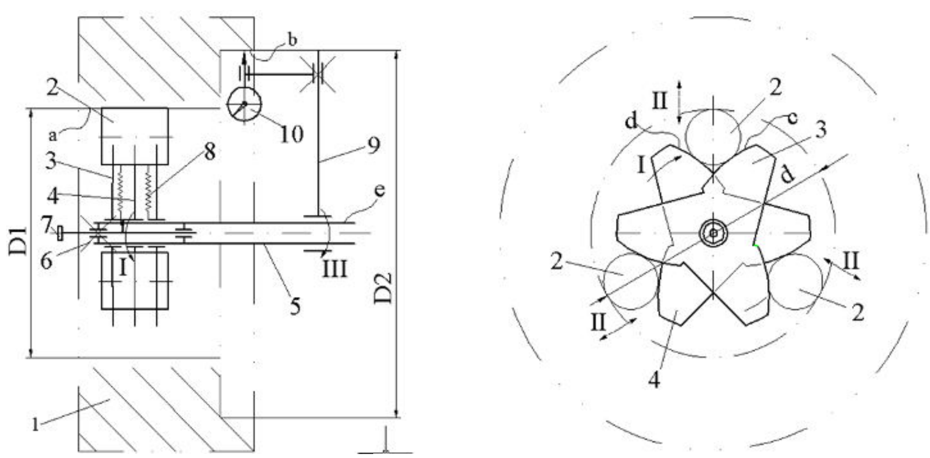

Fig. 1. Portable device

For generation of schematic diagrams of this portable control device, adopted by the measuring scheme, it has been identified a number of requirements to be met (Figure1):
• It is necessary to materialize the axis of inner tolerated cylindrical surface (*a* and *b* surfaces); this requirement is imposed by the adopted scheme measurement;
• It is necessary to materialize the axis of inner cylindrical specified as datum (by the calibrated rollers 2, and the mobile and fix disks 3 and 4);

• The measuring of deviation from coaxiality of inner cylindrical surfaces is achieved with a portable control device (with the cylindrical body 5) that must provide both orientation and positioning relative to the workpiece (1) and the measurement;
• Performing measurement of deviation from coaxiality (distance between the materialized rotation axes) using an indicating instrument (the indicating instrument 10 and its support 9);
• Providing guidance of the control device on inner cylindrical surfaces of different diameters (the active surface *e*);
•Ensure the measuring deviation from coaxiality of inner cylindrical surfaces of parts with different distances between the cylindrical surfaces considered (by movement of calibrated rollers by hand wheels 7).

3 The graphic solution for control device dimensioning

Dimensional element of the workpiece that is decisive in determining the characteristic dimensions of the control device is the diameter *D* of the inner cylindrical surface of the workpiece because it determines the overall dimensions of the control device. To establish the characteristic dimensions of the device control it was considered the nominal values for diameter *D* of the inner cylindrical surface of the workpiece. This range of values is set between 90 and 130 mm.

The decisive size in determining the overall dimensions of the self centering mechanism with calibrated roller from the control device structure is the minimum diameter of the cylindrical inner surface, in which the centering mechanism should be introduced. Thus, the diameter of this mechanism must have the diameter less than the diameter of the cylindrical inner surface.

The characteristics dimensions of the control device are dimensions that determine the overall of all assemble sizes which determine the structure of the device subassemblies, the lengths of running components who execute displacements, etc. After the obtaining mode, the characteristic dimensions of the device control fall into two distinct categories:
• The characteristic dimensions adopted;
• The characteristics dimensions calculated.

In the considered situation an important place in the control device designed the following adopted characteristic dimensions are relevant:
• The diameter of centering mechanism with calibrated roller (the three fixed and mobile discs, will have a smaller diameter than the minimum diameter of the surface to be inspected;
• The length of the cylindrical body of the self centring device with calibrated rollers (the length of the cylindrical body will be greater than the maximum value of the length of the control);
• The diameter of calibrated rollers. Calibrated rollers, when their generators are brought into contact with the inner cylindrical surface of control, are designed to materialize the cylinder adjacent thereto; by moving their radials to come into contact with the inner cylindrical surface.

But for this selfcentering device the calculated characteristics dimensions depends on the size characteristic of the device control, for ensuring that measurement functions, the orientation of control device for limiting the course of moving parts that perform rotational motion or translation.

To designed control device must considered the following characteristic dimensions:
• Travel length of calibrated rollers - To materialize the adjacent cylinder of the inner cylindrical surface with different values of diameter, the calibrated rollers must move on

radial direction with the distance l_c, called the length of stroke; it is calculated by the relationship 1:

$$l_c = \frac{D_{max} - D_{min}}{2} \quad (1)$$

where D_{max} and D_{min} are the extreme diameters of the controlled workpiece.

• The angle of rotation of the mobile disc – The mobile disc determine the displacement on radial direction of the calibrated rollers so as to cover the specified value range for the diameter of the inner cylindrical surface with which they come into contact.

In Table 1 are presented the successive position of the calibrated rollers, corresponding to the rotation of the mobile disc with values from 0 ° to 40 °.β is the angle between the fix disc 2 and mobile disc 3 in his initial position , when α (the rotation angle of mobile disc) have the value zero (Fig. 2,a).

The solution for determining the rotation angle can be obtained by calculation or graphic representation and in the present paper was chosen the graphics solution. Graphical method for obtaining the angle shown in the Table 1 can be seen in Figure 2.

Table 1. Device dimensioning

Graphical representation	**Calculation**
Fig. 2 a)	α- rotation angle of mobile disc 3; α=0°; β –angle between the fix disc 2 and mobile disc 3; β= 46°; d- diameter of materialized adjacent cylinder ; d=130 mm.
Fig. 2 b)	α- rotation angle of mobile disc 3; α=5°; β –angle between the fix disc 2 and mobile disc 3; β= 46°; d- diameter of materialized adjacent cylinder ; d=125 mm.
Fig. 2 c)	α- rotation angle of mobile disc 3; α=10°; β –angle between the fix disc 2 and mobile disc 3; β= 46°; d- diameter of materialized adjacent cylinder ; d=118 mm
Fig. 2 d)	α- rotation angle of mobile disc 3; α=15°; β –angle between the fix disc 2 and mobile disc 3; β= 46°; d- diameter of materialized adjacent cylinder ; d=111 mm
Fig. 2 e)	α- rotation angle of mobile disc 3; α=20°; β –angle between the fix disc 2 and mobile disc 3; β= 46°; d- diameter of materialized adjacent cylinder ; d=106 mm
Fig. 2 f)	α- rotation angle of mobile disc 3; α=25°; β –angle between the fix disc 2 and mobile disc 3; β= 46°; d- diameter of materialized adjacent cylinder ; d=99 mm
Fig. 2 g)	α- rotation angle of mobile disc 3; α=30°; β –angle between the fix disc 2 and mobile disc 3; β= 46°; d- diameter of materialized adjacent cylinder ; d=96 mm
Fig. 2 h)	α- rotation angle of mobile disc 3; α=35°; β –angle between the fix disc 2 and mobile disc 3; β= 46°; d- diameter of materialized adjacent cylinder ; d=93 mm
Fig. 2 i)	α- rotation angle of mobile disc 3; α=40°; β –angle between the fix disc 2 and mobile disc 3; β= 46°; d- diameter of materialized adjacent cylinder ; d=90 mm

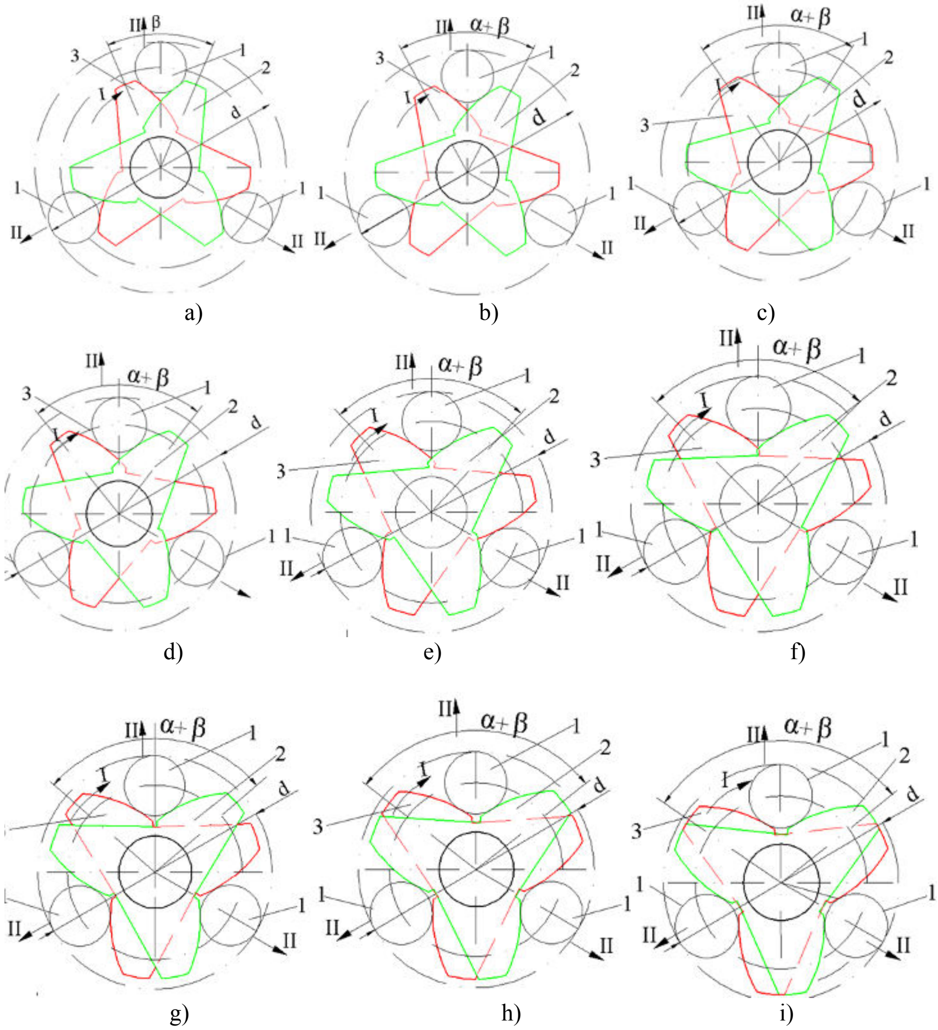

Fig. 2. Graphical dimensioning.

These dimensional characteristics are determined by workpiece dimensions. So must consider:

• Inner diameter cylindrical surface whose axis is specified as a datum axis and determining dimensions orientation- positioning mechanism (subassembly adjacent cylinder to materialize), respectively calibrated roller centering mechanism;

• Inner diameter of the cylindrical surface that measured deviation from concentricity / coaxial and determines the size and positioning mechanism orientation- fixing indicator instrument;

• The values for the total length of the inner cylindrical surfaces of the socket type parts (datum line and tolerated) which determine the length of the cylindrical body of the controller;

• The values for carcass length (distance between walls are charged cylindrical inner surfaces of skeletal parts (baseline and tolerated), which determines the length of the cylindrical body of the controller.

Considering the fact that the control device is portable, it isn't necessary fixing the workpiece with a mechanism of the control device because it installs (it is oriented and positioned) and fixed on the controlled workpiece, within the area / cylindrical surface / thereof. Therefore, the overall dimensions of the piece to control, respectively, the maximum outer diameter and length of the piece (for parts bushing type) are not decisive in determining the characteristic dimensions of the system.

Conclusion

In this paper a new approach has been proposed to verify and determine the geometrical specifications. Conceived and designed controller has the following operational and constructive characteristics: the controlled parameter is the form deviation, the measured technique is the direct one, the zeroing is realised on the workpiece, the number of the controlled parameters is one, the device is portable, have the indicating instrument and the mass about half a kilogram.

The focus was on the dimensioning the control device so that to obtain specified values for measured surfaces and the method is the graphic method. In a future work the authors will study and will determine the measurement uncertainties of the control portable device. Crucial issue given that any control equipment is the measurement error which can certify the validity of measurements performed or not, it is essential to determine the error limits with which it will measure. The sources of error will be identified and will be established the specified relationships and the physical model it will be designed. The experimental results regarding the applicability of the developed device will be the purpose of a future work too.

References

1. ISO 1101:2004 *Geometrical product specifications and verification. Geometrical tolerancing. Tolerancing of form, orientation, location and run-out*.
2. *** *The ISO System of Limits and Fits* — Tolerances and Deviations
3. *Geometrical Dimensioning and Tolerancing for Design, Manufacturing and Inspection (Second Edition)*. A Handbook for Geometrical Product Specification using ISO and ASME Standards. Edited by: Georg Henzold, ISBN: 978-0-7506-6738-8
4. Yuhe Li, Yongrong Qiu, Yanxiang Chen, Kaisen Guan. Opt. and Lasers in Eng. **62,** 31–37 (2014)
5. X.B. Zhang, X.Q. Jiang, Z. Li.A. Key Eng. Mat., **295-296**, 283-288 (2005)
6. Munteanu A., Cioata F. Bul. of Pol. Ins. Iaşi, **62** (2016)
7. T. Damian, *Constructive elements for fine mechanics (*in Romanian*)* (Didactic and Pedagogical Publishing House, Bucharest, 1980)
8. N. Seghedin, *Technological work devices fine mechanics*, (Tehnopress Publishing House, Iasi, 2006)
9. W. Gao, S.W. Kim, H. Bosse, H. Haitjema, Y.L. Chen, X.D. Lu, W. Knapp, A. Weckenmann, W.T. Estler, H. Kunzmann, CIRP Annals – Man.Tech., **64**, **2**, 773-796 (2015)
10. Y.-P. Cang, G.-J. Wu, A.-M. Xie, W.-J. Wang, Ac. Phot. Sinica **38**(11), 2932-2936 (2009)

sensors

Article

A Signal Pattern Extraction Method Useful for Monitoring the Condition of Actuated Mechanical Systems Operating in Steady State Regimes

Adriana Munteanu, Mihaita Horodinca *, Neculai-Eduard Bumbu, Catalin Gabriel Dumitras, Dragos-Florin Chitariu, Constantin-Gheorghe Mihai, Mohammed Khdair and Lucian Oancea

Faculty of Machines Manufacturing and Industrial Management, "Gheorghe Asachi" Technical University of Iasi, 700050 Iasi, Romania; adriana.munteanu@academic.tuiasi.ro (A.M.); neculai-eduard.bumbu@academic.tuiasi.ro (N.-E.B.); catalin-gabriel.dumitras@academic.tuiasi.ro (C.G.D.); dragos-florin.chitariu@academic.tuiasi.ro (D.-F.C.); constantin-gheorghe.mihai@student.tuiasi.ro (C.-G.M.); mohammed.khdair@student.tuiasi.ro (M.K.); lucian.oancea@student.tuiasi.ro (L.O.)

* Correspondence: mihaita.horodinca@academic.tuiasi.ro

Abstract: The aim of this paper is to present an approach to condition monitoring of an actuated mechanical system operating in a steady-state regime. The state signals generated by the sensors placed on the mechanical system (a lathe headstock gearbox) operating in a steady-state regime contain a sum of periodic components, sometimes mixed with a small amount of noise. It is assumed that the state of a rotating part placed inside a mechanical system can be characterized by the shape of a periodic component within the state signal. This paper proposes a method to find the time domain description for the significant periodic components within these state signals, as patterns, based on the arithmetic averaging of signal samples selected at constant time regular intervals. This averaging has the same effect as a numerical filter with multiple narrow pass bands. The availability of this method for condition monitoring has been fully demonstrated experimentally. It has been applied to three different state signals: the active electrical power absorbed by an asynchronous AC electric motor driving a lathe headstock gearbox, the vibration of this gearbox, and the instantaneous angular speed of the output spindle. The paper presents some relevant patterns describing the behavior of different rotating parts within this gearbox, extracted from these state signals.

Keywords: sensors; state signals; mechanical system; gearbox; signal pattern recognition; condition monitoring

Academic Editor: Simon Laflamme

Received: 11 January 2025
Revised: 8 February 2025
Accepted: 11 February 2025
Published: 12 February 2025

Citation: Munteanu, A.; Horodinca, M.; Bumbu, N.-E.; Dumitras, C.G.; Chitariu, D.-F.; Mihai, C.-G.; Khdair, M.; Oancea, L. A Signal Pattern Extraction Method Useful for Monitoring the Condition of Actuated Mechanical Systems Operating in Steady State Regimes. *Sensors* **2025**, *25*, 1119. https://doi.org/10.3390/s25041119

1. Introduction

A reasonable assumption in monitoring and diagnostics is that an actuated mechanical system containing periodically rotating mechanical components (MCs) operating in a stationary regime generates state signals to which all MCs contribute additively depending on their state. A state signal can describe vibration, mechanical power, force, torque, angular speed, etc. These state signals contain constant or slowly varying signal components (CSC) and periodically varying signal components (PVSC), where each CSC and PVSC is usually generated by an MC. The description of the health condition of the MC can obviously be conducted by analyzing the time-domain representation of the CSC and PVSC generated by MC. Since the mechanical system naturally mixes all these components into a single state signal, the first problem to solve for monitoring purposes is to separate the CSC and PVSC components generated by each MC from this signal. Of course, at the current state of the art, the CSC components cannot be separated because they have no characteristic elements that link them to the MC. It is obvious that any PVSC generated in the steady-state regime can be approximated as a sum of harmonically correlated sinusoids (with a fundamental and several harmonics). The separation of any PVSC from a state signal is possible because there is a certain feature that links it to the MC during a steady state regime of operation: the frequency of the fundamental component of the PVSC is equal to the rotational frequency of the MC.

Separating a PVSC is not always easy. For various reasons, the three characteristics of the fundamental and harmonic components within a PVSC as sine waves (amplitude, frequency, and phase at the origin of time) may be constant, slightly variable, or severely variable (especially with respect to amplitude). In some situations, the PVSC may be generated only temporarily, for short periods of time. For each situation, synthetic or analytical techniques and methods for a partial or a complete description of the PVSC exist in the literature.

The best-known technique is the Fast Fourier Transform (FFT) of the state signal, which is used in situations where frequencies and amplitudes are constant or vary very little [1,2], and the result is provided as a spectrum. A conversion is made from the time domain to the frequency domain. Each peak in the spectrum describes the average values of the amplitude and frequency of a component in the PVSC (a fundamental or one of its harmonics). All components of all PVSCs are described in the FFT spectrum. Separation of the spectral peaks describing a particular PVSC generated by a particular MC must be conducted using other methods. The FFT technique has been applied in various situations for monitoring and diagnosis of rotating machines [3–7].

When the PVSC characteristics vary greatly with time or especially when the PVSC is generated temporarily, an alternative to the FFT, the wavelet transform, can be used [8–12]. It is systematically applied in various fields, in particular to analyze state signals for monitoring purposes of rotary machines [4,6,7,11,13,14].

A natural question about the steady-state regimes is: what exactly does this separation of a particular PVSC from a status signal mean? It just means that we should somehow obtain the time-domain representation of just this PVSC. Since the period T of the fundamental sine wave in the PVSC is known, the simplest way to obtain this representation is to filter the variable part of the status signal (converted to numerical format) with a tunable numerical multiple narrow band pass filter [15] whose pass frequencies are harmonically correlated at $1/T$ Hz, $2/T$ Hz, $3/T$ Hz, and so on (up to the Nyquist limit), while preserving the original phases at the origin of time. The time-domain representation of the desired PVSC appears at the filter output. Indirectly, this is the technique used in this paper. This approach (as well as the FFT) is only correct if any two or more harmonics of fundamentals of different PVSCs do not have the same frequency.

For comparison and analysis purposes, it is easier to consider a time-domain representation of a PVSC (as a periodic signal) replaced with a PVSC described by a single period obtained by appropriate averaging of the PVSC. This approach also covers the situation where the PVSC contains slightly varying sinusoidal components (caused, for example, by a slight variation of the MC speed). This is a brief conceptual description of the approach in this paper.

Finding periodic patterns in state signals (especially vibrations) has been the subject of numerous previous theoretical and experimental approaches in signal processing techniques, particularly in the field of fault detection in rotating machinery. The inverse Fourier transform applied to the logarithm of the magnitudes of the power spectrum obtained by the direct Fourier transform of the state signal, known as the Cepstrum technique [16,17], or some other techniques derived from it have been applied in [12,18–20]. Spectral correlation density [21], which examines the correlation between different components of a signal that are related to each other by frequency, or techniques derived from it, was applied in [22–25]. Some other appropriate techniques are also available: cyclostationary analysis [26,27], autocorrelation [28,29], and averaged cyclic periodogram [30].

The concept of signal pattern recognition, as a relatively new approach to determining patterns within the evolution of state signals, is a well-covered theoretical and experimental research topic [31,32]. Signal pattern recognition is a field of machine learning [33,34] that focuses on defining appropriate algorithms for automatically finding patterns in signals, including deep learning based on neural networks [35]. It is associated with computer-based signal processing, achieved through the use of artificial intelligence. Signal pattern recognition is often used to detect abnormal working conditions, usually to detect mechanical faults. Some interesting achievements in mechanical fault detection on rotary machines are described in refs. [36,37] (rolling bearings condition), refs. [38–40] (gears condition), ref. [41] (rotors vibrations), refs. [12,42,43] (induction motors condition), ref. [44] (driving belts condition, a topic also covered in our paper), and refs. [45–47] (detection of chatter in cutting processes).

Generally, vibration description signals are analyzed, but other resources are also used, such as force description signals [48], instantaneous angular speed [47], active electric power [49], and electric current [50].

This diversity of approaches and achievements does not limit the perspectives of possible new contributions. There are still enough new accessible resources that can be highlighted and exploited in the identification of PVSC patterns useful for off-line monitoring and predictive diagnostics of rotating mechanical systems operating in steady-state regimes. This is the objective of the present work, which proposes a simple method to extract the PVSC patterns through a selective averaging process of the samples of the state signal. The availability of this method is proved by PVSC extraction from various state signals describing the operation of a lathe gearbox running in a steady-state regime as active electrical power, vibrations, and instantaneous angular velocity. A setup and a theoretical approach already presented and described in [3] will be extensively used here for experimental purposes.

The rest of the paper is organized as follows:

- Section 2 presents the materials and methods, mainly the averaging method of state signal samples used to define the PVSC patterns and the experimental setup;
- Section 3 presents some experimental results (with the PVSC patterns detected in active electrical power, vibration, and instantaneous angular velocity);
- Section 4 is reserved for discussion, with a brief review of the requirements of the averaging method, of the performances in pattern detection, with a summary of the advantages and shortcomings, and future research directions.

2. Materials and Methods

2.1. The Pattern Extraction Method

An analog signal $s(t)$ provided by an appropriate sensor placed on a mechanical system running in a steady-state regime is usually described (after analog-to-digital conversion) by a sequence of p equidistant numerical samples (with a constant sampling time Δt between any two successive samples), with the k-th sample written as $s[k]$, taken at the time $t = k \cdot \Delta t$.

Suppose the signal s contains a PVSC with constant period T (or with $1/T$ constant frequency) and at least m periods. A signal pattern extraction method of PVSC is proposed below. A pattern of this PVSC, as a time-domain representation over a period T, can be obtained mathematically with a good approximation using an extraction method by averaging selected samples (EMASS) at regular time intervals from the signal s. This regular time interval is exactly the period T. With m big enough, the selection rule of these samples results from the definition of a sample $s_T[h]$ of this pattern, according to:

$$s_T[h] \approx \frac{1}{m}\sum_{i=1}^{m} s\left[h + \left\lfloor (i-1)\cdot\frac{T}{\Delta t}\right\rceil\right] \qquad \text{with} \quad h = 1,\ 2, \ldots, \left\lfloor \frac{T}{\Delta t}\right\rceil \tag{1}$$

Here $\lfloor x \rceil$ is the nearest integer to x. If the ratio $n = T/\Delta t$ is exactly an integer and the signal s has at least $p = m \cdot n$ samples, then a sample $s_T[h]$ of this pattern is more easily written as:

$$s_T[h] \approx \frac{1}{m}\sum_{i=1}^{m} s[h + (i-1)\cdot n] \qquad \text{with} \quad h = 1,\ 2, \ldots, n \tag{2}$$

According with Equation (2), a sample $s_T[h]$ of this pattern is calculated as the average of m equidistant samples from signal s, more specifically as the average of these samples: $s[h]$, $s[h + n]$, $s[h + 2\cdot n]$, …, $s[h + m\cdot n]$. Because usually $T/\Delta t$ is not an integer, the description of a sample $s_T[h]$ of this pattern with Equation (1) is more exact and always used in the experimental approaches of this work.

If, for simplicity, $p = m\cdot n$, then the pattern s_T can be artificially extended to p samples so that an extended pattern s_{Te} of PVSC becomes a signal consisting of the joining of m identical periods s_T, one after another. Thus, the extended pattern s_{Te} can also be defined with n concatenated sets of m identical defined samples, with $n = \lfloor T/\Delta t \rceil$. The samples from the *hth* set of extended pattern s_{Te} (with h = 1, 2, …, n) are defined with a good approximation as:

$$s_{Te}[h + (d-1)\cdot n] \approx \frac{1}{m}\sum_{i=1}^{m} s\left[h + \left\lfloor (i-1)\cdot\frac{T}{\Delta t}\right\rceil\right] \qquad \text{with} \quad d = 1,\ 2,\ \ldots, m \tag{3}$$

The left side of Equation (3) describes the concatenation rule of sets. In the extended pattern s_{Te}, h = 1 defines the samples 1, 1 + n, 1 + 2n, …, 1 + (m − 1)·n, while h = n defines the samples n, 2n, …, $m\cdot n$.

This signal s_{Te} can be viewed as being generated at the output of a tunable numerical multiple narrow bandpass filter, at whose input the signal s is applied (and processed according to Equation (3)). This filter has the pass frequencies on j/T Hz, with j = 1, 2, …, $\lfloor 2/\Delta t \rceil$. Here $\lfloor 2/\Delta t \rceil$ is the Nyquist limit.

As a particular example, the dependence of transmittance by frequency for this filter is partially depicted in Figure 1, for a frequency range between 1 and 300 Hz, as a result of a numerical simulation in Matlab with Δt = 1/50,000 s, T = 1/33 s, $n = \lfloor 50,000/33 \rceil = 1515$ and m = 60. A numerical sine wave with amplitude of 1 and a frequency f in the frequency range is fed into the filter as signal s. The amplitude of the output signal s_{Te} is equal to the transmittance at the frequency f.

As clearly indicated in Figure 1, mainly the input signal components (sine waves) having $j/T = j\cdot 33$ Hz frequencies pass through the filter unaffected (with undiminished or canceled amplitudes). A zoomed-in detail in area A is depicted in Figure 2 (centered on the pass band frequency of 198 = 6·33 Hz). It is clear that the transmittance is not ideal (because of the small lateral lobes); however, this filter can be used acceptably for the extraction of periodic signal components, as the experimental results will show below.

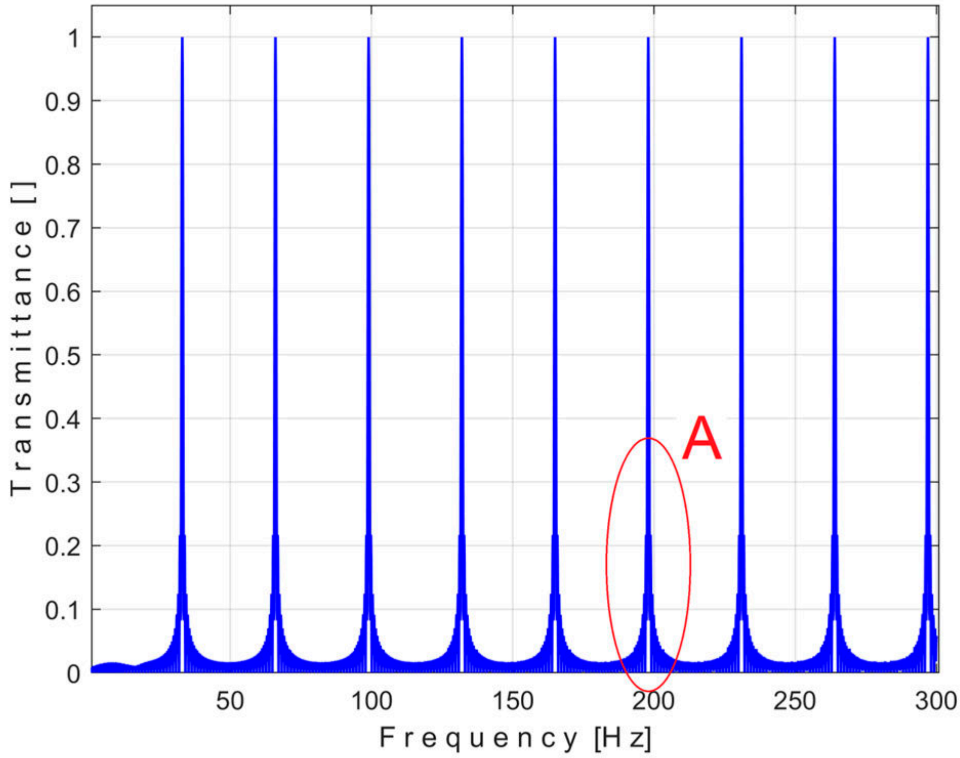

Figure 1. Filter transmittance versus frequency (numerical simulation (Δt = 1/50,000 s, T = 1/33 s, $n = \lfloor 50,000/33 \rceil = 1515$ and m = 60).

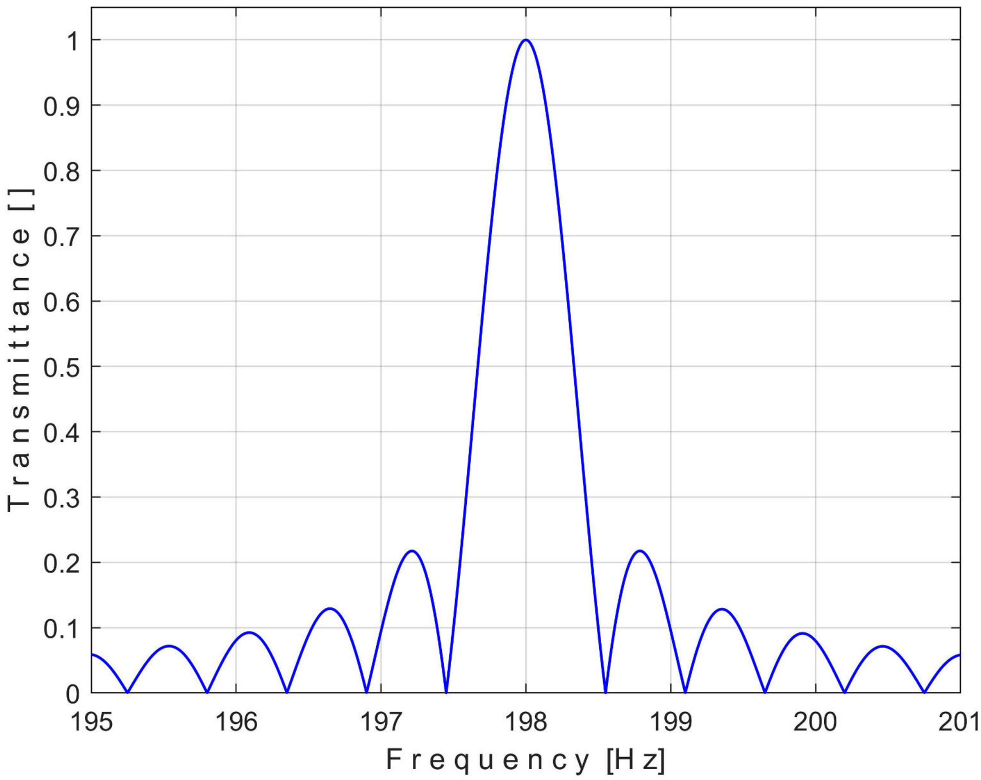

Figure 2. A zooming in in area A from Figure 1.

It is intuitive that this filter does not introduce any phase shift. An illustration of the effectiveness of the proposed EMASS can be realized as follows. The signal s is defined to be periodic as a sum of harmonically correlated harmonic components (a fundamental of period T and several harmonics with period's $l \cdot T$) as follows (as an example):

$$s[k] = \sum_{l=1}^{40} l \cdot \sin\left(\frac{2 \cdot \pi \cdot l \cdot k \cdot \Delta t}{T} + l\right) \quad (4)$$

Here is considered Δt = 1/25,000 s and T = 1 s.

The EMASS is used to extract the periodic pattern s_T from the signal s, with m = 50, according to Equation (2), because $n = T/\Delta t = \lfloor T/\Delta t \rceil$ = 25,000. It is expected that the correct operation of the EMASS should be confirmed by the perfect identity between the pattern s_T and the first period of the signal s. This identity is confirmed if any difference $s[k] - s_T[k] = 0$ (also called residual) for any k = 1, 2, . . ., n, or for any time t expressed as $k \cdot \Delta t$.

If we plot how these residuals $s[k] - s_T[k]$ evolve over time $k \cdot \Delta t$, we should obtain a line that coincides with the t-axis. Figure 3 shows the time-domain representation of the residuals over a period T = 1 s (this being the time duration of the pattern s_T).

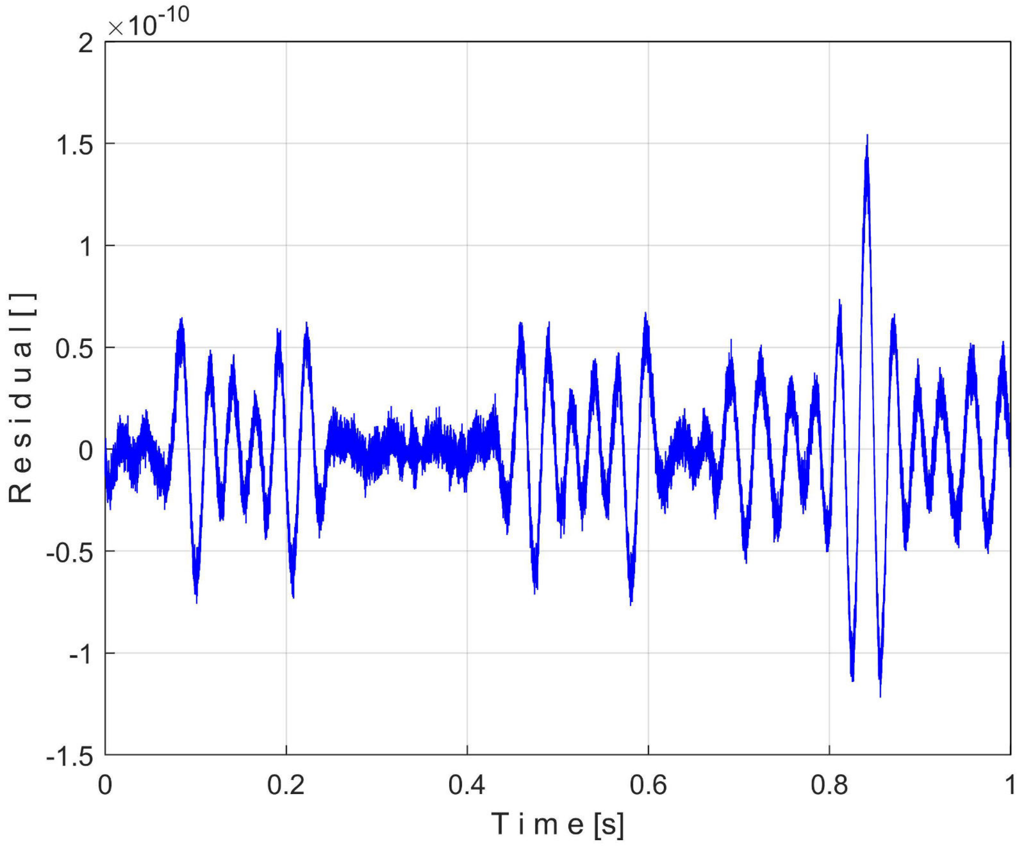

Figure 3. The time-domain representation of the residuals $s[k] - s_T[k]$ over time $k \cdot \Delta t$, with k = 1, 2, . . ., n, T = 1 s, Δt = 25,000.

Figure 3 proves that this theoretical assumption (with the residuals represented as a line identical to t-axis) is not totally true for unknown reasons. However, the maximum peak-to-peak amplitude of the residuals (3×10^{-10}) is extremely small, so it can be considered that the proposed EMASS and the filter described in Equation (3) work as presumed. This approach also confirms that the EMASS and the filter do not introduce any phase shift.

It is obvious that the best result of extraction and filtering is obtained when $T/\Delta t = \lfloor T/\Delta t \rceil$. This has already been proved in Figure 3, where we obtained the smallest peak-to-peak residual.

Obviously, the biggest peak-to-peak amplitude of the residual—and the better result for extraction and filtering—is obtained when $|T/\Delta t - \lfloor T/\Delta t \rceil| = 0.5$. Curve 1 from Figure 4 shows the worst-case time-domain representation of the residuals of the pattern extraction of the signal simulated in Equation (4), with $T = 1$ and $\Delta t = 1/25{,}000.5$ s when $|T/\Delta t - \lfloor T/\Delta t \rceil| = 0.5$. There is a 2.49 peak-to-peak amplitude of the residual.

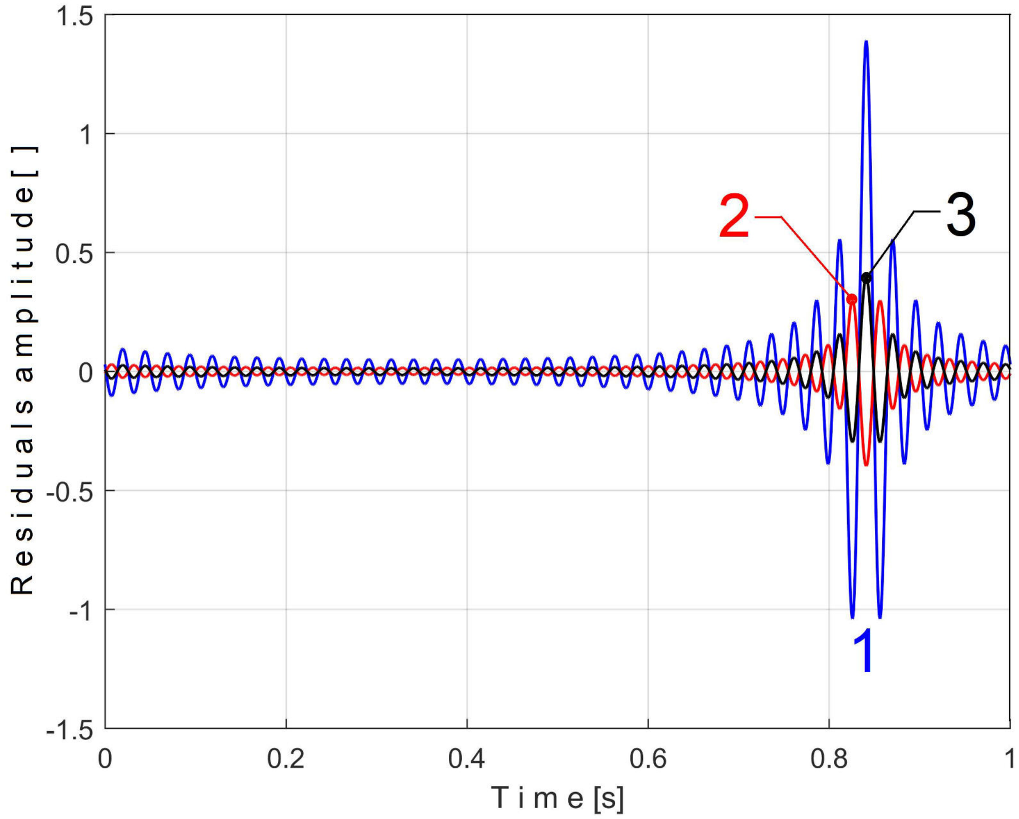

Figure 4. The time-domain representations of the residuals $s[k] - s_T[k]$ over time $k{\cdot}\Delta t$, with $k = 1, 2, \ldots, n$, $T = 1$ s. Curve 1—$\Delta t = 1/25{,}000.5$ (with $|T/\Delta t - \lfloor T/\Delta t \rceil| = 0.5$); Curve 2—$\Delta t = 1/25{,}000.493$ (with $|T/\Delta t - \lfloor T/\Delta t \rceil| = 0.493$); Curve 3—$\Delta t = 1/25{,}000.507$ (with $|T/\Delta t - \lfloor T/\Delta t \rceil| = 0.493$).

However, this peak-to-peak amplitude of the residual is not significant compared with the peak-to-peak amplitude of s_T (1430.9). By comparison, in Figure 4, curve 2 depicts the time-domain representation of the residuals if $\Delta t = 1/25{,}000.493$ s, and curve 3 depicts the residuals if $\Delta t = 1/25{,}000.507$ s. In both scenarios $|T/\Delta t - \lfloor T/\Delta t \rceil| = 0.493$ as a consequence the peak-to-peak amplitude of the residuals (curves 2 and 3) strongly decreases.

This worst-case $|T/\Delta t - \lfloor T/\Delta t \rceil| = 0.5$ often happens because the value of T. This worst case can be avoided by resampling the signal s (by changing Δt) in order to obtain $|T/\Delta t - \lfloor T/\Delta t \rceil| = 0$.

There is another way to illustrate the effectiveness of EMASS. Consider a random noise signal r_n where each sample is generated as a random number in the interval $[-5, 5]$. Consider that this random noise signal is mixed with a periodical signal s (playing the role of a PVSC in this simulation) described as:

$$s[k] = \sum_{l=1,2,20} \sin\left(2{\cdot}\pi{\cdot}25{\cdot}l{\cdot}k{\cdot}\Delta t + \frac{\pi}{2}\right) \tag{5}$$

In Figure 5, curve 1 shows the result of the addition of signals $r_n + s$ during a period $T = 1/25$ s, where both simulated signals have the same sampling times $\Delta t = 1/100{,}000$ s.

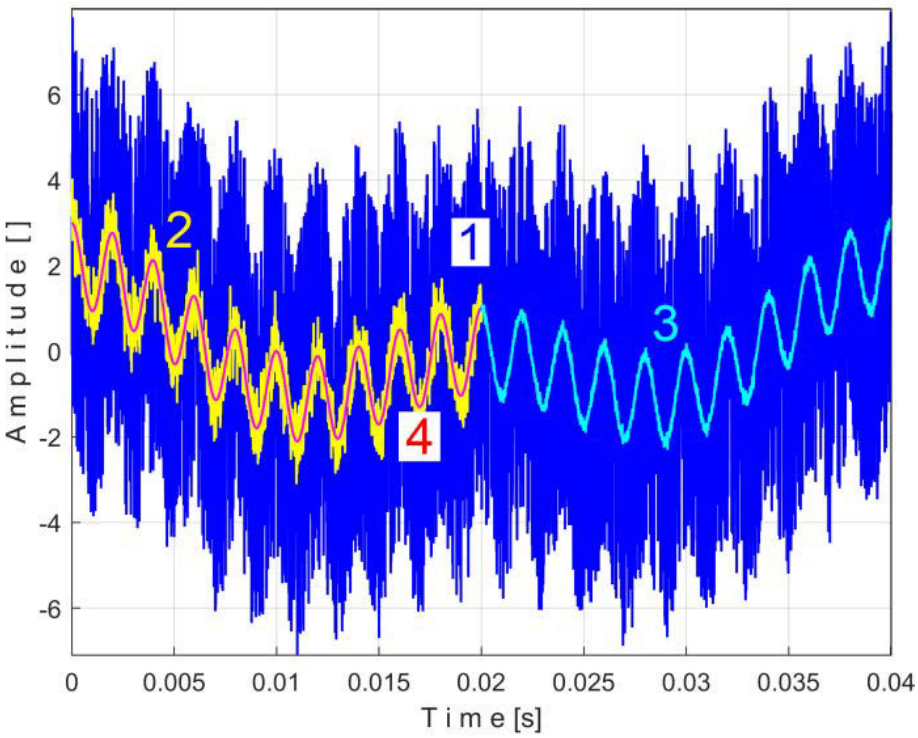

Figure 5. 1—A period $T = 1/25$ s of the signal $r_n + s$; 2—The first half of the pattern s_T with $m = 50$; 3—The second half of the pattern s_T with $m = 1200$; 4—A period T of signal s.

In Figure 5, curve 2 shows the first half of the pattern s_T of this simulated PVSC extracted from the $r_n + s$ signal using EMASS, with $m = 50$ and $T = 1/25$ s.

Due to the high noise of r_n, the EMASS with $m = 50$ produces a relatively noisy description of the pattern s_T. A better result is shown in Figure 5, curve 3, which shows the second half of a new pattern s_T of this simulated PVSC obtained by EMASS with $m = 1200$.

Curve 4 shows a period T of the simulated PVSC. It is obvious that the higher the value of m, the better the quality of the PVSC pattern will be. If the PVSC frequency is not strictly constant, this conclusion does not hold. This will be proved experimentally later.

In the previous simulation, it was shown that a very large value of m is required to reasonably reduce the influence of noise. This could be seen apparently as an argument against the effectiveness of the EMASS. However, this situation is very rare in practice due to the nature and magnitude of the noise. In our investigations on real state signals, appropriately chosen, the noise level was very low and did not cause any particular problems with respect to the purpose of our work.

With the signal s acquired under experimental conditions, as delivered by a sensor placed on an actuated mechanical system operating in the steady-state regime, correct extraction of the pattern s_T of a PVSC by EMASS usually requires the use of Equation (1).

We should mention that it is mandatory to know (or to find somehow) the most accurate value of the period T of PVSC. An obvious approach is available for determining the exact value of the period T. Knowing an approximate value of T, we can set an interval around this value. We systematically change the value of T in this interval until we obtain with EMASS (Equation (1)) a pattern s_T with maximum peak-to-peak amplitude. Thus, the correct s_T pattern and the exact value of the period T are determined. The correctness of this approach was confirmed experimentally, as will be shown later.

It should also be mentioned that if the signal s contains (for example) two periodic components (1, 2) with periods T_1, T_2, and if the i-th harmonic of component 1 has the same period as the j-th harmonic of component 2 (or $T_1/i = T_2/j$), then EMASS will produce distorted results in the description of both patterns s_{T1} and s_{T2}; these two harmonics will be incorrectly described as belonging to both patterns.

This method of extracting a periodic signal pattern has been partially presented and was the subject of some experimental research related to the PVSC pattern found in instantaneous active electrical power, as a characterization of a three-phase AC asynchronous motor running at idle [51] and related to the PVSC pattern found in the evolution of the roughness of a 2D surface manufactured by milling with a ball nose end mill [52].

2.2. The Experimental Setup

An experimental setup already described in detail in [3] is used here (Figures 6 and 7). As an electrically driven mechanical system (with a three-phase AC asynchronous motor), a lathe headstock gearbox is used (with the kinematic scheme partially shown in Figure 7). In this approach, three different state signals provided by appropriate sensors are considered relevant for condition monitoring purposes during a steady-state regime (at idle) of the lathe gearbox: the active electrical power P_a absorbed by the driving motor, the vibration signal vs., and the instantaneous angular speed IAS at the output spindle as signal I_{as}.

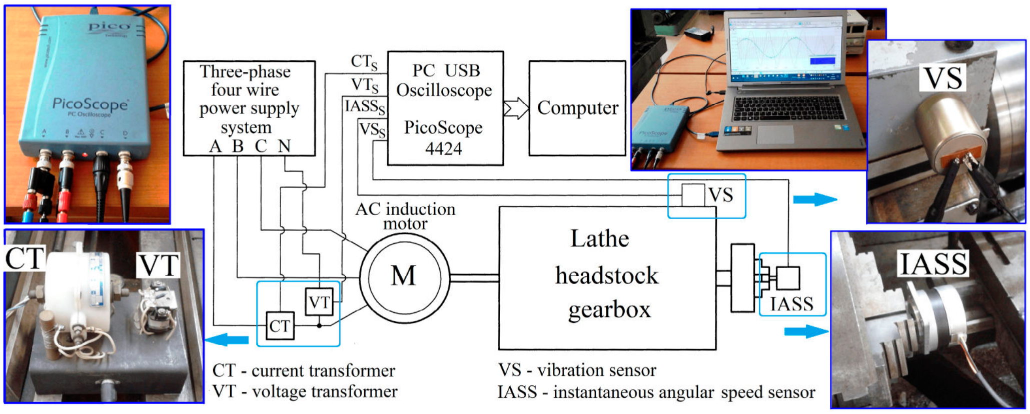

Figure 6. A description of the experimental setup [3].

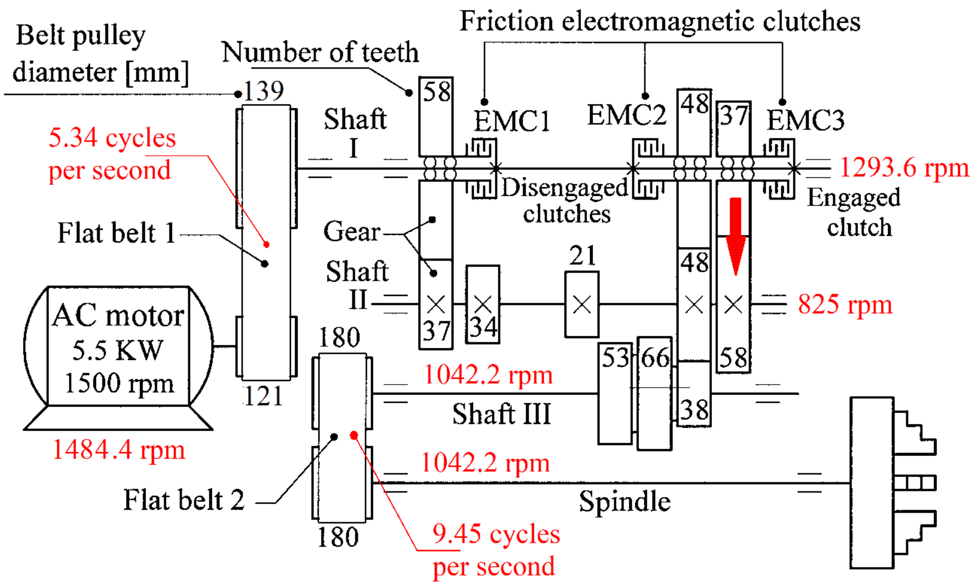

Figure 7. The gearing diagram of the lathe headstock gearbox [3].

There are some simple reasons for choosing these three state signals. First, it highlights the availability of EMASS for processing different state signals. The best description of the behavior of a mechanical component (part) of a gearbox is in the time domain representation of the mechanical power, which is well reflected in the evolution of the active electrical power. The vibration signal is traditionally used for monitoring and diagnosis. The instantaneous angular speed is strictly related to the evolution of the torque delivered by the electric motor. There are differences and similarities that should be explored and exploited.

The active electric power P_a is mathematically defined [3] based on the signals supplied by a voltage transformer (VT) and a current transformer (CT). The vibration signal is provided by a vibration sensor (VS) [3]. The signal I_{as} involved in the description of the instantaneous angular speed (IAS) of the spindle is provided by an IAS sensor IASS placed in the jaw chuck of the spindle [3]. All signals are sampled using a numerical oscilloscope [3] connected to a computer. The signal processing was carried out in Matlab R2019b.

The establishment of each signal has been extensively explained in two previous papers (ref. [3] for P_a, and V_s, ref. [53] for I_{as}). The gearbox is running in steady state at idle (according to the gearing diagram depicted in Figure 7); the MC rotation speeds (experimentally revealed) are highlighted in red.

Next, only the variable parts P_{av}, vs., and I_{asv} of these signals are considered experimentally in order to extract by EMASS the patterns of the PVSCs induced by the MCs of the gearbox during the operation at a constant speed of rotation, if these PVSCs are present and have sufficiently high amplitude. These patterns are useful for characterizing the state of each of these MCs (condition monitoring).

3. Results

3.1. EMASS Applied to Active Electrical Power Signal

Figure 8 shows the time-domain representation of P_a (curve 1), a long sequence of 200 s (with p_a = 5,000,000 samples, Δt = 1/25,000 s, 12-bit resolution). To obtain the P_{av} signal (as an s_P signal), the constant and the very low frequency variable part of P_a were mathematically subtracted from P_a. This very low-frequency variable part (curve 2) was obtained by low-pass filtering of P_a (using numerical multiple moving average filters [54]). Since this filtering produces false values at the beginning and end of the filtered sequence (zones Z_A and Z_B in Figure 8), these zones are removed from P_{av} (so P_{av} is shorter than P_a, since it has only p_{av} = 4,984,501 samples).

The time-domain representation of P_{av} is shown in Figure 9, with a zoomed-in detail (with 1.5 detail of 1.5 s duration from the beginning, shown in the rectangle on the right). This is a first simple proof that P_{av} is a deterministic signal with a very low level of noise. In the time-domain representation of P_{av}, many signals are mixed, most of them generated by the MC of the gearbox, as will be shown below.

There is a second, more reliable proof that the P_{av} signal is deterministic with a low level of noise: how the FFT spectrum of P_{av} appears, as described in Figure 10.

According to a study performed before [3], each of the labeled peaks (A, B, . . . , E) indicates the average frequency (inverse of the period) and the average amplitude of the fundamental sine wave of the PVSC generated by the flat belt 1 (A), the flat belt 2 (B), the shaft II (C), the shaft III and the spindle (D), and the shaft I (E). Some other significant peaks describe other sine waves as harmonics of these fundamentals. The frequency (and period as well) of some fundamentals and their harmonics may vary slightly here due to a slight variation in motor rotational speed.

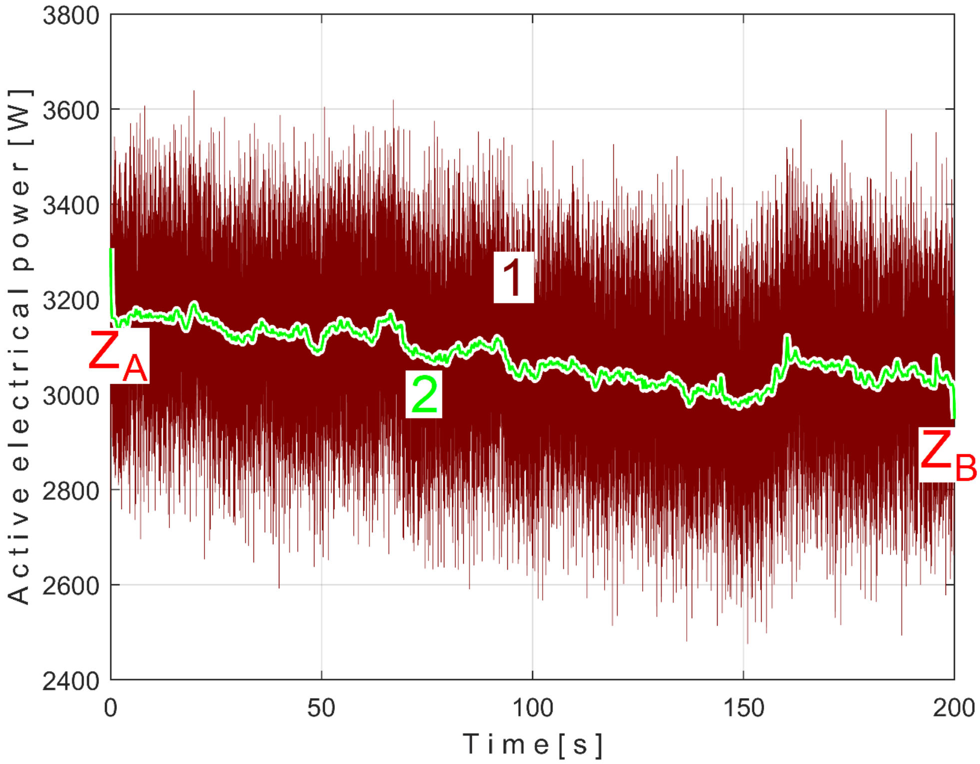

Figure 8. The time-domain representations of: 1—P_a; 2—the very low frequency variable part of P_a.

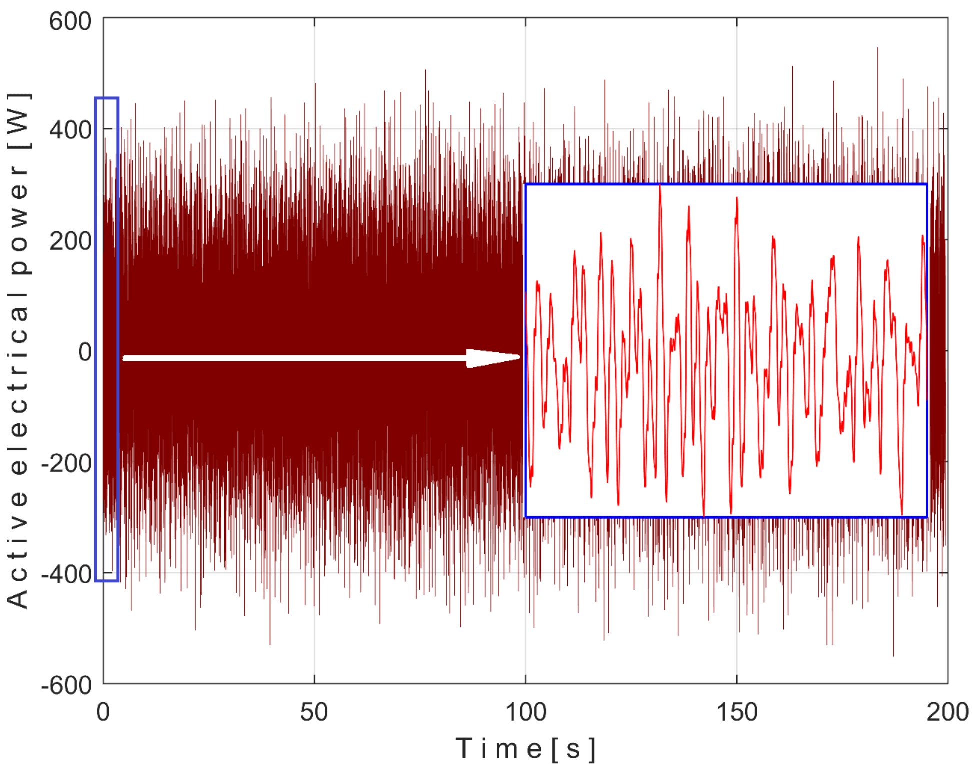

Figure 9. The time-domain representation of P_{av}.

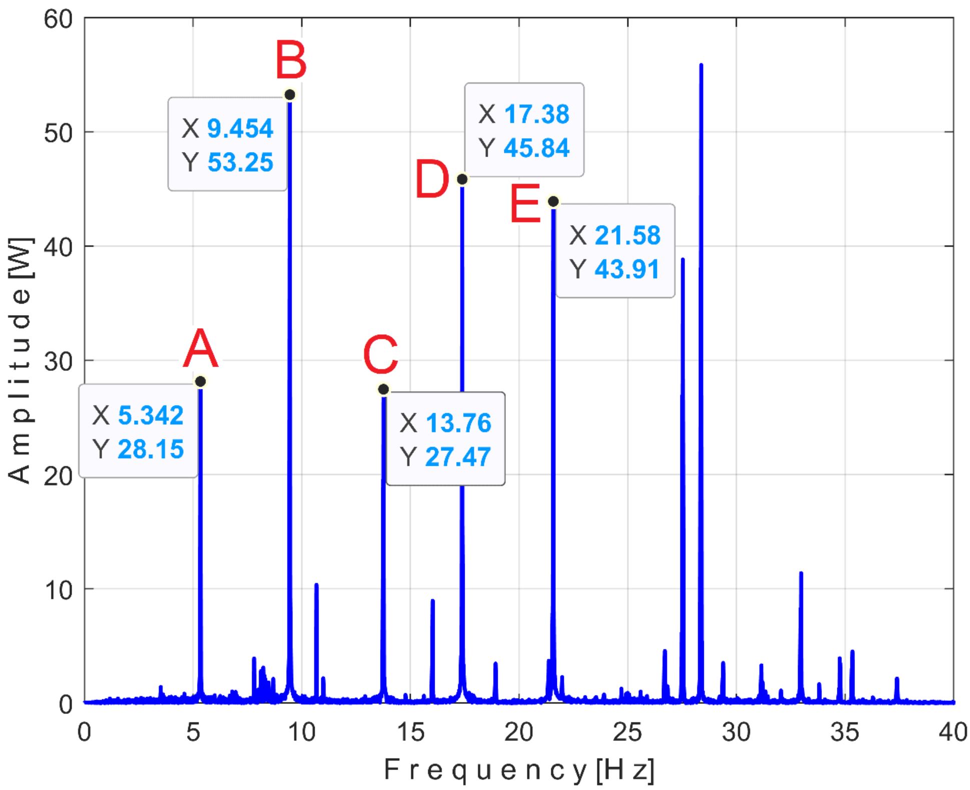

Figure 10. The FFT spectrum of P_{av} with A, B, . . ., E the fundamentals of PVSC generated by these MCs: A—the flat belt 1; B—the flat belt 2; C—the shaft II; D—the shaft III and the main spindle; E—the shaft I.

The patterns of each of these PVSCs (as s_{PTA}, s_{PTB}, . . ., s_{PTE}) can be extracted from the signal s_P by EMASS based on Equation (1). There is a first way to confirm partially the availability of EMASS, related to the average frequencies f_{PA}, f_{PB}, . . ., f_{PE} of peaks A, B, . . ., E revealed in Figure 10. For each marked peak in the FFT spectrum (e.g., for the peak A), with EMASS applied at the maximum possible value of m (tending to $m_{max} = \lfloor p_{av}/(T/\Delta t) - 0.5 \rceil$) we search in a small frequency range centered on the value given in the FFT spectrum (e.g., f_{PA} = 5.34 Hz) for the frequency (period, $T_{PA} = 1/f_A$) at which the pattern (s_{PTA}) has the maximum peak-to-peak amplitude. This is the mean value of the frequency of the respective peak (f_{PA}), determined indirectly by EMASS, which is expected to be close to that already shown in the FFT spectrum. This hypothesis is fully confirmed with the results depicted in Table 1.

Table 1. The average values of frequency of peaks (describing the fundamental of PVSC) A, B, . . . E.

	f_{PA} [Hz]	f_{PB} [Hz]	f_{PC} [Hz]	f_{PD} [Hz]	f_{PE} [Hz]
Found using FFT	5.342	9.454	13.76	17.38	21.58
Found using EMASS	5.3408 (m = 1061)	9.4589 (m = 1872)	13.76513 (m = 2728	17.3865 (m = 3453)	21.5761 (m = 4288)

For a more understandable graphical representation, we propose a partial extension of the patterns s_{PTA}, s_{PTB}, . . ., s_{PTE}, up to the duration of 5 periods of their fundamentals, as s_{PTAe5}, s_{PTBe5}, . . ., s_{PTEe5}. For example, the s_{PTAe5} extended pattern is described similarly with Equation (3) as:

$$s_{PTAe5}[h + (d-1)\cdot n] \approx \frac{1}{m}\sum_{i=1}^{m} s_P\left[h + \left\lfloor (i-1)\cdot\frac{T_{PA}}{\Delta t} \right\rceil\right] \qquad \text{with} \quad d = 1,\ 2,\ \ldots,\ 5 \qquad (6)$$

These extended patterns s_{PTAe5}, s_{PTBe5}, . . ., s_{PTEe5} can be obtained by extending the patterns s_{PTA}, s_{PTB}, . . ., s_{PTE}, each one found by EMASS applied to the P_{av} signal, with an appropriate value of m, with $m < m_{max}$.

To show the repeatability of the extended patterns s_{PTAe5}, s_{PTBe5}, . . ., s_{PTEe5}, there is an interesting possibility: to superimpose two extended patterns of the same PVSC, both calculated with EMASS with the same m, the first extended pattern (e.g., as being s_{PTAe5a}) calculated on the first half of the total number of P_{av} samples (from 1 to $p_{av}/2$, for almost 100 s), and the second extended pattern (e.g., as being s_{PTAe5b}) calculated on the second half of P_{av} samples (from $p_{av}/2$ to p_{av}, also for almost 100 s).

Figure 11 shows the superimposed extended patterns s_{PTAe5a} (curve 1, m = 530) and s_{PTAe5b} (curve 2, m = 530) related by the PVSC generated by the flat belt 1. We found that the average frequency f_{PA} to consider in EMASS for each extended pattern (which produces the maximum peak-to-peak amplitude of the pattern) is slightly different: f_{PAa} = 5.3368 Hz for s_{PTAe5a} and f_{PAb} = 5.3414 Hz for s_{PTAe5b}. The beginning sample of the second half of the P_{av} signal (in a first approach $p_{av}/2$) from which the second extended pattern (s_{PTAe5b}) has been deduced is conveniently changed to obtain the most correct possible overlap of the two patterns. A characterization of the flat belt 1 behavior was obtained by means of the extended pattern shape, extracted by EMASS from P_{av}.

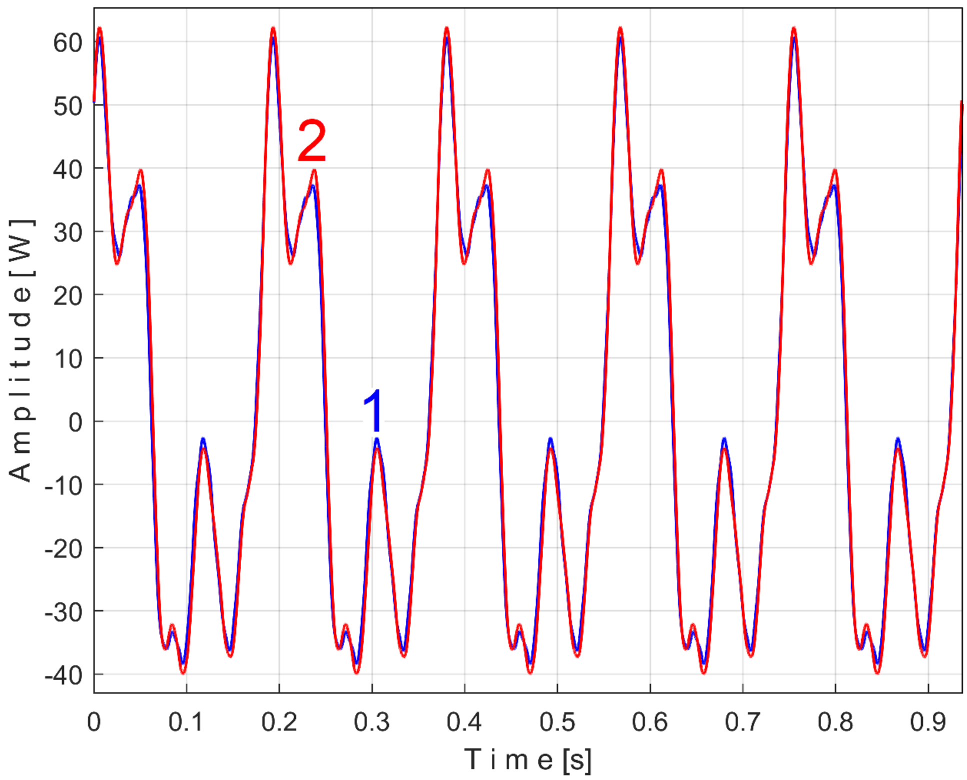

Figure 11. The extended patterns (m = 530) describes the PVSC generated by the first flat belt in signal s_P: 1—s_{PTAe5a} (f_{PAa} = 5.33748 Hz); 2—s_{PTAe5b} (f_{PAb} = 5.34162 Hz).

The analytical description of the extended patterns can be found by using the *Curve Fitting Tool* application from Matlab, as the sum of harmonically correlated sinusoidal components (sine waves). Figure 12 shows the s_{PTAe5b} pattern (as curve 1), the pattern based on the analytical description as the addition of eight harmonically correlated sinusoidal components (as curve 2, an addition of a fundamental F_{PA} and seven harmonics H_{PA1}, H_{PA2}, . . ., H_{PA6}, and H_{PA8}), and the residuals (curve 3) as the difference between. These sinusoidal components are described in Table 2.

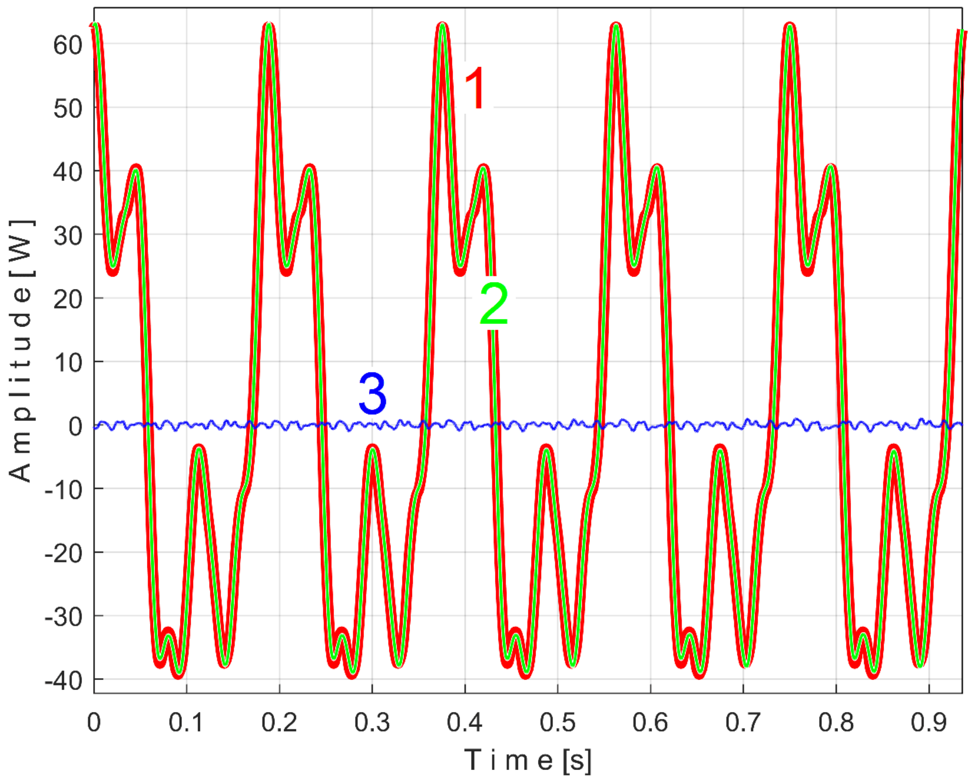

Figure 12. 1—The extended pattern s_{PTAe5b} (m = 530, f_{PAb} = 5.3414 Hz); 2—The analytical description of this pattern (with eight sinusoidal components, Table 2); 3—The residual (the difference between curves 1 and 2).

Table 2. The amplitudes, frequencies, and phases at the origin of time for the sinusoidal components involved in the description (by addition) of the PVSC generated by the first flat belt within the active electrical power.

	$\mathbf{F_{PA}}$	$\mathbf{H_{PA1}}$	$\mathbf{H_{PA2}}$	$\mathbf{H_{PA3}}$	$\mathbf{H_{PA4}}$	$\mathbf{H_{PA5}}$	$\mathbf{H_{PA6}}$	$\mathbf{H_{PA8}}$
Amplitude [W]	37.19	15.33	15.5	6.268	8.482	2.157	4.499	0.446
Frequency [Hz]	5.341	10.684	16.026	21.374	26.706	32.053	37.401	48.080
Phase at origin of time [rad]	0.9581	0.1707	2.359	1.204	0.5218	2.307	1.266	−1.863

We should mention that a very complicated procedure for finding the shape of the extended pattern for the PVSC generated by the first flat belt has already been presented in previous work [3].

There is another important argument for the correctness of the proposed EMASS. Let us take a sequence of P_{av} with the duration of 50 periods T_{PA} (234,300 samples for 9.372 s) from its beginning (as s_{P50}). Correspondingly, the exact value of the frequency f_{PA} = 5.33448 Hz and the extended pattern s_{PTAe50} were determined, with m = 50. In Figure 13, the FFT spectrum of the sequence s_{P50} (in the range 0–40 Hz) is marked as 1. The FFT spectrum of the signal s_{P1r50} resulting from the mathematical extraction of this extended pattern s_{PTAe50} from the analyzed sequence s_{P50} is marked as 2. The k-th sample of s_{P1r50} is described as $s_{P1r50}[k] = s_{P50}[k] - s_{PTAe50}[k]$. It is clear that the fundamental A and its 6 harmonics (A_1, A2, . . ., A_6) have disappeared from the spectrum 2 as a result of the mathematical subtraction of the extended pattern s_{PTAe50} from the signal s_{P50}. For any other area (except the blue peaks), the two spectra are identical (spectrum 2 is perfectly superimposed on spectrum 1).

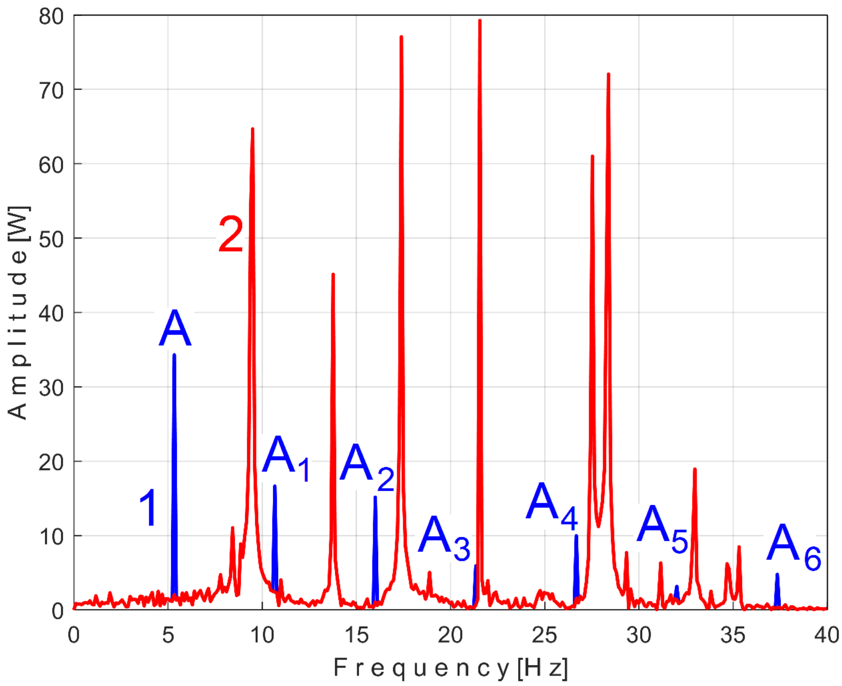

Figure 13. The FFT spectra of: 1—the sequence s_{P50}; 2—the signal s_{P1r50}.

Similarly with Figure 11, Figure 14 shows the superimposed extended patterns s_{PTBe5a} (curve 1, m = 935) and s_{PTBe5b} (curve 2, m = 935) related to the PVSC generated by the flat belt 2. Each extended model is the result of applying EMASS on one half of the signal P_{av} (or s_P as well). We found that the average frequency f_{PB} to consider in EMASS for each extended pattern (which produces the maximum peak-to-peak amplitude of the pattern) is quite similar: f_{PBa} = 9.45223 Hz for s_{PTBe5a} and f_{PBb} = 9.45981 Hz for s_{PTBe5b}.

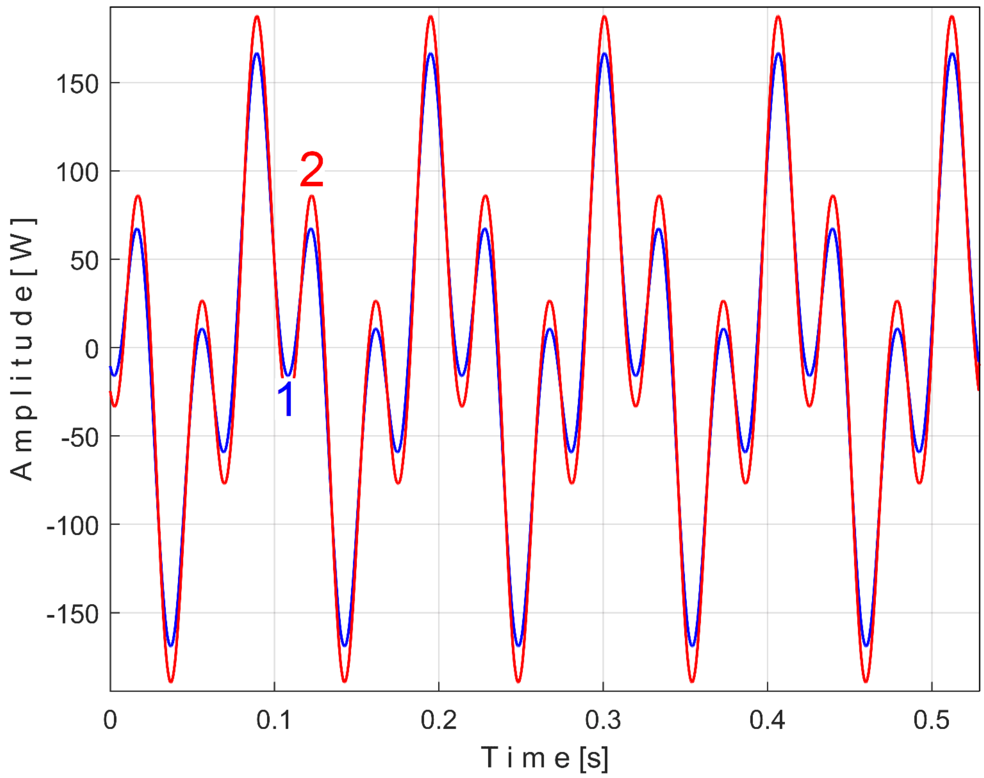

Figure 14. The extended patterns (m = 935) describing the behavior of second flat belt in signal s_P: 1—s_{PTBe5a} (f_{PBa} = 9.45223 Hz); 2—s_{PTBe5b} (f_{PBb} = 9.45981 Hz).

There are not very significant differences between the extended patterns, except for the peak-to-peak amplitude, which is most likely related to the increase in temperature. It should be noted, however, that the peak-to-peak amplitude of the PVSC of the active electrical power induced by the flat belt 2 is much greater than the PVSC induced by the flat belt 1. Most likely, the flat belt 2 is close to the breakage limit, as it is 35 years older than the first one.

An extended pattern s_{PTBe89} with 235,494 samples was generated from a sequence of 89 periods T_{PB} at the beginning of P_{av}, with m = 89 and the best approximation of the average value of the frequency f_{PB} = 9.446896 Hz in EMASS. This pattern is downsized at first to 234,300 samples and renamed $s_{PTBe89*}$. Now the $s_{PTBe89*}$ extended pattern has the same number of samples as the sequence s_{P50} and the extended pattern s_{PTAe50} (both previously used to generate Figure 13). This $s_{PTBe89*}$ extended pattern can also be mathematically removed from the s_{P1r50} signal; a new signal is obtained as s_{P2r50}, with a sample described as $s_{P2r50}[k] = s_{P1r50}[k] - s_{PTBe89*}[k] = s_{P50}[k] - s_{PTAe50}[k] - s_{PTBe89*}[k]$. The downsizing of s_{PTBe89} until $s_{PTBe89*}[k]$ was necessary to perform the mathematical subtraction above. All three patterns should have the same number of samples.

This signal, s_{P2r50}, is described with 234,300 samples taken from the beginning of P_{av} (as sequence s_{50}), but after removing from extended signal s_{P50}, the PVSC generated by the first and second flat belts, through the s_{PTAe50} and $s_{PTBe89*}$ extended patterns, is virtual signals. The result of this subtraction is highlighted in the FFT spectrum of signal s_{P2r50} marked with 3 in Figure 15, which is an extension of the result from Figure 13.

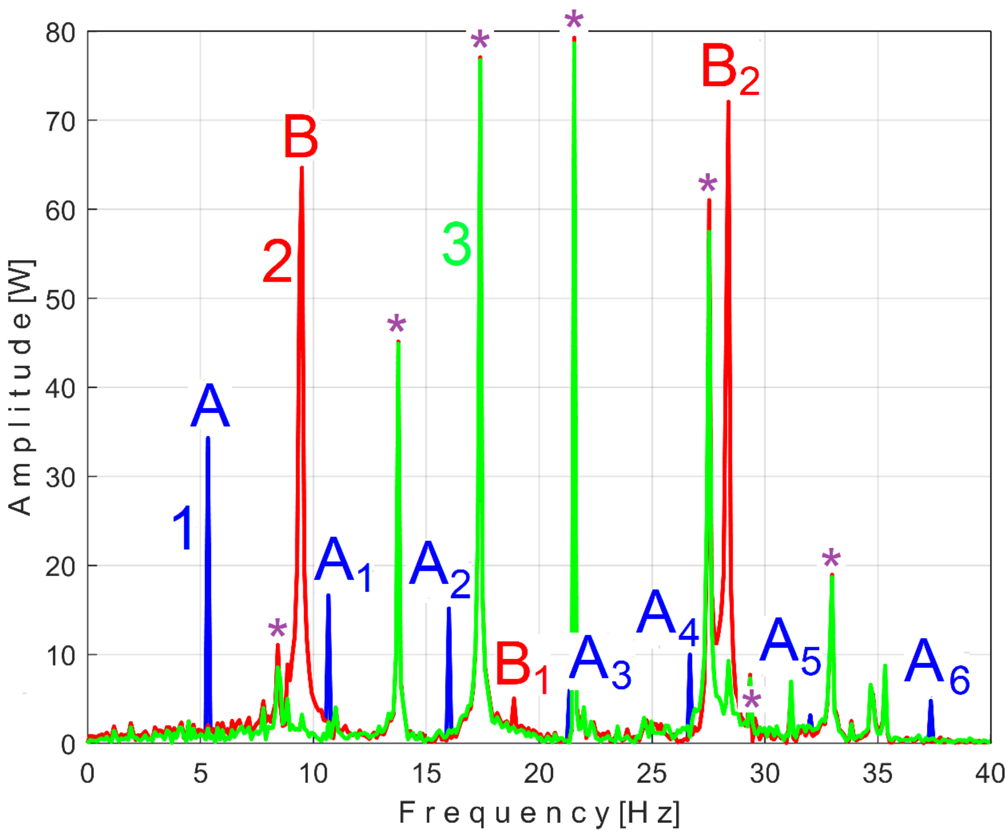

Figure 15. The results of removing the extended patterns s_{PTAe50} and $s_{PTBe89*}$ from s_{P50} in FFT spectrum. 1—The FFT spectrum of the sequence s_{P50} (already depicted in Figure 13); 2—The overlapped FFT spectrum of sequence s_{P1r50} (already depicted in Figure 13); 3—The overlapped FFT spectrum of sequence s_{P2r50}. The symbol * indicates an abnormal decrease of peaks in spectrum 3.

It is clear that, in addition to the result and comments of Figure 13, the removal of the PVSC generated by the second flat belt also causes the disappearance of the peaks associated with this component (the fundamental B and the harmonics B_1 and B_2) from the FFT spectrum. Obviously, looking at Figure 15, the components B and B_2 do not disappear completely, but rather some peaks of the FFT spectrum are diminished (the peaks marked with the symbol *). There is a partial explanation for this shortcoming: the periodic component generated by this second flat belt changes its amplitude more strongly in time than the first flat belt, as can be seen in Figure 14, in comparison with Figure 11.

Due to the slight change in rotation frequencies over time, the removal of the extended patterns from a lengthier P_{av} signal sequence no longer produces the same results in the FFT spectrum, characterized by the complete disappearance of peaks.

Similarly with Figures 11 and 14, Figure 16 shows the superimposed extended patterns s_{PTCe5a} (curve 1, $m = 1350$) and s_{PTCe5b} (curve 2, $m = 1350$) related to the periodical component generated by the shaft II. We found that the average frequency f_{PC} (or period $T_{PC} = 1/f_{PC}$) to consider in EMASS for each extended pattern (which produces the maximum peak-to-peak amplitude of the pattern) is quite similar: $f_{PCa} = 13.75435$ Hz for s_{PTCe5a} and $f_{PCb} = 13.759$ Hz for s_{PTCe5b}. Except for a small difference between peak-to-peak amplitudes, there is a very good coincidence between patterns.

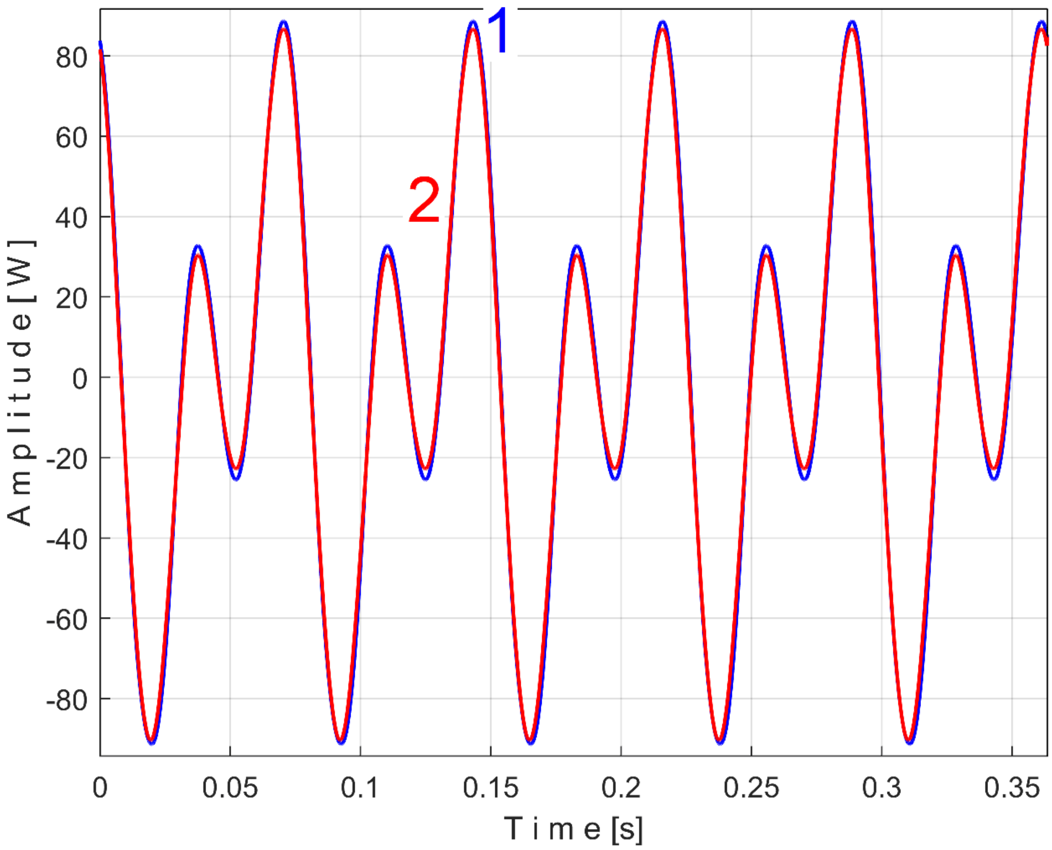

Figure 16. The extended patterns ($m = 1350$) describing the behavior of shaft II in signal s_P: 1—s_{PTCe5a} ($f_{PCa} = 13.75435$ Hz); 2—s_{PTCe5b} ($f_{PCb} = 13.759$ Hz).

Figure 17 shows the superimposed extended patterns s_{PTDe5a} (curve 1, $m = 1720$) and s_{PTDe5b} (curve 2, $m = 1720$) related to the periodical component generated by the shaft III and spindle. We found that the average frequency f_{PD} (for a period $T_{PD} = 1/f_{PD}$) to consider in EMASS for each extended pattern (which produces the maximum peak-to-peak amplitude of the pattern) is quite similar: $f_{PDa} = 17.37406$ Hz for s_{PTDe5a} and $f_{PDb} = 17.38745$ Hz for s_{PTDe5b}.

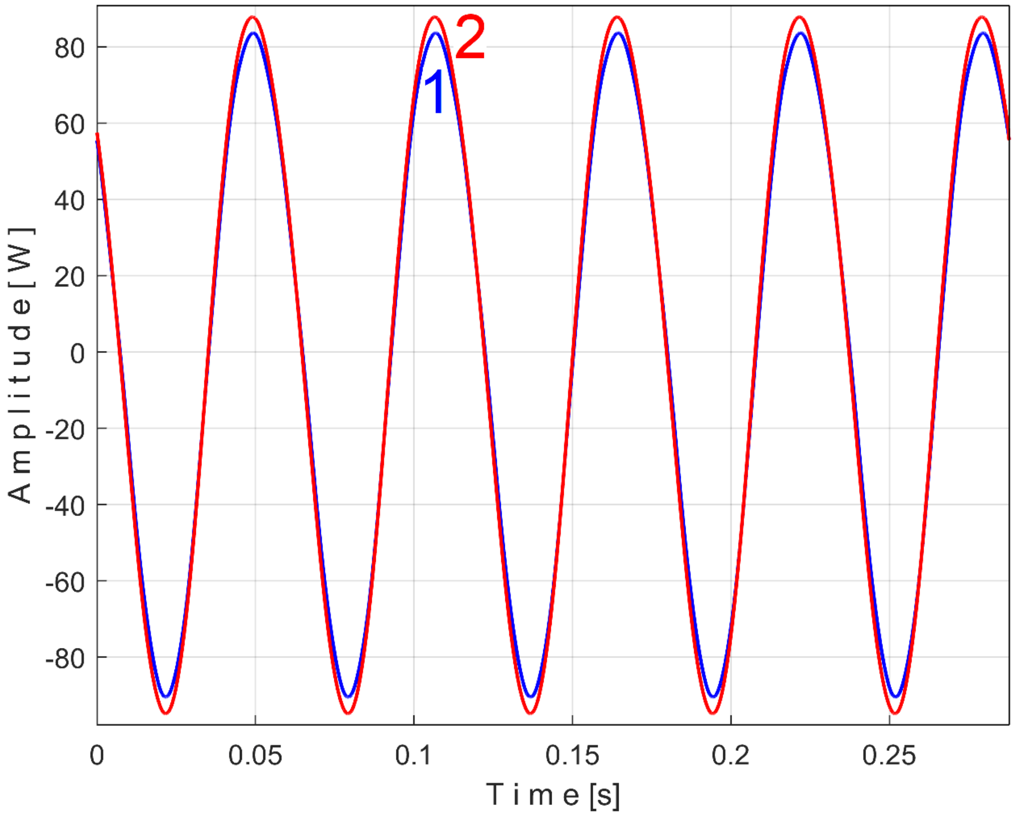

Figure 17. The extended patterns (m = 1720) describing the behavior of the shaft III and spindle in signal s_P: 1—s_{PTDe5a} (f_{PDa} = 17.37406 Hz); 2—s_{PTDe5b} (f_{PDb} = 17.38745 Hz).

Since the shaft III and spindle apparently have the same rotational speeds, the EMASS cannot generate a pattern for each of them. In reality, due to the slippage of belt 2, the rotational speeds are not exactly the same.

Figure 18 shows the superimposed extended patterns s_{PTEe5a} (curve 1, m = 2130) and s_{PTEe5b} (curve 2, m = 2130) related to the periodical component generated by the shaft I. The average frequency f_{PE} (for a period $T_{PE} = 1/f_{PE}$) to consider in EMASS for each extended pattern (which produces a maximum peak-to-peak amplitude of the pattern) is quite similar: f_{PEa} = 21.5606 Hz for s_{PTEe5a} and f_{Peb} = 21.5781 Hz for s_{PTEe5b}. A small change in amplitude of the pattern s_{PTEe5b} is evident.

The mechanical inertia of the gearbox affects the shape and the size of the extended patterns of the PVSC inside P_{av}. It is obvious that $f_{PAa} < f_{PAb}$ (Figure 11), $f_{PBa} < f_{PBb}$ (Figure 14), . . ., $f_{PEa} < f_{PEb}$ (Figure 18). This is due to the increase in the motor speed, probably because of the increase in the supply voltage frequency, and certainly because of the decrease in the internal friction due to lubrication.

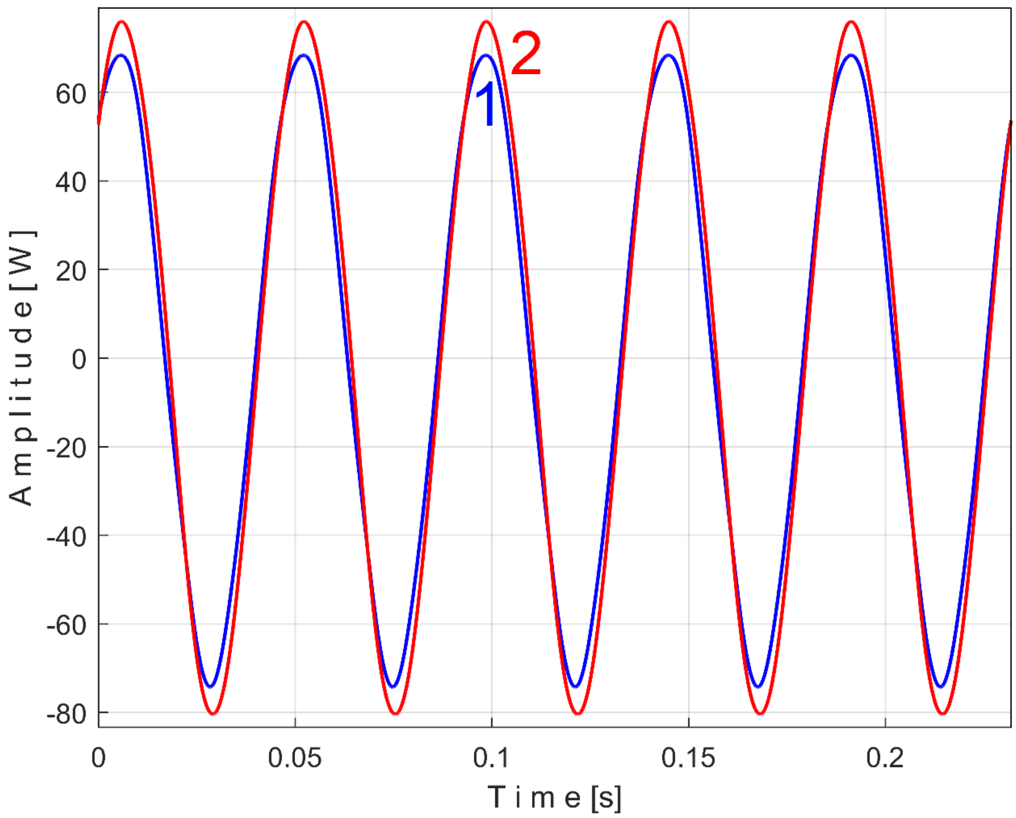

Figure 18. The extended patterns (m = 2130) describe the behavior of shaft II in signal s_P: 1—s_{PTEe5a} (f_{PEa} = 21.5606 Hz); 2—s_{PTDe5b} (f_{PEb} = 21.5781 Hz).

3.2. Some Results Obtained by Analyzing Vibration Signal Using EMASS

A similar analysis can be conducted directly on the vibration signal V_s, written as s_V. This signal was acquired during the same steady-state regime as for active electrical power P_a previously studied, a sequence of 200 s, with p_a = 5 MSa or 5,000,000 samples Δt = 1/25,000 s as the sampling time. This signal is depicted in Figure 19.

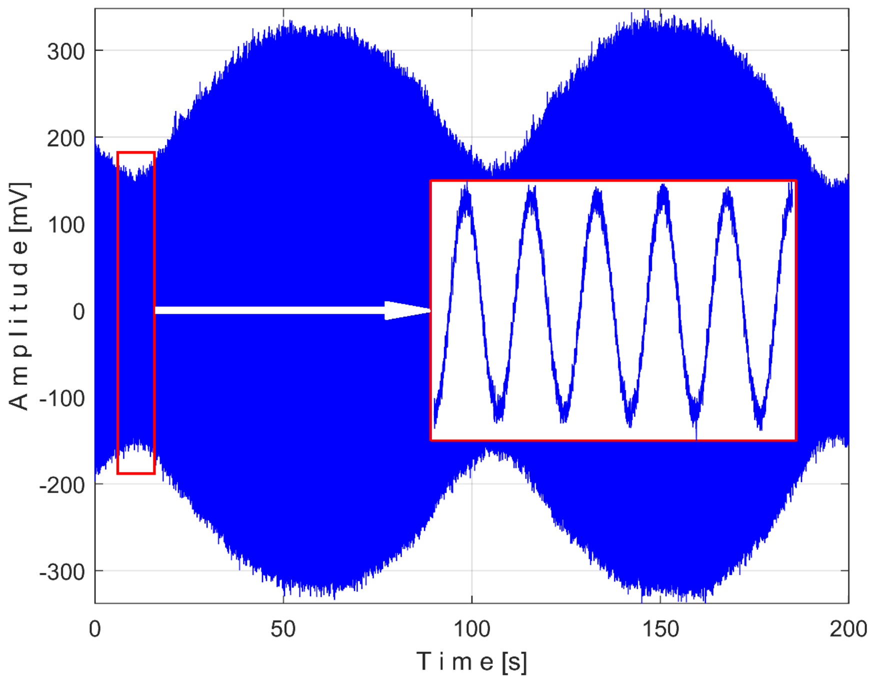

Figure 19. The time-domain representation of the signal V_s.

This signal vs. describes a beating phenomenon, explained and studied in detail in [55]. The shaft III and the spindle (both with mechanical unbalance) rotate at almost the same instantaneous angular speed; a beating phenomenon (with nodes and anti-nodes) occurs. There is a dominant vibration, shown in an enlarged detail in Figure 19 (on the right), with almost the same frequency as the rotation frequency of the spindle. The partial FFT spectrum of this signal is shown in Figure 20, in a frequency range between 0 and 40 Hz. A zoomed section of this spectrum is shown in the middle, with the same frequency range and the amplitude range severely diminished for magnification: between 0 and 4.2 mV.

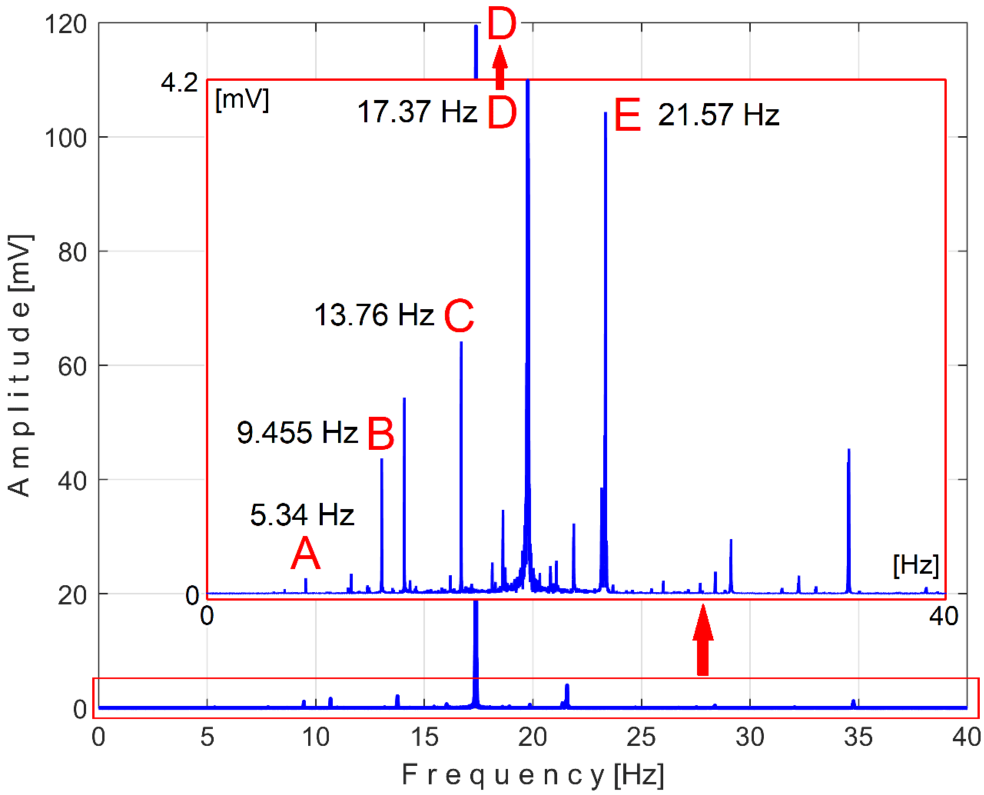

Figure 20. The FFT spectrum of vs. with A, B, . . ., E the fundamentals of PVSC generated by these MCs: A—the flat belt 1; B—the flat belt 2; C—the shaft II; D—the shaft III and the spindle; E—the shaft I.

It is surprising that in the FFT spectrum of the vs. signal, the same A, B, . . . E fundamentals of the PVSC are present as previously seen in the FFT spectrum of P_{av} (Figure 10). This means that the same phenomena are reflected in the time-domain representation of the active electrical power and vibration. Note that the fundamental A is described with diminished amplitude because it has a frequency below the natural frequency of the sensor, 8 Hz. As expected, there is a dominant PVSC with D as fundamental (with a 17.37 Hz frequency and 119.3 mV amplitude) with the origin already explained above in Figure 19.

Even if the vibration description signal contains the beat phenomenon and even if there is a large dominant PVSC (with D as fundamental), the EMASS is able to produce interesting results for monitoring. Related to the behavior of the first flat belt, Figure 21 shows the superimposed extended patterns s_{VTAe5a} (curve 1, m = 533 for almost 2.5 MSa at the beginning of s_V) and s_{VTAe5b} (curve 2, m = 530 for almost the next 2.5 MSa of s_V). Same as above, we found that the right value of average frequency f_{VA} (for a period $T_{VA} = 1/f_{VA}$) to consider in EMASS for each extended pattern is slightly different: f_{VAa} = 5.33736 Hz for s_{VTAe5a} and f_{VAb} = 5.34151 Hz for s_{VTAe5b}. As a first approach, since the two patterns appear to be strongly affected by noise, they are plotted in Figure 21 after a numerical low-pass filtering (using a moving average filter with 100 samples in the average). Same as previously overlapped extended patterns, the sample at the beginning of the s_V sequence from which the second extended pattern (s_{VTAe5b}) has been deduced (almost $p_a/2$) is conveniently changed to obtain the most correct possible overlap of the two patterns.

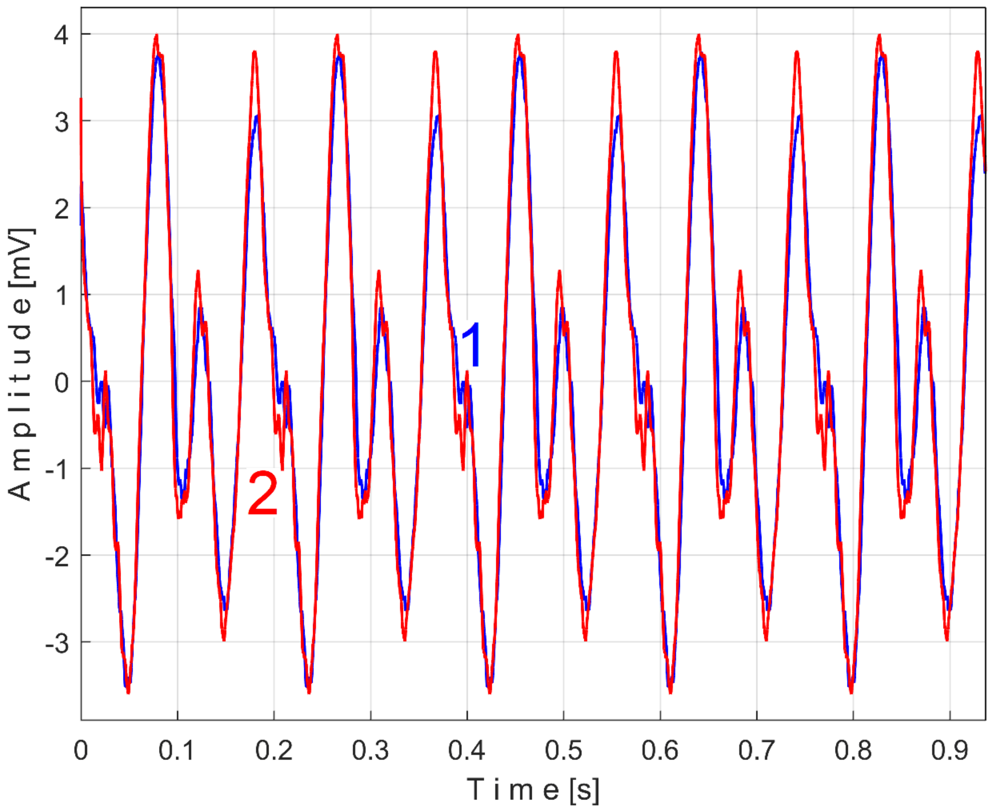

Figure 21. The low-pass filtered extended patterns (m = 533) describing the behavior of the flat belt 1 in signal s_V: 1—s_{VTAe5a}, f_{VAa} = 5.33736 Hz; 2—s_{VTAe5b}, f_{VAb} = 5.34151 Hz.

As can be seen in Figure 21, there are sufficient similarities between the two extended patterns (despite the relatively long durations between the sequences from which they were derived, almost 100 s) to prove the validity of this resource for describing the condition of the first flat belt using EMASS of vibration signal s_V. It should be noted that in the patterns of this flat belt, the fundamental A has a low amplitude (due to the low sensitivity of the sensor at low frequency), but there are some harmonics with higher amplitudes. It is interesting to highlight the resources offered by the unfiltered time-domain representation of these two overlapped extended patterns, shown in Figure 22, where there are still obvious similarities between them. We propose to realize the extension of the pattern s_{VTAe5b} to 50 periods, as $s_{VTAe50b}$, with 234,000 samples. The partial FFT spectrum of this extended pattern is shown in Figure 23, in a range between 0 and 175 Hz. This figure also shows a zoomed-in detail of this partial spectrum (the same frequency range). This extension of the pattern was necessary to achieve a high-frequency resolution of the FFT spectrum.

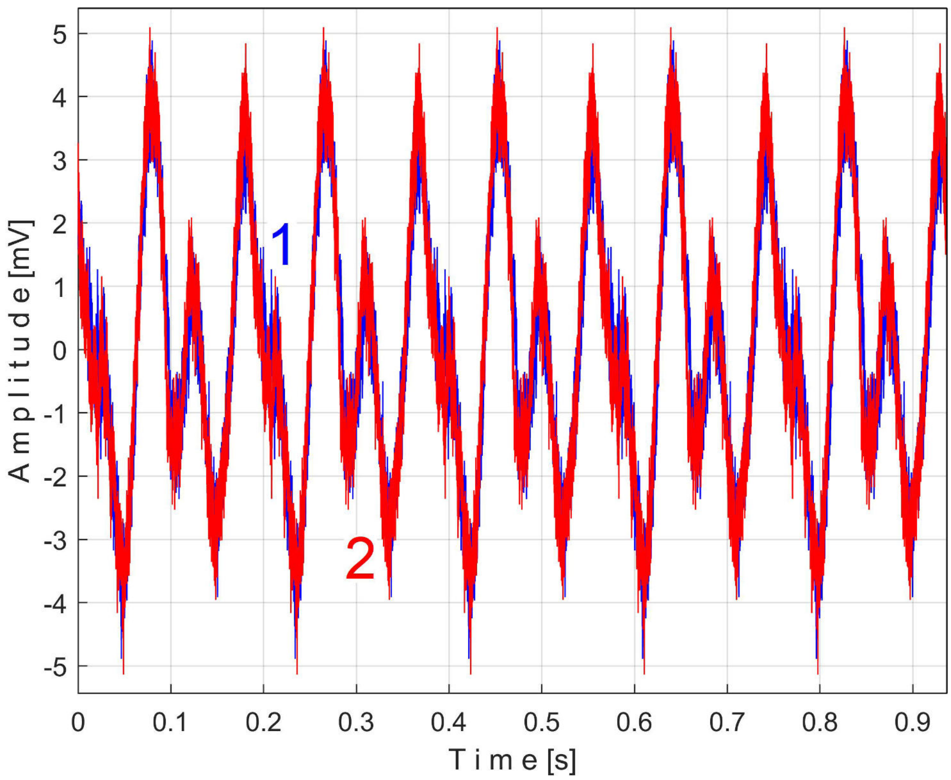

Figure 22. The unfiltered extended patterns 1 and 2 from Figure 21.

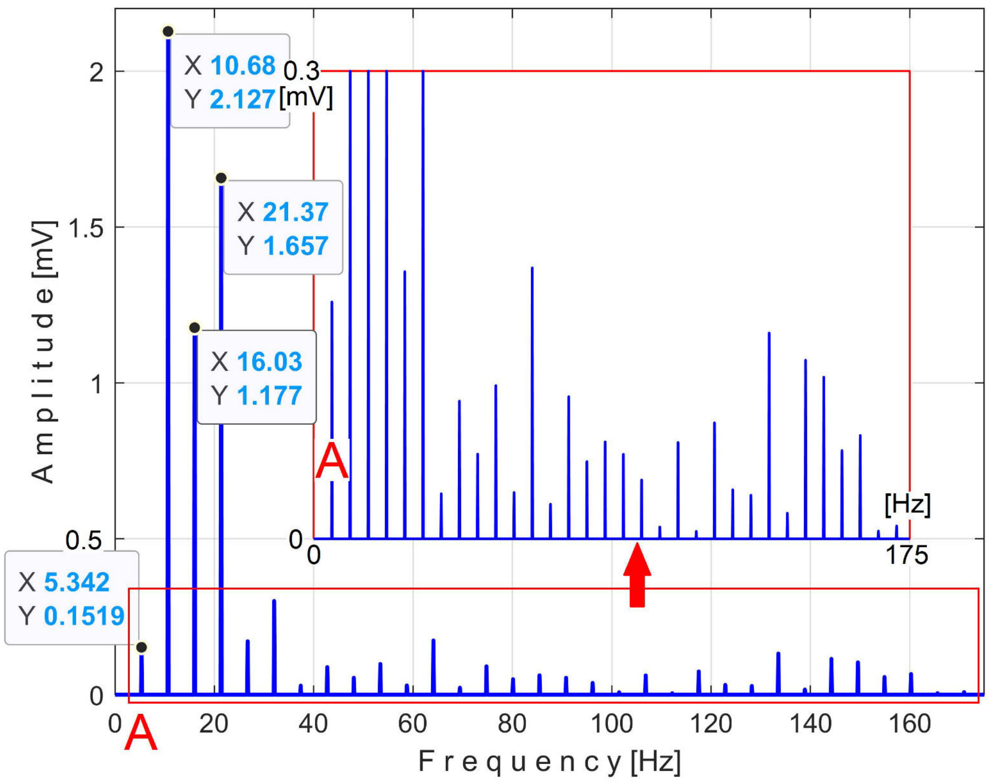

Figure 23. The FFT spectrum of the extended unfiltered pattern $s_{VTAe50b}$.

The first remark related to Figure 23: the appearance of the FFT spectrum proves that there is no noise in the extended pattern $s_{VTAe50b}$ (so neither in unfiltered s_{VTAe5a} nor in s_{VTAe5b} patterns). In addition, this signal is strictly deterministic, being defined as the sum of strictly harmonically correlated components with frequency spacing exactly equal to the value of f_{VAb}.

This is another strong argument in favor of the usefulness of EMASS for describing the state of a mechanical component of the mechanical system under investigation. The spectral content highlighted here in the case of the first belt vibration extended pattern was not observed in the case of the active electrical power extended pattern because this power is defined by numerical low-pass filtering of the instantaneous electrical power [3]. The high-frequency harmonics are eliminated by filtering.

It is important to note that all the extended patterns of PVSC from active electrical power presented above can be similarly characterized by means of the FFT spectrum. Both variants of any extended pattern (filtered and unfiltered) can be used to monitor the condition of a rotating MC. The filtered version has the advantage of a quick estimation of the condition.

Related to the behavior of the second flat belt, Figure 24 shows the superimposed extended patterns s_{VTBe5a} (curve 1, m = 935 for almost 2.5 MSa at the beginning of s_V) and s_{VTBe5b} (curve 2, m = 935 for almost the next 2.5 MSa of s_V). The average frequency f_{VB} (for a period $T_{VB} = 1/f_{VB}$) to consider in EMASS for each extended pattern (which produces a maximum peak-to-peak amplitude of the pattern) is again slightly different: f_{VBa} = 9.4525 Hz for s_{VTAe5a} and f_{VBb} = 9.4596 Hz for s_{VTAe5b}. Figure 25 shows the same extended patterns but filtered, using a moving average filter with 30 samples in the average.

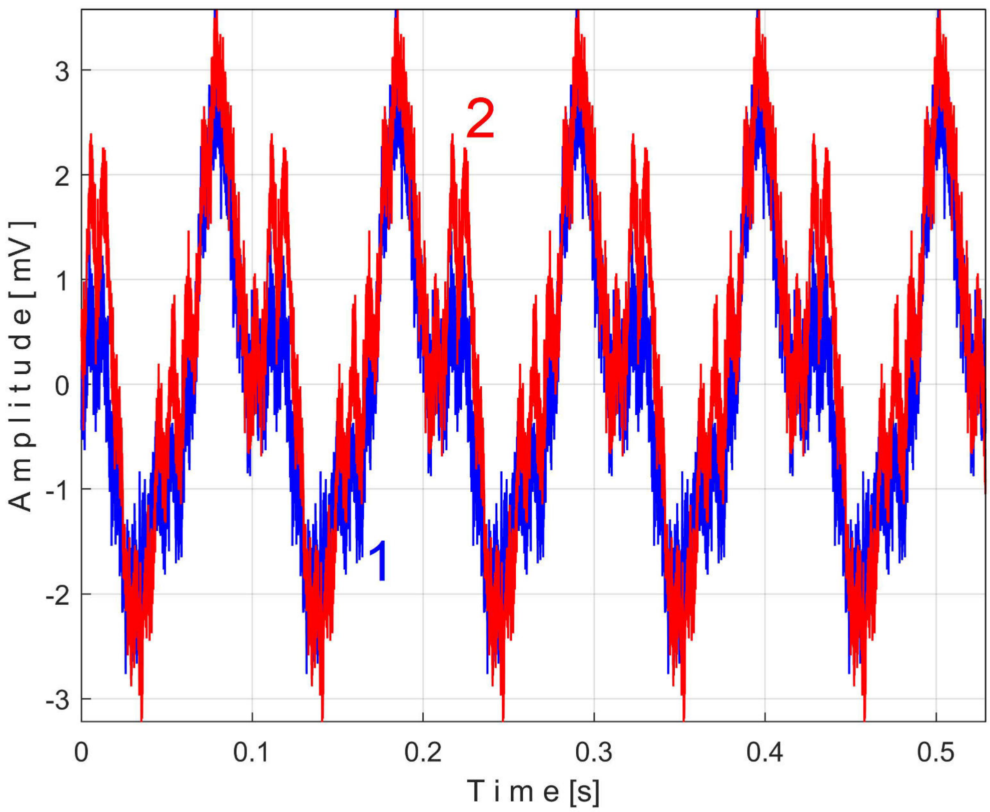

Figure 24. The unfiltered extended patterns (m = 935) describing the behavior of the flat belt 2 in signal s_V: 1—s_{VTBe5a}, f_{VBa} = 9.4525 Hz; 2—s_{VTBe5b}, f_{VBb} = 9.4596 Hz.

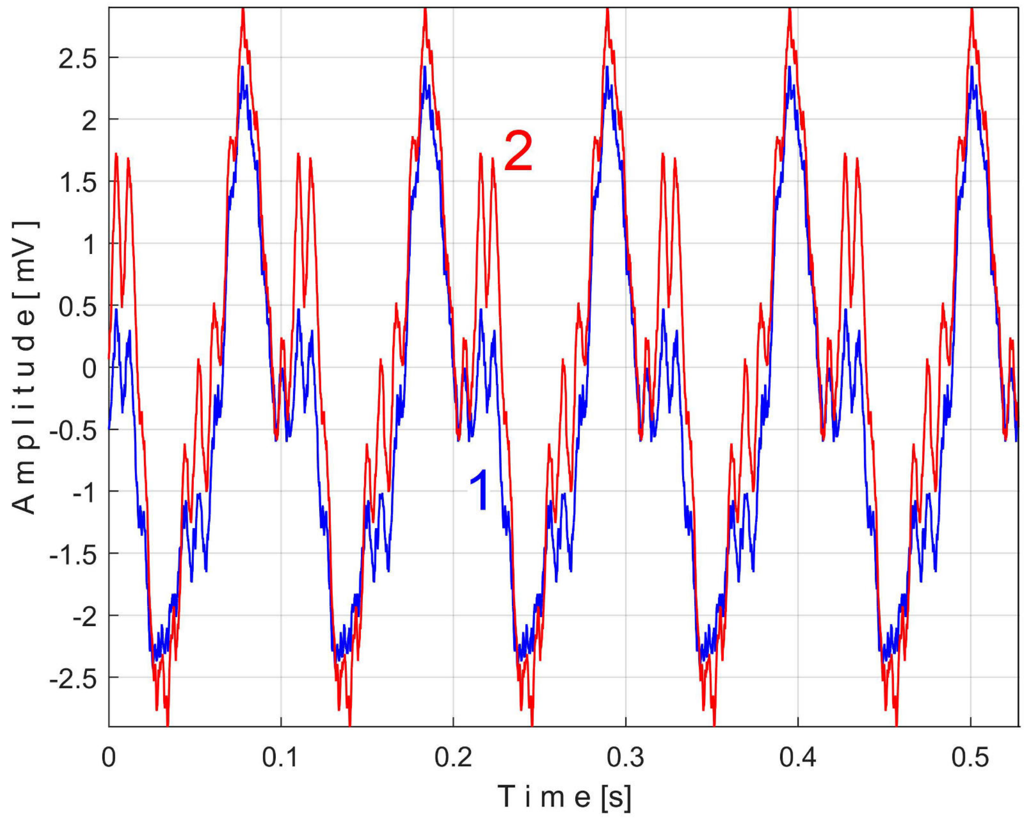

Figure 25. The low-pass filtered extended patterns 1 and 2 from Figure 24 (using a moving average filter with 30 samples in the average).

There are certain similarities between the filtered patterns, but also differences, probably due to the change in temperature of the belt during operation. It should be noted that flat belt 2 introduces a greater peak-to-peak variation in the active electrical power pattern compared to flat belt 1 (see Figures 11 and 14). Conversely, flat belt 2 introduces less variation than flat belt 1 in the description of vibration patterns (see Figures 21 and 25).

Figure 26 shows the superimposed extended patterns generated by the shaft II: s_{VTCe5a} (curve 1, m = 1365 for almost 2.5 MSa at the beginning of s_V, with f_{VCa} = 13.75399 Hz) and s_{VTCe5b} (curve 2, m = 1365 for almost the next 2.5 MSa samples of s_V, with f_{VCb} = 13.76565 Hz). Figure 27 shows the same extended patterns treated with a numerical low-pass filtering, using a double-moving average filter (with 37 and 50 samples in the average).

An examination can now be made of the components of one of the unfiltered patterns in Figure 26, e.g., s_{VTCe5b}. Using the *Curve Fitting Tool* application from Matlab, an approximation of this pattern has been identified based on the first two most representative sinusoidal components. This approximation abeled ${s_{VTCe5b}}^{2c}$ is described as:

$$s_{VTCe5b^{2c}}[k] = 3.629 \cdot \sin(86.57 \cdot k \cdot \Delta t + 2.206) + 1.324 \cdot \sin(4152 \cdot k \cdot \Delta t - 1.207) \tag{7}$$

Figure 28 shows these two superimposed patterns: s_{VTCe5b} pattern as curve 2 (already shown in Figure 26) and ${s_{VTCe5b}}^{2c}$ as curve 3, mathematically described by Equation (7).

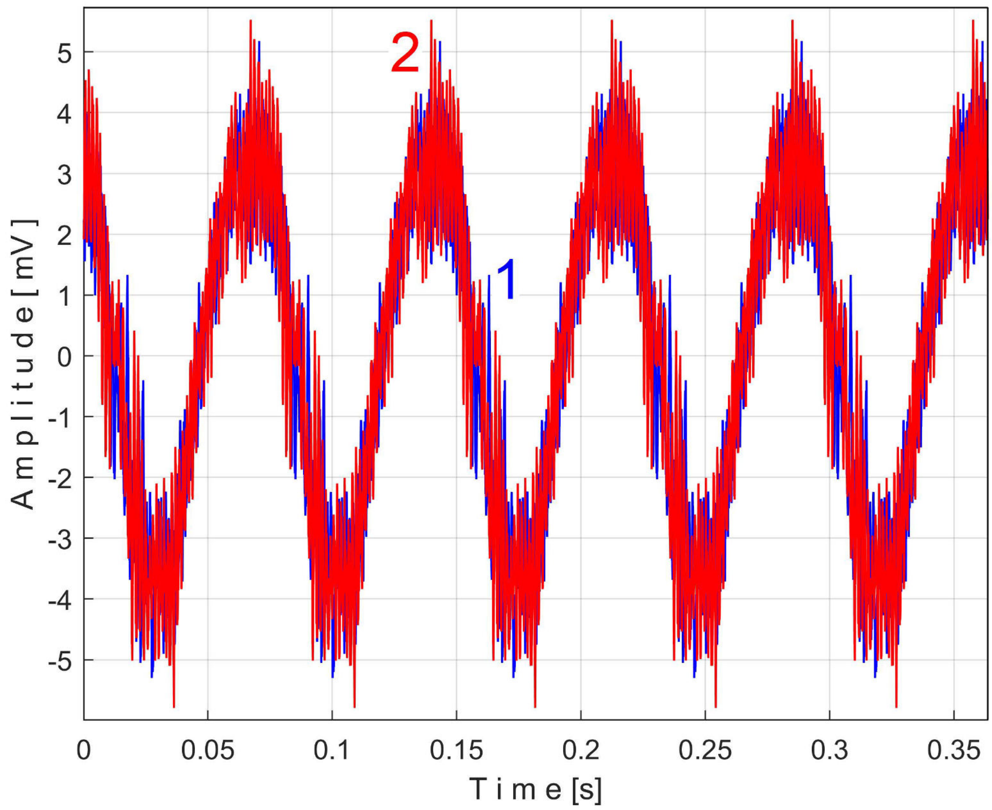

Figure 26. The unfiltered extended patterns (m = 1365) describing the behavior of shaft II in signal s_V: 1—s_{VTCe5a}, f_{VCa} = 13.75399 Hz; 2—s_{VTCe5b}, f_{VCb} = 13.76565 Hz.

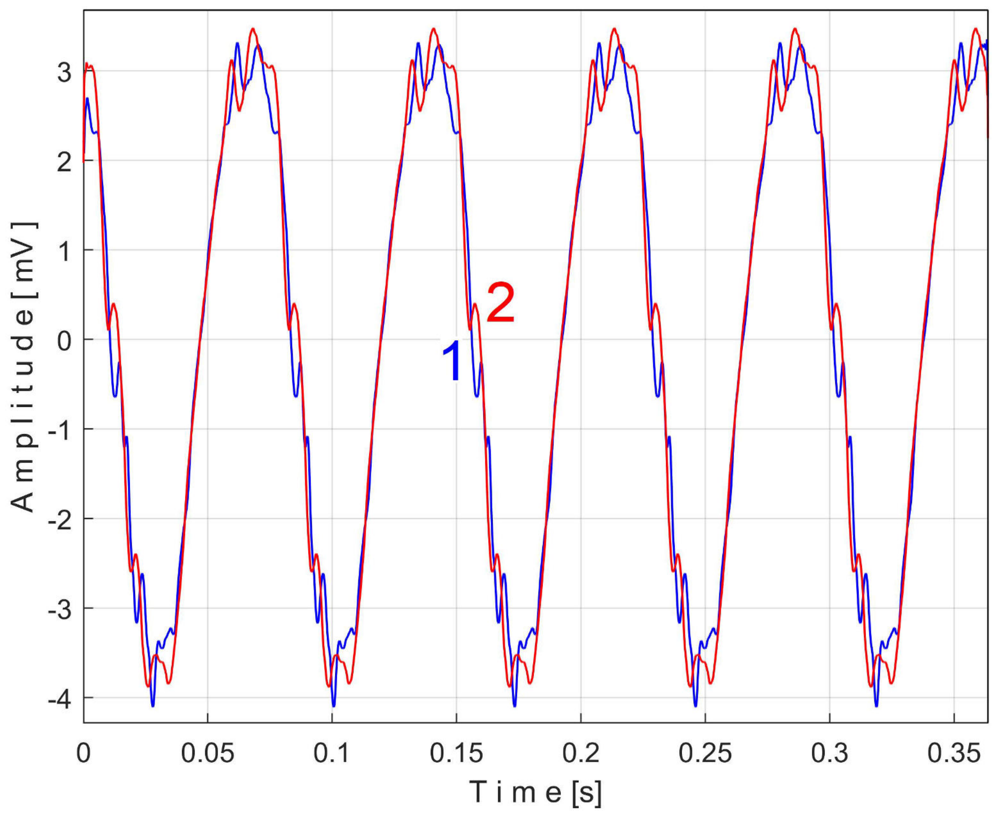

Figure 27. The low-pass filtered extended patterns 1 and 2 from Figure 26 (using a double moving average filter with 37 and 50 samples in the average).

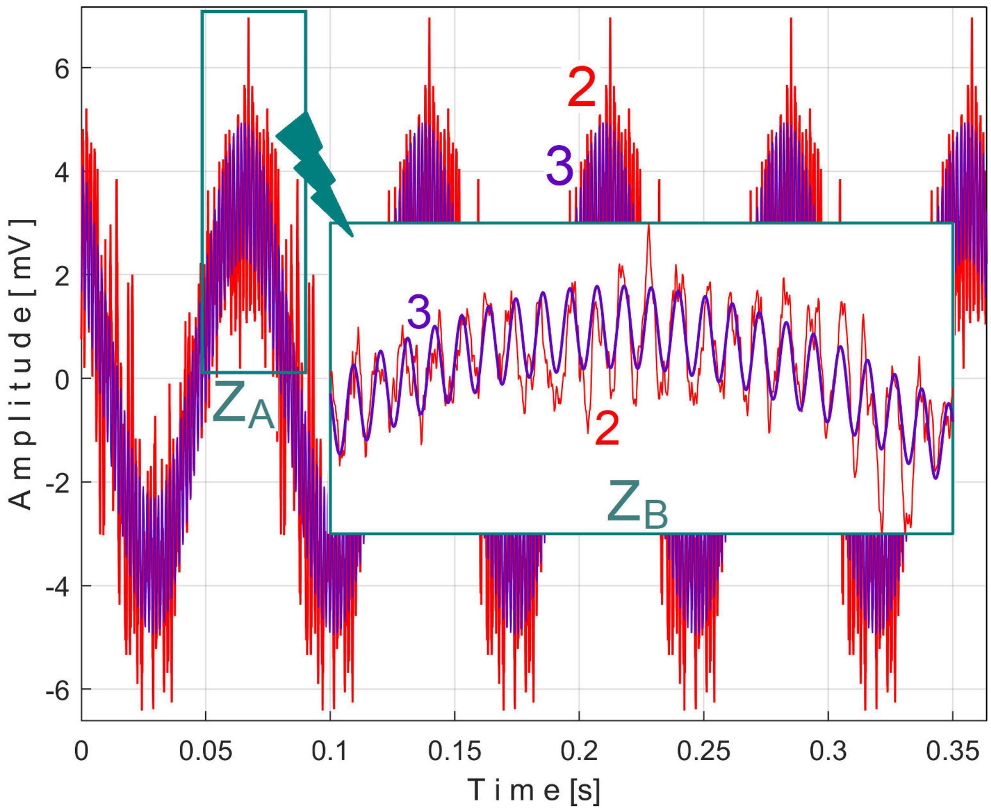

Figure 28. 2—The unfiltered pattern s_{VTCe5b}; 3—An approximation of this pattern based on Equation (7) as $s_{VTCe5b}{}^{2c}$.

A detail from zone Z_A illustrating the fit of the two curves is magnified in region Z_B.

As expected, the angular frequency of the first component, or fundamental (as ω_1 = 86.57 rad/s), is related to the frequency f_{VCb} (with $2{\cdot}\pi{\cdot}f_{VCb} \approx \omega_1$, so 86.4921 rad/s $\approx$ 86.57 rad/s). The EMASS ensures that the second component of $s_{VTCe5b}{}^{2c}$ from Equation (7) (with angular frequency ω_2 = 4152 rad/s) is necessarily harmonically correlated with the fundamental. This is totally confirmed because ω_2/ω_1 = 47,9611 $\approx$ 48. This very small difference is explained by the approximations of the fitting procedure in finding the values of the constants from Equation (7).

Obviously, this second component in Equation (7) must correspond to a vibrational phenomenon. The most plausible explanation for the origin of this phenomenon is that—as shown in Figure 7—a toothed wheel with 48 teeth is mounted on shaft II in free meshing (not transmitting mechanical power). The second component in Equation (7) is generated by the meshing sequence of the teeth of this wheel as a vibration-generating phenomenon with a frequency 48 times higher than the rotational frequency of shaft II.

It is clear that this second component of Equation (7) is always present in the vibration signal s_V. Moreover, it should be emphasized that EMASS is applied to the signal s_V, which is related by a PVSC with period $T_{VC}{}^{48} = T_{VC}/48$. The extended pattern of this component on five periods $T_{VC}{}^{48}$ (as $s_{VTC}{}^{48}{}_{e5a}$ pattern) is shown as curve 1 in Figure 29 (m = 3250, on the first 4.94 s of the signal s_V, with the best approximation of the frequency of this PVSC $f_{VC}{}^{48}{}_a$ = 660.045986 Hz). The same analysis using EMASS was performed on a new s_V signal sequence starting at the 100th second (m = 3250 with the best approximation of the frequency at this variable component $f_{VC}{}^{48}{}_b$ = 660.53362 Hz). An extended pattern ($s_{VTC}{}^{48}{}_{e5b}$) was generated, represented by curve 2 in Figure 29, and shifted appropriately to obtain the best overlap with curve 1. The similarities of these patterns are more than obvious, even though they are described with a small number of samples (190).

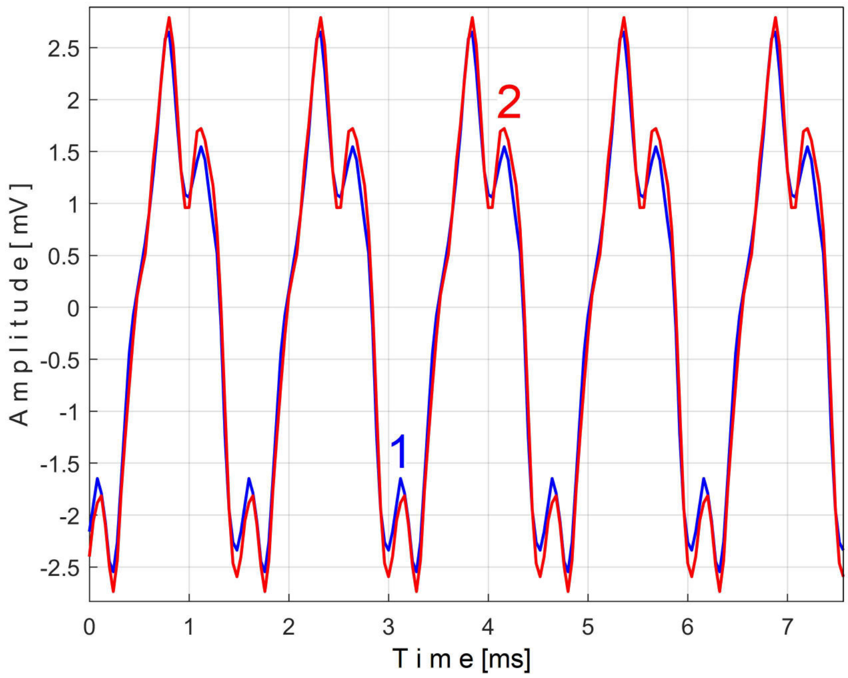

Figure 29. The extended patterns (m = 3250) describing the behavior of component $T_{VC}{}^{48}$ in signal s_V: 1—$s_{VTC}{}^{48}{}_{e5a}$, $f_{VC}{}^{48}{}_a$ = 660.045986 Hz; 2—$s_{VTC}{}^{48}{}_{e5b}$, $f_{VC}{}^{48}{}_b$ = 660.53362 Hz.

Similarly, EMASS can be used to determine if there is a PVSC induced by the 58-toothed gearwheel placed on shaft II as a toothed wheel that transmits mechanical power. The extended pattern of this PVSC on five periods $T_{VC}{}^{58}$ (as $s_{VTC}{}^{58}{}_{e5a}$ pattern) is shown as curve 1 in Figure 30 (m = 3250, on the first 4.04 s of the signal s_V, with the best approximation of the frequency at this variable component $f_{VC}{}^{58}{}_a$ = 797.5646 Hz ≈ 58 · f_{VCa} = 58·13.75399 Hz = 797.73142 Hz). A new extended pattern of this component on five periods $T_{VC}{}^{58}$ (as $s_{VTC}{}^{58}{}_{e5b}$ pattern) is shown as curve 2 in Figure 30 (m = 3250, on 4.04 s, starting with the 100th second of the signal s_V, with the best approximation of the frequency at this variable component $f_{VC}{}^{58}{}_b$ = 798.1551 Hz ≈ 58 · f_{VCb} = 58·13.76565 Hz = 798.4077 Hz).

Again, a good similarity of the two patterns from Figure 30 was obtained. Each pattern is described with 155 samples. This proves that the vibrations induced by this toothed wheel occur systematically and that the EMASS is obviously a good option in gearbox condition research. Increasing the sampling rate of the signal s_V increases the number of samples of the patterns from Figure 29 to Figure 30.

As the speed of the electromotor driving the gearbox increases slightly over time (due to the decrease in mechanical load through the effect of the viscosity decreasing of the lubricating oil), all the frequencies of the PVSC studied so far increase slightly over time. Therefore, it should be mentioned that the shape of the patterns generated by the proposed EMASS depends relatively strongly on the value of m, especially in the case of high-frequency PVSC (e.g., for the $T_{VC}{}^{48}$ periodic component with the patterns already shown in Figure 29 for m = 3250). Figure 31 reproduces these two patterns (curves 1 and 2) but also the extended patterns resulting from EMASS with the maximum possible value for m, with m = 65,700 (curves 3 and 4).

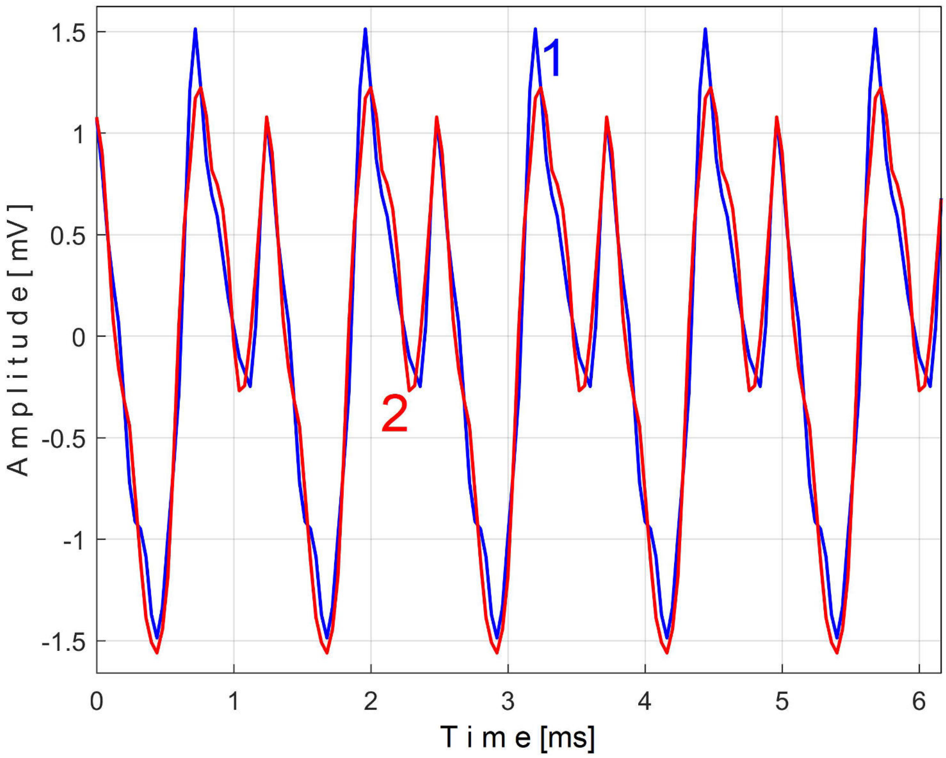

Figure 30. The extended patterns (m = 3250) describing the behavior of component $T_{VC}{}^{58}$ in signal s_V: 1—$s_{VTC}{}^{58}{}_{e5a}$, $f_{VC}{}^{58}{}_a$ = 797.5646 Hz; 2—$s_{VTC}{}^{58}{}_{e5b}$, $f_{VC}{}^{58}{}_b$ = 798.1551 Hz.

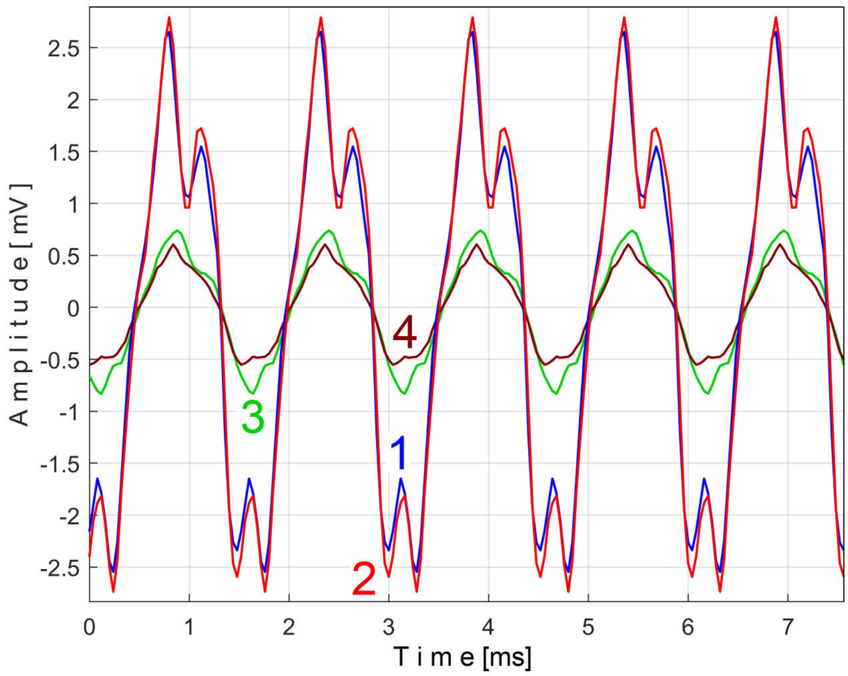

Figure 31. 1, 2—The extended patterns (m = 3250) with $T_{VC}{}^{48}$ in signal s_V: 1—$s_{VTC}{}^{48}{}_{e5a}$, $f_{VC}{}^{48}{}_a$ = 660.045986 Hz; 2—$s_{VTC}{}^{48}{}_{e5b}$, $f_{VC}{}^{48}{}_b$ = 660.53362 Hz. 3,4—The extended patterns (m = 65,700) with $T_{VC}{}^{48}$ in signal s_V: 3—$s_{VTC}{}^{48}{}_{e5a}$, $f_{VC}{}^{48}{}_a$ = 660.19726 Hz; 4—$s_{VTC}{}^{48}{}_{e5b}$, $f_{VC}{}^{48}{}_a$ = 660.58252 Hz.

Curve 3 shows the pattern for m = 65,700 (as $s_{VTC}{}^{48}{}_{e5a}$) from the analysis of almost 2.5 MSa from signal s_V (with $f_{VC}{}^{48}{}_a$ = 660.19726 Hz). Curve 4 shows the pattern for

m = 65,700 (as $s_{VTC}{}^{48}{}_{e5b}$) from the analysis of the next almost 2.5 MSa from signal s_V (with $f_{VC}{}^{48}{}_b$ = 660.58252 Hz).

Figure 32 shows the superimposed extended patterns generated by the shaft I, for m = 2155, as s_{VTDe5a} (curve 1, for almost 2.5 MSa at the beginning of s_V, with f_{VDa} = 21.56087 Hz) and s_{VTDe5b} (curve 2, for almost the next 2.5 MSa samples of s_V, with f_{VDb} = 21.57886 Hz). Figure 33 shows the same extended patterns treated with numerical low-pass filtering, using a moving average filter (with 30 samples in the average).

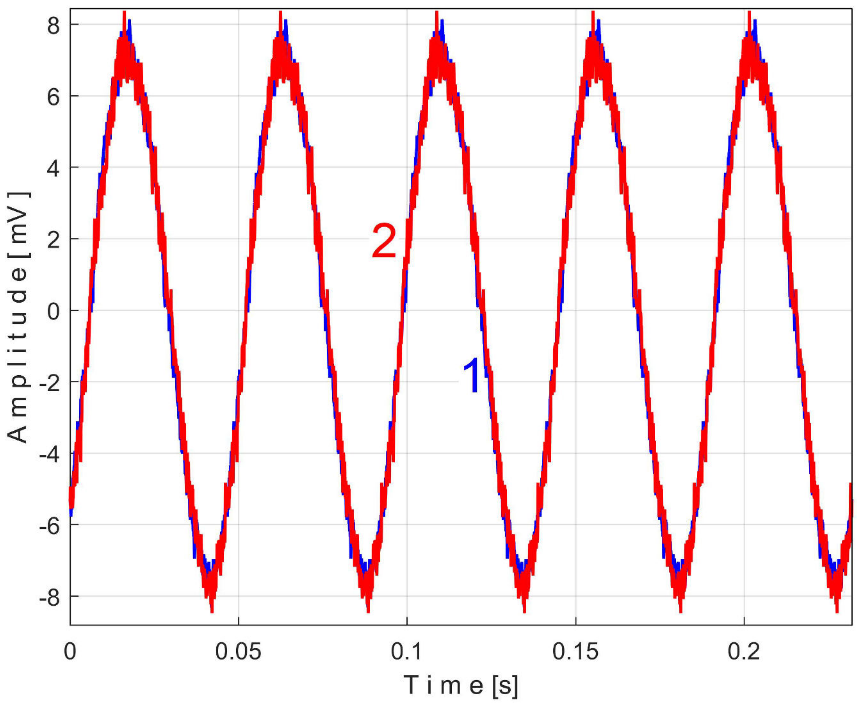

Figure 32. The unfiltered extended patterns (m = 2155), which describes the behavior of shaft I in signal s_V: 1—s_{VTCe5a}, f_{VDa} = 21.56087 Hz; 2—s_{VTDe5b}, f_{VDb} = 21.57886 Hz.

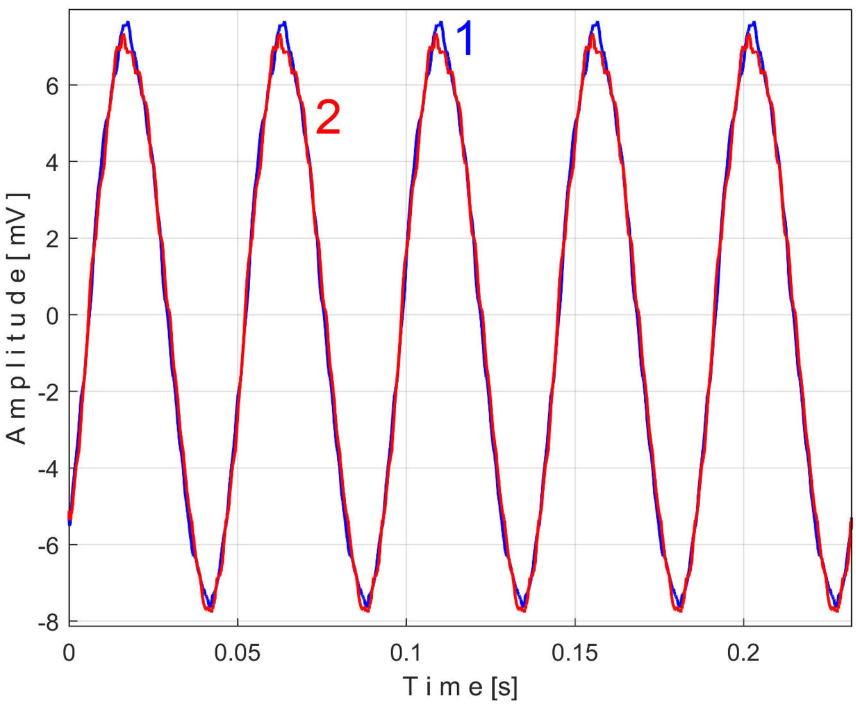

Figure 33. The low-pass filtered extended patterns 1 and 2 from Figure 32.

It should be noted that the two filtered extended patterns derived from the vibration analysis by EMASS are more similar for this shaft than for any of the flat belts previously presented (belt 1 in Figure 21 and belt 2 in Figure 25). Similar studies can be performed on the periodic components associated with the rotation of the shaft I and the spindle.

3.3. Some Results Obtained by Analyzing Instantaneous Angular Speed Using EMASS

An instantaneous angular speed (IAS) sensor (as IASS) was placed in the jaw chuck of the spindle (Figures 6 and 7). This sensor is actually a stepper motor that plays the role of a two-phase, 50-pole AC generator [53]. At relatively high IAS, this sensor generates two sine-wave signals (equal amplitudes, 90 degrees out of phase) with 50 periods per revolution. These signals are processed appropriately in order to produce IAS, using an interesting approach presented in [56] and appropriately adapted here. This approach is based on determining the angle of rotation of the sensor rotor and the numerical derivative of this angle with respect to time. The time-domain representation of the IAS during an identical steady-state regime considered previously (but shorter, with a duration of only 10 s and a sampling rate of 100,000 s^{-1}) is shown in Figure 34.

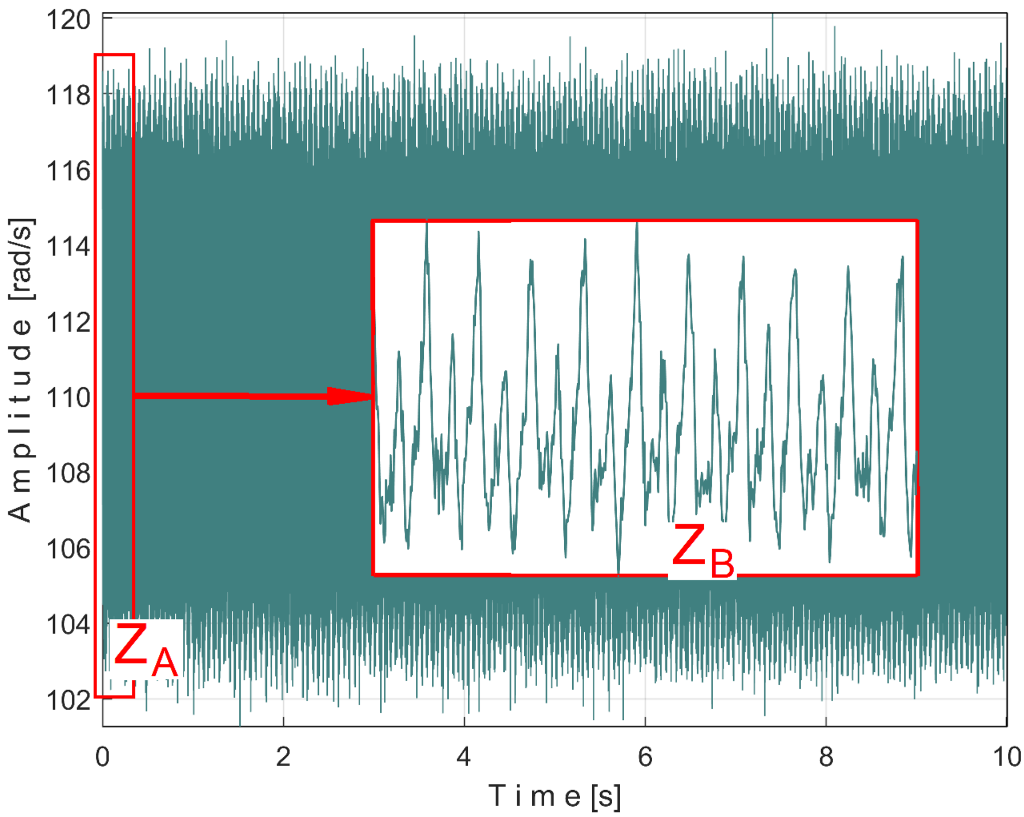

Figure 34. The time-domain representation of the IAS spindle during 10 s of steady-state regime.

A detail from zone Z_A, at the beginning of IAS (with 587 samples, during 5.87 ms), is shown magnified in zone Z_B. A significant variability of the IAS signal is observed (as peak-to-peak amplitude, with a maximum value of 18.87 rad/s) around the mean value of 109.47 rad/s, corresponding to a mean rotation frequency of 109.47/2/π = 17.4227 Hz. This high variability is due to the fact that this AC generator (actually built to be used as a stepper motor) has mechanical and electrical design imperfections and introduces a PVSC related to these imperfections, which is greatly amplified by numerical derivation.

The frequency of the fundamental sine wave of this PVSC is equal to the rotational frequency (period) of the spindle and shaft III. To use EMASS properly (here with a smaller allowed value for m, because the IAS sequence is short), this PVSC should be removed somehow, e.g., using a moving average filter with the number of samples in the average equal to the number of samples per spindle rotation period (here 5739 samples). This means that the pattern generated by the spindle cannot be correctly obtained by EMASS. Figure 35 shows the variable part of the filtered IAS, seen from here onwards as signal s_I .

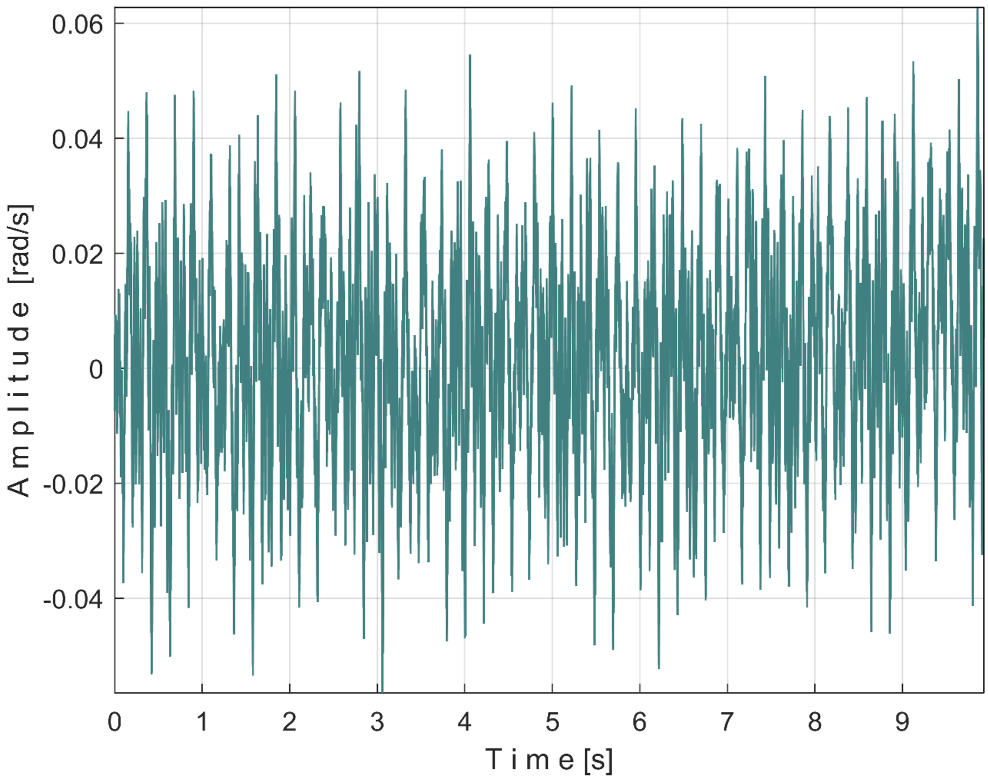

Figure 35. The time-domain representation of variable part of the filtered IAS (s_I) from Figure 34.

Of course, all other PVSC of the signal s_I are affected by this filtering, some with reduced amplitude and others being eliminated. However, some of them can still be detected by EMASS.

Figure 36 shows the partial FFT spectrum of the signal s_I, between 0 and 40 Hz, with 0.100715 Hz resolution.

Surprisingly, this spectrum contains the four fundamental sine waves (A, B, C, and E) and some of their harmonics (B_1, B_2, C_1) of the PVSCs previously highlighted in the active electrical power spectrum (Figure 10) and the vibration signal spectrum (Figure 20). This is the first important argument in favor of using the signal s_I in condition monitoring using EMASS. As can be clearly seen, the fundamental sine wave of PVSC generated by the rotation of the spindle and the shaft III in signal s_I (D in Figures 10 and 20) has been completely eliminated from the s_I spectrum from Figure 36, due to the filtering of the IAS signal performed before.

In the same way as above, the EMASS can be used in the signal processing of the signal s_I to extract the extended patterns of the available PVSC.

Related to the behavior of the first flat belt mirrored in signal s_I (with the fundamental A in Figure 36), Figure 37 shows the superimposed extended unfiltered patterns s_{ITAe5a} (curve 1, m = 25 for 467,075 samples at the beginning of s_I) and s_{ITAe5b} (curve 2, m = 25 for the next 467,800 samples of s_I). The average frequency f_{IA} is slightly different for each pattern: f_{IAa} = 5.40021 Hz for s_{ITAe5a} and f_{IAb} = 5.4107 Hz for s_{ITAe5b}. .

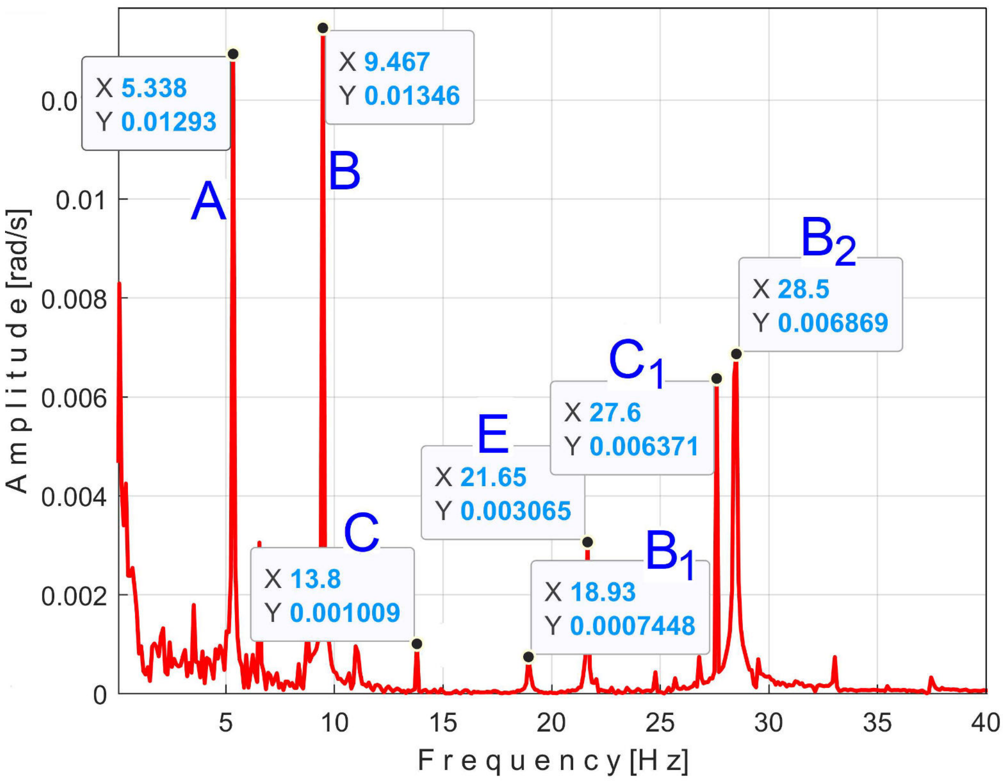

Figure 36. The partial FFT spectrum of signal s_I (0–40 Hz range).

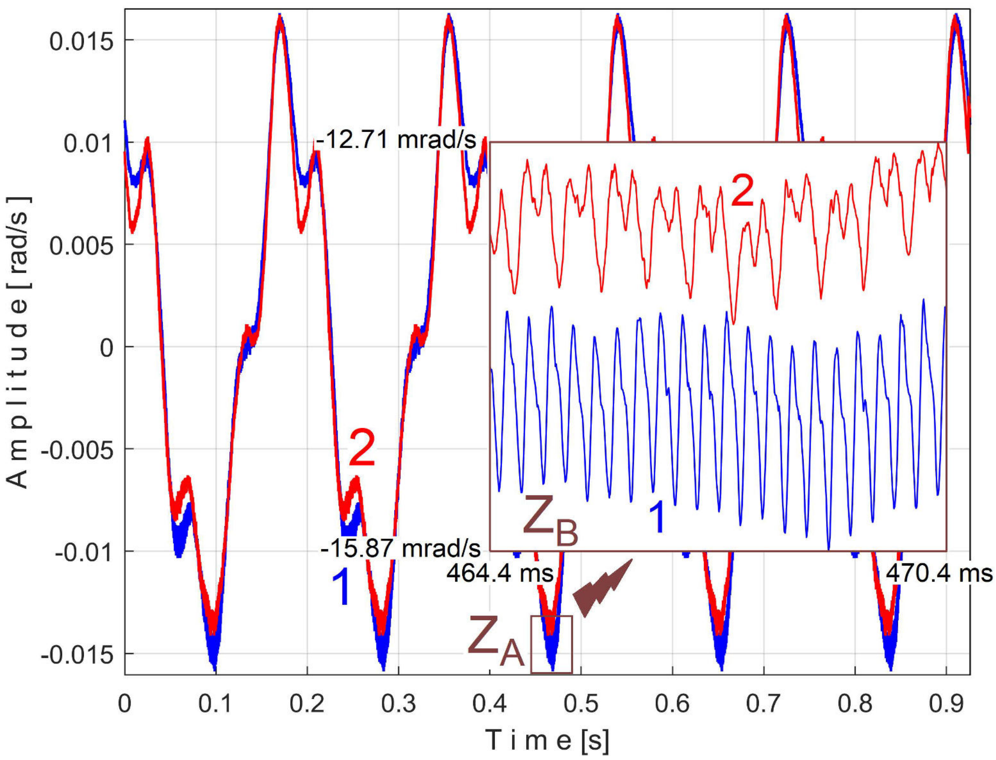

Figure 37. The unfiltered extended patterns (m = 25) describing the behavior of the first flat belt in signal s_I: 1—s_{ITAe5a}, f_{IAa} = 5.40021 Hz; 2—s_{ITAe5b}, f_{IAb} = 5.4107 Hz.

As expected, there is a good match between the two extended patterns. Surprisingly, the PVSC induced by the flat belt in the signal s_I is detected and described by the IAS sensor even if this sensor is placed far away from this belt.

A detail in zone Z_A on Figure 37 is magnified in zone Z_B. One can see here (especially with respect to the pattern s_{ITAe5a}) the existence of a variable signal component, the origin of which will be explained later in the discussion of Figures 38 and 39.

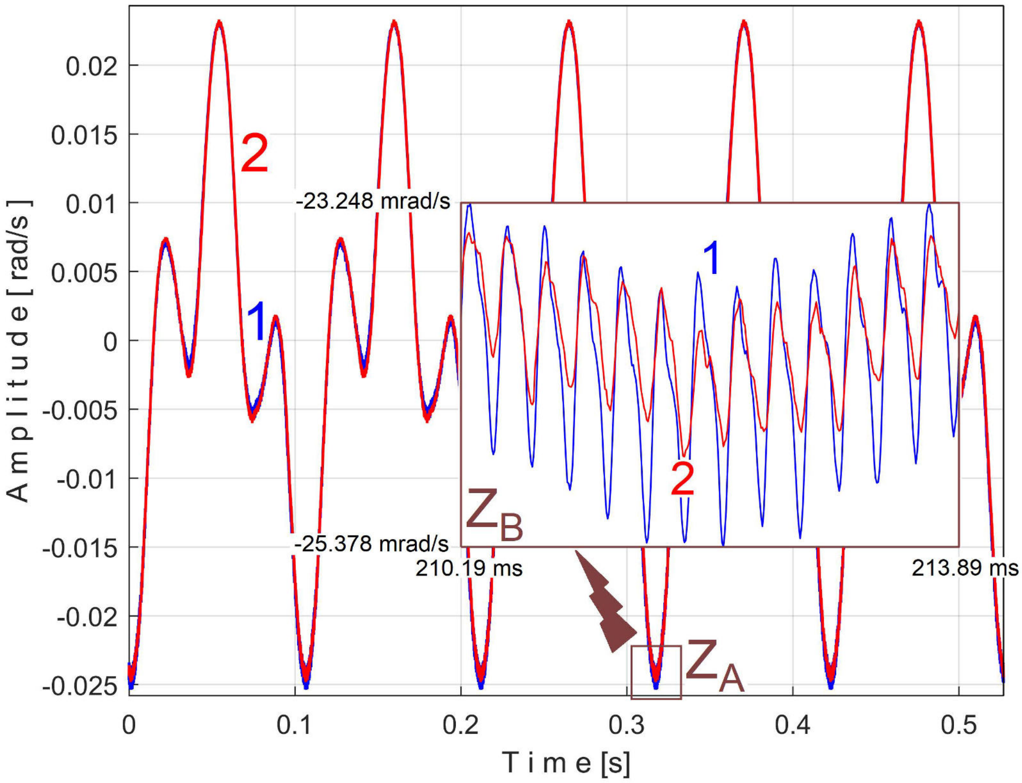

Figure 38. The unfiltered extended patterns (m = 46) describing the behavior of the second flat belt in signal s_I: 1—s_{ITBe5a}, f_{IBa} = 9.48999 Hz; 2—s_{ITBe5b}, f_{IBb} = 9.49061 Hz.

Related to the behavior of the second flat belt mirrored in s_I (with the fundamental B in Figure 36), Figure 38 shows the superimposed extended unfiltered patterns s_{ITBe5a} (curve 1, m = 46 for 484,702 samples at the beginning of s_I) and s_{ITBe5b} (curve 2, m = 46 for the next 484,702 samples of s_I). The average value of the frequency used in EMASS was f_{IBa} = 9.48999 Hz and f_{IBb} = 9.49061 Hz.

A detail from zone Z_A (with 370 samples, during 3.7 ms) is shown magnified in zone Z_B. This is an example of a distortion phenomenon of the extended patterns already anticipated in Section 2 of this paper.

It should be noted that the PVSC generated by spindle and shaft III in the signal s_I has not been completely removed by the IAS filtering; some of its upper harmonics still remain in the signal s_I. Only the fundamental sine wave D of this PVSC has been completely removed, as shown in Figure 36. It was found that the period of the 369th harmonic of the fundamental of the PVSC generated by the second belt (as $T_{IBa}{}^{369} = T_{IBa}/369$ or $T_{IBb}{}^{369}$ $= T_{IBb}/369$) is practically equal to the period of the 201st harmonic of the fundamental of the PVSC generated by the spindle (as $T_{IDa}{}^{201} = T_{IDa}/201$ or $T_{IDb}{}^{201} = T_{IDb}/201$), in other words, $369{\cdot}f_{IBa} \approx 201{\cdot}f_{IDa} \approx 3501.80$ Hz or $369{\cdot}f_{IBb} \approx 201{\cdot}f_{IDb} \approx 3502.035$ Hz. For this reason, the sinusoidal component with period $T_{IDa}{}^{201}$ (or $T_{IDb}{}^{201}$) appears in the extended pattern s_{ITBe5a} (or s_{ITBe5b}) as the false sinusoidal component $T_{IBa}{}^{369}$ (or $T_{IBb}{}^{369}$), as shown in Figure 38 in zone Z_B. Also in these extended patterns appears any other sinusoidal component having the period $T_{IDa}{}^{201}/j \approx T_{IBa}{}^{369}/j$ (or $T_{IDb}{}^{201}/j \approx T_{IBb}{}^{369}/j$).

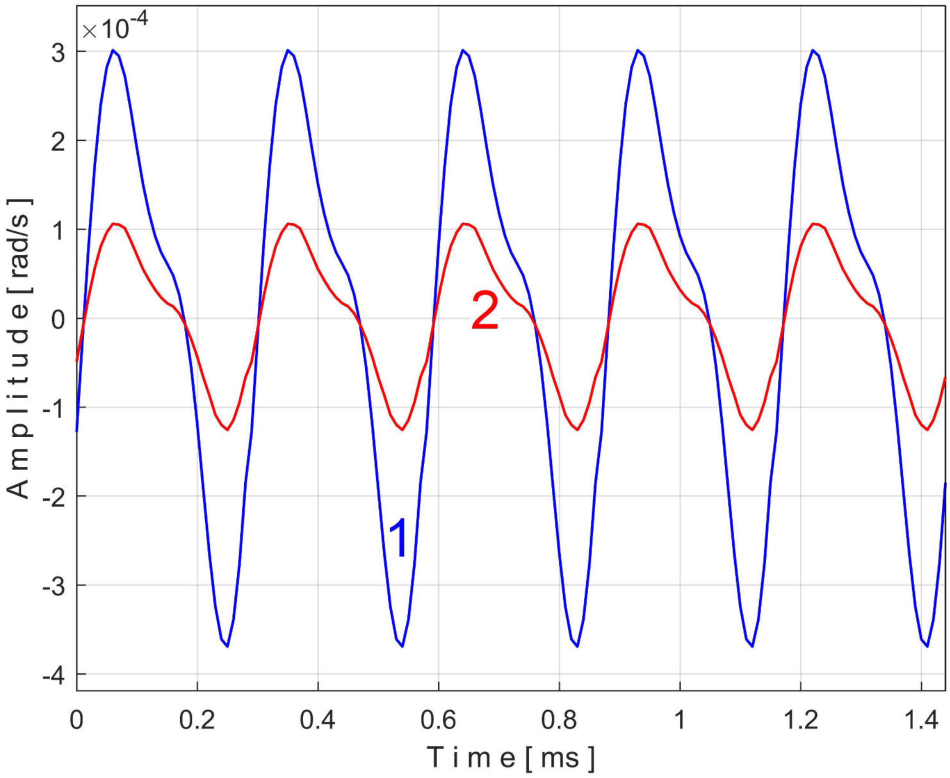

Figure 39. The unfiltered extended patterns (m = 17,100) of the false variable component with periods $T_{IBa}{}^{369}$ and $T_{IBb}{}^{369}$ in signal s_I: 1—$s_{ITB}{}^{369}{}_{e5a}$, $f_{IB}{}^{369}{}_a$ = 3501.7959 Hz; 2—$s_{ITB}{}^{369}{}_{e5b}$, $f_{IB}{}^{369}{}_b$ = 3501.7417 Hz.

Of course, it is possible to find the extended patterns $s_{ITB}{}^{369}{}_{e5a}$ and $s_{ITB}{}^{369}{}_{e5b}$ of the false variable component with the fundamental with very small period $T_{IBa}{}^{369}$ and $T_{IBb}{}^{369}$. These extended patterns (with 145 samples) were each determined with EMASS as before, on almost half the number of samples (495,900) from signal s_I (for m = 17,100), and are shown in Figure 39.

As can be clearly seen in Figure 39, there are some similarities between these patterns (as shapes, not as amplitudes), already found earlier in Figure 38 as shown in region Z_B. We discovered that these false signal variable components, $T_{IDa}{}^{201}$ and $T_{IDb}{}^{201}$, also occur in the s_{ITAe5a} and s_{ITAe5b} extended patterns already revealed in Figure 37 (highlighted in the region Z_B), as having $T_{IAa}{}^{648}$ (or $T_{IAb}{}^{648}$) as harmonics of the fundamental A within the PVSC generated by the flat belt 1.

Related to the behavior of shaft II mirrored in signal s_I (with fundamental C in Figure 36), Figure 40 shows the superimposed extended unfiltered patterns s_{ITCe5a} (as curve 1, m = 68 on 491,776 samples at the beginning of s_I) and s_{ITCe5b} (as curve 2, m = 68 for the next 491,776 samples of signal s_I). The average value of the frequency used in the EMASS was f_{ICa} = 13.826942 Hz and f_{ICb} = 13.79066 Hz. Since there are ten periods on each extended pattern, it is obvious that the amplitude of the first harmonic (described in Figure 36 with the peak C_1) is much bigger than the fundamental sine wave, described in Figure 36 with the peak C.

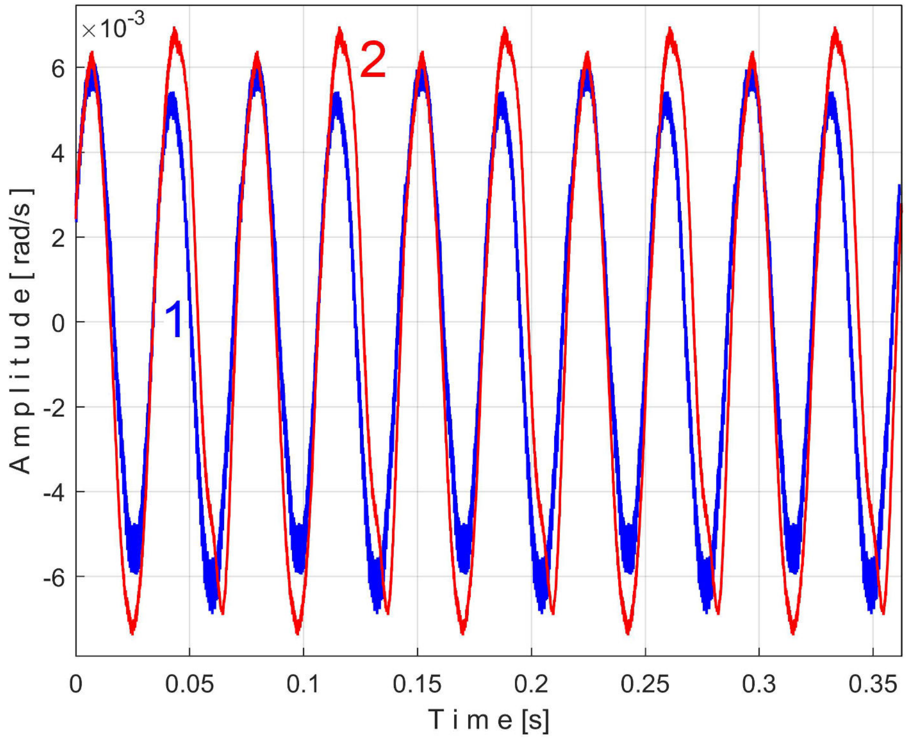

Figure 40. The unfiltered extended patterns (m = 68) describing the behavior of the shaft I in signal s_I: 1—s_{ITCe5a}, f_{ICa} = 13.826942 Hz; 2—s_{ITCe5b}, f_{ICb} = 13.79066 Hz.

Related to the behavior of shaft I mirrored in signal s_I (with fundamental E in Figure 36), Figure 41 shows the superimposed extended unfiltered patterns s_{ITEe5a} (as curve 1, m = 106 for 489,720 samples at the beginning of s_I) and s_{ITEe5b} (as curve 2, m = 106 for the next 489,720 samples of s_I).

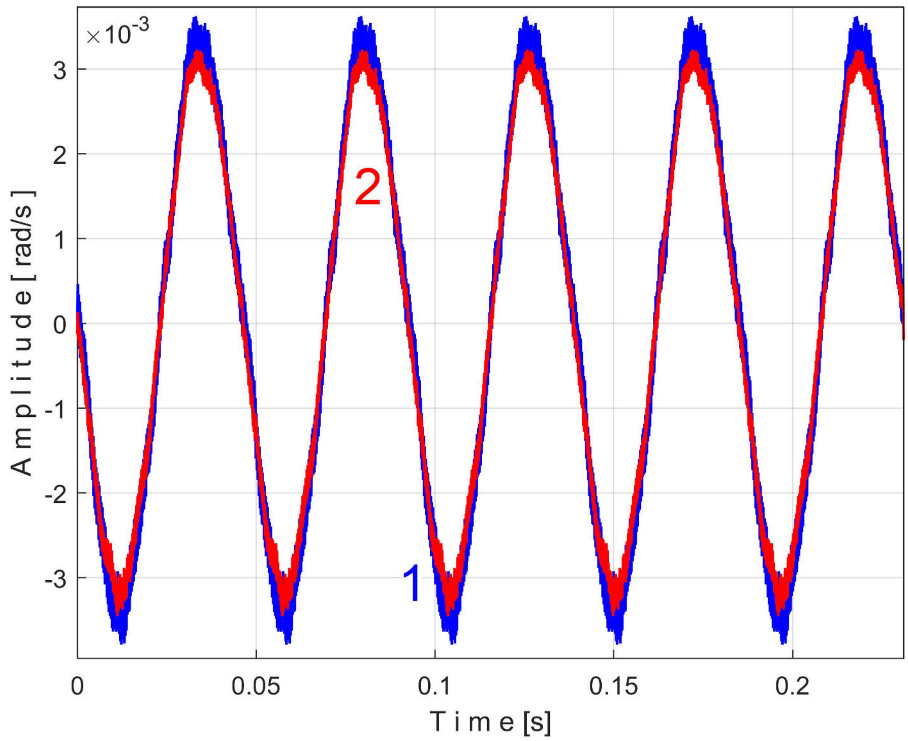

Figure 41. The unfiltered extended patterns (m = 106) describing the behavior of the shaft II in signal s_I: 1—s_{ITEe5a}, f_{IEa} = 21.6422 Hz; 2—s_{ITEe5b}, f_{IEb} = 21.64315 Hz.

The average value of the frequency used in the EMASS was f_{IEa} = 21.6422 Hz and f_{IEb} = 21.64315 Hz. In Figures 40 and 41, false variable components also appear, as described earlier. Eliminating these false variable components in the extended patterns requires a simple approach, such as determining their mathematical description (by curve fitting, as was conducted earlier in Figure 12) and removing them from the PVSC.

The EMASS can be used to process state signals produced by many other types of sensors describing a steady-state regime at idle or during a working process.

4. Discussion

The facilities of numerical description and sampling of the signal sequences generated by the sensors (such as resolution, sampling rate, and number of samples), as well as the facilities for assisted computation, allow their processing by various relatively simple numerical techniques and methods.

Among these techniques, this paper proposes an extraction method by averaging selected samples (EMASS) at regular time intervals as a procedure for determining the pattern of any periodically varying signal component (PVSC) present in state signals during a steady-state regime of a driven mechanical system, which gives interesting experimental results for three different signals: active electrical power, vibration, and instantaneous angular speed. These state signals were provided by appropriately different sensors placed in different locations on a lathe gearbox headstock. The patterns found in these signals using the proposed EMASS characterize the correct or incorrect functioning of mechanical components (MC) of the mechanical system in a steady-state regime, with a constant speed of rotation, and are useful for offline monitoring of their condition.

4.1. A Brief Overview of the Requirements for Pattern Extraction Using EMASS

The computer programs conceived by us in Matlab and only occasionally an application in Matlab (*Curve Fitting Tool*) were used to prepare, apply, and analyze the proposed EMASS. To find the samples of the pattern of any PVSC within the state signal (based on Equation (1)), or the samples of any extended pattern (based on Equation (3)), it is necessary to know:

- The samples of the variable part of the state signal are long enough in duration.
- The exact value of the sampling time (sampling interval) Δt of the numerical description of the state signal is constant and small enough.
- The number of samples of this signal.
- The exact value of period T (or frequency) of the PVSC.
- The number of time intervals is conveniently chosen (m), preferably as large as possible.

The most difficult issue in the application of EMASS is the determination of the exact value of the period T (or frequency) of the PVSC. In our approach, we have defined and validated an efficient method: in a chosen (small) range for the period (frequency) value, we search for the value at which the peak-to-peak amplitude of the resulting pattern found by EMASS is maximal. The range is centered on the approximate value of the period (frequency) of the PVSC given by the FFT spectrum or by the kinematic scheme of the actuated mechanical system. After each search result, the range is narrowed, and the search is repeated a sufficient number of times to obtain the most accurate period (frequency) value.

The efficiency of this method of accurately determining the value of the PVSC period (frequency), which was systematically used in this paper, can be comparatively demonstrated as shown in Figure 42. In the case of the PVSC of the active electric power induced by the first flat belt (Figure 7), the extended pattern s_{PTAe5a} was found (Figure 11, as curve

1, for m = 530, for which the exact frequency f_{PAa} = 5.33748 Hz was determined). This extended pattern is redrawn identically as curve 1 here below, in Figure 42.

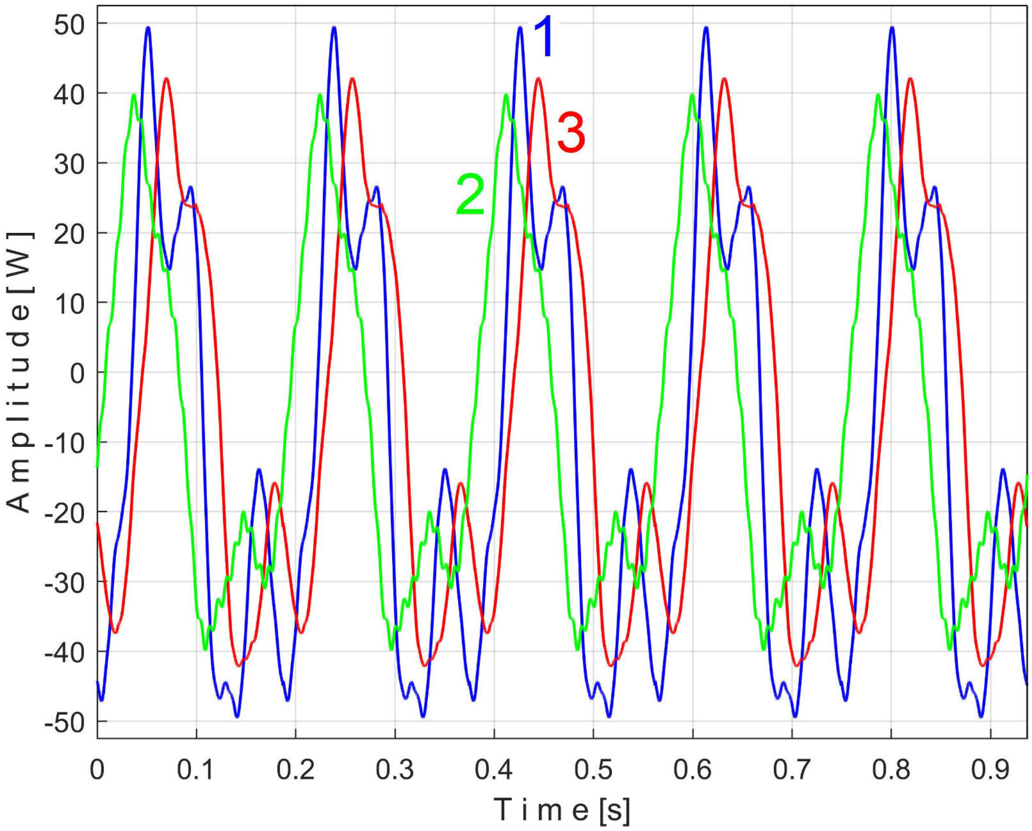

Figure 42. The influence of frequency (period) variation on extended pattern s_{PTAe5a} shape (from Figure 11, m = 530): 1—s_{PTAe5a} (correct frequency f_{PAa} = 5.33748 Hz); 2—$s_{PTAe5a-}$ (deliberately wrong, very slightly lower frequency $f_{PAa\text{-}}$ = 5.335 Hz = f_{Paa} − 0.00248 Hz); 3—$s_{PTAe5a+}$ (deliberately wrong, very slightly higher frequency f_{PAa+} = 5.339 Hz = f_{PAa} + 0.00152 Hz).

In Figure 42, curve 2 shows an extended pattern (as $s_{PTAe5a-}$) under the same condition but determined by EMASS with an intentionally imprecise, very slightly lower frequency (as $f_{PAa\text{-}}$ = 5.335 Hz), and curve 3 shows this extended pattern (as $s_{PTAe5a+}$) but determined by EMASS with an intentionally imprecise, very slightly higher frequency (as f_{PAa+} = 5.339 Hz). The difference between the extended patterns is obvious (also favored by the large value of m), despite the very small changes in frequency. It is obvious that the extended pattern 1, corresponding to the exact frequency, has the largest peak-to-peak amplitude and more accurately describes the behavior of the flat belt 1.

It is important to note that even in the absence of an approximate period (frequency) value of a variable periodic component, it is possible to use the proposed EMASS, starting with a sufficiently large frequency range. The period (frequency) value for a possible PVSC is found to be the period (frequency) that produces a pattern with the largest peak-to-peak amplitude.

When two extended patterns (or extended patterns as well) with obvious similarities that characterize the same variable signal component (at different time instants) are to be compared (by overlapping, e.g., Figure 11, Figure 14, Figure 16, etc.), one of them is taken as the reference, and the other is shifted until the best overlap is obtained. Shifting is accomplished by changing the first sample of the state signal used in the extended pattern determination. Any offset component (or DC bias as well) of the extended pattern should be eliminated.

If the two patterns have relatively large differences in shape, for a correct overlapping, the first sample of the state signal used to find each pattern is shifted so that each pattern starts at the phase origin of its fundamental. This phase origin is converted in zero-crossing time. The description of the phase origin of the fundamental was found using the *Curve Fitting Tool* from Matlab. This technique has been used systematically below to obtain the next figures. A method of curve fitting in Matlab—slower but giving accurate results—has been developed [3] and used by us.

4.2. Consideration on the Capability of Patterns to Reflect Changes of Steady-State Regimes

If these patterns are useful for monitoring, it is expected that as the stationary operating conditions of the gearbox change, the behavior of the various MCs will also change, which will be reflected in the change in shape of these patterns. This assumption is briefly confirmed below. A recording of the time-domain representation of the active electric power (the same number of samples and sampling time as before) has been made for a new steady-state regime characterized by the operation of only the electromotor, the flat belt 1, and the shaft I. All the electromagnetic clutches are disengaged; the shafts II, III, and the spindle do not rotate. Figure 43 shows the extended patterns s_{PTAe5a} (with $m = 530$) generated by the flat belt 1 in the active electrical power during the two steady-state regimes: the extended pattern 1 (from the study above, with all the MC of the gearbox in rotation, a duplication of curve 1 from Figure 11, $f_{PAa} = 5.33748$ Hz) and, with overlap, the extended pattern 2 (for this new gearbox configuration, $f_{PAa} = 5.386069$ Hz). Since the mechanical power transmitted through the belt is lower in the new gearbox configuration, the shape and peak-to-peak amplitude of the extended pattern 2 are significantly different.

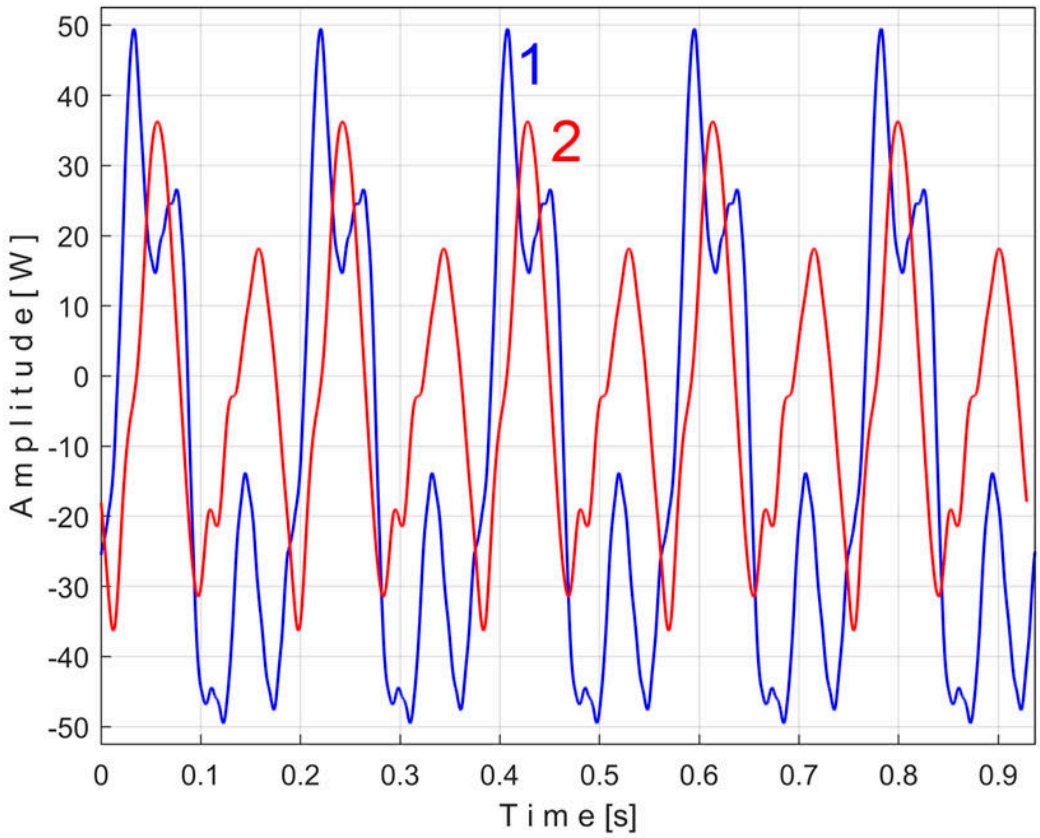

Figure 43. The extended patterns s_{PTAe5a} ($m = 530$): 1—with all the gearbox parts in rotary motion (a copy of curve 1 from Figure 11, $f_{PAa} = 5.33748$ Hz); 2—during the new steady-state regime $f_{PAa} = 5.386069$ Hz.

Similarly, Figure 44 shows the extended patterns s_{PTEe5a} (with m = 2130) produced by the shaft I during the same two compared steady-state regimes: curve 1 (a duplication of curve 1 from Figure 18, f_{PEa} = 21.5606 Hz) and, with overlap, curve 2 (for this new gearbox configuration, f_{PEa} = 21.7923 Hz).

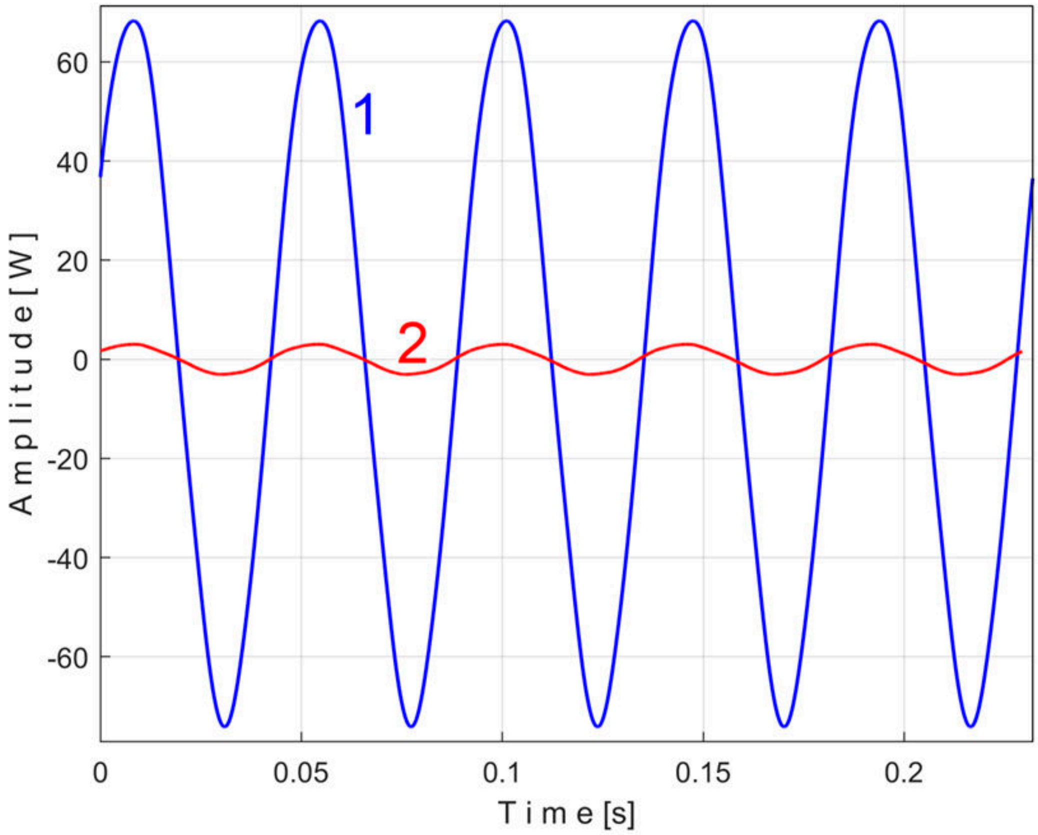

Figure 44. The extended patterns s_{PTEe5a} (m = 2130): 1—with all the gearbox parts in rotary motion (a copy of curve 1 from Figure 18, f_{PEa} = 21.5606 Hz); 2—during the new steady-state regime, f_{PEa} = 21.7923 Hz.

The peak-to-peak amplitudes for the extended pattern 2 are greatly reduced for the same reason: less mechanical power is being transmitted through this shaft in this new gearbox configuration.

4.3. On the Capability of EMASS to Extract Patterns of PVSC of Small Amplitude

This capability has already been fully demonstrated experimentally in the case of the analysis of the signal s_V describing the vibration (the patterns from Figures 29–31), but also in the case of the analysis of the signal s_I describing the variable part of the filtered instantaneous angular speed (the patterns from Figures 38 and 39).

It can be shown that the proposed EMASS can also detect patterns of small amplitude PVSC in the s_P signal. Thus, the extended pattern of PVSC generated by the electric motor in the s_P signal could be detected as a time domain representation (s_{PTMe5}) with the gearbox in the configuration shown in Figure 7. The value of the frequency of the fundamental sine wave within PVSC was sought between 24 and 25 Hz. The EMASS applied to the first half of the signal s_P produced an extended pattern (as s_{PTMe5a} with m = 2465, f_{PMa} = 24.69481 Hz) drawn as curve 1 in Figure 45; the second half produced an extended pattern (as s_{PTMe5b} with m = 2465, f_{PMa} = 24.712903 Hz), drawn as curve 2 in Figure 45. Each extended pattern starts at a zero-crossing moment of its fundamental.

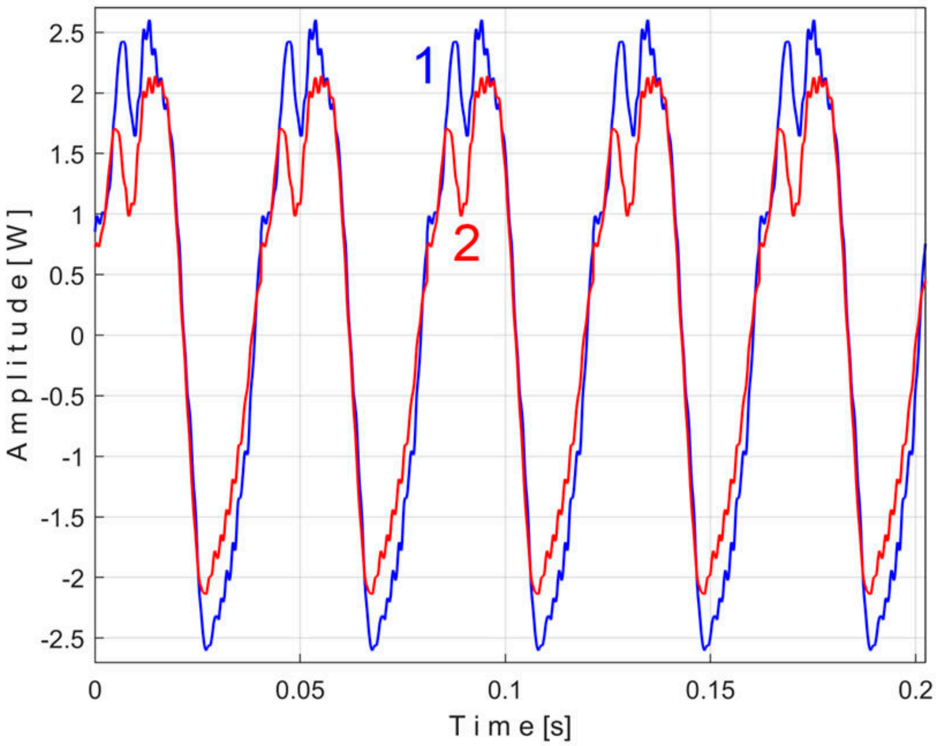

Figure 45. The extended patterns s_{PTMe5} generated by electric motor (m = 2465) during first steady-state regime: 1—s_{PTMe5a}, f_{PMa} = 24.69481 Hz; 2—s_{PTMe5b}, f_{PMb} = 24.712903 Hz.

Figure 46 describes similarly the extended patterns of PVSC generated by the motor during the new configuration of the gearbox (only the motor, the flat belt 1, and the shaft I in rotary motion).

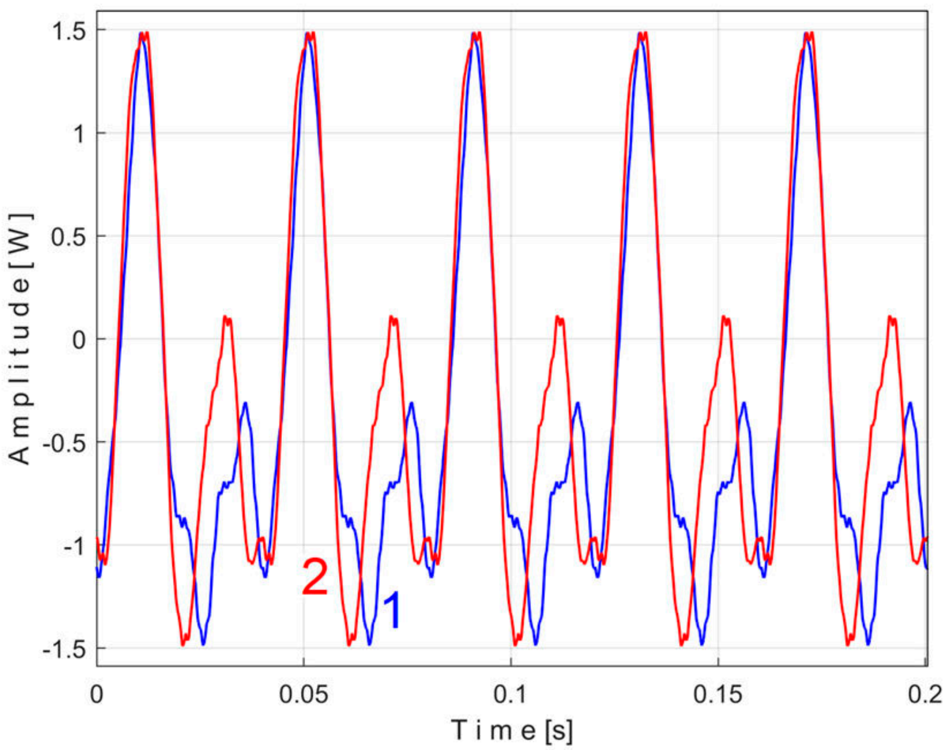

Figure 46. The extended patterns s_{PTMe5} generated by electric motor (m = 2465) during the new steady-state regime: 1—s_{PTMe5a}, f_{PMa} = 24.91988 Hz; 2—s_{PTMe5b}, f_{PMb} = 24.93528 Hz.

As can be clearly seen, there are relatively good similarities between these extended patterns 1 and 2 drawn in Figures 45 and 46. The differences are probably due to heating during operation (the patterns 1 are generated by analyzing 100 s of the status signal; the patterns 2 are generated by analyzing the next 100 s of the status signal).

4.4. On the Capability of the EMASS to Detect Patterns for High-Frequency (Small Period) PVSC

This capability has already been fully demonstrated before in the analysis of the vibration signal s_V (as shown in Figures 28–31) and instantaneous angular speed signal s_I (as shown in Figures 37–39). Since the active electrical power is defined as a result of low-pass numerical filtering of the instantaneous electrical power, the high-frequency variable components are not available inside the signal s_P.

There is an interesting reason why the vibration description signal is best suited for the pattern-based research of high-frequency periodic variable components: the sensor used is a generator type that provides at its output an electric voltage s_V proportional to the derivative (velocity) of the vibratory motion of the support on which it is placed. This derivative favors the description of high-frequency components (greatly increasing their amplitude). The use of an accelerometer would be even more appropriate since it provides a voltage proportional to the second derivative of the vibratory motion.

For a better utilization of the proposed EMASS in this regard, the conversion rate of the signal being studied (e.g., s_V) must necessarily be greatly increased. Because of the relatively low sampling rate used in our research (25,000 samples per second for s_P and s_V signals), the extended patterns in Figure 30 contain only 38 samples per period.

4.5. A Summary of the Benefits of Using EMASS

The main advantage of the proposed EMASS is the obtaining, by numerical calculation, a pattern characterizing the functioning of any rotating mechanical component of the mechanical system operating in the steady-state regime, associated with its rotation period. Compared to a considered reference pattern, its changes over time (due to wear, failure, or change of operating conditions) can be used for offline condition monitoring of the MC.

Characterization patterns of PVSC using EMASS can be determined from signals generated by any type of sensor capable of describing fast phenomena. In our work, we have exemplified signals describing active electrical power, vibration, and instantaneous angular velocity.

Each pattern found by EMASS is, in fact, a sum of sinusoidal components with a fundamental and several harmonics. After being determined by EMASS, each pattern can be extended and partially described with amplitudes and frequencies of its sinusoidal components by FFT analysis (e.g., according to Figure 21), or fully described analytically using the *Curve Fitting Tool* application in Matlab (e.g., according to Figure 12 and Table 2) or any other curve fitting procedure applied to the pattern. The EMASS provides a synthetic description of a pattern (through the coordinates of its points), while a curve-fitting procedure provides an analytical description of this pattern with a formula, as a sum of sinusoidal components, giving the values of amplitude, frequency, and the phase of the time origin of each one. The condition of an MC, or the anomalies in its operation, can be evaluated in two different stages: first, roughly, relatively quickly, based on the shape and peak-to-peak amplitude of its pattern; second, more precisely, based on the analytical description of the fundamental sinusoidal components or/and their harmonics. The evaluation result in each stage can be provided automatically by a computer.

It should be mentioned that obtaining the analytical description of the pattern of an MC can also be conducted directly, by analyzing the state signal with the Curve Fitting Tool application, and not by analyzing the synthetic description of the pattern provided by EMASS, as proposed in this paper. Unfortunately, the direct analysis of the state signal (already proposed in [3]) is very difficult, time-consuming, and subject to possible errors. This is because the operation with the Curve Fitting Tool application usually assumes that the sinusoidal components that could belong to a pattern are automatically searched and selected not by their harmonic frequency correlation but by the value of the amplitudes, descending from the largest to the smallest.

We believe that the monitoring and diagnosis based on the study of EMASS patterns have the advantage of being easy to implement and apply in the automotive industry, in manufacturing systems, and, in general, in any work process supported by mechanical systems. Our research has reached the stage of experimental validation in the laboratory. For the future, we are preparing the practical application and the formulation of some appropriate industrial implementation strategies.

4.6. Some Shortcomings of Using the Proposed EMASS

The first major shortcoming in the application of the proposed EMASS is that it cannot automatically identify and eliminate false components within the patterns. Two PVSCs with periods T_1 and T_2 (or with fundamental frequencies of $1/T_1$ and $1/T_2$) may have interferences of their harmonics, e.g., the i^{st} harmonic for T_1 and the j^{st} harmonic for T_2, if $T_1/i = T_2/j$. The proposed EMASS finds (incorrectly) the harmonic with period T_1/i described in the pattern of the component with period T_2 and (also incorrectly) the harmonic with period T_2/j described in the pattern of the component with period T_1. This shortcoming has already been highlighted in the comments to Figure 38. Of course, this shortcoming is also present when other signal component analysis techniques, such as FFT, are in use.

If the period T of the VPSC whose pattern is to be extracted is not constant and varies very slightly (as systematically happens in our experiments), then a second major shortcoming arises: the shape and peak-to-peak amplitude of the pattern depend strongly on the value of m. The larger m is, the smaller this amplitude will be (and the upper harmonics of the pattern will be greatly attenuated). This phenomenon has already been observed in Figure 31 (where the $T_{VC}{}^{48}$ plays the role of T). In this situation also a third shortcoming occurs: a correct pattern extraction requires the exact determination of the average period (frequency) on each analyzed sequence of the state signal.

Unfortunately, the use of small values of m introduces the fourth shortcoming, which is highlighted in Figure 47. It shows the extended pattern $s_{PTDe5a1}$ of the VPSC obtained by EMASS generated by the shaft III and the spindle in the signal s_P extracted from the first twenty T_{PDa1} periods (curve 1, m = 20, f_{PDa1} = 17.35793 Hz) and a similar pattern, $s_{PTDe5a2}$, extracted from the first 100 T_{PDa2} periods (curve 2, m = 100, f_{DPa2} = 17.3638 Hz).

A detail from zAA detail from zone Z_A is shown in zone Z_B. In zone Z_B an abnormal jump (discontinuity) can be observed on both curves, in zone Z_C. The smaller the m is, the larger the jump will be. This means that the patterns over a period are incorrectly described; the ordinate of the last sample of the current period (here the second in Z_A) of the extended pattern is very different from the ordinate of the first sample of the next period (here the third in Z_A). In other words, a period of the extended pattern is incorrectly defined; it does not begin and end with points that have very close, almost identical ordinates. We should note that, in fact, this jump exists in all the patterns presented so far, but because a high value of m is practically negligible.

It is obvious that the value of m should be as large as possible. It is also obvious that a large value of m distorts the shape of the VPSC pattern when its frequency is slightly variable. This disadvantage is partially eliminated if the monitoring and diagnosis are limited to the comparison of two patterns of the same VPSC generated by an MC under the same operating conditions at different times, with the patterns extracted using EAMSS mandatory with m having the same value. This was conducted systematically in this study.

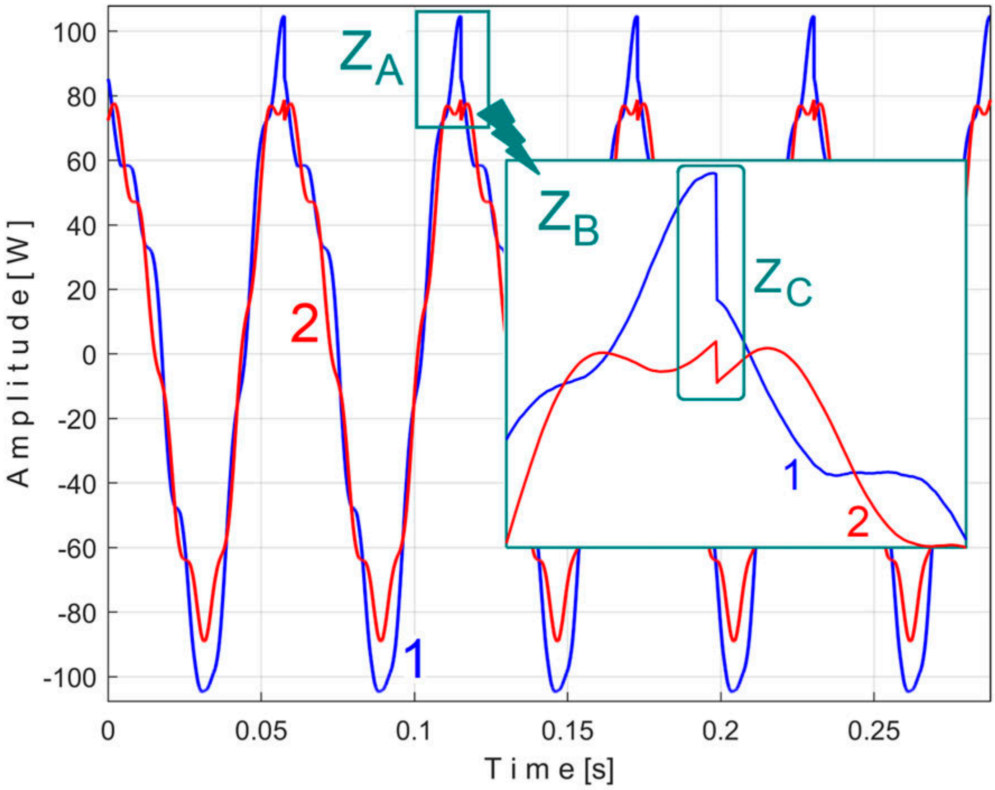

Figure 47. The extended patterns describing the behavior of the shaft III and spindle in signal s_P (using small values of m) are 1—$s_{PTDe5a1}$ (m = 20, f_{PDa1} = 17.35793 Hz) and 2—$s_{PTDe5a2}$ (m = 100, f_{PDa2} = 17.3638 Hz).

As already mentioned, a correct and complete description of the patterns (especially those with a short fundamental period) implies the need to use a sampling rate (frequency) as high as possible in the numerical description of the analyzed state signal. A higher resolution of the numerical signal (in our research, the resolution expressed in bits is 12) is also useless.

4.7. Future Research Directions

Firstly, we intend to find a method of improving the accuracy of patterns for the situation when the period of the fundamental of VPSC is slightly variable. In other words, to reduce the negative influence of high values of m on the shape of the pattern.

Second, we want to investigate whether numerical resampling of the state signals increases the accuracy of the extracted patterns. In other words, to change the value of the sampling time Δt for each PVSC (by resampling) such that the ratio $T/\Delta t$ is an integer, regardless of the value of T.

In a future approach, we aim to extract patterns by EMASS using very high sampling rates of signals, especially in vibration signals (as they are the easiest to acquire). The vibration description signals have several important advantages: they are easy to obtain using simple sensors, they provide signals less affected by attenuation or distortion phenomena (compared to the active electrical power), and they do not introduce significant measurement anomalies (compared to the instantaneous angular speed). We want to obtain highly reliable patterns describing the condition of some other MCs (e.g., bearings, gears, etc.) or even cutting tools during a working process of machine tools (e.g., for milling tools, with patterns that characterize the involvement of each tooth of the tool in the cutting process).

We also intend to highlight the research resources offered by the application EMASS to any state signal containing PVSC and, in particular, to reveal and investigate the patterns in instantaneous electrical power absorbed by the drive motors used to actuate mechanical systems. The description signal of the active electrical power (used until now, coming from the low-pass filtering of the instantaneous electrical power) has some limitations: it strongly attenuates (or even eliminates) the higher harmonics.

We also propose to investigate how to reduce the vulnerability to noise for small peak-to-peak amplitude patterns.

Author Contributions: Conceptualization, A.M., M.H., C.G.D. and N.-E.B.; methodology, M.H., A.M., C.G.D. and N.-E.B.; software M.H., A.M., C.G.D. and D.-F.C.; validation M.H., A.M. and C.G.D.; investigation, A.M., M.H., C.-G.M., M.K., N.-E.B. and L.O.; resources, C.G.D., D.-F.C. and A.M.; data curation, M.H., A.M., C.G.D., C.-G.M., N.-E.B. and D.-F.C.; writing—original draft preparation, A.M., M.H., N.-E.B., C.-G.M., D.-F.C., M.K., L.O. and C.G.D.; writing-review and editing A.M., M.H., D.-F.C., N.-E.B., C.G.D. and C.-G.M.; supervision and project administration, M.H. and A.M.; funding acquisition, D.-F.C., A.M. and C.G.D. All authors have read and agreed to the published version of the manuscript.

Funding: This work was funded by the “National Research Grants—ARUT” projects of the Technical University “Gheorghe Asachi” of Iasi, Romania, project number GnaC2023_269.

Institutional Review Board Statement: Not applicable.

Informed Consent Statement: Not applicable.

Data Availability Statement: The data presented in this paper are available upon request and addressed to the corresponding author.

Conflicts of Interest: The authors declare no conflicts of interest.

References

1. Stojanović, V. Fast Fourier Transform: Theory and Algorithms. Massachusetts Institute of Technology. Available online: https://ocw.mit.edu/courses/6-973-communication-system-design-spring-2006/49a17bd0078f7723100ac1395a476595_lecture_8.pdf (accessed on 4 February 2025).
2. Ruetsch, G.; Fatica, M. Applications of the Fast Fourier Transform. In *CUDA Fortran for Scientists and Engineers*, 2nd ed.; Ruetsch, G., Fatica, M., Eds.; Morgan Kaufmann: Burlington, MA, USA, 2024; pp. 154–196.
3. Horodinca, M.; Bumbu, N.-E.; Chitariu, D.-F.; Munteanu, A.; Dumitras, C.G.; Negoescu, F.; Mihai, C.-G. On the Behaviour of an AC Induction Motor as Sensor for Condition Monitoring of Driven Rotary Machines. *Sensors* **2023**, *23*, 488. [CrossRef] [PubMed]
4. Gangsar, P.; Tiwari, R. Signal Based Condition Monitoring Techniques for Fault Detection and Diagnosis of Induction Motors: A State-of-the-Art Review. *Mech. Syst. Signal Process.* **2020**, *144*, 106908. [CrossRef]
5. Irfan, M.; Saad, N.; Ibrahim, R.; Asirvadam, V.S. Condition Monitoring of Induction Motors via Instantaneous Power Analysis. *J. Intell. Manuf.* **2017**, *28*, 1259–1267. [CrossRef]
6. Jalayer, M.; Orsenigo, C.; Vercellis, C. Fault Detection and Diagnosis for Rotating Machinery: A Model Based on Convolutional LSTM, Fast Fourier and Continuous Wavelet Transforms. *Comput. Ind.* **2021**, *125*, 103378. [CrossRef]
7. Al-Badour, F.; Sunar, M.; Cheded, L. Vibration Analysis of Rotating Machinery Using Time-frequency Analysis and Wavelet Techniques. *Mech. Syst. Signal Process.* **2011**, *25*, 2083–2101. [CrossRef]
8. Polikar, R. The Engineer’s Ultimate Guide to Wavelet Analysis. The Wavelet Tutorial. Rowan University, College of Engineering, USA. Available online: https://cseweb.ucsd.edu/~baden/Doc/wavelets/polikar_wavelets.pdf (accessed on 4 January 2025).
9. Debnath, L.; Ahmad Shah, F. *Wavelet Transforms and Their Applications*, 2nd ed.; Birkhäuser: Basel, Switzerland, 2015.
10. The Wavelet Transform. Available online: http://mhmc.csie.ncku.edu.tw/web_tw/courses/dsp113fall/Ch10_Wavelet-Supplementary-2024.pdf (accessed on 4 February 2025).
11. Yan, R.; Shang, Z.; Xu, H.; Wen, J.; Zhao, Z.; Chen, X.; Gao, R.X. Wavelet transform for rotary machine fault diagnosis:10 years revisited. *Mech. Syst. Signal Process.* **2023**, *200*, 110545. [CrossRef]

12. Liang, B.; Iwnicki, S.D.; Zhao, Y. Application of Power Spectrum, Cepstrum, Higher Order Spectrum and Neural Network Analyses for Induction Motor Fault Diagnosis. *Mech. Syst. Signal Process.* **2013**, *39*, 342–360. [CrossRef]
13. Shi, Z.; Yang, X.; Li, Y.; Yu, G. Wavelet-based Synchroextracting Transform: An Effective TFA Tool for Machinery Fault Diagnosis. *Control Eng. Pract.* **2021**, *114*, 104884. [CrossRef]
14. Baydar, N.; Ball, A. Detection of Gear Failures via Vibration and Acoustic Signals Using Wavelet Transform. *Mech. Syst. Signal Process.* **2003**, *17*, 787–804. [CrossRef]
15. Naganarasaiah Goud, K.; Rakshitha, C.; Sahitya, K.; Naresh Babu, B.; Naveen, C. Design and Performance Analysis of Multi-Band Band Pass Filter Using Meander-Line Resonator. In Proceedings of the 6th International Conference on Communications and Cyber Physical Engineering, ICCCE 2023, Hyderabad, India, 28–29 April 2023; Kumar, A., Mozar, S., Eds.; Lecture Notes in Electrical Engineering. Springer: Singapore, 2024; Volume 1096. [CrossRef]
16. Randall, R.B. A History of Cepstrum Analysis and its Application to Mechanical Problems. *Mech. Syst. Signal Process.* **2017**, *107*, 3–19. [CrossRef]
17. Randall, R.B.; Antoni, J.; Smith, W.A. A Survey of the Application of the Cepstrum to Structural Modal Analysis. *Mech. Syst. Signal Process.* **2019**, *118*, 716–741. [CrossRef]
18. Yao, P.; Wang, J.; Zhang, F.; Li, W.; Lv, S.; Jiang, M.; Jia, L. Intelligent Rolling Bearing Imbalanced Fault Diagnosis Based on Mel-Frequency Cepstrum Coefficient and Convolutional Neural Networks. *Measurement* **2022**, *205*, 112143. [CrossRef]
19. Liu, Y.; Jiang, Z.; Haizhou, H.; Xiang, J. Asymmetric Penalty Sparse Model Based Cepstrum Analysis for Bearing Fault Detections. *Appl. Acoust.* **2020**, *165*, 107288. [CrossRef]
20. Morariu, A.R.; Wictor Lund, W.; Björkqvist, J. Engine Vibration Anomaly Detection in Vessel Engine Room. *IFAC-PapersOnLine* **2022**, *55*, 465–469. [CrossRef]
21. Brandt, A.; Manzoni, S. *Introduction to Spectral and Correlation Analysis: Basic Measurements and Methods, In Handbook of Experimental Structural Dynamics*; Allemang, R., Avitabile, P., Eds.; Springer: New York, NY, USA, 2020.
22. Antoni, J.; Xin, G.; Hamzaoui, N. Fast Computation of the Spectral Correlation. *Mech. Syst. Signal Process.* **2017**, *92*, 248–277. [CrossRef]
23. Cottone, G.; Di Paola, M. A New Representation of Power Spectral Density and Correlation Function by Means of Fractional Spectral Moments. *Probab. Eng. Mech.* **2010**, *25*, 348–353. [CrossRef]
24. Shevgunov, T.; Efimov, E.; Guschina, O. Estimation of a Spectral Correlation Function Using a Time-Smoothing Cyclic Periodogram and FFT Interpolation—2N-FFT Algorithm. *Sensors* **2023**, *23*, 215. [CrossRef] [PubMed]
25. Xiao, C.; Tang, H.; Ren, Y.; Xiang, J.; Kumar, A. A Fault Frequency Bands Location Method Based on Improved Fast Spectral Correlation to Extract Fault Features in Axial Piston Pump Bearings. *Measurement* **2021**, *171*, 108734. [CrossRef]
26. Miao, H. Adaptive Filter Design for Cyclostationary Processes Associated with Sine-wave Extraction Operation. *Digital Signal Process.* **2024**, *154*, 104698. [CrossRef]
27. Wang, Z.; Li, H.; Feng, G.; Zhen, D.; Gu, F.; Ball, A.D. An Enhanced Cyclostationary Method and its Application on the Incipient Fault Diagnosis of induction Motors. *Measurement* **2023**, *221*, 113475. [CrossRef]
28. Liu, T.; Li, L.; Noman, K.; Li, Y. Local Maximum Instantaneous Extraction Transform Based on Extended Autocorrelation Function for Bearing Fault Diagnosis. *Adv. Eng. Inf.* **2024**, *61*, 102487. [CrossRef]
29. Cai, B.; Zhang, L.; Tang, G. Encogram: An Autonomous Weak Transient Fault Enhancement Strategy and its Application in Bearing Fault Diagnosis. *Measurement* **2023**, *206*, 112333. [CrossRef]
30. Jaafar, K.; Alsalaet, J.K. Fast Averaged Cyclic Periodogram Method to Compute Spectral Correlation and Coherence. *ISA Trans.* **2022**, *129 Pt B*, 609–630. [CrossRef]
31. Bishop, C.M. *Pattern Recognition and Machine Learning*; Springer: Singapore, 2006.
32. Little, M.A. *Machine Learning for Signal Processing: Data Science, Algorithms, and Computational Statistics*; Oxford University Press: Oxford, UK, 2019.
33. Kelleher, J.D.; Mac Namee, B.; D'Archy, A. *Fundamentals of Machine Learning for Predictive Data Analytics*; The MIT Press: Cambridge, MA, USA, 2015.
34. Burkov, A. The Hundred-Page Machine Learning Book. 2019. Available online: https://www.amazon.com/Hundred-Page-MachineLearning-Book/dp/199957950X (accessed on 4 February 2025).
35. Schmidhuber, J. Deep Learning in Neural Networks: An Overview. *Neural Netw.* **2015**, *61*, 85–117. [CrossRef] [PubMed]
36. Daga, A.P.; Garibaldi, L. Diagnostics of Rotating Machinery through Vibration Monitoring: Signal Processing and Pattern Analysis. *Appl. Sci.* **2024**, *14*, 9276. [CrossRef]
37. Fu, S.; Wu, Y.; Wang, R.; Mao, M. A Bearing Fault Diagnosis Method Based on Wavelet Denoising and Machine Learning. *Appl. Sci.* **2023**, *13*, 5936. [CrossRef]
38. Liang, R.; Ran, W.; Chen, Y.; Zhu, R. Fault Diagnosis Method for Rotating Machinery Based on Multi-scale Features. *Chin. J. Mech. Eng.* **2023**, *36*, 141. [CrossRef]

39. Keleşoğlu, C.; Küçük, H.; Demetgül, M. Fault Diagnosis of Bevel Gears Using Neural Pattern Recognition and MLP Neural Network Algorithms. *Int. J. Precis. Eng. Manuf.* **2020**, *21*, 843–856. [CrossRef]
40. Cui, L.; Yao, T.; Zhang, Y.; Gong, X.; Kang, C. Application of Pattern Recognition in Gear Faults Based on the Matching Pursuit of a Characteristic Waveform. *Measurement* **2017**, *104*, 212–222. [CrossRef]
41. Bie, F.; Bie, F.; Zhang, Y.; Zhang, Y.; Zhang, Y.; Zhang, Y.; Li, Q.; Li, Q.; Ding, X.; Ding, X.; et al. Research on Compound Fault Pattern Recognition of Rotor System Based on Grid Search VMD Parameters Combined with RCMDE-Relief-F-GRNN. *J. Mech. Sci. Technol.* **2024**, *38*, 5899–5912. [CrossRef]
42. Choudhary, A.; Goyal, D.; Shimi, S.L.; Akula, A. Condition Monitoring and Fault Diagnosis of Induction Motors: A Review. *Arch. Comput. Methods Eng.* **2019**, *26*, 1221–1238. [CrossRef]
43. Shao, S.-Y.; Sun, W.-J.; Yan, R.-Q.; Wang, P.; Gao, R.X. A Deep Learning Approach for Fault Diagnosis of Induction Motors in Manufacturing. *Chin. J. Mech. Eng.* **2017**, *30*, 1347–1356. [CrossRef]
44. Kirankumar, M.; Rajeshwari, N.; Kumari, P.; Raghavendra, B.K.; Vyankatesh, K.S. Fault Diagnosis in Belts Using Signal Processing Techniques and Machine Learning. In Proceedings of the Intelligent Systems in Computing and Communication, First International Conference, ISCComm 2023, Moodabidri, India, 8–9 December 2023; Proceedings, Part I; Shreekumar, T., Dinesha, L., Sreeja, R., Eds.; Communications in Computer and Information Science; Springer: Cham, Switzerland, 2025; Volume 2231. [CrossRef]
45. Sener, B.; Ugur Gudelek, M.; Murat Ozbayoglu, A.; Ozgur Unver, H. A Novel Chatter Detection Method for Milling Using Deep Convolution Neural Networks. *Measurement* **2021**, *182*, 109689. [CrossRef]
46. Ntemi, M.; Paraschos, S.; Karakostas, A.; Gialampoukidis, I.; Vrochidis, S.; Kompatsiaris, I. Infrastructure Monitoring and Quality Diagnosis in CNC Machining: A Review. *CIRP J. Manuf. Sci. Technol.* **2022**, *38*, 631–649. [CrossRef]
47. Lamraoui, M.; Thomas, M.; El Badaoui, M.; Girardin, F. Indicators for Monitoring Chatter in Milling Based on Instantaneous Angular Speeds. *Mech. Syst. Signal Process.* **2014**, *44*, 72–85. [CrossRef]
48. Seong, S.T.; Jo, K.T.; Lee, Y.M. Cutting Force Signal Pattern Recognition Using Hybrid Neural Network in End Milling. *Trans. Nonferrous Met. Soc. China* **2009**, *19* (Suppl. S1), s209–s214. [CrossRef]
49. Bousaleh, G.; Darwiche, M.; Hassoun, F. Pattern Recognition Techniques Applied to Electric Power Signal Processing. *Int. J. Eng. Innov. Technol.* **2013**, *2*, 43–49.
50. Soualhi, M.; Nguyen, K.T.P.; Medjaher, K. Pattern Recognition Method of Fault Diagnostics Based on a New Health Indicator for Smart Manufacturing. *Mech. Syst. Signal Process.* **2020**, *142*, 106680. [CrossRef]
51. Chitariu, D.-F.; Horodinca, M.; Mihai, C.-G.; Bumbu, N.-E.; Dumitras, C.G.; Seghedin, N.-E.; Edutanu, F.-D. Condition Monitoring of a Three-Phase AC Asynchronous Motor Based on the Analysis of the Instantaneous Active Electrical Power in No-Load Tests. *Appl. Sci.* **2024**, *14*, 6124. [CrossRef]
52. Horodinca, M.; Chifan, F.; Paduraru, E.; Dumitras, C.G.; Munteanu, A.; Chitariu, D.-F. A Study of 2D Roughness Periodical Profiles on a Flat Surface Generated by Milling with a Ball Nose End Mill. *Materials* **2024**, *17*, 1425. [CrossRef]
53. Horodinca, M.; Ciurdea, I.; Chitariu, D.F.; Munteanu, A.; Boca, M. Some Approaches on Instantaneous Angular Speed Measurement Using a Two-phase n Poles AC Generator as Sensor. *Measurement* **2020**, *157*, 107636. [CrossRef]
54. Smith, S.W. Moving Average Filters. In *The Scientist and Engineer's Guide to Signal Processing*; California Technical Publishing: San Diego, CA, USA, 1999.
55. Chitariu, D.-F.; Negoescu, F.; Horodinca, M.; Dumitras, C.G.; Dogan, G.; Ilhan, M. An Experimental Approach on Beating in Vibration Due to Rotational Unbalance. *Appl. Sci.* **2020**, *10*, 6899. [CrossRef]
56. Zhao, M.; Jia, X.; Lin, J.; Lei, Y.; Lee, J. Instantaneous Speed Jitter Detection Via Encoder Signal and its Application for the Diagnosis of Planetary Gearbox. *Mech. Syst. Signal Process.* **2018**, *98*, 16–31. [CrossRef]

materials

Article

A Study of 2D Roughness Periodical Profiles on a Flat Surface Generated by Milling with a Ball Nose End Mill

Mihaita Horodinca *, Florin Chifan, Emilian Paduraru, Catalin Gabriel Dumitras , Adriana Munteanu and Dragos-Florin Chitariu

Digital Manufacturing Systems Department, Gheorghe Asachi Technical University of Iasi, 700050 Iasi, Romania; florin.chifan@academic.tuiasi.ro (F.C.); emilian.paduraru@academic.tuiasi.ro (E.P.); catalin-gabriel.dumitras@academic.tuiasi.ro (C.G.D.); adriana.munteanu@academic.tuiasi.ro (A.M.); dragos-florin.chitariu@academic.tuiasi.ro (D.-F.C.)
* Correspondence: mihaita.horodinca@academic.tuiasi.ro

Abstract: This paper presents a study of 2D roughness profiles on a flat surface generated on a steel workpiece by ball nose end milling with linear equidistant tool paths (pick-intervals). The exploration of the milled surface with a surface roughness tester (on the pick and feed directions) produces 2D roughness profiles that usually have periodic evolutions. These evolutions can be considered as time-dependent signals, which can be described as a sum of sinusoidal components (the wavelength of each component is considered as a period). In order to obtain a good approximate description of these sinusoidal components, two suitable signal processing techniques are used in this work: the first technique provides a direct mathematical (analytical) description and is based on computer-aided curve (signal) fitting (more accurate); the second technique (synthetic, less accurate, providing an indirect and incomplete description) is based on the spectrum generated by fast Fourier transform. This study can be seen as a way to better understand the interaction between the tool and the workpiece or to achieve a mathematical characterisation of the machined surface microgeometry in terms of roughness (e.g., its description as a collection of closely spaced 2D roughness profiles) and to characterise the workpiece material in terms of machinability by cutting.

Keywords: 2D roughness profiles; milling; ball nose end mill; measurement; characterisation; curve (signal) fitting; fast Fourier transform

Citation: Horodinca, M.; Chifan, F.; Paduraru, E.; Dumitras, C.G.; Munteanu, A.; Chitariu, D.-F. A Study of 2D Roughness Periodical Profiles on a Flat Surface Generated by Milling with a Ball Nose End Mill. *Materials* **2024**, *17*, 1425. https://doi.org/10.3390/ma17061425

Academic Editors: Kejia Zhuang, Hongguang Liu, Jian Weng, Gang Wang, Dongdong Xu and Benkai Li

Received: 1 March 2024
Revised: 12 March 2024
Accepted: 16 March 2024
Published: 20 March 2024

1. Introduction

The surface roughness of steel work pieces machined by milling with ball nose cutters appears to be closely related to the interaction between the tool and the workpiece, and the machinability of the workpiece material by cutting. It depends mainly on the shape, geometry, and position of the tool (tilt angle, axial depth of cut, effective cutting diameter), the machining parameters (cutting speed, feed, and direction), the milling strategy (tool path pattern, step over distance), and the cutting forces (involved in the elastic deformations of the tool). Some non-systematic phenomena are also occasionally involved in the definition of this roughness: relative vibrations between tool and workpiece, self-excited vibrations, local variations in the hardness of the workpiece material, tool wear, cutting edge adhesion or fractures, etc. Therefore, under the most suitable milling conditions, the roughness is mainly characterised by a micro-geometry with a regular (periodic) shape, with equidistant pick (path) and feed interval scallops [1] on the pick and feed directions.

A better understanding of the interaction between tool and workpiece during any cutting (machining) process requires a thorough investigation of the surface roughness. The first approach to this investigation is the experimental sampling of the surface roughness description using appropriate equipment. The most common method to achieve this sampling is the use of contact profilometers [2–10] as a reliable but time-consuming method. Some other methods use the non-contact surface exploration by lasers [11], laser interferometry [12,13], laser confocal microscopes [14], optical systems [15–18], machine vision systems [19], or are inspired by research into the optical properties of surfaces (ability to split white light, diffractive properties) using scanning electron microscopy and atomic force microscopy [20].

As the description of a 3D surface roughness by sampling is generally obtained by joining many 2D roughness profiles (e.g., as a grid on pick and feed directions), the study of these surfaces mainly means a study of each of these 2D roughness profiles (2DRPs), often as a periodic evolution [2,4,5,8,11,15,16,18,20,21]. Some investigation techniques on this topic are available in the literature, most of which reveal the presence of numerous permanent sinusoidal components within these 2DRPs (as wavinesses [21], with dominants and some harmonics). Some previous studies indicate the availability of techniques to describe the components using synthetic rather than analytical methods, treating the 2DRPs mainly as digital time-dependent signals. The simplest synthetic description of the components can be obtained by digital filtering [22], in particular by selective band-pass filtering [8]. A relatively better approach to this synthetic description is possible using the power spectral density (by Fast Fourier Transform, FFT) of 2DRPs as time-dependent signals [2,7,8,19,21]. On an FFT spectrum (with amplitude on the y-axis and conventional frequency as the inverse of the wavelength on the x-axis), each significant sinusoidal component within a 2DRP is described as a peak. However, the availability of the FFT is generally seriously limited by the insufficiently low resolution of the conventional frequency (R_{cf}) on the spectrum. The use of a high sampling rate (or sampling frequency f_s) for 2DRP description (in order to have a high Nyquist limit $f_{Nq} = f_s/2$) should be mandatorily accompanied by a high number (N) of samples (or a large size length of 2DRP) in order to have a conveniently small resolution of conventional frequency $R_{cf} = f_s/N$. If this resolution is not small enough, some peaks in the spectrum will be missing or will have incorrectly described amplitudes (smaller than normal). This is a major inconvenience of the FFT that has not yet been resolved in these previous approaches. However, there is an additional drawback to the FFT analysis: the synthetic description of the sinusoidal components is incomplete (their phases at the origin of time are missing).

In some cases, the 2DRPs, considered as time-dependent signals, contain short sinusoidal components that do not persist permanently. For these situations (not considered in our work), where generally short oscillations (waves) occur transiently, the FFT analysis is not at all appropriate, but there are available other specific investigation techniques (inspired by the study of vibrations), e.g., based on Wavelet Transform (as Continuous Wavelet Transform [7], Frequency Normalised Wavelet Transform [23,24], and Wavelet Packet Transform [25]).

The main purpose of this work is focused on the study of periodic 2DRPs (considered as time-dependent signals) in order to determine the best analytical approximation of them (as a pattern), as close as possible to experimental evolutions, as a sum of significant sinusoidal components. Each sinusoidal component (analytically defined by the amplitude, a conventional angular frequency, and a phase at the conventional time origin) is a description of waviness on the machined surface of the workpiece. The inverse of the conventional frequency (as the conventional period) is the wavelength of the waviness.

Specifically, these 2DRPs are experimentally sampled in feed and pick directions (using a contact profilometer) on a theoretically flat surface milled with a ball nose end mill (on a steel workpiece in our approach). In order to analyse the 2DRP, a curve fitting procedure in Matlab R2019b (based on the Curve Fitting Toolbox) is favoured in this approach. In contrast to the FFT procedure (also discussed here), the curve fitting procedure can now be applied to relatively small (in length) 2DRPs, providing a high degree of accuracy in the analytical description of sinusoidal components. Similar to the FFT procedure, the curve fitting procedure has the same Nyquist limit ($f_{Nq} = f_s/2$); in other words, it is not possible to find out the analytical descriptions of sinusoidal components having conventional frequency above the Nyquist limit f_{Nq}. The curve fitting procedure allows for an interesting approach: a 2DRP in the analytical description can be artificially resized by mathematical extrapolation (increasing the number of samples N, while keeping the same sampling rate f_s). The accuracy of the FFT spectrum of this resized 2DRP is significantly improved due to a lower conventional frequency resolution, so that the FFT spectrum is now better suited to synthetically describe the content (in sinusoidal components) of a 2DRP.

There is an interesting option in the 2DRP analysis: one period of the synthetically described roughness pattern is obtained by a special kind of moving averaging. This averaging drastically reduces both the sinusoidal components harmonically uncorrelated and the noise. The analytical description of this pattern is also achieved by curve fitting.

The following sections of this paper are organised as follows: Section 2 presents the materials and methods, Section 3 presents the results and discussions, and Section 4 presents the conclusions.

2. Materials and Methods

A flat surface was milled on a workpiece made of 90MnCrV8 steel (hardness 60 HRC) using a 12 mm diameter, 3 flute, TiAlN coated carbide ball nose end mill (as GARANT Diabolo solid carbide ball nose slot drill HPC 12 mm, from the Hoffmann Group, Bucharest, Romania), tilted at 25 degrees to the pick direction and perpendicular to the feed direction, with the following cutting regime parameters: 5200 rpm, 1560 mm/min feed rate, constant axial cutting depth of 0.1 mm and 0.4 mm step over (with theoretically equal pick-interval scallops height [26]). Figure 1 shows a conceptual description of the down milling process (with the workpiece in cyan, the tool in red, the feed direction in green, and the direction of rotation in blue). The magenta-coloured straight line (d1) represents the pick direction, and the black straight line (d2) represents the feed direction, with both conventionally used for experimental sampling of 2DRP. Figure 2 shows a view of the tool and workpiece (with the cutting process stopped) on an OKUMA GENOS M460R-VE CNC vertical machining centre (Charlotte, NC, USA).

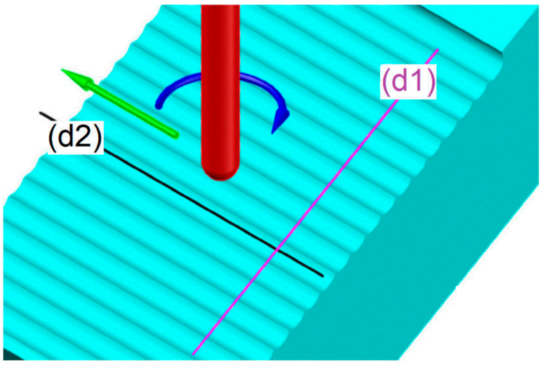

Figure 1. A conceptual description of the cutting process.

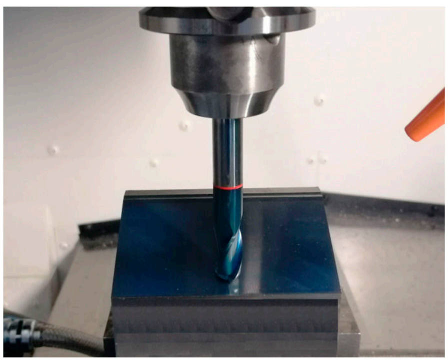

Figure 2. A view of the milling setup.

Figure 3 shows a view of the roughness sampling setup (using a SURFTEST SV-2100W4 contact profilometer, from Mitutoyo (Bucharest, Romania), with 0.0001 µm resolution, 2 µm stylus tip radius), with the flat milled surface placed in a horizontal position (here for sampling in pick direction).

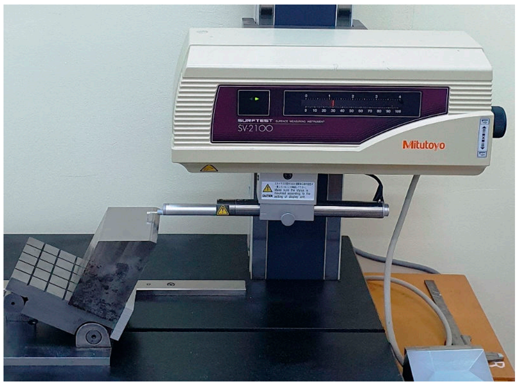

Figure 3. A view on the roughness sampling setup.

The numerical description of a 2DRP is delivered as a two-column .txt file describing N = 8000 equidistant samples (Δx = 0.5 µm sampling interval between samples on the x-axis, for a total distance of 4 mm). This file can be easily loaded into Matlab R2019b and analysed as a time-dependent signal (by FFT and curve (signal) fitting). Figure 4 shows a 4 mm long 2DRP, sampled in the pick direction (plotted in Matlab).

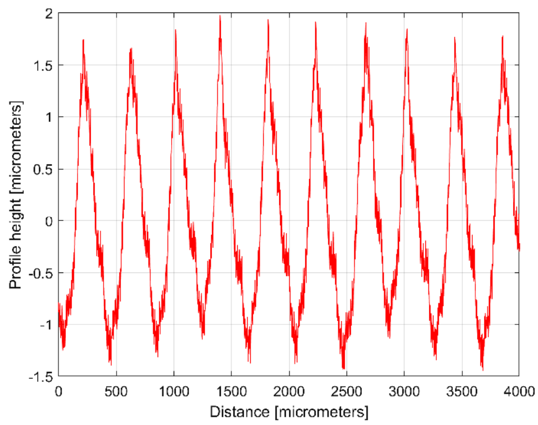

Figure 4. Graphical description of a 2DRP sampled on work piece, in the pick direction.

Here the profilometer resolution (0.0001 µm) was experimentally confirmed (as the minimum describable variation of the y-coordinate). As expected, there is a dominant periodic component within the 2DRP of Figure 4. A rough estimation indicates that this dominant has 10 periods, with each period being equal to the milling step over (400 µm), and an average pick-interval scallop height of 2.5 µm.

Figure 5 shows a partial view of the FFT spectrum of this 2DRP with real amplitudes (in Matlab). The 2DRP from Figure 4 was processed with FFT as a time-dependent signal (the x-coordinates of the samples are seen as signal samples time; the y-coordinates are seen as signal level). The sampling interval Δx on the x-axis (Δx = 0.5 µm) is seen as the conventional sampling period Δt on the t-axis. An x-coordinate on the x-axis of Figure 5 is equivalent to a conventional frequency or the inverse of a conventional period, or the inverse of a wavelength λ. A peak on the FFT spectrum (e.g., the highest peak 1, represented by an x-coordinate of 0.0025 µm^{-1} and a y-coordinate of 1.138 µm) indicates that there is a dominant sinusoidal component in the 2DRP with wavelength $\lambda = 1/x$ (e.g., $\lambda_1 = 1/0.0025 = 400$ µm for peak 1). This is exactly the step over value (pick feed) previously highlighted. In Figure 5, some other relevant peaks (2, 3, 4, and 5) represent sinusoidal components, harmonically correlated with the dominant, having the wavelengths $\lambda_1/2 = 200$ µm, $\lambda_1/3 = 133.(3)$ µm, $\lambda_1/4 = 100$ µm, and $\lambda_1/5 = 80$ µm. The conventional sampling period $\Delta t = 0.5$ µm corresponds to the sampling frequency (rate) $fs = 1/\Delta t = 2$ µm^{-1} which is a conventional Nyquist limit (frequency) of $f_{Nq} = f_s/2 = 1$ µm^{-1}. In other words, the smaller synthetically describable wavelength of a sinusoidal component within the 2DRP by FFT spectrum is defined as $\lambda_{min} = (f_{Nq})^{-1} = (f_s/2)^{-1} = 1$ µm.

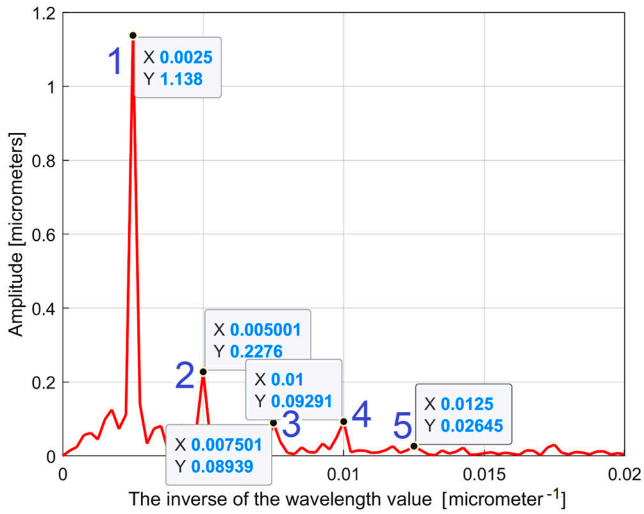

Figure 5. A partial view on the FFT spectrum of 2DRP from Figure 4.

However, as Figure 5 clearly shows, the conventional frequency resolution $R_{cf} = f_s/N = 2/8000 = 0.00025$ µm^{-1} is not small enough in order to describe an accurate spectrum. In the spectrum from Figure 5 there are only $0.02/R_{cf} = 0.02/0.00025 = 80$ samples. There are certainly other harmonics (with higher conventional frequencies) that are not visible in the spectrum. A longer 2DRP (obtained by increasing the number of samples at the same sampling frequency) significantly reduces the conventional frequency resolution. It should also be noted that the FFT spectrum does not provide the phase at the origin of the conventional time ($x = 0$) for sinusoidal components. A better approach proposed in this paper considers that within the $y(x)$ 2DRP there is a consistent deterministic part $y_d(x)$ and a less significant non-deterministic part $y_{nd}(x)$, mainly as noise, with $y(x) = y_d(x) + y_{nd}(x)$. In general, for periodic 2DRPs, this deterministic part $y_d(x)$ can be described as the sum of n sinusoidal components:

$$y_d(x) = \sum_{j=1}^{n} y_{dj}(x) = \sum_{j=1}^{n} A_j \cdot \sin(\omega_j \cdot x + \varphi_j) \tag{1}$$

In Equation (1), A_j are amplitudes, ω_j are conventional angular frequencies (related by wavelengths λ_j, with $\omega_j = 2\pi/\lambda_j$), and φ_j are conventional phase shifts at the origin ($x = 0$). Here, x (the current position of the profilometer stylus on the x-axis) plays the role of time.

The curve (signal) fitting procedure (using the Curve Fitting Tool from Matlab) allows for the values of A_j, ω_j, and φ_j to be determined with a good approximation. A sine model (as f(x) = a1*sin(b1*x + c1)) was used for a first fit, with x—coordinates as X data and y—coordinates as Y data. In this model, a1, b1, and c1 play the role of A_1, ω_1, and φ_1 values in defining the first sinusoidal component $y_{d1}(x)$. The first curve fit gives $A_1 = 1.151$ µm, $\omega_1 = 0.01558$ rad/µm, and $\varphi_1 = 4.1871$ rad, whereby typically this curve fitting procedure finds the description of the highest amplitude component. It systematically searches for those suitable A_1, ω_1, and φ_1 values that satisfy the condition: $\sum\lfloor y(x) - y_{d1}(x)\rfloor = \min$. This first sinusoidal component $y_{d1}(x)$ is shown (as dominant) in blue in Figure 6, superimposed on $y(x)$, shown in red (an evolution already described in Figure 4). The component $y_{d1}(x)$ can be described mathematically as:

$$y_{d1}(x) = A_1 \cdot \sin(\omega_1 \cdot x + \varphi_1) = 1.151 \cdot \sin(0.01557 \cdot x + 4.1871\ ) \tag{2}$$

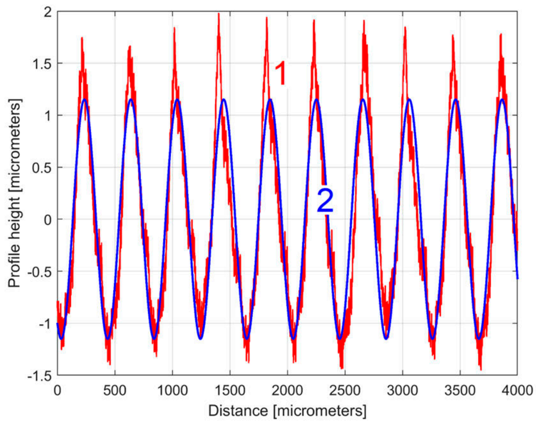

Figure 6. 1—The 2DRP from Figure 4; 2—The first (dominant) sinusoidal component ($y_{d1}(x)$) found by curve (signal) fitting (Equation (2)).

The description of $y_{d1}(x)$ from Equation (2) allows for the mathematical removal from $y(x)$, with the result shown in Figure 7 as the first residual ($r_1(x)$) of 2DRP, as $r_1(x) = y(x) - y_{d1}(x)$, after the first curve fitting (drawn at the same scale as Figure 6). The decrease in the y-coordinates of the residual profile is additional evidence of the quality of the mathematical description of $y_{d1}(x)$ found by curve fitting.

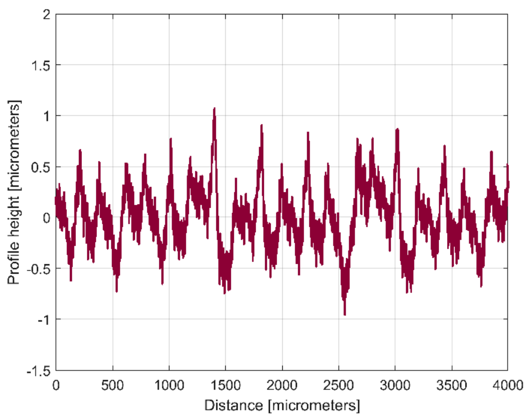

Figure 7. The first residual 2DRP after first analysis by curve fitting (as $r_1(x) = y(x) - y_{d1}(x)$).

It is clear that the dominant component $y_{d1}(x)$ does indeed fit $y(x)$. Its amplitude A_1 is close to that shown in the FFT spectrum (peak 1), and its wavelength $\lambda_1 = 2\pi/\omega_1 = 2\pi/0.01558 = 403.285$ µm is close to the step over value or pick feed (400 µm) during the milling process. The conventional frequency of $y_{d1}(x)$ is $1/\lambda_1 = 0.002479$ µm^{-1}, which is more precisely described by comparison with Figure 5, as related to the first peak (there $1/\lambda_1 = 0.0025$ µm). Related by the difference between the measured wavelength $\lambda_1 = 403.285$ µm (determined by curve fitting) and the pick feed (400 µm, as theoretical wavelength λ_1 generated by the CNC machining centre), a logical conclusion must be drawn: we suspect an inaccurate control of the x movement of the contact profilometer during the 2DRP measurement (involved in the measured λ_1) rather than inaccurate control of the pick feed during the milling process. In Figure 6, there are not exactly ten periods of the dominant $y_{d1}(x)$, as the ratio between the 2DRP length (4000 µm) and the theoretical wavelength (400 µm) suggests.

It is clear that this procedure can be repeated many times in an identical way (automatically, by programming in Matlab), and the mathematical description of the sinusoidal component $y_{dj}(x)$ can be found by curve fitting of the $(j-1)$th residual of 2DRP, as $r_{j-1}(x)$, described by Equation (3):

$$r_{j-1}(x) = y(x) - \sum_{k=1}^{j-1} y_{dk}(x) \tag{3}$$

Of course, in the curve-fitting procedure (as in the case of the FFT spectrum), exceeding of the Nyquist limit is forbidden ($\omega j < 2\pi f_{Nq}$ or $\lambda_j > (f_{Nq})^{-1}$).

Hypothetically, considering that $y_{nd}(x) = 0$, a perfect mathematical description of $y_d(x)$ (after n similar curve-fitting steps), should produce an $r_n(x) = 0$ for the nth residual of 2DRP (graphically represented as a straight line placed exactly on the x-axis).

The viability of this method of determining the mathematical description of a roughness profile (using a similar curve-fitting method developed in Matlab) has previously been demonstrated [27] in the analysis of other types of complex signals (vibration, active electrical power, instantaneous angular speed, etc.) containing many sinusoidal components.

3. Results and Discussion

3.1. Analysis of 2D Roughness Profiles in the Pick Direction by Curve Fitting

The analysis of the previously sampled 2DRP (Figure 4) was similarly performed using repetitively this curve fitting procedure a further 121 times. The mathematical description of these 122 sinusoidal components within $y(x)$ was found (these components having amplitudes greater than the resolution of the contact profilometer). Figure 8 shows the 2DRP (already shown in red in Figures 4 and 6) superimposed on an approximation of $y_d(x)$ by mathematical addition of these 122 sinusoidal components (shown in blue). In the same figure, the 122nd residual of 2DRP ($r_{122}(x)$), shown in purple, is superimposed. Figure 9 shows a zoomed section of area A from Figure 8.

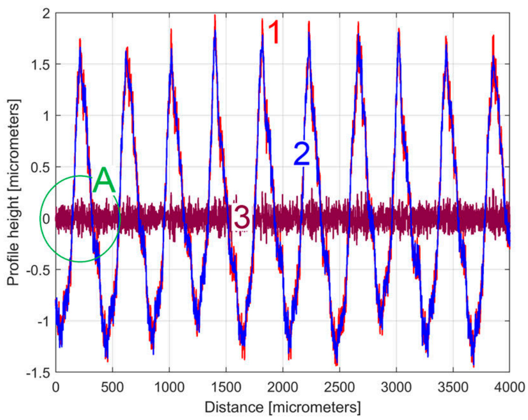

Figure 8. 1—The 2DRP; 2—An approximation of $y_d(x)$ through $y_{dh}(x)$ with 122 components; 3—The 122nd residual $r_{122}(x)$.

It is obvious that there is a good fit between the approximation of $y_d(x)$ and $y(x)$. Compared to Figure 7, there is a significantly smaller residual of 2DRP, which mainly describes the non-deterministic part $y_{nd}(x)$ of $y(x)$ and the measurement noise. In a simple approach, this noise—which does not significantly affect the fitting results—can be greatly reduced by numerical low-pass filtering.

As is well known [28], any evolution of a signal in time (or similar, e.g., this 2DRP in pick direction) can be well approximated as a sum of sinusoidal components. In our approach, it is more interesting to find the approximate analytical description of 2DRP (strictly related to the milling process) as a sum of harmonically correlated sinusoidal components (as $y_{dh}(x)$) with a fundamental at 0.01557 rad/µm as conventional angular frequency ω_1 (Equation (2)) related by pick feed or step over and some harmonics (at 2·0.01557 rad/µm, 3·0.01557 rad/µm, etc.). In other words, the deterministic part of $y(x)$ should be seen as $y_d(x) = y_{dh}(x) + y_{dnh}(x)$, where $y_{dnh}(x)$ is a sum of sinusoidal non-harmonically correlated components. Of course, this new type of approximation is available here because $y_{dh}(x)$ is dominant ($y_d(x) \approx y_{dh}(x)$).

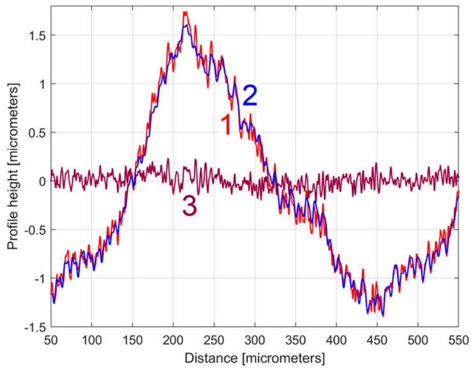

Figure 9. A zoom-in detail in area A from Figure 8.

Among the 122 identified sinusoidal components, 30 components (Hi) were found to be well harmonically correlated (and involved in the definition of $y_{dh}(x)$ from Equation (4)) with a good approximation, with the values of A_{Hi} (amplitudes), ω_{Hi} (conventional angular frequencies), and φ_{Hi} (phases in origin) given in Table 1.

$$y_{dh}(x) \approx \sum_{i=1}^{30} A_{Hi} \cdot \sin(\omega_{Hi} \cdot x + \varphi_{Hi}) \tag{4}$$

Table 1. The values of A_{Hi}, ω_{Hi}, and φ_{Hi} involved in the mathematical description of 30 well harmonically correlated sinusoidal components within $y_{dh}(x)$ of the 2DRP, in the pick direction.

Harmonic # (Hi)	Amplitude A_{Hi} [µm]	Conventional Angular Frequency ω_{Hi} [rad/µm]	Wavelength $\lambda_{Hi} = 2\pi/\omega_i$ [µm]	Phase φ_{Hi} at Origin (x = 0) [rad]
H1	A_{H1} = 1.148	ω_{H1} = 0.01557	λ_{H1} = 403.544	φ_{H1} = 4.2031
H2	0.2459	0.03118 (as 2.0025·ω_{H1})	201.53 (as λ_{H1}/2.0024)	1.412
H3	0.09367	0.04669 (as 2.9987·ω_{H1})	134.57 (as λ_{H1}/2.9988)	4.3261
H4	0.1116	0.06239 (as 4.0070·ω_{H1})	100.70 (as λ_{H1}/4.0074)	2.456
H5	0.02461	0.07848 (as 5.0404·ω_{H1})	80.061 (as λ_{H1}/5.0405)	3.085
H7	0.03816	0.1092 (as 7.0138·ω_{H1})	57.538 (as λ_{H1}/7.0135)	4.785
H8	0.009202	0.1245 (as 7.9961·ω_{H1})	50.467 (as λ_{H1}/7.9962)	5.8120
H9	0.0236	0.1404 (as 9.0173·ω_{H1})	44.752 (as λ_{H1}/9.0173)	3.4731
H10	0.02267	0.1558 (as 10.0064·ω_{H1})	40.328 (as λ_{H1}/10.0065)	4.6591
H11	0.0129	0.1714 (as 11.0083·ω_{H1})	36.658 (as λ_{H1}/11.0083)	1.21
H12	0.01171	0.1873 (as 12.0295·ω_{H1})	33.546 (as λ_{H1}/12.0296)	5.3275

Table 1. *Cont.*

Harmonic # (Hi)	Amplitude A_{Hi} [μm]	Conventional Angular Frequency ω_{Hi} [rad/μm]	Wavelength $\lambda_{Hi} = 2\pi/\omega_i$ [μm]	Phase φ_{Hi} at Origin (x = 0) [rad]
H13	0.01317	0.2027 (as 13.0186·ω_{H1})	30.997 (as λ_{H1}/13.0188)	1.796
H14	0.01174	0.2181 (as 14.0077·ω_{H1})	28.808 (as λ_{H1}/14.0081)	5.8364
H15	0.01097	0.2337 (as 15.0096·ω_{H1})	26.885 as λ_{H1}/15.0100)	5.3481
H16	0.01386	0.2493 (as 16.0016·ω_{H1})	25.203 (as λ_{H1}/16.0117)	3.097
H18	0.01152	0.2805 (as 18.0154·ω_{H1})	22.399 (as λ_1/18.0162)	5.5279
H19	0.0192	0.2961 (as 19.0173·ω_{H1})	21.219 (as λ_{H1}/19.0180)	0.628
H22	0.01029	0.3425 (as 21.9974·ω_{H1})	18.345 (as λ_{H1}/21.9975)	3.9651
H23	0.008842	0.3586 (as 23.0315·ω_{H1})	17.521 (as λ_{H1}/23.0320)	2.8171
H24	0.02065	0.3741 (as 24.0270·ω_{H1})	16.795 (as λ_{H1}/24.0276)	4.3321
H25	0.009471	0.3896 (as 25.0225·ω_{H1})	16.127 (as λ_{H1}/25.0229)	1.299
H26	0.01693	0.4053 (as 26.0308·ω_{H1})	15.502 (as λ_{H1}/26.0317)	1.822
H27	0.01081	0.4208 (as 27.0263·ω_{H1})	14.931 (as λ_{H1}/27.0273)	4.2351
H28	0.009238	0.4365 (as 28.0347·ω_{H1})	14.394 (as λ_{H1}/28.0356)	1.563
H29	0.007853	0.4524 (as 29.0559·ω_{H1})	13.888 (as λ_{H1}/29.0570)	0.7781
H31	0.01326	0.4833 (as 31.0405·ω_{H1})	13.000 (as λ_{H1}/31.0418)	0.5155
H32	0.01014	0.4985 (as 32.0167·ω_{H1}	12.604 (as λ_{H1}/32.0171)	3.9471
H38	0.008485	0.5924 (as 38.0475·ω_{H1})	10.606 (as λ_{H1}/38.0487)	5.7423
H41	0.02497	0.6392 (as 41.0533·ω_{H1})	9.829 (as λ_{H1}/41.0565)	1.478
H42	0.01782	0.6548 (as 42.0552·ω_{H1})	9.595 (as λ_{H1}/42.0577)	0.9996

Some harmonics in Table 1 are missing (e.g., H6, H17, H20, H21, etc.).

Figure 10 shows an equivalent of Figure 8 but with an approximation of $y_d(x)$ by $y_{dh}(x)$, according to Equation (4) and Table 1. Figure 11 shows a zoomed detail in area A of Figure 10 (similar to Figure 9).

A comparison of Figures 10 and 11 with Figures 8 and 9 shows that the fit is acceptable but less good than before, an aspect that is well highlighted by the evolution of the residual ($r_{30}(x)$). In particular, in some areas (e.g., B, C, and D in Figure 10) the fit between $y(x)$ and $y_{dh}(x)$ is locally less good. There are several reasons for this mismatch. Firstly, we should consider the angular position of the milling tool (due to its rotation). This position was not necessarily the same each time when its axis intersects the line (e.g., (d1) on Figure 1) where the 2DRP was sampled (the pick-interval scallops geometry on this line from the working piece is slightly different). Secondly, there is a variable flexional deformation of the milling tool in the direction of this line (pick feed direction).

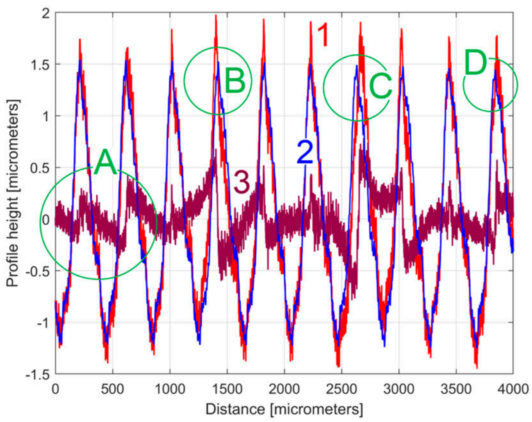

Figure 10. 1—The 2DRP; 2—An approximation of $y_d(x)$ with the profile $y_{dh}(x)$ with 30 components described in Table 1; 3—The 30th residual $r_{30}(x)$.

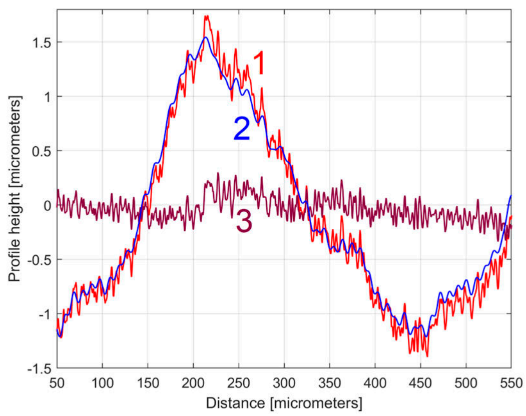

Figure 11. A zoom-in detail in area A from Figure 10.

However, in this approach, the evolution of $y_{dh}(x)$ (shown separately in Figure 12) provides one of the best characterisations of the 2DRP, which is systematically related to the interaction between the milling tool and the workpiece (and obviously by the properties of its material).

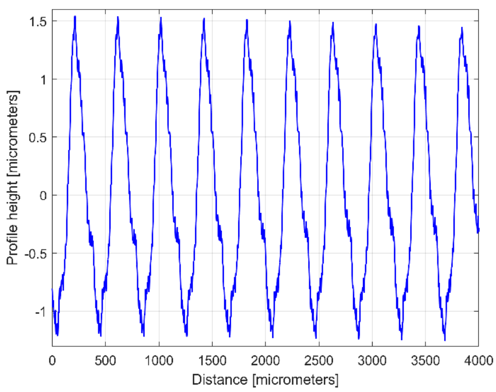

Figure 12. The evolution of the $y_{dh}(x)$ profile.

Due to a small imprecision in the curve (signal) fitting process, there is not a perfect harmonic correlation between the 30 components within $y_{dh}(x)$, as clearly indicated in Table 1 (with $\omega_{Hi} \approx Hi{\cdot}\omega_{H1}$ or $\lambda_{Hi} \approx \lambda_{H1}/Hi$), and the evolution of $y_{dh}(x)$ from Figure 12 is not strictly periodic, as expected.

This inconvenience can be easily avoided by roughly considering $\omega_{Hi} = H_i \cdot \omega_{H1}$ in Equation (4). A more rigorous approach is to replace above the conventional angular frequency ω_{H1} with a more precisely equivalent value ω_{He1}, calculated as follows:

$$\omega_{He1} = \left(\sum_{i=1}^{30} \frac{A_{Hi}}{A_{H1}}\right)^{-1} \cdot \sum_{i=1}^{30} \frac{A_{Hi}}{A_{H1}} \frac{\omega_{Hi}}{H_i} = 0.0155785 \text{ rad}/\mu\text{m} \tag{5}$$

In Equation (5), ω_{He1} is the weighting (by amplitude A_{Hi}) of the conventional angular frequency $\omega_{Hi}$of each harmonic, relative to the amplitude A_{H1} of the first harmonic H1 (as dominant). However, here particularly, there is no significant difference between ω_{H1} and ω_{He1}.

With this value ω_{He1}, the description of $y_{dh}(x)$ from Equation (4) can be rewritten as $y_{dhe}(x)$ according to Equation (6) and plotted according to Figure 13.

$$y_{dhe}(x) = \sum_{i=1}^{30} A_{Hi} \cdot \sin(H_i \cdot \omega_{He1} \cdot x + \varphi_{Hi}) \tag{6}$$

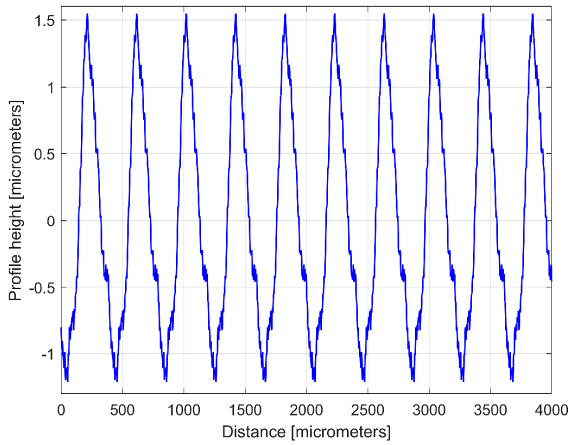

Figure 13. The evolution of the $y_{dhe}(x)$ profile.

This $y_{dhe}(x)$ profile can be accepted as a systematic characterisation (pattern) of the 2DRP in the pick direction. An even more interesting characterisation is obtained if this $y_{dhe}(x)$ profile is described by artificially shifting the origin on x-axis (x = 0) in the abscissa $(2\pi - \varphi_{H1})/\omega_{He1}$ of the first zero crossing (from negative to positive values) of the dominant sinusoidal component (H1 in Table 1). Now the profile $y_{dhe}(x)$ becomes $y_{dhe0}(x)$, described mathematically by Equation (7) and shown graphically in blue in Figure 14. Here, the magenta curve describes the dominant component (H1), also shifted to new origin (as $H1_0$), with ω_{H1} replaced by ω_{He1}.

$$y_{dhe0}(x) = \sum_{i=1}^{30} A_{Hi} \cdot \sin\left[H_i \cdot \omega_{He1} \cdot \left(x + \frac{2\pi - \varphi_{H1}}{\omega_{He1}}\right) + \varphi_{Hi}\right] \tag{7}$$

With Equation (7) rewritten as Equation (8), this motion to a new origin is equivalent to a positive phase shift (with $H_i \cdot (2\pi - \varphi_{H1})$) at the origin for each sinusoidal component.

$$y_{dhe0}(x) = \sum_{i=1}^{30} A_{Hi} \cdot \sin\left[H_i \cdot \omega_{He1} \cdot x + \varphi_{Hi} + H_i \cdot (2\pi - \varphi_{H1})\right] \tag{8}$$

Figure 15 shows a zoomed detail of Figure 14, with a first period of the $y_{dhe0}(x)$ profile and of the $H1_0$ sinusoidal component.

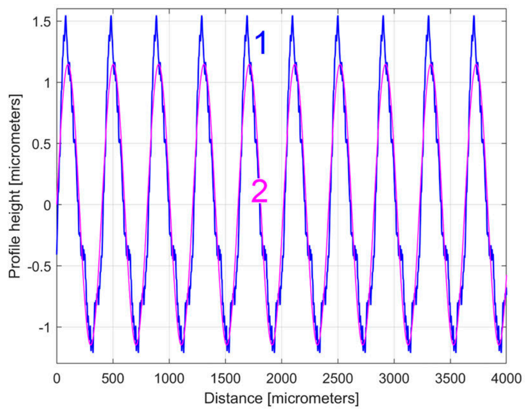

Figure 14. 1—The evolution of $y_{dhe0}(x)$ profile; 2—The evolution of the dominant component $H1_0$.

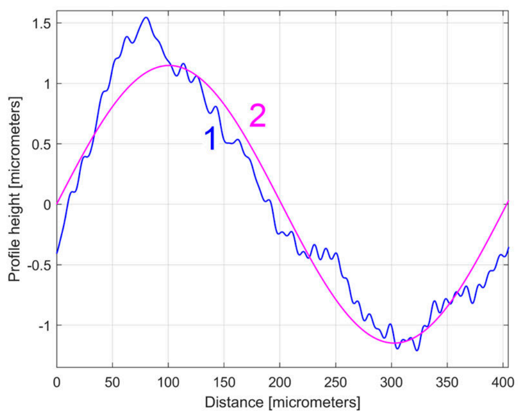

Figure 15. A detail of Figure 14 with the first period of the $y_{dhe0}(x)$ profile and $H1_0$.

This $y_{dhe0}(x)$ type of 2DRP is useful when comparing two (or more) 2DRPs sampled under similar conditions. In this approach, a second 2DRP was sampled on the same flat milled surface on a straight line parallel to (d1) on the pick direction, with a randomly chosen distance between (several millimetres).

As an equivalent to Figure 10, Figure 16 shows this new 2DRP (as $y(x)$, in red) with the same number of samples (8000) and sampling interval (Δx = 0.5 μm), overlaid with the $y_{dh}(x)$ profile (in blue) and the residual (in purple). This time only 12 harmonically related sinusoidal components inside $y_{dh}(x)$ were found (Table 2) among the 122 sinusoidal components in $y_d(x)$. The areas A–D mark some mismatches between the $y(x)$ and $y_{dh}(x)$ profiles.

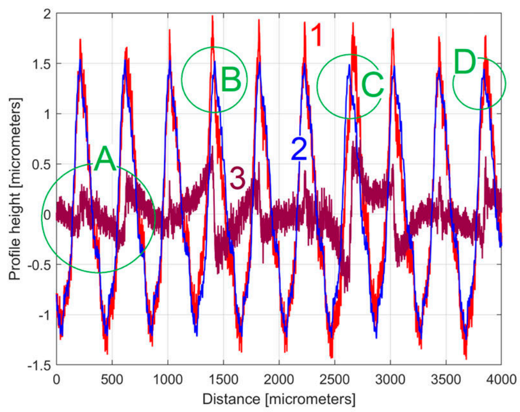

Figure 16. 1—A new 2DRP; 2—An approximation of $y_d(x)$ with $y_{dh}(x)$ profile having 12 components; 3—The 12th residual $r_{12}(x)$.

Table 2. The values A_{Hi}, ω_{Hi}, and φ_{Hi} involved in the mathematical description of 12 harmonically correlated sinusoidal components within $y_{dh}(x)$ of the 2nd 2DRP, sampled in the pick direction.

Harmonic # (Hi)	Amplitude A_{Hi} [μm]	Conventional Angular Frequency ω_{Hi} [rad/μm]	Wavelength $\lambda_{Hi} = 2\pi/\omega_i$ [μm]	Phase φ_{Hi} at Origin (x = 0) [rad]
H1	A_{H1} = 1.124	ω_{H1} = 0.01552	λ_{H1} = 404.8444	φ_{H1} = 0.4821
H2	0.2406	0.03099 (as 1.9968·ω_{H1})	202.7488 (as $\lambda_{H1}/1.9968$)	0.407
H3	0.08159	0.04671 (as 3.0097·ω_{H1})	134.5148 (as $\lambda_{H1}/3.0097$)	5.2621
H4	0.1232	0.06224 (as 4.0103·ω_{H1})	100.9509 (as $\lambda_{H1}/4.0103$)	6.1897
H5	0.0234	0.07745 (as 4.9903·ω_{H1})	81.1257 (as $\lambda_{H1}/4.9903$)	4.9971
H6	0.008268	0.09263 (as 5.9604·ω_{H1})	67.8310 (as $\lambda_{H1}/5.9684$)	0.205
H7	0.03793	0.1088 (as 7.0103·ω_{H1})	57.7499 (as $\lambda_{H1}/7.0103$)	3.7771
H9	0.01861	0.1404 (as 9.0464·ω_{H1})	44.7520 (as $\lambda_{H1}/9.0464$)	0.1429
H10	0.02616	0.1558 (as 10.0387·ω_{H1})	40.3285 (as $\lambda_{H1}/10.0387$)	3.6981
H11	0.01256	0.1712 (as 11.0309·ω_{H1})	36.7008 (as $\lambda_{H1}/11.0309$)	2.608
H13	0.01106	0.2026 (as 13.0541·ω_{H1})	31.0128 (as $\lambda_{H1}/13.0541$)	2.05
H22	0.0107	0.3425 (as 22.0683·ω_{H1})	18.3451 (as $\lambda_{H1}/22.0683$)	1.326

As an equivalent to Figure 14, Figure 17 shows the evolution of the $y_{dhe0}(x)$ profile (in green) superimposed on the evolution of the dominant component $H1_0$ (in brown).

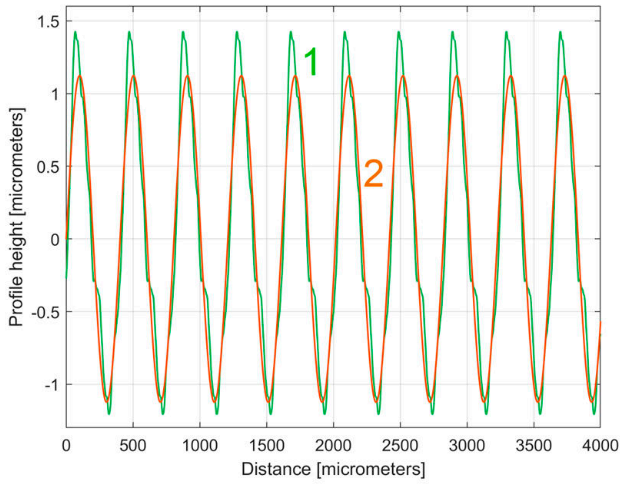

Figure 17. 1—The evolution of the $y_{dhe0}(x)$ profile; 2—The evolution of the dominant component $H1_0$. An equivalent of Figure 14.

It is interesting here to note the similarities (by comparison) between the $y_{dhe0}(x)$ profiles (from Figures 14 and 17) by their overlap in Figure 18. This is possible because both profiles start from a zero crossing (from negative to positive y-ordinates) of their dominant component $H1_0$. A zoomed detail of the first period of Figure 18 is shown in Figure 19.

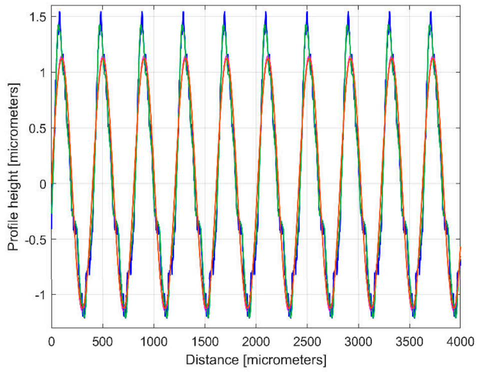

Figure 18. An overlap of both $y_{dhe0}(x)$ profiles (for 1st and 2nd 2DRP) and their dominants $H1_0$.

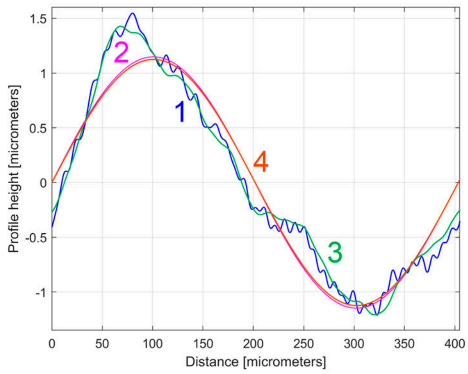

Figure 19. A zoomed detail of Figure 18: 1, 3—the $y_{dhe0}(x)$ profiles; 2, 4—the dominants $H1_0$.

As can be seen in Figure 18 and especially in Figure 19, there are strong similarities between the $y_{dhe0}(x)$ profiles 1 and 3 (and also between the dominant components $H1_0$ 2 and 4). This proves that the proposal of this $y_{dhe0}(x)$ pattern is a useful approach in a comparative analysis of 2DRPs sampled under similar conditions (especially direction) on a flat milled surface with a ball nose end mill.

3.1.1. Synthesis of a 2D Roughness Profile Pattern on a Period by Profile Averaging

There is another simple way of obtaining a synthetic (non-analytical) description of a pattern useful for characterizing the periodic 2DRPs graphically represented by m conventional periods: the y-coordinate of a point on this pattern (as $y_{ap}(x)$) is an average of the y-coordinates of m samples of 2DRP (calculated using a moving average, with m samples selectively selected for averaging). The distance (measured on the x-axis) between each two consecutive samples considered within the average is exactly the conventional period of the dominant H1, as the equivalent wavelength λ_{He1} calculated with $\lambda_{He1} = 2\pi/\omega_{He1}$. A y-coordinate value of this—pattern $y_{ap}(x)$ is determined by calculation as Equation (9):

$$y_{ap}(x) = \frac{1}{m}\sum_{i=0}^{m-1} y(x + i \cdot \lambda_{He1}) \qquad \text{with } x = 0 \div \lambda_{He1} \tag{9}$$

The length of this $y_{ap}(x)$ pattern is exactly the conventional period (the wavelength λ_{He1}). A better approach is to describe this $y_{ap}(x)$ pattern starting from the zero crossing of the dominant H1 (as $y_{ap0}(x)$, Equation (10)), where this starting point still has the x-coordinate $(2\pi - \varphi_{H1})/\omega_{He1}$.

$$y_{ap0}(x) = \frac{1}{m}\sum_{i=0}^{m-1} y\left(x + \frac{2\pi - \varphi_{H1}}{\omega_{He1}} + i \cdot \lambda_{He1}\right) \qquad \text{with } x = 0 \div \lambda_{He1} \tag{10}$$

Here, x is the x-coordinate of a generic point on the pattern $y_{ap0}(x)$. In Equation (10), in almost all previous equations (except Equation (5)) and in the sampled 2DRP, the x-coordinate is described numerically as $x = l \cdot \Delta x$ for the lth sample, $l = 1 \div N$. Here above, $x + (2\pi - \varphi_{H1})/\omega_{He1} + i \cdot \lambda_{He1}$ and $x + i \cdot \lambda_{He1}$ in Equation (9) are also x-coordinates (numerically described) of samples placed on 2DRP.

Figure 20 shows this $y_{ap0}(x)$ pattern, established by averaging, for the first sampled 2DRP (with $m = 9$). This averaging (acting as a form of digital filtering) greatly attenuates the non-sinusoidal components (noise) as well as the harmonic uncorrelated components with the dominant H1, but it retains the harmonically correlated (averaged) components if they occur systematically. In other words, it is expected that this $y_{ap0}(x)$ pattern is similar with the first period of the $y_{dhe0}(x)$ profile (already shown in Figure 15). This is fully confirmed in Figure 21, where the $y_{ap0}(x)$ pattern, the $y_{dhe0}(x)$ profile, and the dominant $H1_0$ (the first periods) are overlapped.

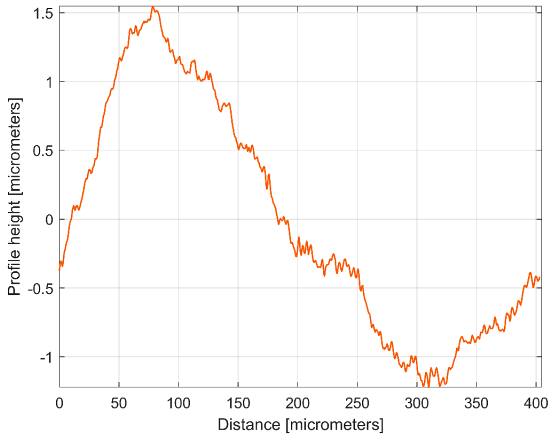

Figure 20. The $y_{ap0}(x)$ pattern of the first 2DRP.

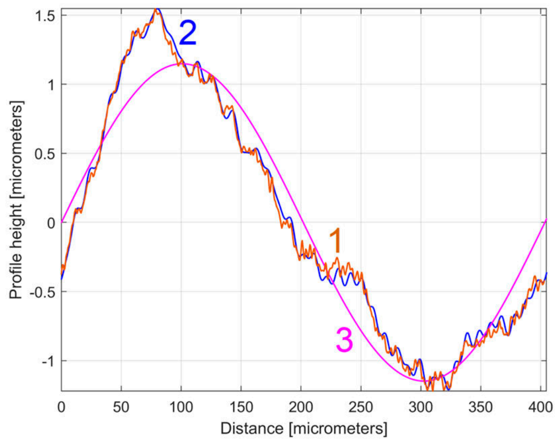

Figure 21. 1—The $y_{ap0}(x)$ pattern of the first 2DRP; 2—The first period of the $y_{dhe0}(x)$ profile; 3—The dominant $H1_0$.

Similar considerations can be made for the $y_{ap0}(x)$ pattern of the 2nd 2DRP sampled in the pick direction, as shown in Figure 22.

There is an interesting utility of these $y_{ap0}(x)$ patterns, similar to the utility of the first periods of the $y_{dhe0}(x)$ profiles, already shown in Figure 19. It allows us to synthetically characterize the roughness profiles, possibly for comparison. As an example, Figure 23 shows the overlap of the $y_{ap0}(x)$ patterns for both sampled 2DRPs in the pick direction.

As expected, there is a very good similarity between the $y_{ap0}(x)$ patterns, which is even better than between the $y_{dhe0}(x)$ profiles (from Figure 19).

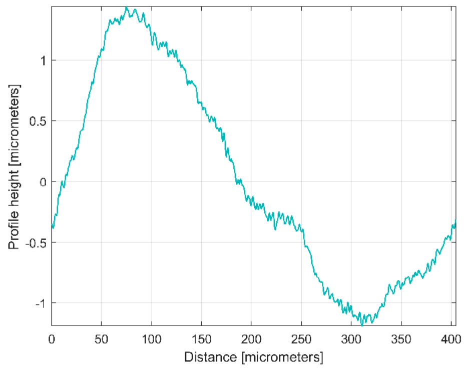

Figure 22. The $y_{ap0}(x)$ pattern of the 2nd 2DRP.

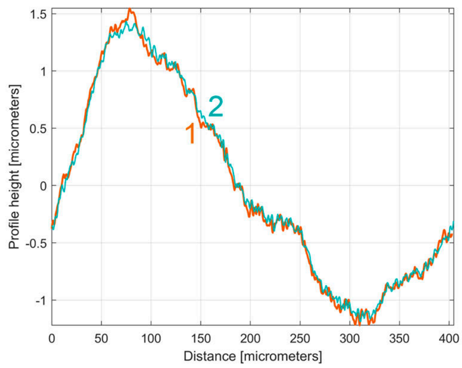

Figure 23. A graphical overlapping of the $y_{ap0}(x)$ patterns: 1—for 1st 2DRP; 2—for 2nd 2DRP.

There is an interesting and simpler way to obtain a more trustworthy mathematical description of the $y_{dhe0}(x)$ profiles (as $y_{dhe0t}(x)$) through analysis by curve (signal) fitting of the mathematically extended $y_{ap0}(x)$ patterns over a large number of periods (e.g., 10), while keeping the same sampling interval Δx = 0.5 µm. Figure 24 shows the $y_{ap0}(x)$ pattern for the 1st 2DRP, the first period of the $y_{dhe0t}(x)$ profile, and the residual $y_{ap0}(x) - y_{dhe0t}(x)$. The $y_{dhe0t}(x)$ profile is described as the sum of 30 harmonically correlated sinusoidal components found in the extended $y_{ap0}(x)$ pattern. Now, by comparison with the results from Figure 21, the similarity between the $y_{ap0}(x)$ pattern and the $y_{dhe0t}(x)$ profile is consistently improved.

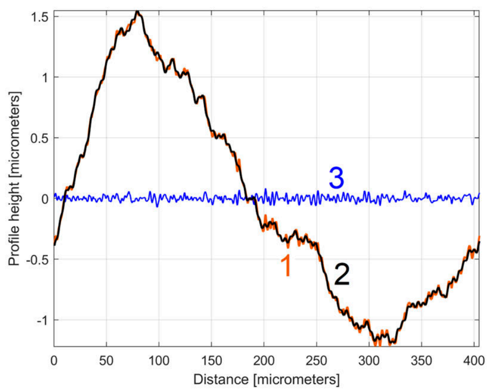

Figure 24. 1—The $y_{ap0}(x)$ pattern for 1st 2DRP; 2—The first period from the $y_{dhe0t}(x)$ profile; 3—The residual $y_{ap0}(x) - y_{dhe0t}(x)$.

The first periods from these $y_{dhe0t}(x)$ profiles (for each 2DRP, each one as a sum of 30 harmonically correlated sinusoidal components) obtained using this new approach are shown in Figure 25.

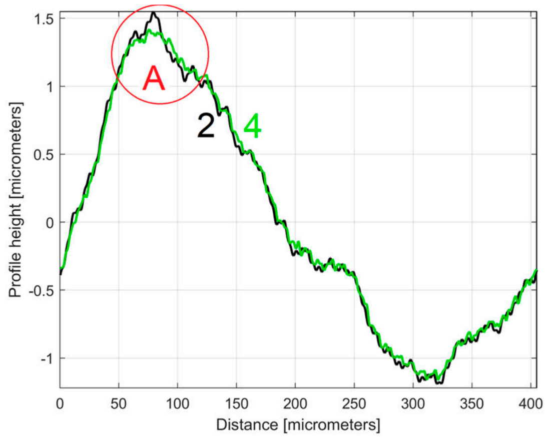

Figure 25. The first period of the $y_{dhe0t}(x)$ profiles: 2—for 1st 2DRP; 4—for 2nd 2DRP.

Compared to Figure 19 (where the profiles $y_{dhe0}(x)$ are overlapped), in Figure 25 the $y_{dhe0t}(x)$ profiles are much more similar, with the exception of area A. As expected, there are very strong similarities between the $y_{dhe0t}(x)$ profiles of Figure 25 and the $y_{ap0}(x)$ patterns of Figure 23.

3.1.2. An Approach on FFT Spectrum in 2D Roughness Profile Description

There is another interesting resource that can be exploited related to the mathematical description of the $y_{dh}(x)$ profile, and in particular the $y_{dhe}(x)$ profile. As already mentioned in Section 1, the length of any of two analytical profiles can be artificially increased by mathematical extrapolation (by increasing the number of samples from N to $p{\cdot}N$), while keeping the same sampling rate f_s (or the same sampling interval Δx = 0.5 µm). In this way, the conventional frequency resolution (as R_{cfe}) of the FFT spectrum for each of the two extrapolated profiles ($R_{cfe} = f_s/pN$) is significantly reduced (by p times compared to the spectra of the original profiles having $R_{cf} = f_s/N$ conventional frequency resolution), while the Nyquist limit remains unchanged. The quality description of the sinusoidal profile components by means of the FFT spectrum increases significantly.

As a first example, related by the first 2DRP, Figure 26 shows partially (in the range $0 \div 0.02$ µm^{-1} of conventional frequency) the FFT spectrum for the $y(x)$ profile (in red, a spectrum already presented before in Figure 5)—and for the extrapolated $y_{dhe}(x)$ profile (in blue, with p = 10). Figure 27 presents both spectra over an extended conventional frequency range ($0 \div 0.08$ µm^{-1}), with the first 27 harmonic correlated sinusoidal components (with $\omega_{Hi}= H_i \cdot \omega_{He1}$).

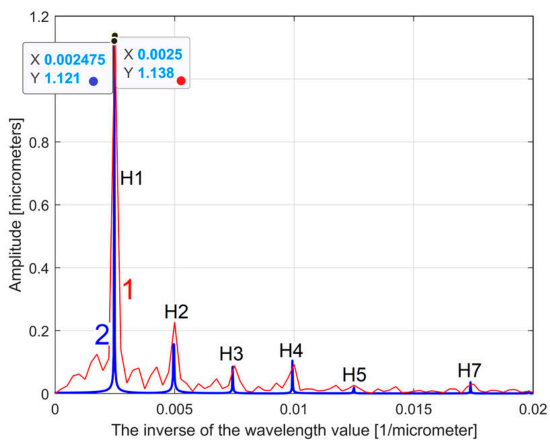

Figure 26. A partial view of the FFT spectrum: 1—of the $y(x)$ profile; 2—of the extrapolated $y_{dhe}(x)$ profile, with p = 10. The peaks H1–H7 depict harmonic correlated components.

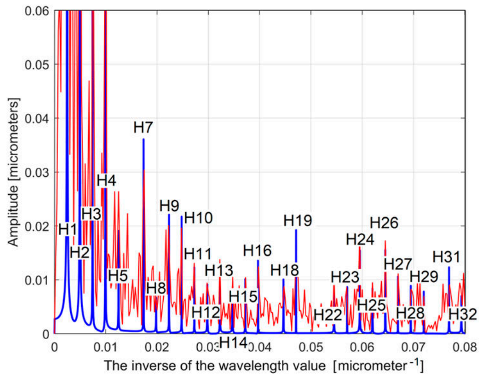

Figure 27. An extended view of the FFT spectra of the $y(x)$ profile (in red) and the extrapolated $y_{dhe}(x)$ profile, with p = 10 (in blue). The peaks H1–H32 depict harmonic correlated components.

Because in this approach the conventional angular frequencies ω_{H1} and ω_{He1} have very similar values (Table 1 and Equation (5)), the FFT spectrum of the extrapolated $y_{dh}(x)$ and $y_{dhe}(x)$ profiles are very similar. Changing the origin of the $y_{dhe}(x)$ profile (to produce the $y_{dhe0}(x)$ profile) does not produce any change on the FFT spectrum (which is insensitive to the phase shifting). The FFT spectra of the extrapolated $y_{dhe}(x)$ and $y_{dhe0}(x)$ profiles are identical.

It is obvious that the FFT spectrum of the extrapolated $y_{dhe}(x)$ profile can also be used as a pattern to compare two (or more) 2DRPs, sampled on the same surface, under identical conditions. The similarities between the partial FFT spectra of the extrapolated $y_{dhe}(x)$ profiles (with p = 10) found in both 2DRPs analysed before, are clearly highlighted in Figure 28, with a zoom on the y-axis shown in Figure 29. In both figures, in order to facilitate the comparison, the FFT spectrum of extrapolated $y_{dhe}(x)$ of the 2nd analysed 2DRP has been artificially shifted by 0. 02 µm upwards and 0.0005 µm^{-1} to the right.

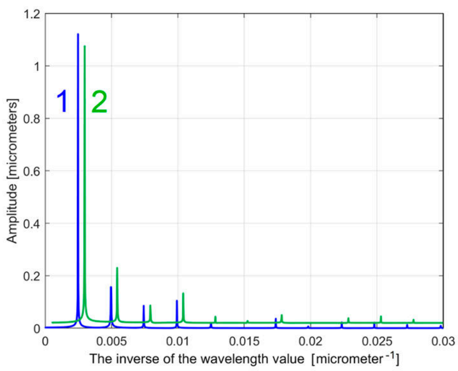

Figure 28. A partial view of the FFT spectra of extrapolated $y_{dhe}(x)$ profiles with p = 10; 1—for 1st 2DRP; 2—for 2nd 2DRP (shifted).

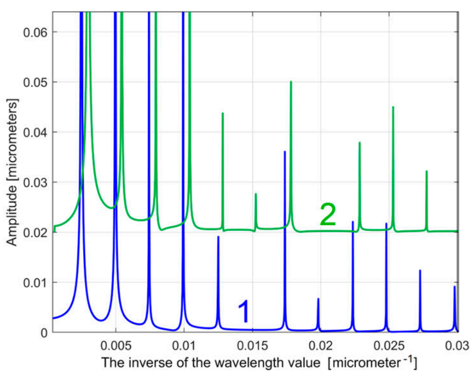

Figure 29. A zoomed image on y-axis of the FFT spectra from Figure 28.

A simpler and more reliable approach is to examine the resources provided by the compared FFT spectra of mathematically extended $y_{ap0}(x)$ patterns (related by both 2DRPs) over a large number of periods.

3.2. Analysis of 2D Roughness Profiles in the Feed Direction

A similar study can be made on the 2DRPs sampled on the same machined surface, in the feed direction, parallel to (d2), under identical conditions, number of samples, and sampling rate (sampling interval). Each of these 2DRPs is expected to describe a periodic succession of feed-interval scallops, as traces left by the tips of the milling tool edges during its rotation and feed motion. For a milling tool having three teeth, a 5600 rpm rotation speed, and a feed rate of 1560 mm/min, the conventional period of these feed-interval scallops should be equal to the feed per tooth f_t = 0.1 mm.

Figure 30 shows a first 2DRP sampled in the feed direction (coloured in red), the deterministic harmonically correlated part $y_{dh}(x)$ (as a sum of 11 components, coloured in blue), and the residual $r_{11}(x)$ coloured in purple. Figure 31 shows the overlap of the first two periods of the dominant $H1_0$ (curve 1), the first two periods of the profile $y_{dhe0}(x)$ (curve 2), and the pattern $y_{ap0}(x)$—with m = 11—extrapolated on two periods (curve 3). As expected, there is a relatively good fit between them.

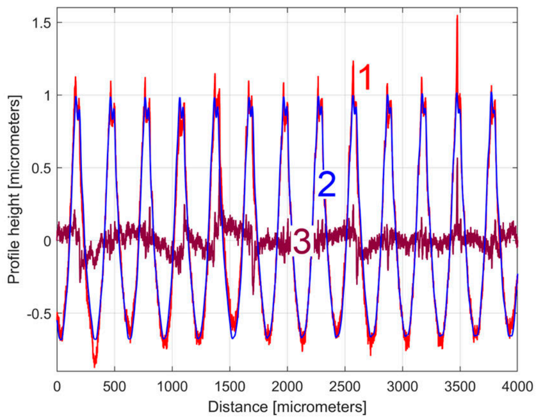

Figure 30. 1—A first 2DRP; 2—The profile $y_{dh}(x)$ with 11 components; 3—The 11th residual $r_{11}(x)$.

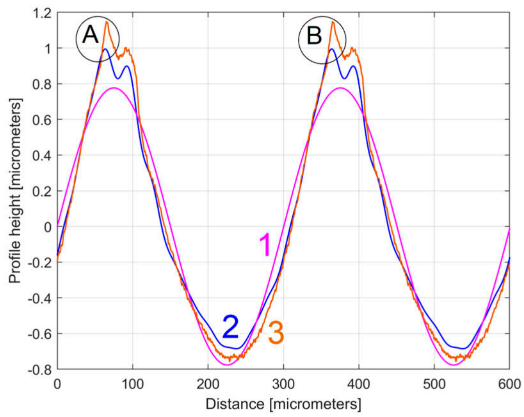

Figure 31. Some results of the analysis of the first 2DRP. Two conventional periods of: 1—the dominant component $H1_0$; 2—the profile $y_{dhe0}(x)$; 3—the pattern $y_{ap0}(x)$.

Unexpectedly, the conventional angular frequency ω_{He1} = 0.020921 rad/µm defines the wavelength $\lambda_{He1} = 2\pi/\omega_{He1}$ = 300.32 µm, as a conventional period, three times greater than the feed per tooth (100 µm), but practically equal to the feed per rotation f_r of the milling tool. This means that the 2DRP in the feed direction reveals an abnormal behaviour of the milling tool, since because it turns off of its axis (with run out [3]), a single tooth is involved in the definition of the final machined surface (roughness). Obviously, the theoretical 2DRP in the feed direction consists mainly of a group of 2D curve (trochoidal) arcs, as parts of the trajectories of points on the teeth cutting edges. Figure 32 shows a conceptual simulation (without milling tool run-out) of these identical trochoidal trajectories (Tr1, Tr2, and Tr3) at a high feed rate (for clarity of approach). Figure 33 describes these trajectories with a particular run-out of milling tool: the centre of tool rotation is in opposite direction to the point involved in generating the trajectory Tr2. In both figures, for down milling, the theoretical 2DRP is described by arcs between the lowest intersection points of the trajectories.

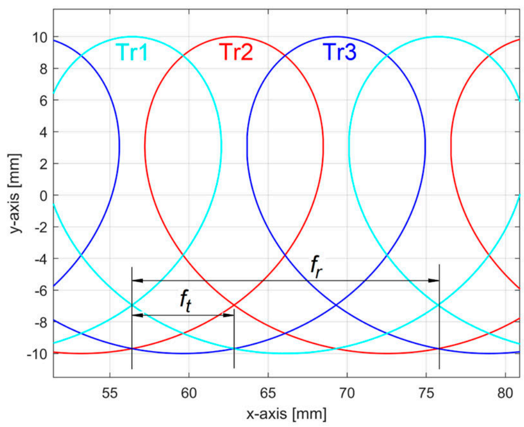

Figure 32. A simulation of 2D trajectories of points placed on teeth cutting edges (no run-out).

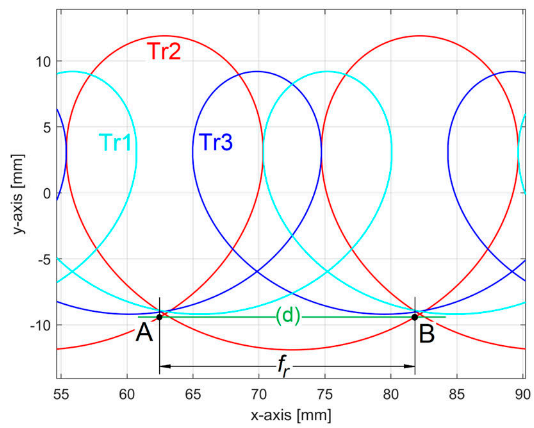

Figure 33. A simulation of 2D trajectories of points placed on teeth cutting edges (with run-out).

If the run-out is large enough, then the theoretical 2DRP is described by arcs placed on a single trochoidal trajectory as in Tr2 in Figure 33. Here, (d) is the workpiece surface reference line before milling. A conventional period of the dominant component in 2DRP is equal with the feed per rotation (f_r) and not with the feed per tooth ($f_t = f_r/3$). The points A, B in Figure 33 are located in the areas A, B in Figure 31. We should mention that, as opposed to Figure 33, Figure 31 does not have the same scale on the x and y-axis.

A similar and comparative study can be made in relation to a second 2DRP sampled on a straight line (feed direction) as a parallel direction to (d2) in Figure 1. As opposed to the analysis of the 2DRP in the pick direction, now this second 2DRP was sampled along a straight line carefully placed as accurately as possible over a whole number of pick intervals. A correct comparison requires that the first and second theoretical 2DRP should be the result of the trajectories of the same points on the teeth cutting edges.

The equivalent of Figure 30 is shown in Figure 34 and the equivalent of Figure 31 is depicted in Figure 35. As expected, similar to Figure 31, there is a relatively good fit between the dominant component $H1_0$, the $y_{dhe0}(x)$ profile, and the pattern $y_{ap0}(x)$.

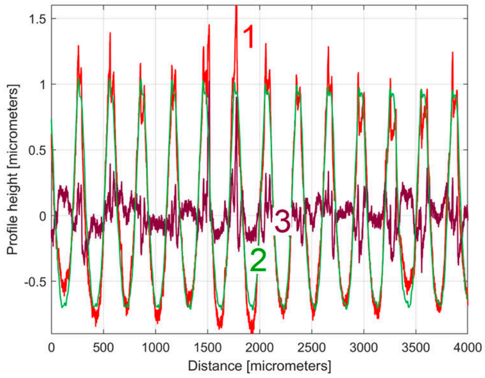

Figure 34. 1—A second 2DRP; 2—The profile $y_{dh}(x)$ having 11 components; 3—The 11th residual $r_{11}(x)$.

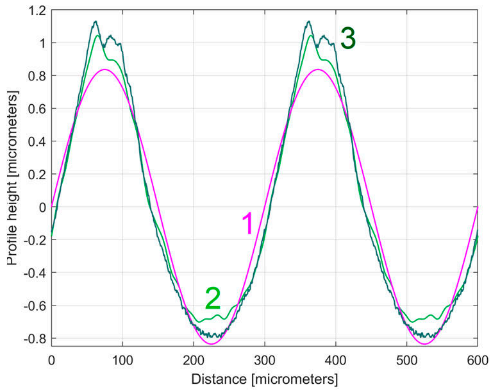

Figure 35. Some results of the analysis of the second 2DRP. Two conventional periods of: 1—the dominant component $H1_0$; 2—the profile $y_{dhe0}(x)$; 3—the pattern $y_{ap0}(x)$.

As previously stated, related by the first 2DRP in the feed direction, the same abnormal behaviour of the milling tool persists, because for the run-out it is the case that a single tooth is involved in defining the final machined surface, and the conventional angular frequency ω_{He1} = 0.020946 rad/µm defines the wavelength $\lambda_{He1} = 2\pi/\omega_{He1}$ = 299.97 µm, as a conventional period or feed per rotation f_r (very close to that determined for the first profile), which is three times greater than the feed per tooth (100 µm).

A comparison of Figures 31 and 35 shows that, similar to the study in the pick direction, there are also strong similarities between these two different 2DRPs sampled in the feed direction. Figure 36 shows two periods of the overlapped profiles $y_{dhe0}(x)$, Figure 37 shows the overlap of the extended patterns $y_{ap0}(x)$ with two periods, and Figure 38 shows the first two overlapped periods of the $y_{dhe0t}(x)$ profiles.

However, it should be noted that the coincidence of these two $y_{dhe0}(x)$ profiles (Figure 36) is less good than in the case of the $y_{dhe0}(x)$ profiles for 2DRPs sampled in the pick direction (Figure 19). A similar conclusion can be drawn for the fit of the $y_{ap0}(x)$ patterns (by comparing Figures 23 and 37) or for the $y_{dhe0t}(x)$ profiles (Figures 25 and 38). The main reason for these mismatches is the lack of certainty that the two analysed 2DRPs were generated by the same points of the tool edges (an error that must be eliminated for an accurate analysis).

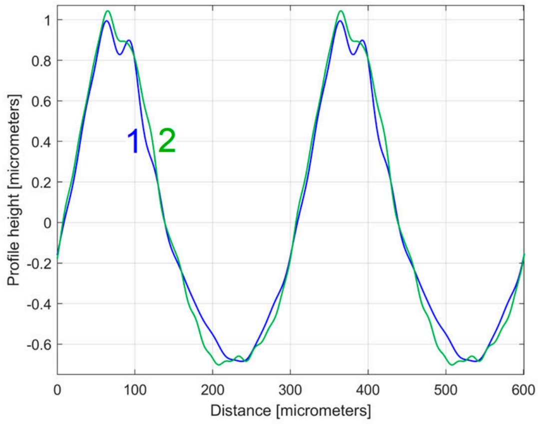

Figure 36. An overlap of the $y_{dhe0}(x)$ profiles (two periods) for the 1st and 2nd 2DRP (1 and 2).

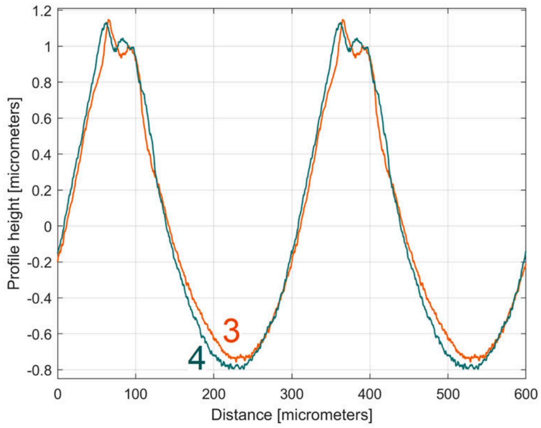

Figure 37. An overlap of the $y_{ap0}(x)$ patterns (two periods) for the 1st and 2nd 2DRP (3 and 4).

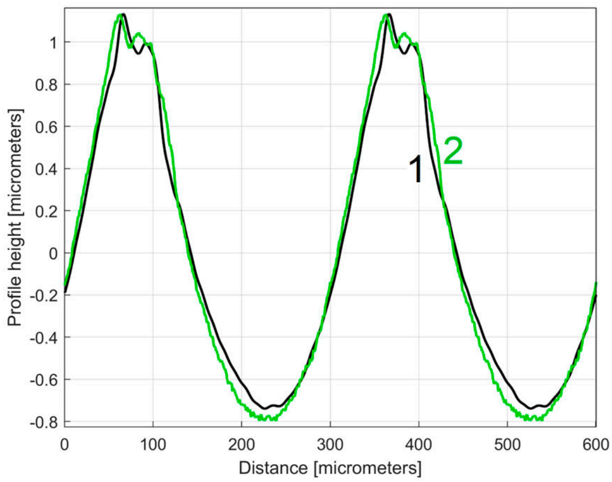

Figure 38. The first two periods of the $y_{dhe0t}(x)$ profiles: 1—for the 1st 2DRP; 2—for the 2nd 2DRP.

As already stated before, the description of the $y_{dhe0t}(x)$ profiles is more reliable (in relation to the $y_{ap0}(x)$ patterns) than the description of the $y_{dhe0}(x)$ profiles.

It is also possible to make a comparison between the FFT spectra of the extrapolated $y_{dhe}(x)$ profiles of both 2DRPs, with $p = 10$, as Figure 39 indicates, with zooming in on the y-axis, as shown in Figure 40. For easier comparison, the FFT spectrum of the extrapolated $y_{dh}(x)$ of the 2nd analysed 2DRP has been artificially shifted by 0.01 μm upwards and 0.0005 μm^{-1} to the right.

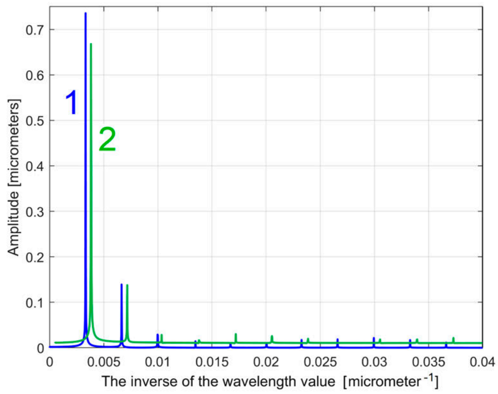

Figure 39. A partial view of the FFT spectra of the extrapolated $y_{dhe}(x)$ profiles with p = 10: 1—for the first 2DRP; 2—for the second 2DRP (shifted).

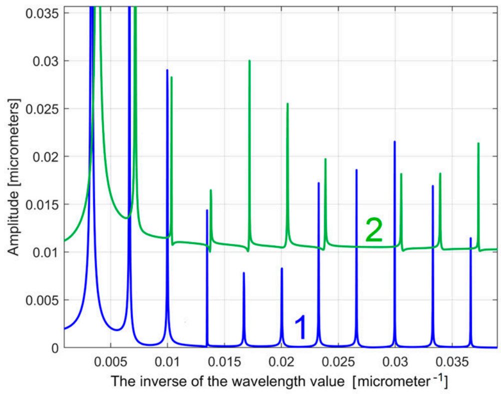

Figure 40. A zoomed image on the y-axis of the FFT spectra from Figure 39.

The similarities between spectra of the extrapolated $y_{dhe}(x)$ profiles are certainly related by conventional peak frequencies but less certainly related by the peak amplitudes.

4. Conclusions

The proposed method for analysing and finding (by curve/signal fitting) the mathematical description of the periodic part of an experimental 2D roughness profile, 2DRP (as a sum of sinusoidal components harmonically correlated), provides reliable results, experimentally confirmed, useful for the characterisation of the milled surface (as a sum of wavinesses in two perpendicular directions), the interaction between the tool and workpiece during the milling process (in particular of flat surfaces machined with a ball nose end mill, constant step over), and the machinability of workpiece materials by a cutting process.

This paper proposes an analytical definition of a periodic profile as the best systematic characterisation (pattern) of an experimental 2DRP sampled with a contact profilometer (in pick and feed directions). A very similar periodic profile (but without an analytical description) is generated by a special type of sample averaging within the experimental 2DRP. These periodic profiles are useful for comparison purposes between different experimental 2DRPs, or to validate a predictive model for 2DRP [12,29,30], or to obtain the mathematical description of the microgeometry of a milled surface.

As suggested during the review of this paper, a possible approach would be to use a curve fitting formula using the milling process parameters (and also tool condition and characteristics) as variables. This will be a challenge for a future approach. In the current approach (valid for any type of evolution of a physical quantity with a dominant periodic component), the fitting formula (a sinusoidal function), repetitively applied to obtain the best characterisation of the 2DRP profile as the sum of significantly harmonically correlated sinusoidal components (used as a pattern), indirectly provides some information related to the milling process, such as the peak to peak amplitude of the resultant is the pick-interval or feed-interval scallop height, and the conventional angular frequency of the fundamental describes the pick feed (pick direction 2DRP) or feed per tooth (feed direction 2DRP) as a relationship between tool rotation speed and feed rate. The analysis of the shapes of the experimental 2DRP patterns and the highlighting of differences with the theoretical patterns allows for the qualitative description of some anomalies of the machining process, such as the tool run-out (already shown in this paper), tool wear or cutting edges fracture, elastic bending deformation of the tool, etc.

This paper proves that the mathematical extrapolation of the analytically defined periodic profile of 2DRP improves the availability of a known but underutilized method of roughness analysis based on the spectrum of the periodic profile (seen as a time-dependent signal) generated by Fast Fourier Transform (FFT), with a low (conventional) frequency resolution.

Of course, generalisation of these results to the analysis of other types of milled surfaces, machined on other milling machines, with other types of tools on other workpiece materials (and possibly using other roughness sampling methods), is entirely feasible in a future approach.

As a future approach, we also intend to extend this study to the investigation of the 3D mathematical description of the roughness microgeometry of the complex milled surfaces, experimentally sampled with a suitable optical system.

Author Contributions: Conceptualization, M.H. and F.C.; methodology, M.H., E.P., C.G.D. and A.M.; software M.H. and C.G.D.; validation F.C., E.P. and A.M.; investigation E.P., M.H. and D.-F.C.; resources C.G.D. and D.-F.C.; data curation, M.H., E.P., C.G.D., A.M. and D.-F.C.; writing—original draft preparation, M.H., F.C., C.G.D. and A.M.; writing—review and editing, E.P. and D.-F.C.; supervision and project administration, M.H. and C.G.D.; funding acquisition, C.G.D. All authors have read and agreed to the published version of the manuscript.

Funding: This work was supported by Gheorghe Asachi Technical University of Iasi, Romania.

Institutional Review Board Statement: Not applicable.

Informed Consent Statement: Not applicable.

Data Availability Statement: The data presented in this paper are available upon request addressed to the corresponding author. The data are not publicly available due to privacy.

Acknowledgments: Many thanks to Mitutoyo Romania for the donation of the roughness measuring equipment. We would like to thank our colleagues Neculai-Eugen Seghedin and Eugen Carata who previously equipped the department with several modern CNC machines and equipment. Some of these were used in this study. We also thank our colleague Florentin Cioata for his support and advice.

Conflicts of Interest: The authors declare no conflicts of interest.

References

1. Chen, J.S.; Huang, Y.K.; Chen, M.S. A study of the surface scallop generating mechanism in the ball-end milling process. *Int. J. Mach. Tools Manuf.* **2005**, *45*, 1077–1084. [CrossRef]
2. Costes, J.P. A predictive surface profile model for turning based on spectral analysis. *J. Mater. Process. Technol.* **2013**, *213*, 94–100. [CrossRef]
3. Ren, Z.; Fang, Z.; Kobayashi, G.; Kizaki, T.; Sugita, N.; Nishikawa, T.; Kugo, J.; Nabata, E. Influence of tool eccentricity on surface roughness in gear skiving. *Precis. Eng.* **2020**, *63*, 170–176. [CrossRef]
4. Álvarez-Flórez, J.; Buj-Corral, I.; Vivancos-Calvet, J. Analysis of roughness, force and vibration signals in ball-end milling processes. *J. Trends Dev. Mach. Assoc. Technol.* **2015**, *19*, 1–4.
5. Zahaf, M.Z.; Benghersallah, M. Surface roughness and vibration analysis in end milling of annealed and hardened bearing steel. *Measur. Sens.* **2021**, *13*, 100035. [CrossRef]
6. Bai, J.; Zhao, H.; Zhao, L.; Cao, M.; Duan, D. Modelling of surface roughness and studying of optimal machining position in side milling. *Int. J. Adv. Manuf. Technol.* **2021**, *116*, 3651–3662. [CrossRef]
7. Grzesik, W.; Brol, S. Wavelet and fractal approach to surface roughness characterization after finish turning of different workpiece materials. *J. Mater. Process. Technol.* **2009**, *209*, 2522–2531. [CrossRef]
8. Drbúl, M.; Martikáň, P.; Bronček, J.; Litvaj, I.; Svobodová, J. Analysis of roughness profile on curved surfaces. *MATEC Web Conf.* **2018**, *244*, 01024. [CrossRef]

9. Dumitras, C.G.; Chitariu, D.F.; Chifan, F.; Lates, C.G.; Horodinca, M. Surface Quality Optimization in Micromachining with Cutting Tool Having Regular Constructive Geometry. *Micromachines* **2022**, *13*, 422. [CrossRef]
10. Seyedi, S.S.; Shabgard, M.R.; Mousavi, S.B.; Heris, S.Z. The impact of SiC, Al_2O_3, and B_2O_3 abrasive particles and temperature on wear characteristics of 18Ni (300) maraging steel in abrasive flow machining (AFM). *Int. J. Hydrogen Energy* **2021**, *46*, 33991–34001. [CrossRef]
11. Krolczyk, G.; Legutko, S. Experimental analysis by measurement of surface roughness variations in turning process of duplex stainless steel. *Metrol. Meas. Syst.* **2014**, *XXI*, 759–770. [CrossRef]
12. Shang, S.; Wang, C.; Liang, X.; Cheung, C.F.; Zheng, P. Surface roughness prediction in ultra-precision milling: An extreme learning machine method with data fusion. *Micromachines* **2023**, *14*, 2016. [CrossRef]
13. Wang, N.; Jiang, F.; Zhu, J.; Xu, Y.; Shi, C.; Yan, H.; Gu, C. Experimental study on the grinding of an Fe-Cr-Co permanent magnet alloy under a small cutting depth. *Micromachines* **2022**, *13*, 1403. [CrossRef] [PubMed]
14. Li, J.; Xu, W.; Shen, T.; Jin, W.; Wu, C. Evaluating surface roughness of curved surface with circular profile based on arithmetic circular arc fitting. *AIP Adv.* **2023**, *13*, 125312. [CrossRef]
15. Kundrák, J.; Felhő, C.; Nagy, A. Analysis and prediction of roughness of face milled surfaces using CAD model. *Manuf. Technol.* **2022**, *22*, 555–572. [CrossRef]
16. Lazkano, X.; Aristimunno, P.X.; Aizpuru, O.; Arrazola, P.J. Roughness maps to determine the optimum process window parameters in face milling. *Int. J. Mech. Sci.* **2022**, *221*, 107191. [CrossRef]
17. Varga, J.; Ižol, P.; Vrabel', M.; Kaščák, L.; Drbúl, M.; Brindza, J. Surface Quality Evaluation in the Milling Process Using a Ball Nose End Mill. *Appl. Sci.* **2023**, *13*, 10328. [CrossRef]
18. Żurawski, K.; Żurek, P.; Kawalec, A.; Bazan, A.; Olko, A. Modeling of Surface Topography after Milling with a Lens-Shaped End-Mill, Considering Runout. *Materials* **2022**, *15*, 1188. [CrossRef]
19. Palani, S.; Natarajan, U. Prediction of surface roughness in CNC end milling by machine vision system using artificial neural network based on 2D Fourier transform. *Int. J. Adv. Manuf. Technol.* **2011**, *54*, 1033–1042. [CrossRef]
20. Lou, Z.; Yan, Y.; Wang, J.; Zhang, A.; Cui, H.; Li, C.; Geng, Y. Exploring the structural color of micro-nano composite gratings with FDTD simulation and experimental validation. *Opt. Express* **2024**, *32*, 2432–2451. [CrossRef]
21. Zeng, Q.; Qin, Y.; Chang, W.; Luo, X. Correlating and evaluating the functionality-related properties with surface texture parameters and specific characteristics of machined components. *Int. J. Mech. Sci.* **2018**, *149*, 62–72. [CrossRef]
22. Filtration Techniques for Surface Texture. Available online: https://guide.digitalsurf.com/en/guide-filtration-techniques.html (accessed on 15 February 2024).
23. Josso, B.; Burton, D.R.; Lalor, M.J. Frequency normalised wavelet transform for surface roughness analysis and characterisation. *Wear* **2002**, *252*, 491–500. [CrossRef]
24. Josso, B.; Burton, D.R.; Lalor, M.J. Wavelet strategy for surface roughness analysis and characterization. *Comput. Methods Appl. Mech. Eng.* **2001**, *191*, 829–842. [CrossRef]
25. Wang, X.; Shi, T.; Liao, G.; Zhang, Y.; Hong, Y.; Chen, K. Using wavelet packet transform for surface roughness evaluation and texture extraction. *Sensors* **2017**, *17*, 933. [CrossRef]
26. Hao, H.; He, D.; Li, Z.; Hu, P.; Chen, Y.; Tang, K. Efficient cutting path planning for a non-spherical tool based on an iso-scallop height distance field. *Chin. J. Aeronaut.* **2023**, *in press*, *uncorrected proof*. [CrossRef]
27. Horodinca, M.; Bumbu, N.-E.; Chitariu, D.-F.; Munteanu, A.; Dumitras, C.-G.; Negoescu, F.; Mihai, C.-G. On the behaviour of an AC induction motor as sensor for condition monitoring of driven rotary machines. *Sensors* **2023**, *23*, 488. [CrossRef]
28. Lecture: Sums of Sinusoids (of Different Frequency). Available online: http://www.spec.gmu.edu/~pparis/classes/notes_201/notes_2019_09_12.pdf (accessed on 15 February 2024).
29. Chen, C.-H.; Jeng, S.-Y.; Lin, C.-J. Prediction and analysis of the surface roughness in CNC end milling using neural networks. *Appl. Sci.* **2022**, *12*, 393. [CrossRef]
30. Peng, Z.; Jiao, L.; Yan, P.; Yuan, M.; Gao, S.; Yi, J.; Wang, X. Simulation and experimental study on 3D surface topography in micro-ball-end milling. *Int. J. Adv. Manuf. Technol.* **2018**, *96*, 1943–1958. [CrossRef]